2008 SUMMER RESEARCH PROGRAM FOR HIGH SCHOOL JUNIORS

AT THE

UNIVERSITY OF ROCHESTER'S

LABORATORY FOR LASER ENERGETICS

STUDENT RESEARCH REPORTS

PROGRAM COORDINATOR

Dr. R. Stephen Craxton

March 2009 **Laboratory Report 357**

2008 SUMMER RESEARCH PROGRAM FOR HIGH SCHOOL JUNIORS
AT THE
UNIVERSITY OF ROCHESTER'S
LABORATORY FOR LASER ENERGETICS

STUDENT RESEARCH REPORTS

PROGRAM COORDINATOR

Dr. R. Stephen Craxton

LABORATORY FOR LASER ENERGETICS
University of Rochester
250 East River Road
Rochester, NY 14623-1299

During the summer of 2008, 15 students from Rochester-area high schools participated in the Laboratory for Laser Energetics' Summer High School Research Program. The goal of this program is to excite a group of high school students about careers in the areas of science and technology by exposing them to research in a state-of-the-art environment. Too often, students are exposed to "research" only through classroom laboratories, which have prescribed procedures and predictable results. In LLE's summer program, the students experience many of the trials, tribulations, and rewards of scientific research. By participating in research in a real environment, the students often become more excited about careers in science and technology. In addition, LLE gains from the contributions of the many highly talented students who are attracted to the program.

The students spent most of their time working on their individual research projects with members of LLE's scientific staff. The projects were related to current research activities at LLE and covered a broad range of areas of interest including experimental diagnostic development and analysis, computational modeling of implosion hydrodynamics and radiation physics, database development, materials science, cryogenic target characterization, target vibration analysis, and engineering device development. The students, their high schools, their LLE supervisors, and their project titles are listed in the table. Their written reports are collected in this volume.

The students attended weekly seminars on technical topics associated with LLE's research. Topics this year included laser physics, fusion, holography, fiber optics, optical manufacturing, the physics of music, and electronic paper. The students also received safety training, learned how to give scientific presentations, and were introduced to LLE's resources, especially the computational facilities.

The program culminated on 27 August with the "High School Student Summer Research Symposium," at which the students presented the results of their research to an audience including parents, teachers, and LLE staff. Each student spoke for approximately ten minutes and answered questions. At the symposium the 12th annual William D. Ryan Inspirational Teacher Award was presented to Ms. Jane Bowdler, a mathematics teacher at Brockport High School. This award honors a teacher, nominated by alumni of the LLE program, who has inspired outstanding students in the areas of science, mathematics, and technology. Ms. Bowdler was nominated by Priya Rajasethupathy, a participant in the 2000 Summer Program.

A total of 233 high school students have participated in the program since it began in 1989. The students this year were selected from approximately 50 applicants. Each applicant submitted an essay describing their interests in science and technology, a copy of their transcript, and a letter of recommendation from a science or math teacher.

In the past, several participants of this program have gone on to become semifinalists and finalists in the prestigious, nationwide Intel Science Talent Search. This tradition of success continued this year with the selection of two students (Jay Amin and Rachel Kurchin) as among the 300 semifinalists nationwide in this competition.

LLE plans to continue this program in future years. The program is strictly for students from Rochester-area high schools who have just completed their junior year. Application information is mailed to schools and placed on the LLE website in early February with an application deadline near the end of March. For more information about the program, please contact Dr. R. Stephen Craxton at LLE.

This program was supported by the U.S. Department of Energy Office of Inertial Confinement Fusion under Cooperative Agreement No. DE-FC52-08NA28302.

High School Students and Projects (Summer 2008)			
Name	**High School**	**Supervisor**	**Project Title**
Jay Amin	Rush-Henrietta	C. Dorrer	Characterization of Ultrashort Optical Pulses by Spectral Shearing Interferometry
Chris Baldwin	Honeyoye Falls-Lima	R. W. Kidder	Exploring Metadata for Laser Diagnostics and Control Systems on the OMEGA EP Laser System
Mohammad Husain Bawany	Brighton	R. Janezic	Development of the Cryogenic Target Information System
Krysta Boccuzzi	Mercy	E. Kowaluk	Investigating the Causes of and Possible Remedies for Sensor Damage in Digital Cameras Used on the OMEGA Laser Systems
David Brummond	Honeyoye-Falls Lima	C. Stoeckl	Controlling a Data Acquisition System with Java
Nicholas Hensel	Fairport	D. Jacobs-Perkins	High-Speed Measurements of Target-Support Vibrations Using Line-scan Cameras
Rachel Kurchin	Harley	R. S. Craxton, M. D. Wittman	Characterization of a Cryogenic Fuel Capsule in a Transparent Hohlraum
Alexis Kurmis	Greece Arcadia	T. C. Sangster, T. Duffy	Counting System for the Carbon Activation Diagnostic
Mangaladevi Patil	Pittsford Mendon	K. L. Marshall	Contamination Resistant Sol-Gel Antireflective Coatings by Vapor-Phase Silanization
Angela Ryck	Fairport	R. S. Craxton	Optimization of Cone-in-Shell Implosions
Collin Sowinski	Penfield	W. T. Shmayda	Minimization of Tritium Contamination on Surfaces
Jack Stokes	Fairport	S. Ingraham, D. J. Lonobile	Investigation of Brushless DC Motor Commutation Techniques
James Tsay	Phillips Academy	R. Epstein	K-Shell Emission-Line Backlighter Source Optimization
Brian Wang	Webster Thomas	J. F. Myatt, P. A. Jaanimagi	The Effects of Space Charge on Electron Pulse Broadening in Streak Cameras
Bradley Wideman	Fairport	F. J. Marshall	Automated Determination of Crystal Reflectivity in the X-ray Laboratory

Characterization of Ultrashort Optical Pulses by Spectral Shearing Interferometry

Jay Amin

Characterization of Ultrashort Optical Pulses by Spectral Shearing Interferometry

Jay Amin

Rush-Henrietta Senior High School
Henrietta, NY

Advisor: Dr. Christophe Dorrer

Laboratory for Laser Energetics
University of Rochester
Rochester, NY

Summer 2008

Abstract

Ultrashort optical pulses are integral to various fields. Thus, the characterization of these pulses is crucial in understanding the results of experiments and applications using them. A diagnostic for laser systems was created to determine the shapes of ultrashort optical pulses using the principle of spectral shearing interferometry (SSI). By strongly chirping an optical pulse using a pair of parallel diffraction gratings and mixing it in a lithium triborate LiB_3O_5 (LBO) nonlinear crystal with two test pulse replicas delayed by 1.9 ps, sum harmonic generation of the input laser beam was achieved. The SSI interferogram was then characterized by an Ocean Optics Spectrometer using a novel “2ω method” to determine pulse characteristics. The diagnostic was tested on the diagnostic compressor of the Multi-TeraWatt (MTW) laser system at the Laboratory for Laser Energetics, successfully determining the compressor distance for which the optical pulses were shortest.

1. Introduction

Ultrashort optical pulses are widely used in several areas of physics. Common usages are in high-speed optical communications and high-temporal-resolution spectroscopy of physical systems. In optical telecommunications, using the shortest optical pulses possible allows for the greatest amount of data to be sent in a given period. Other usages include high-intensity laser-matter interactions. Using chirped pulse amplification, a short optical pulse can be stretched, amplified, and compressed, producing a final short pulse with very high power.[1,2] Experimental usages of ultrashort optical pulses cannot be deemed accurate unless the shape of the test pulses is as intended. Thus knowing the temporal shape of optical pulses is crucial to scientific research.

The most significant obstacle to determining the shapes of pulses is that direct measurements in the time domain using a photodetector are simply not fast enough, for ultrashort pulses are on the order of femtoseconds. Therefore, measurements must be made in the spectral domain and the temporal shape of the pulse must be calculated from the data using a Fourier transform. There are currently three categories of methods used to accurately determine the shapes of these pulses, fundamental to physical theories: spectrographic, tomographic, and interferometric.[3,4] The spectrographic methods are most commonly used, with frequency-resolved optical gating (FROG)[5], frequency-domain phase measurements (FDPM)[6], and the spectrally and temporally resolved upconversion technique (STRUT)[7] among the many that require sophisticated data inversion techniques and algorithms to reconstruct the electric field. Tomography, though having a noniterative data inversion method[8], requires the one-dimensional field to be represented in two dimensions, thus increasing greatly the amount of data that must be collected. Interferometric techniques, therefore, are the simplest direct method that can be used to characterize optical pulses using properties such as electric field and phase, for they only need a one-dimensional data set to model the one-dimensional field, and can utilize a simple direct data inversion to determine pulse characteristics. The novel, self-referencing interferometric technique used by Iaconis and Walmsley[9], referred to as spectral phase interferometry for direct electric-field reconstruction (SPIDER), is employed in this study. This method is particularly popular for its collinear geometry, its lack of moving parts, and its lack of reliance on a fast detector or a well-characterized reference pulse.[9]

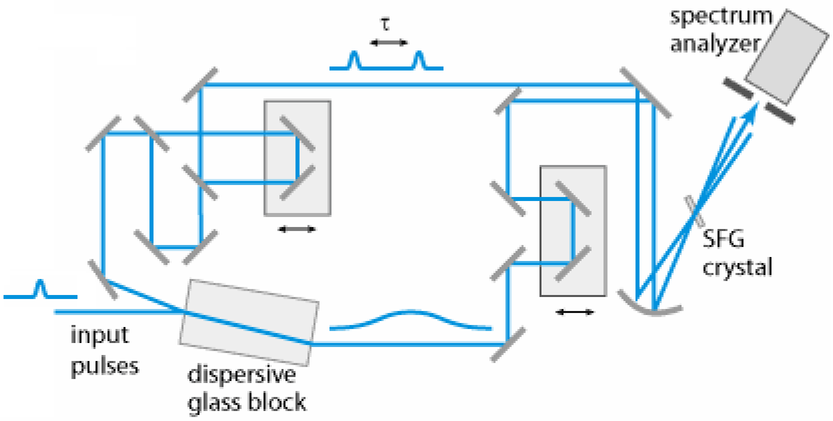

Figure 1. A setup for ultrashort optical pulse characterization using the SPIDER method.

As shown in Fig. 1, the key to the SPIDER method is splitting the test pulse in two, so that one pulse can be split into two identical copies separated by a time delay using a Michelson interferometer, for example, and the other can be stretched with a dispersive block, for example. Stretching a pulse chirps it so that its frequency varies linearly with time. Spectral shearing occurs when the chirped pulse and the two identical copies of the test pulse are mixed in a sum-frequency generating (SFG) crystal. The spectral shear refers to the difference in optical frequencies represented by the two identical copies when overlapped on the chirped pulse after upconversion. This process was utilized, in concept, for the diagnostic created and described in this paper. However, key changes were made that allow the device to be more stable, simple, and cost effective. These changes include replacing the Michelson interferometer with an etalon, using a grating pair to stretch the pulse rather than a dispersive glass block, and converging the two focused pulse beams with a planoconvex lens instead of a convex mirror.

2. Spectral Shearing Interferometry

Since photodetectors were too slow to make direct measurements of ultrashort optical pulses, spectral shearing interferometry (SSI) based diagnostics were created so that we could indirectly make measurements of the ultrafast pulses using these photodetectors. A commonly-used spectral shearing interferometer is shown in Fig. 2.[3] The interferometer creates two replicas of the test pulse using a beamsplitter. One beam is delayed by a linear spectral phase modulator and the other is frequency shifted by a linear temporal phase modulator. Then, the two pulses are recombined on another beamsplitter, allowing the resulting signal to be resolved using a spectrometer.

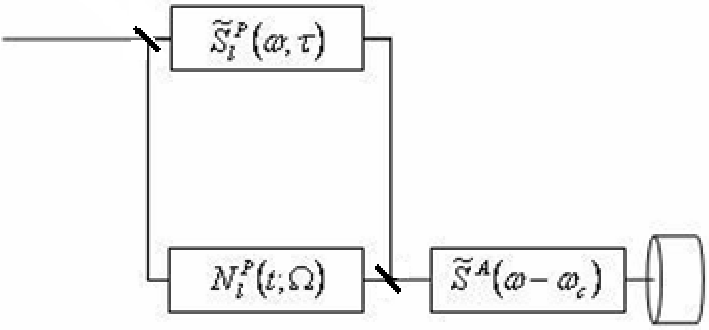

Figure 2. An SSI-based interferometer with two parallel phase filters.

The temporal phase modulator shifts the spectrum of the input pulse by Ω, noted in the figure by its response function

$$N^P{}_l\,(t;\,\Omega) = \exp[-i\Omega t] \qquad (1)$$

where *N* is the nonstationary filter, *P* indicates that it is a phase-only filter, and *l* means the phase modulation is linear. Similarly, the linear spectral phase modulator has a response function of

$$\tilde{S}^{P}{}_{l}(\omega;\ \tau) = \exp[i\omega\tau] \tag{2}$$

which states that the input pulse is delayed by τ. The signal after the two pulses are combined and passed through a spectrometer is

$$D(\omega_c;\ \Omega,\ \tau) = \int d\omega \left|\ \tilde{S}^{A}(\omega - \omega_0)\cdot\{[\int d\omega'\ \tilde{N}^{P}{}_{l}(\omega' - \omega_0)\ \tilde{E}(\omega')] + \tilde{S}^{P}{}_{l}(\omega)\ \tilde{E}(\omega)\}\right|^2 \tag{3}$$

where the electric fields of the optical pulses are recorded as a function of the filter parameters for *N* and the Fourier transform of the pulse's output energy, $\tilde{E}(\omega)$, is

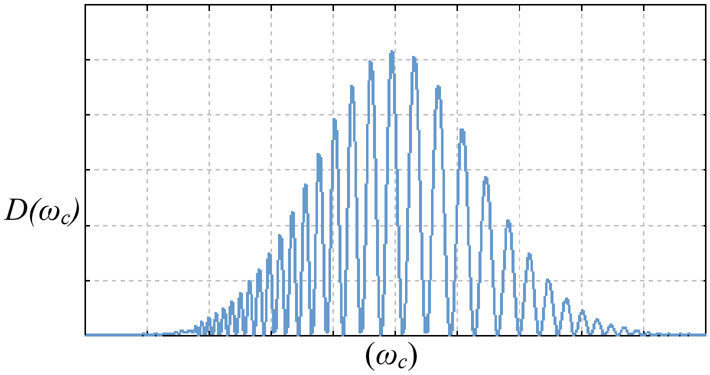

Figure 3. A general spectral interferogram of the interference between two spectrally sheared pulses.

recorded as a function of the filter parameters for *S*. Thus, it is also multiplied by the amplitude-only time-stationary filter of the spectrometer, $\tilde{S}^{A}$, which was used to resolve the signal. Since the spectral shift and temporal delay are fixed, the signal can be re-expressed as

$$D(\omega_c) = |\tilde{E}(\omega_c - \Omega)|^2 + |\tilde{E}(\omega_c)|^2 + 2|\tilde{E}(\omega_c - \Omega)\,\tilde{E}(\omega_c)|\cos[\Phi_\omega(\omega_c - \Omega) - \Phi_\omega(\omega_c) - \tau\omega_c]. \quad (4)$$

where $D(\omega_c)$ is a standard shearing interferogram as shown in Fig. 3.

3. Determining the Spectral Phase

The spectral phase of the data can be obtained from the interferogram by analyzing the relative positions of the fringes which are nominally spaced in frequency by $2\pi/\tau$ as shown in Fig. 3. This is done by rewriting the interferogram as

$$D(\omega_c) = D^{(dc)}(\omega_c) + \exp[-i\tau\omega_c]D^{(-ac)}(\omega_c) + \exp[i\tau\omega_c]D^{(+ac)}(\omega_c). \quad (5)$$

where

$$D^{(dc)}(\omega_c) = |\tilde{E}(\omega_c - \Omega)|^2 + |\tilde{E}(\omega_c)|^2. \quad (6)$$

$$D^{(-ac)}(\omega_c) = |\tilde{E}(\omega_c - \Omega)\,\tilde{E}(\omega_c)|\,\exp[i(\Phi_\omega(\omega_c - \Omega) - \Phi_\omega(\omega_c))]. \quad (7)$$

and thus

$$\mathrm{D}^{(+\mathrm{ac})}(\omega_c) = |\tilde{E}(\omega_c - \Omega)\,\tilde{E}(\omega_c)|\,\exp[-i(\Phi_\omega(\omega_c - \Omega) - \Phi_\omega(\omega_c))]. \quad (8)$$

This rewritten interferogram is Fourier transformed as first shown by Takeda, et al.[10]

$$\begin{aligned}\tilde{D}(t) = {} & FT\{D^{(dc)}(\omega_c);\ \omega_c \rightarrow t\} \\ & + FT\{D^{(-ac)}(\omega_c);\ \omega_c \rightarrow t + \tau\} \\ & + FT\{D^{(+ac)}(\omega_c);\ \omega_c \rightarrow t - \tau\}. \quad (9)\end{aligned}$$

Fig. 4 shows the Fourier transform of the interferogram. The *dc* term centered at t=0 is the sum of the two spectra for the pulses, and since having no phase information, this is filtered away. The *ac* term at $-\tau$ is also filtered away because only one *ac* term, that at $t=\tau$, is needed to generate the spectral phase. This is accomplished with a fourth-order super-Gaussian filter, $H(t)$, of full width τ and centered at $t=\tau$:

$$\tilde{D}^{(filter)}(t) = H(t-\tau)\,\tilde{D}(t) = FT\{D^{(+ac)}(\omega_c);\ \omega_c \rightarrow t-\tau\}. \qquad (10)$$

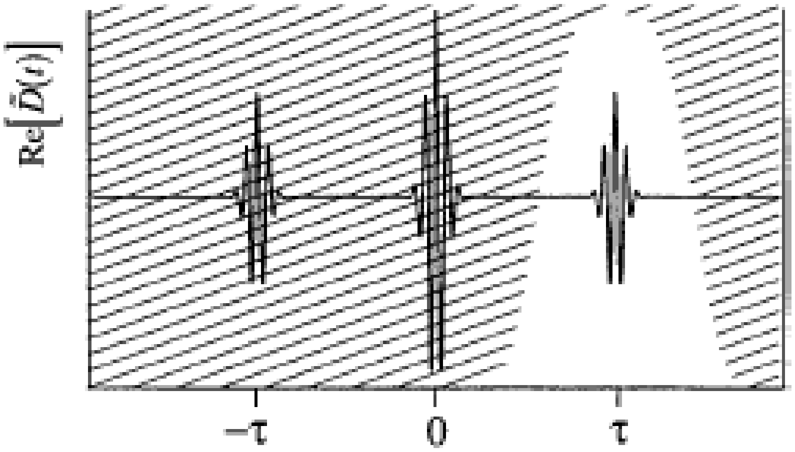

Figure 4. The Fourier transform of the interferogram in Fig. 3. The shaded region represents the section of the function that is ignored by the filter.

The desired spectral phase difference is simply the argument of the inverse transform of $\tilde{D}^{(filter)}(t)$, which is also the isolated ac term is:

$$\Phi_\omega(\omega_c) - \Phi_\omega(\omega_c - \Omega) + \tau\omega_c = \arg\,[D^{(+ac)}(\omega_c)] = \arg\,[IFT\{\tilde{D}^{(filter)}(t);\ t \rightarrow \omega_c\}]. \qquad (11)$$

Then the linear phase term $\tau\omega_c$ must be removed by subtracting a baseline linear phase. This baseline linear phase is determined by using an interferometer to record the spectral interferogram of the pair of pulses without the spectral shear. Finally, the spectral phase can be reconstructed from the spectral phase difference by concatenation.

Concatenation returns the spectral phase at intervals of Ω across the spectrum, so the spectral phase at some frequency is set equal to zero allowing the spectral phase for all frequencies to be multiples of the spectral shear away from ω_0. By adding all the phase differences, the phase for frequencies separated by the spectral shear is reconstructed.

4. Methodology

The diagnostic which was built utilizes the SSI method of SPIDER with the previously mentioned novel innovations. The key elements in these innovations, outlined in Fig. 5, will be discussed in this section.

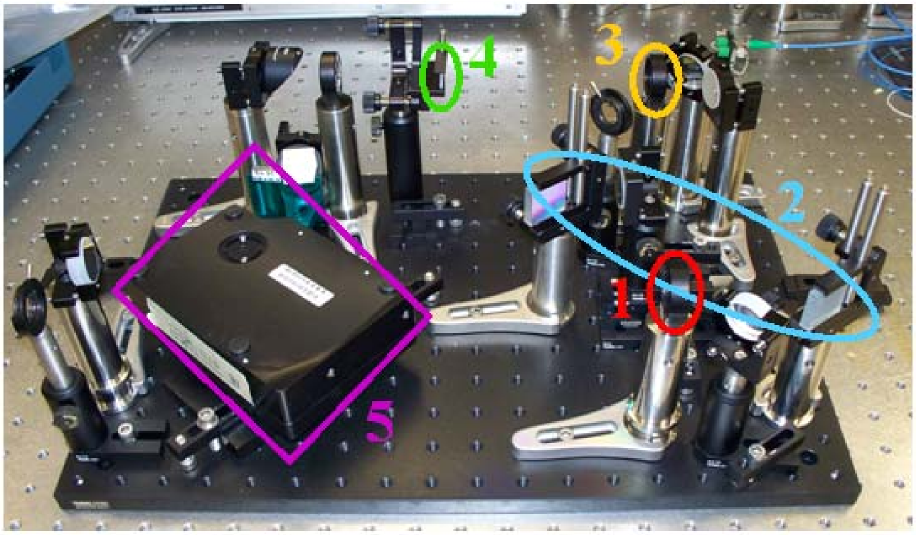

Figure 5. The SSI diagnostic built for this study. Labeled are the key elements of the diagnostic. (1) Etalon (2) Double-pass two-grating compressor (3) Planoconvex Lens (4) Nonlinear crystal (5) Ocean Optics Spectrometer.

4.1 Generation of Time-Delayed Replicas Using an Etalon

There are two limitations to the value that can be used for the relative delay between pulses in the test pair. The delay, τ, must not be so large that the spectrometer cannot resolve the fringes in the interferogram, but not so small that the data inversion routine cannot separate the *dc* and *ac* terms. Therefore, to generate the time-delayed replicas, there are two main approaches: the usage of an interferometer, such as the Michelson; or an etalon. The Michelson interferometer (Fig. 6) utilizes two gold-plated beamsplitters: one to divide the incoming test pulse into two arms, one of which has a variable distance due to the mounting of a set of perpendicular mirrors on a translation stage, and the other to recombine the pulses from the two arms. One the other hand, the etalon is a simple glass microscope slide that reflects ~4% of the incoming light on each of its two faces, separated by 0.20 mm. This delays the reflections from each face in this diagnostic by nearly 1.9 picoseconds. Interferometric accuracy requires stability in τ since jitter between the test pulses can destroy phase information. An etalon is unaffected by such vibrations, while a Michelson requires additional stabilization. The etalon is more stable, compact, and less expensive than a Michelson interferometer,

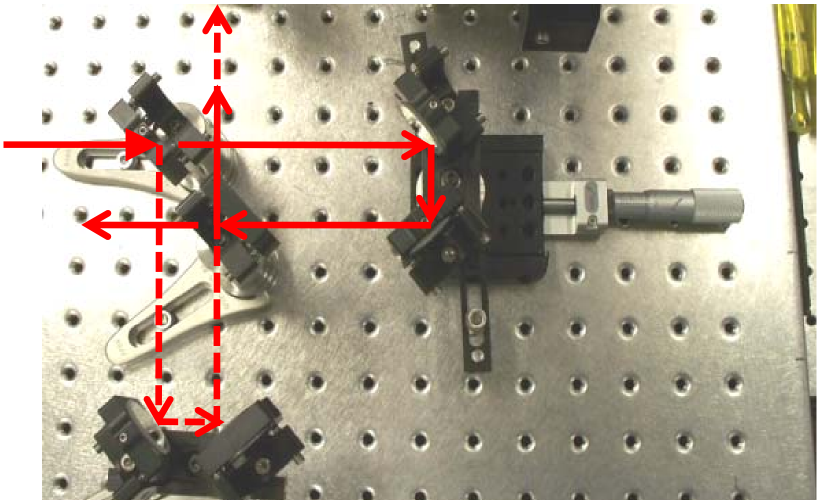

Figure 6. A Michelson interferometer built during this internship for another project. Solid red arrows indicate transmitted beams through the beamsplitters and the dashed arrows represent reflected beams.

which must be carefully aligned and checked before every test due to its numerous components. Therefore, an etalon was used.

4.2 Generation of the Chirped Pulse

The etalon allows ~92% of the incoming light to transmit directly through into what is called the double-pass two-grating compressor. By arranging two diffraction gratings parallel to each other so that the diffracted beam of one grating diffracts off the other, ultrashort pulses are stretched and chirped.[11] The diffraction of the input test pulse in the compressor effectively chirps the pulse. This means that the different frequencies of the light are separated so that they arrive in a staggered fashion with respect to one another. The gratings in the device created are ruled with 1200 lines/mm and the second order dispersion of the chirped pulse caused by these gratings shifts the phase by a stretcher dispersion of $\Phi'' = -1.3\ \mathrm{ps}^2$. Therefore, since $\Omega = -\tau / \Phi''$, Ω, the spectral

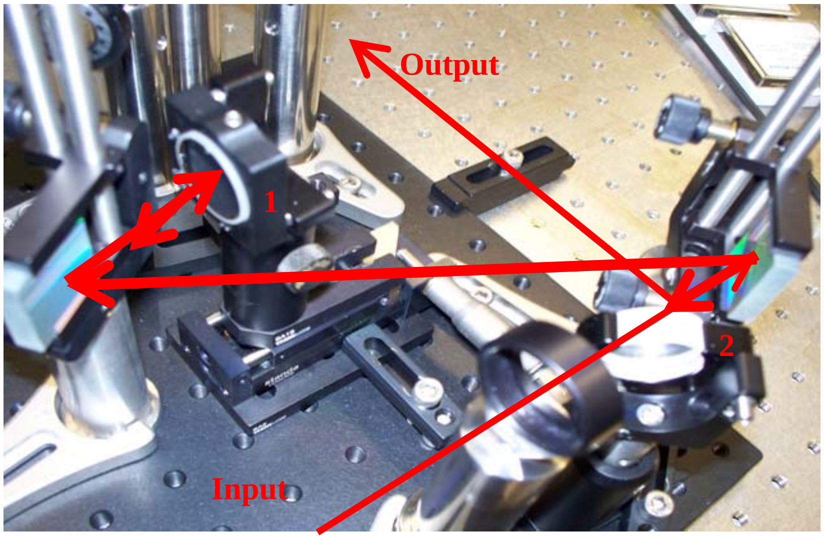

Figure 7. The input pulse travels along the same path as it exits but at a different angle, due to the tilting of mirror #1 (on the left). This allows the beam to reflect off mirror #2 in the bottom right corner, sending the chirped pulse to the output of the compressor.

separation of the two replicas in the pulses reflected off the etalon after nonlinear conversion with the chirped pulse will be 1.45 ps^{-1}, which is roughly a wavelength separation of 0.8 nm. A particularly useful feature of the double-pass two-grating compressor created in the diagnostic was the mounting of a mirror on a translation stage (mirror #1 on Fig. 7), perpendicular to the beam diffracted by the second diffraction grating. This ensured that the beam was collimated when entering the compressor on the second pass and allowed the compressor distance to be changed so that the chirped pulse and the sheared replicas would temporally overlap in the nonlinear crystal used for sum harmonic generation.

4.3 Sum Harmonic Generation in a Nonlinear Crystal

Before the two replicas of the test pulse and the chirped pulse beam can be mixed in the nonlinear crystal they must be focused. A planoconvex lens with a focal length of 15 cm was used to focus the two parallel input beams, causing them to intersect in the crystal (Fig. 8). This is particularly significant because when the beam from the

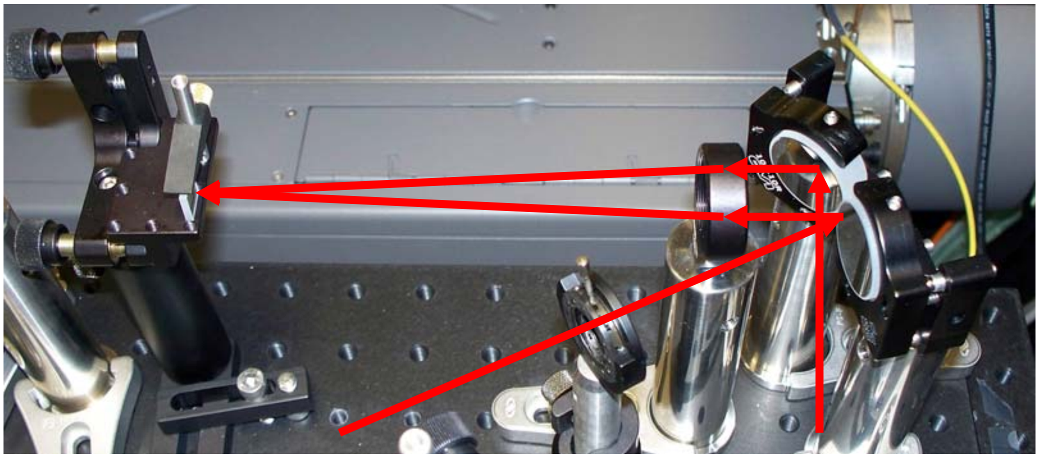

Figure 8. The alignment mirrors on the right redirect the chirped pulse beam and the replicated pulse beam, making them parallel as they enter the planoconvex lens. The lens focuses the two beams so that they intersect in the nonlinear crystal.

compressor is overlapped with the beam reflected from the etalon, each of the replicas in the reflected beam off the etalon should match up with a distinct frequency on the chirped pulse. Thus, the pulses can be separated temporally by τ and also separated spectrally by Ω. To mix the two signals into one that can be resolved by a spectrometer, they are nonlinearly converted. Though often generalized as sum frequency generation, second harmonic generation (SHG) doubles the frequency of the input light source, thus halving the wavelength. Therefore, the Nd:YLF laser source used that operated at 1053 nm was effectively converted to 526.5 nm as the frequency changed from ω to 2ω, converting the input beam of infrared light to green light. An interferogram in the green is therefore read by the spectrometer.

The crystal used was a 2 mm biaxial LBO, LiB_3O_5, which was cut for SHG phase-matching at 11.8°. The Type I SHG caused by this crystal guarantees that the ordinary polarized inputs of the chirped pulse and the sheared pulses will create a pulse of twice the original frequency. Both the chirped pulse and sheared pulse beam polarizations were aligned with the ordinary axes of the crystal. The beams were carefully overlapped in the crystal temporally by adjusting the path lengths of the reflected and transmitted beams from the etalon, and spatially, using the alignment mirrors. By carefully adjusting the x- and y-orientation angles of the crystal, SHG was optimized to yield a measurable signal.

4.4 Resolving the Spectral Interferogram

A CCD array at the output of a spectrometer can resolve the spectral interferogram, once properly calibrated. The spectrometer used, an Ocean Optics HR2000, has a resolution of 0.5 nm at 1053 nm. Thus it could effectively resolve the fringes separated by 2π/τ, a delay of 1.9 ps. Fig. 9 is a sample SSI interferogram of the upconverted pulses after passing through the diagnostic.

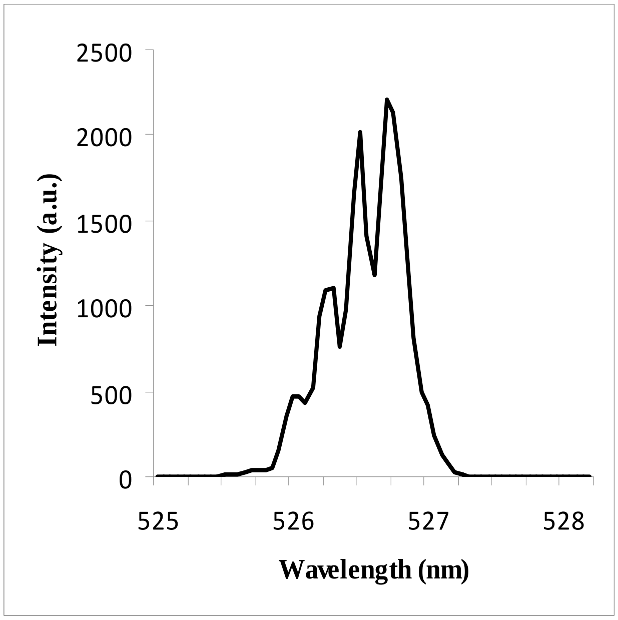

Figure 9. The SSI interferogram from the diagnostic. The ideal Gaussian shape of the pulse is not clearly apparent due to the low resolution of the spectrometer on this scale, which shows fringe points. However, the pulse is shown to have been effectively upconverted due to the centering on $\lambda_{input}/2$, which is 526.5 nm.

The technique created and employed in the capturing of the interferogram was aptly dubbed the "2*ω* method." Spectrometers contain a diffraction grating that allows the input pulse to have all of its frequencies separated, similar to the chirping of the double-pass two-grating compressor in the diagnostic (see Fig. 10). The properties of the diffraction grating can be summarized by the equation

$$\sin(\theta_i) + \sin(\theta_d) = n\lambda / d \tag{12}$$

where θ_i is the incidence angle on the grating, θ_d is the diffracted angle off the grating, n is the order of diffraction, λ is the wavelength of the input light, and d is the groove spacing of the diffraction grating. The unique aspect of this simple equation in the operation of the diagnostic is that both the SSI interferogram following nonlinear conversion and the spectrum of the pulse under test can be determined by the spectrometer without additional calibration. The quantities *d* and $\sin(\theta_i)$ are constant because *d* is a property of the grating and the incidence angle on the grating will not change if the properties of the light source are changed. At ω, the λ of the input light is 1053 nm and first-order diffraction occurs. However, at 2ω, λ is 526.5 nm; therefore, second-order diffraction occurs. Thus, both types of light cause the same diffracted angle and can be read directly by the spectrometer. Each CCD pixel corresponds to a certain frequency of light, so even if every frequency in the light pulse is doubled, the pulse shape of the output will still be the same when determined by the spectrometer.

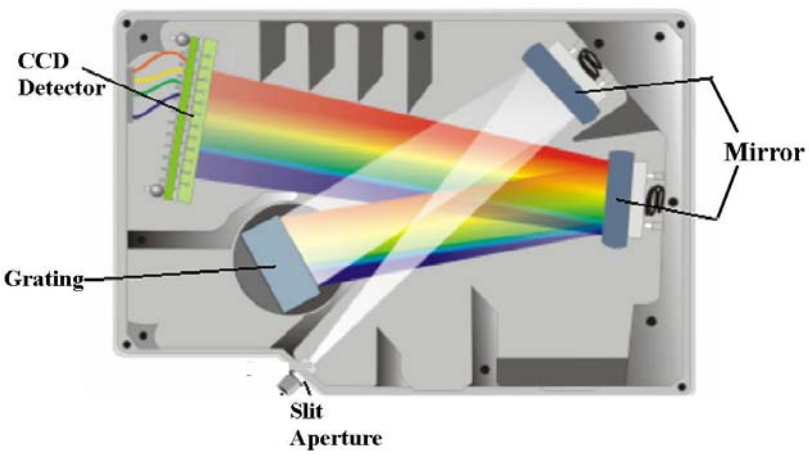

Figure 10. The schematic for the Ocean Optics HR2000 spectrometer.

5. Results

The diagnostic was tested on the Multi-Terawatt (MTW) laser system, a 5 Hz, optical parametric chirped-pulse amplifier laser system, capable of delivering >250 mJ of energy per pulse.

The diagnostic compressor of MTW is similar to the grating pair in the diagnostic in that there are two diffraction gratings parallel to each other (Fig. 11); however, the diagnostic compressor of MTW is used to create ultrashort pulses, rather than chirp them. The diagnostic was set at the output of the diagnostic compressor chamber to measure these pulses. By altering, lengthwise, the position of diffraction grating #2 (on the right in Fig. 11), the ultrashort pulses being sent through the laser system were stretched and compressed. The diagnostic was able to determine the distance that would induce the most linear phase over the given temporal domain, which would in turn create the ideal ultrashort, Gaussian optical pulse. A reference distance between the gratings was already known for creating the shortest pulses and the diagnostic was able to accurately confirm this distance, noted as "Reference" in Fig. 12a, b.

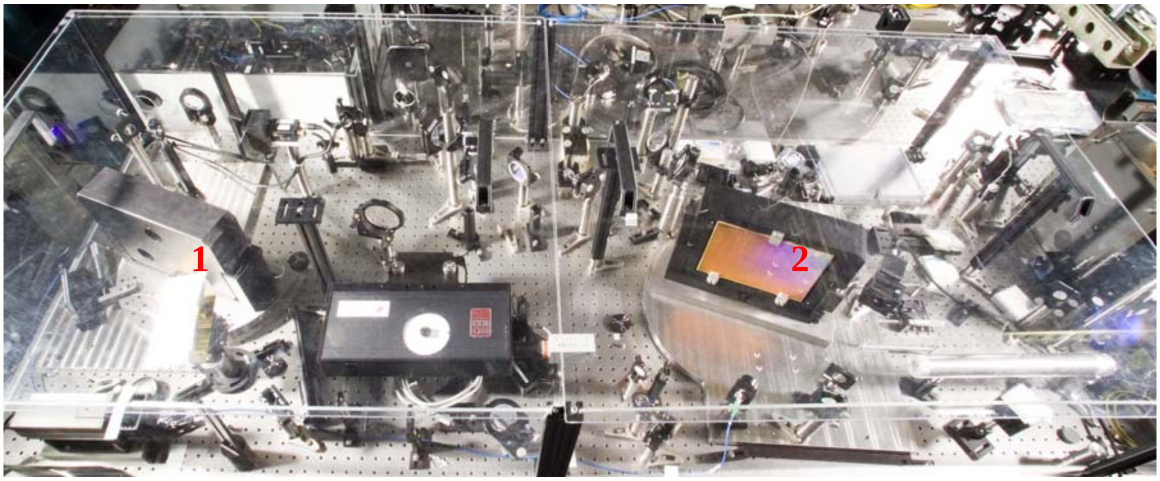

Figure 11. The diagnostic compressor of MTW. The diffraction gratings are labeled 1 and 2. Grating #2 was adjusted longitudinally to determine the best compressor distance for creating ideal ultrashort optical pulses.

The diagnostic was successful in confirming that the reference distance between

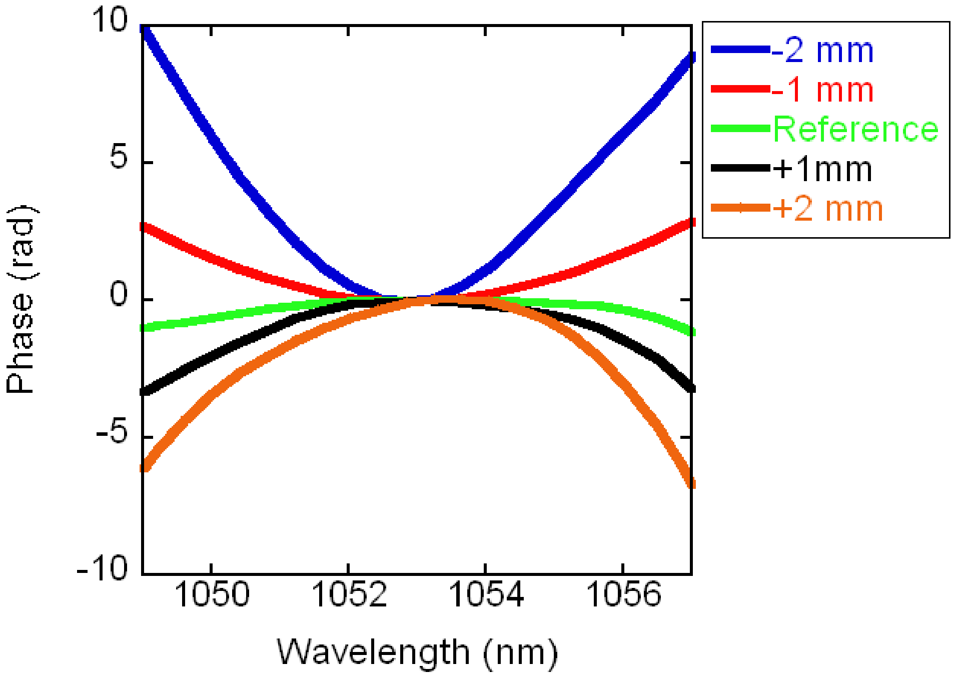

Figure 12a. The spectral phases of the ultrashort pulses created by changing the distance of the diagnostic compressor in MTW. The reference distance has the most linear phase, indicating that the temporal shape of the pulse will be most ideal.

the gratings in the diagnostic compressor was the ideal distance for creating the shortest pulses. As Fig. 12a shows, the spectral phase of the measured pulse at the Reference distance is most linear over the domain of the pulse's spectrum. The greater the difference in distance between the gratings from Reference, the more quadratic the phases became, indicating that the temporal shapes of these pulses had been stretched and their durations increased. The temporal shapes of the pulses were then determined in essence by Fourier transforming the spectral representation of the pulse (i.e. determined from the measured optical spectrum and spectral phase). The diagnostic confirms the predictions from the phases. By changing the longitudinal distance between the two diffraction gratings by ±1 mm from Reference, the shape of the pulse was effectively stretched from 450 ±5 femtoseconds to 1.7 ±0.01 picoseconds, measured as full width at half maximum (FWHM), confirming the shapes of the phases and the accuracy of the

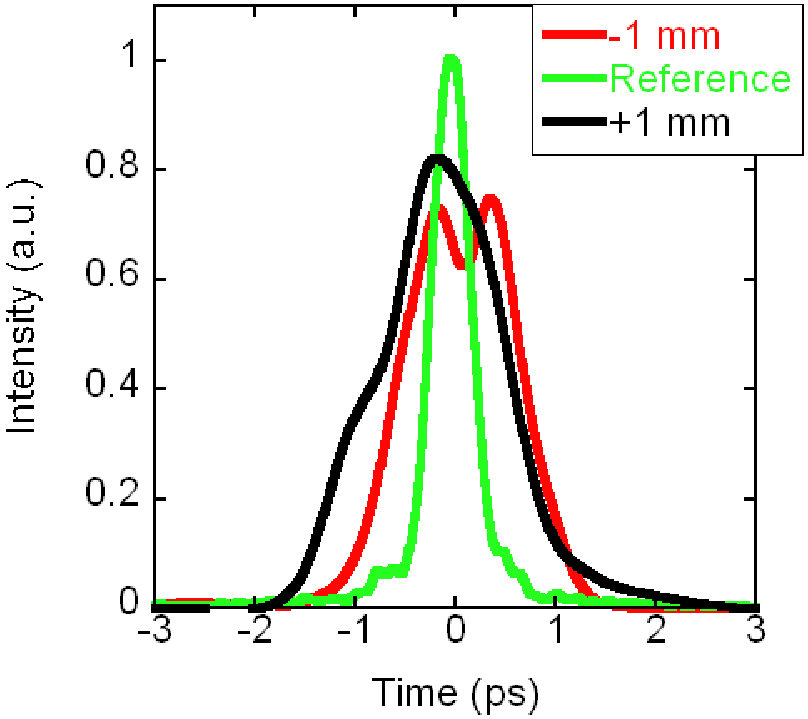

Figure 12b. The SSI interferogram of the pulses from the diagnostic compressor of MTW. The "Reference" distance is clearly the ideal distance for the grating compressor. Changes of ±1 mm greatly altered the shape of the ultrashort Gaussian pulse by temporally stretching its shape.

diagnostic (Fig. 12b). Future experiments have been planned to determine the accuracy of the diagnostic further.

6. Discussion

The diagnostic was able to accurately perform as planned using the concept of spectral shearing interferometry. The temporal shapes of ultrashort optical pulses were determined by characterizing the spectral properties of phase and intensity. These characteristics were determined in a simple, reliable, and noniterative fashion that only required the use of two Fourier transforms and no complex algorithms. Overall, the method required less data than either tomographic or spectrographic techniques and can be easily adapted to ultraviolet light sources by downconversion, as well as infrared by upconversion. The diagnostic is self-referencing and has no moving parts and is entirely collinear, allowing greater stability and thus, greater reliability. Relatively thick nonlinear crystals can be used in this diagnostic as long as the phase can be reconstructed using the spectral fringes and once properly aligned, the spectrometer and nonlinear interaction do not need to be recalibrated.

This diagnostic will be used to characterize ultrashort optical pulses on various laser systems at the Laboratory for Laser Energetics. The abilities of the diagnostic range from general characterization of pulses by determining spectral phase to confirming the effectiveness of chirped pulse amplification and compression.

7. Acknowledgments

I would like to thank my advisor Dr. Christophe Dorrer for his inspirational guidance and support during the project and the building of the diagnostic. I would also like to thank Dr. R. S. Craxton and the University of Rochester's Laboratory for Laser Energetics for allowing me to be part of the scientific research community.

8. References

1. D. Strickland and G. Mourou, *Opt. Commun*. *56*, 219 (1985).
2. N. Ross, P. Matousek, M. Towrie, A. J. Langley, and J. L. Collier, *Opt. Commun*. *144*, 125 (1997).
3. I. A. Walmsley and V. Wong, J. Opt. Soc. Am. B 13, 2453 (1996).

4. C. Iaconis, V. Wong, and I. A. Walmsley, *IEEE J. Select. Topics Quantum Electron.*, *4*, 285 (1998).
5. D. J. Kane and R. Trebino, *IEEE J. Quantum Electron.*, *29*, 571 (1993).
6. V. Wong and I. A. Walmsley, *J. Opt. Soc. Amer. B*, *14*, 944 (1997).
7. J. L. A. Chilla and O. E. Martinez, *Opt. Lett.*, *16*, 39 (1991).
8. H. R. Lange, M. A. France, J. F. Ropoche, B. S. Prade, P. Rousseau, and A. Mysyrowicz, *J. Select. Topics Quantum Electron.*, *4*, 295 (1998).
9. C. Iaconis and I. A. Walmsley, *Opt. Lett.*, *23*, 792 (1998).
10. M. Takeda, H. Ina, and S. Kobayashi, *J. Opt. Soc. Amer.*, *72*, 156 (1982).
11. E. B. Treacy, *IEEE J. Quantum Electron.*, *5*, 454 (1969).

Exploring Metadata for Laser Diagnostics and Control Systems on the OMEGA EP Laser System

Chris Baldwin

Exploring Metadata for Laser Diagnostics and Control Systems on the OMEGA EP Laser System

Chris Baldwin
Honeoye Falls-Lima High School
Advisor: Mr. Rick Kidder
Summer 2008

Abstract

For this project, an application was made that illustrates the advantages of an ontology over the current databases in use at LLE, which tend to be ad-hoc and poorly documented. An ontology is a way of organizing the data of a system based on the data's characteristics (ie: the metadata). By connecting the data via their properties, the ontology creates a model of the system, and thus derives its strength. This project focuses on the gain that an ontology provides by allowing programs to simulate "cause and effect", something that would be much harder to do under the current organization of data. The application implements an ontology of the OMEGA EP laser system and uses "causes and effect" to predict the effects on laser diagnostics timing as changes are made to the system. The program allows the user to make typical changes, such as switching between long pulse and short pulse, as well as to add/remove subsystems. The timings on the diagnostics are affected accordingly. All of this is done without any reference to the actual parts of the laser system, and thus the program functions the same regardless of how the ontology is configured. Ontologies can have wide-ranging applications at LLE, but the important thing to note is that more metadata needs to be readily available for ontologies to have much practical value.

1. Introduction

1.1 Background

Since its start, LLE has amassed an enormous amount of data. Currently, this data is stored in two locations: a PDM (Project Data Management) file system and several Oracle databases. The PDM file system indexes files like Word documents, Powerpoint presentations, and several other formats into sections based on their topics. Accessing the files is a matter of navigating through PDM sections and subsections, although if one knows the desired file's code one can enter it directly into a search bar. The Oracle database, on the other hand, is a collection of tables that contains the individual pieces of data. Many other tables and data are located on specific workstations.

Naturally, locating specific files and data can be quite challenging, as can be making use of the information. Database users must know exactly what it is they are looking for, and must be aware of where and how to look for it. One way to simplify the process would be to implement an ontology of the OMEGA and EP laser systems. By storing the files and data through an ontology, computers could perform the most tedious aspects of not only retrieving information but also using it.

1.2 Ontologies

Essentially, an ontology is a model of a system, a model that gains its strength through classifying and linking its members. Each member of an ontology, also known as an “individual”, belongs to at least one “class”, which is a type of member that is known to exhibit a specific set of characteristics. For example (see Figure 1), Bill, an individual, is a type of person, a class. This is the classifying aspect of ontologies. As for linking the members, every individual has “properties” that point to other individuals. The properties serve to illustrate how the individuals interact with each other. For instance, Bill's favorite color is blue. “Favorite color is” is a property Bill has, one that in this example points to the color blue.

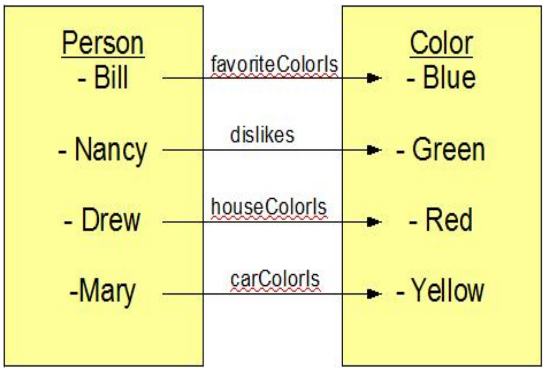

Figure 1: A sample ontology. The boxes represent classes, the examples within individuals, and the arrows properties.

Just like tables and even text files, ontologies store data. Yet ontologies don't store statistics and readings; they store characteristics. Thus the main advantage to an ontology is that it shows what subjects are related, and how they are connected. Most importantly, this is done in a manner that computers can easily understand. With ontologies, computers are able to make many of the connections and inferences that people do.

1.3 Purpose of the Project

In past years of the LLE high school program, work has been done on implementing an ontology for data retrieval.[1,2] Yet an ontology has the potential to do much more than organize LLE's collection of data. A model of the laser systems and subsystems would simplify virtually every computer-based task, and this project is intended to demonstrate that.

In a system as complex as LLE, making one change to the laser systems will have many effects down the line. This makes seemingly straightforward adjustments quite complicated, for many changes will need to be made as opposed to one. Furthermore, when an employee wishes to make these changes many times, the time requirement becomes much larger. However, an ontology would allow for programs to be designed that simplify the entire process. Computers could recognize the numerous changes that go hand-in-hand and perform them on a case-by-case scenario, adapting to subtle changes in the conditions.

2. The Project

2.1 Final Product

At LLE, different types of shots require different configurations of the laser systems, and these different configurations have a variety of effects. The application produced through this project focuses on one specific “cause and effect”: the effect that modifying the OMEGA EP laser's beam path will have on the separate timing of each diagnostic instrument, i.e., when the beam will reach each instrument with respect to a “default” time.

The application is divided into two sections, an ontology and a program implementing the ontology. The ontology illustrates the layout of the OMEGA EP laser system. Furthermore, it marks the diagnostic instruments in the system and gives each one a numerical property representing a delay in the time at which a portion of the beam reaches it. The program allows users to adjust the laser system in a variety of ways, such as by changing the beam's final destination from the sidelighter to the backlighter or by doubling the number of times the beam passes through the main amplifier. All these changes affect when the beam reaches each diagnostic. The program recognizes these changes in delay and adjusts the instruments' delay settings accordingly.

2.2 OMEGA EP Layout

Before an application simulating the OMEGA EP beamlines can be developed, it is necessary to have a basic understanding of the layout. The EP laser facility houses four separate beamlines, all of which are capable of firing in long-pulse mode, and two of which are capable of firing in short-pulse mode. The ontology created for this project focuses on beamlines 1 and 2, which can fire both long and short pulses.

There are four main sections to each beamline, indicated in Figure 2. The beam originates in Laser Sources. It is then injected into the amplifier, which is divided into an upper level and a lower level. After amplification, the beam can take one of two paths, depending on whether it is intended to be long-pulse or

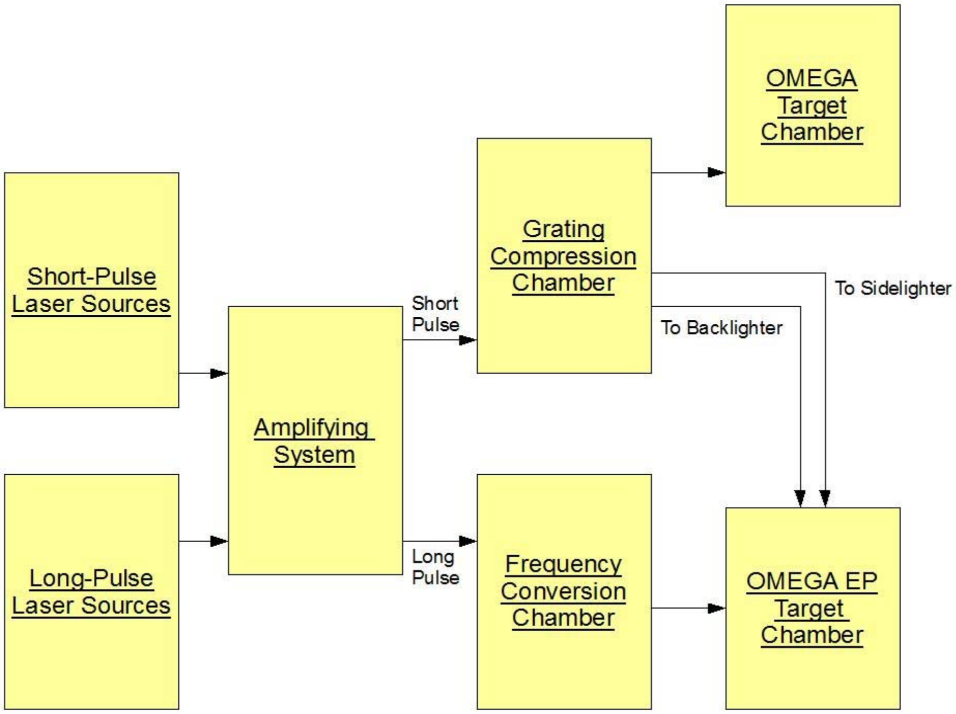

Figure 2: A basic diagram applicable to each of the first two EP beamlines.

short-pulse. If long-pulse, the beam heads into the Frequency Conversion Chamber, where its frequency is tripled into the UV spectrum. The beam then enters the EP target chamber. If short-pulse, the beam enters either the upper or lower Grating Compression Chamber (GCC), from which it can pass into the EP target chamber through the backlighter port or through the sidelighter port, or head into the OMEGA target chamber.

The EP laser system contains three main diagnostic tables, as well as a series of instruments in Laser Sources. After amplification, a portion of the beam can enter the Infrared Diagnostics Table. If long-pulse, part of the beam is directed to the Ultraviolet Diagnostics Table following frequency-conversion. If short-pulse, the beam passes by the Short Pulse Diagnostics Table after the GCC.

2.3 Ontology

The ontology has been designed through OWL (Web Ontology Language),

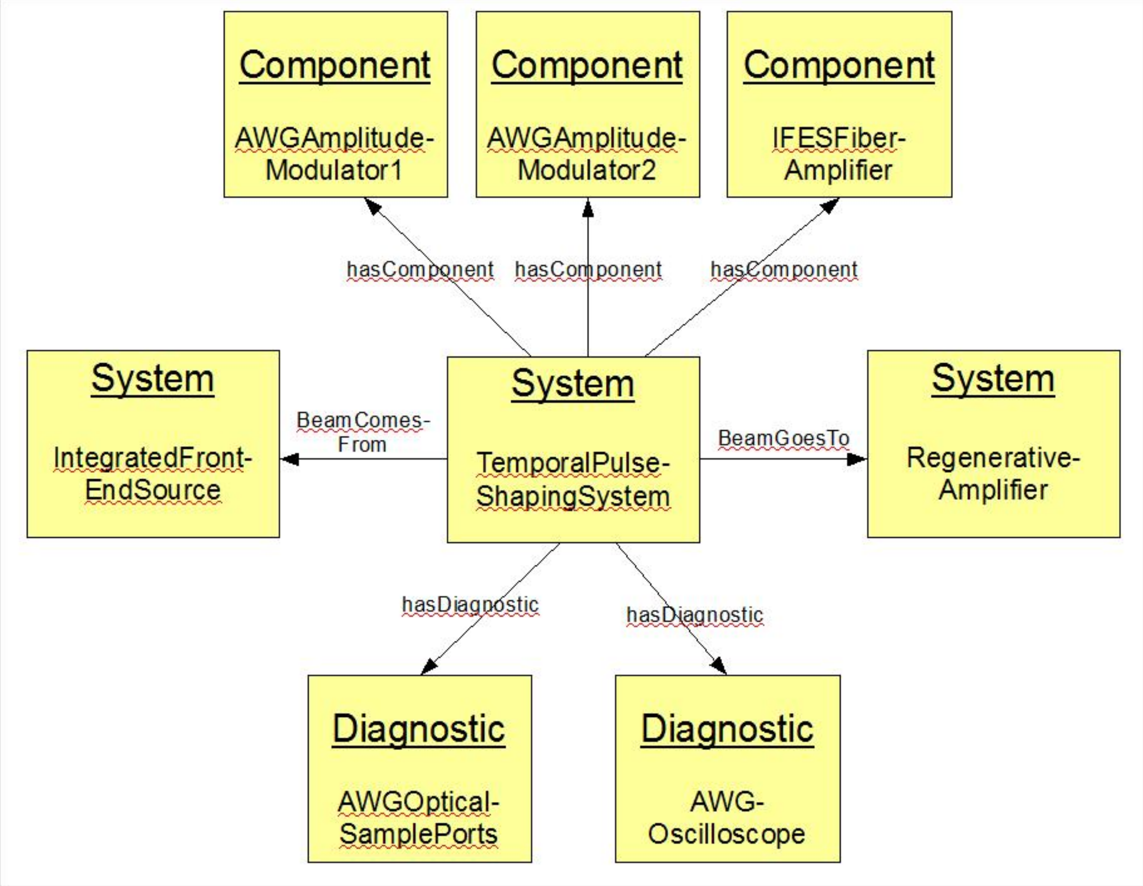

Figure 3: A portion of the ontology, showing the properties of the system, "TemporalPulseShapingSystem".

a modeling language built on XML (eXtensive Modeling Language). Thus, it follows the typical format of clearly defined classes, individuals, and properties. Its key component is the class labeled “Systems”. Each main stage of the EP laser's beam path, such as the temporal pulse shaping system, is an individual in this class. The properties of the temporal pulse shaping system are shown in Figure 3. The systems are linked to each other through the “beamGoesTo” and “beamComesFrom” properties. This creates a “linked list” data structure, in which one block of information points to another block, and only by traversing from one block to the next can information be accessed. Thus tasks such as displaying the path that the beam follows are simply matters of processing the information as it is reached.

The diagnostic instruments are represented in the ontology through a separate class, “Diagnostics”. Every individual in this class has a property pointing to a numerical value. The value represents the instrument's delay, and is modified every time an appropriate change is made to the ontology. As between two systems, diagnostics are linked to the systems on which they are found through the “hasDiagnostic” and “isDiagnosticOf” properties.

Furthermore, the ontology contains classes representing the different paths the beam could follow. Examples are traveling to the backlighter port by way of the upper GCC and traveling to the sidelighter port by way of the lower GCC. Each of these classes contains the individual systems that the beam passes through under that configuration.

2.4 Application

The implementation of the ontology, the program, has been coded with the Java Programming Language, and as such must be run through the Java Virtual Machine. Furthermore, the code makes use of a

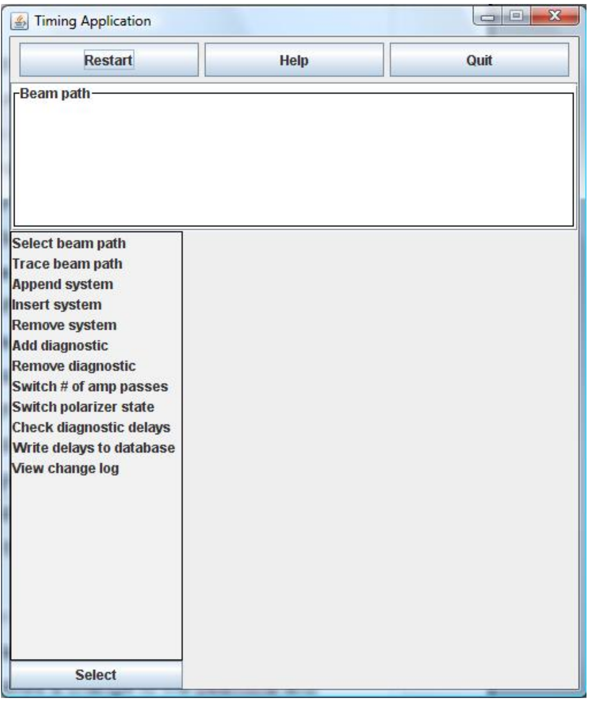

Figure 4: The program window, immediately after the program is initialized.

separate library, designed for programming with ontologies, known as Jena. When run, a window is opened with three main sections (see Figure 4). The first simply contains buttons allowing the user to restart, quit, and display a short set of directions on how to use the application. The second is the menu for manipulating the EP laser ontology. It allows the user to: select and display the beam's path, modify individual systems along the current path, add and remove diagnostics, switch the number of amplifier passes between two and four, switch whether the polarizer is inserted into the amplifying system or not, check the delays on the diagnostics, write the delays to a database, and view a list of what has been done in the current session. The third section is the pair of display panels. The upper panel is solely for displaying the current beam path. The large panel in the bottom-right is for everything else, from selecting where to insert a new system into the beam path to displaying the change log.

The goal of the application is to allow users to make a change to the ontology and to have the computer “understand” the change and take the appropriate actions. Specifically, the user makes a change to the beamline and the computer is to identify what diagnostic instruments' timings are affected and adjust the delays of those instruments. The organization of the ontology allows the computer's tasks to be quite manageable. When a change is made to the beamline, the laser must be fired sooner or later so that the beam arrives at its destination at the original time, “T-0”. This means that the diagnostic instruments affected by a change are those located in front of it relative to the beam's path. Since the systems in the ontology are organized sequentially, finding the appropriate diagnostics is simple. The computer starts at the first system after the change and, moving forward through the list, creates a collection of the diagnostics on the systems it comes across. The computer then removes every diagnostic in this collection from a separate collection containing every diagnostic in the ontology, removing all diagnostics not found on the current beam path as well. Thus all that remains is the diagnostics that are affected. The computer then accesses and rewrites the property of each diagnostic in this collection representing its delay (positive values for delays indicate that the diagnostic is to be fired later than normal, and negative values indicate sooner).

2.5 Timing

There are four separate actions the user can take that affect timing: switching the number of amplifier passes, inserting/removing the polarizer, inserting/removing systems, and changing the beam path. The first two are straightforward. Changing the number of amplifier passes from two to four will require diagnostics before the amplifying system to be triggered sooner, as will inserting the polarizer. Similarly, changing from four passes to two and removing the polarizer will each shorten the length of time in which the beam is passing through the beamline, and necessitate a positive delay.

When a system is inserted into the ontology, it naturally adds length to the beamline. Thus all diagnostics found before the new system must be set to fire earlier. Likewise, removing a system shortens the beamline and requires that all diagnostics before the removal fire later.

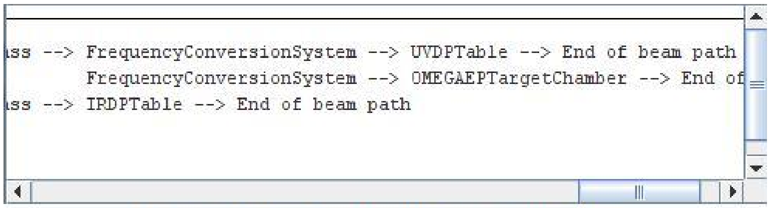

```
ss --> FrequencyConversionSystem --> UVDPTable --> End of beam path
       FrequencyConversionSystem --> OMEGAEPTargetChamber --> End of
ss --> IRDPTable --> End of beam path
```

Long Pulse to the Target Chamber

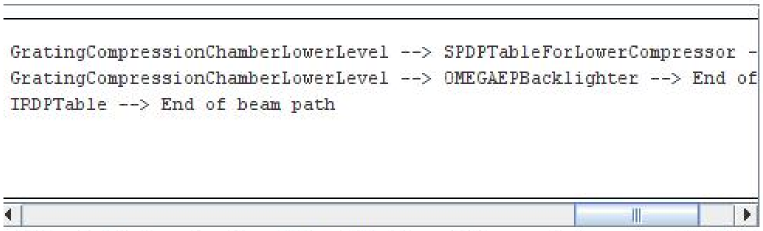

```
GratingCompressionChamberLowerLevel --> SPDPTableForLowerCompressor -
GratingCompressionChamberLowerLevel --> OMEGAEPBacklighter --> End of
IRDPTable --> End of beam path
```

Short Pulse to the Backlighter (through Lower GCC)

Figure 5: A comparison of the final stages of a long pulse mode vs a short pulse mode.

As for the last action, changing the beam path: in the EP laser system, there are six main variations in the beam's path. One is firing in long-pulse mode to the EP target chamber (see Figure 5). One is in short-pulse mode directed to the sidelighter port, by way of the lower Grating Compression Chamber. Two are in short-pulse mode heading to the backlighter port, one through the upper GCC and one through the lower GCC (see Figure 5). Likewise, two are in short-pulse mode heading to the OMEGA target chamber, one through each GCC. The long-pulse mode is 106.95 nanoseconds quicker than the short-pulse mode. Traveling to the sidelighter port is 17.18 ns quicker than to the backlighter port, which is itself 92.1 ns quicker than heading to the

OMEGA target chamber. Finally, passing through the lower GCC is quicker than passing through the upper GCC by 7.24 ns. Adjusting delays for a change in beam path is a matter of separately modifying the diagnostics affected by each component (ex: short-pulse, upper compressor, backlighter).

3. Analysis

3.1 Cause and Effect

Ontologies provide two key benefits to programming, both of which originate from their form of organization. The first is that computers can behave based on the idea of “cause and effect”, that one change will require many changes down the line. The program created effectively demonstrates this concept, although simplistically. A user makes a change to part of the ontology, the beamline, and the computer uses information from the change to adjust another aspect, the timings on certain diagnostics. By grouping the members of the ontology into classes, the computer can recognize that changes in systems imply changes in diagnostics.

3.2 Adaptability

The second benefit of implementing ontologies for programming is adaptability, and this is also demonstrated in the program. When a user makes a change to the beamline, the computer receives information on the change, such as where in the beamline the change was made. The computer makes use of this information to decide what to do next. For example, when a new system is inserted in between the main amplifying system and the Frequency Conversion Chamber, the computer determines what diagnostics are found before the new system and adjusts their delays. When a new system is inserted right after the integrated front end source, the computer again locates and alters the appropriate diagnostics. In both scenarios, the computer performs the same task, yet on different diagnostics in each case. The program will do this for any change, regardless of specifics. It functions under any situation involving a change in the beamline, without excessive hard-coding of data.

3.3 Future Development

There is great potential in the implementation of an ontology at LLE. This project is only one small example of the convenience ontologies could bring. A fully designed ontology would be a great step towards the development of “smart” computers. LLE employees could enter large, general commands into a computer, such as “Switch from long-pulse mode to short-pulse mode”, and the computer could perform all the necessary steps.

Currently, however, the creation of such an ontology is limited. Ontologies are dependent on metadata, i.e., data about data. In the case of ontologies, metadata is the information that individuals' properties point to. The creation of an ontology requires that the metadata is easily accessible and understandable, and if it isn't, the ontology suffers. One major barrier in the development of this project was that it was often unclear as to what delay setting belonged to what diagnostic. The information was there, just not understandable. Thus when the ontology was attempting to create its individuals representing diagnostics, it many times couldn't give the individuals real values for their delays. Before ontologies can truly become part of LLE, the data they require must be made clear and concise.

4. Acknowledgements

I would like to thank Richard Kidder and Stephen Craxton for giving me the opportunity to work at LLE and on this project. I would also like to thank Albert Consentino, Liz Hill, and Jason Puth for their help with the timing aspect of the project; Thomas Klingenberger for his help with the LLE databases; and Dan Gresh and Ricky Marron for their work with ontologies before me.

5. References

1. D. Gresh, “Implementing a Knowledge Database for Scientific Control Systems”, 2006 Summer High School Research Program at the University of Rochester's Laboratory for Laser Energetics, LLE Report No. 348.
2. R. Marron, “Development of an Ontology for the OMEGA EP Laser System”, 2007 Summer High School Research Program at the University of Rochester's Laboratory for Laser Energetics, LLE Report No. 353.

Development of the Cryogenic Target Information System

Mohammad Husain Bawany

Development of the Cryogenic Target Information System

Mohammad Husain Bawany

Brighton High School
Rochester, NY

Advisor: Mr. Roger T. Janezic

Laboratory for Laser Energetics
University of Rochester
Rochester, NY

2008 Summer Research Program

Abstract

Part of the inertial confinement fusion research at the Laboratory for Laser Energetics (LLE) entails the production and implosion of cryogenic targets filled with deuterium or deuterium-tritium (DT). Prior to this project, the databases containing relevant data were dispersed and excessive amounts of time were required to search for simple data. This project involved the creation of a new Web-based comprehensive query that serves as the starting point of an information search. The query allows a user, for the first time, to search for information online based on a variety of target characteristics, such as ice thickness or target outcome. To complement this database, a Layer Analysis Table (an exhaustive target quality database) was also created to focus solely on the layering cycle of cryogenic targets. These new online database features are essential to LLE's future work because researchers are now able to easily connect the characteristics of cryogenic targets to the shot result. This effort has improved data management and will simplify analysis of cryogenic data.

1. Introduction

The LLE Target Fabrication Facility is used to create and assemble an assortment of targets for various experiments. There have been many methods created to prepare, inspect, and mount the targets. A spherical cryogenic target is filled with deuterium or DT at pressures up to 1000 atmospheres and cooled to 18 K, forming a uniform layer of cryogenic fusion fuel (ice) inside an outer plastic shell.[1] Cryogenic targets are denser than gas-filled targets and are able to hold fuel more efficiently. This allows them to yield more energy when they are shot and brought up to a temperature of 100 million degrees Celsius.[2]

When a target is shot, the laser ablates the plastic shell (i.e., the shell is heated and expands outwards). This process creates an opposite reaction, as defined by Newton’s Law, which forces the cryogenic fuel layer to implode.[3]

The fate of a cryogenic target can be altered by a minute change in the thickness of the fuel layer or by the way it is mounted. Due to this, it has become necessary to monitor and record initial target characteristics and the shot outcome in order to make future improvements. If there is no such system, or the system to monitor these characteristics and results is too complex, then it becomes increasingly difficult to improve targets.

In this work, the Cryogenic Target Information System (CTIS) was set up in order to gather remote yet essential data from existing systems and to make it available through one database. By integrating information from all aspects of a target’s life cycle (see figure 1), a comprehensive information system was created that allows for a user-friendly search feature and a manageable flow of data. The CTIS not only consolidates the existing systems into two major systems, the Target Layer Analysis Table and the All Targets Query, but it also makes necessary data available online.

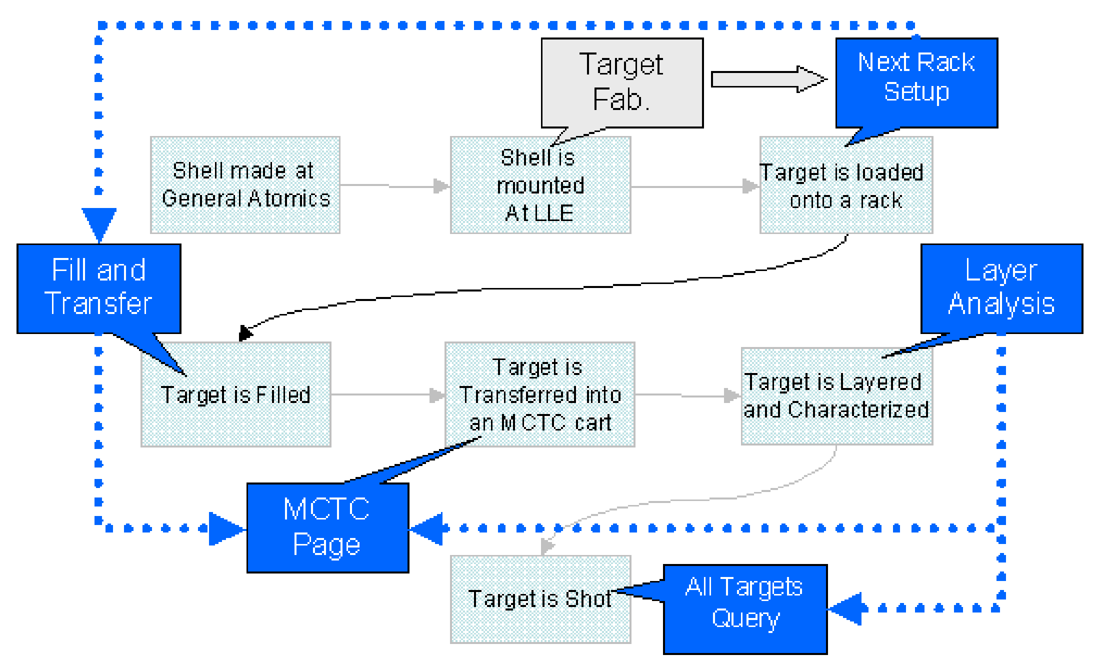

Fig. 1. Target life cycle and corresponding databases after the CTIS. The majority of these databases were consolidated and made available online.

2. Existing databases

Numerous independent databases were in use throughout LLE for each part of the target life cycle. Once a target was received and mounted, the Target Fabrication Database served as a source of information regarding the mount format, shell thickness, and shell material type. As a target was shifted into a rack and filled, the Fill and Transfer Database was used to collect the temperature, moles of gas, ice thickness, and cart number. When the target was layered, there was no single system used to monitor the process. Correct layering of a target is crucial, as a faulty layer often leads to a lost target or an unsuccessful shot. An example of a DT target with a good uniformity is given in figure 2. The shell smoothness and ice thickness must be as close to uniform as possible in order to allow for a high energy yield.

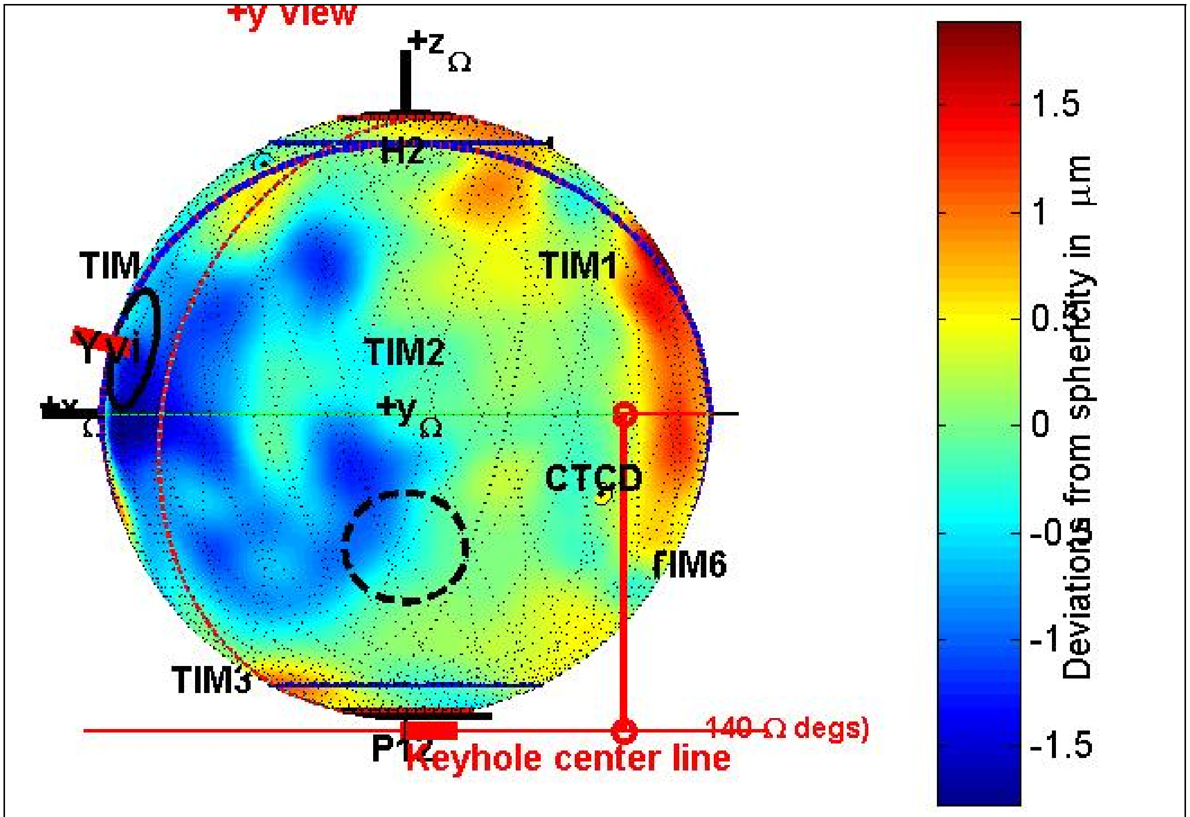

Fig. 2. Three-dimensional picture of a cryogenic DT target indicating the deviations from sphericity of the ice layer thickness. The minute deviations in ice thickness can cause problems when the target is shot by the laser.

Prior to the CTIS, the ice thickness, mount type, layer quality, image analysis, and shell smoothness data was available to very few people. The final stage that a target passed through was the shot process. The data at this stage was collected and maintained individually as a stand-alone file. The shot number, energy yield amount, layer measurements, and shot quality data were stored in this file.

The existing databases were functional and contained a massive amount of data. However, this information was often inaccessible to researchers due to the way in which it was stored. It was exceedingly difficult to navigate through the scattered systems in order to find data that connected initial target characteristics with the shot result.

3. Formation of the Cryogenic Target Information System

To solve this problem, a two-step process had to be followed. Initially, the existing systems were renovated and edited. Crucial information that was scattered throughout these systems was consolidated. A search engine or main page was then added in order to make searching easier. A main page is the primary place for starting a search by means of Target ID, Target Characteristics, Fill Number, or Target Fate. The two systems that have been created are currently being used by LLE scientists and engineers throughout the lab on a daily basis.

3.1 Target Layer Analysis Table

In order to make important layering data available, a new table was developed that allowed users to search for targets based on many characteristics. The Layer Analysis Table (see figure 3) allows targets to be sorted based upon the dates that they were layered and makes it simple to compile statistics. In order to create this table, data had to be translated into an offline Access table based upon a target's ID.

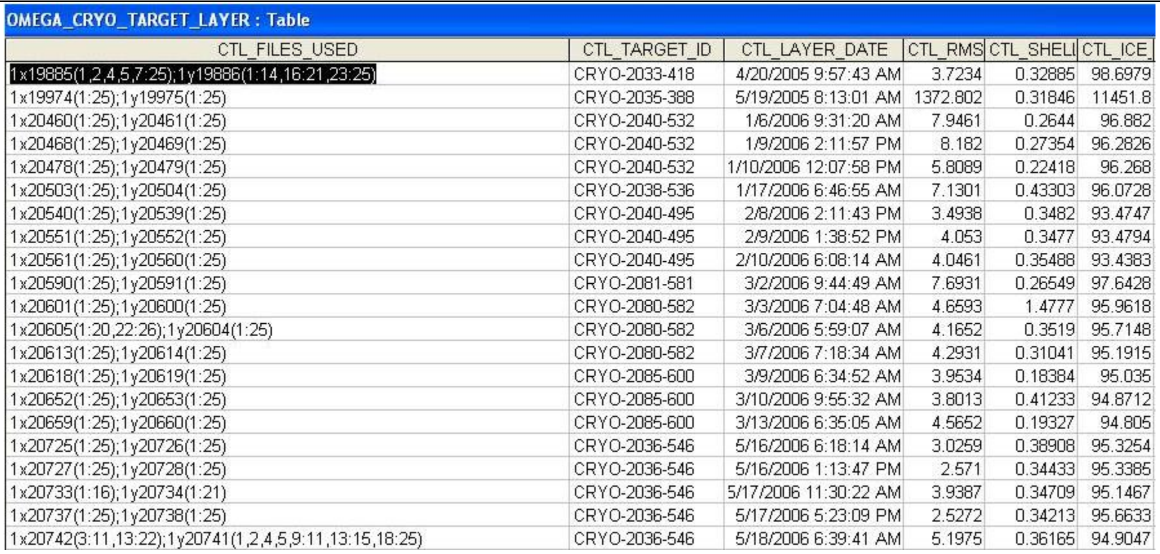

CTL_FILES_USED	CTL_TARGET_ID	CTL_LAYER_DATE	CTL_RMS	CTL_SHEL	CTL_ICE
1x19885(1,2,4,5,7:25);1y19886(1:14,16:21,23:25)	CRYO-2033-418	4/20/2005 9:57:43 AM	3.7234	0.32885	98.6979
1x19974(1:25);1y19975(1:25)	CRYO-2035-388	5/19/2005 8:13:01 AM	1372.802	0.31846	11451.8
1x20460(1:25);1y20461(1:25)	CRYO-2040-532	1/6/2006 9:31:20 AM	7.9461	0.2644	96.882
1x20468(1:25);1y20469(1:25)	CRYO-2040-532	1/9/2006 2:11:57 PM	8.182	0.27354	96.2826
1x20478(1:25);1y20479(1:25)	CRYO-2040-532	1/10/2006 12:07:58 PM	5.8089	0.22418	96.268
1x20503(1:25);1y20504(1:25)	CRYO-2038-536	1/17/2006 6:46:55 AM	7.1301	0.43303	96.0728
1x20540(1:25);1y20539(1:25)	CRYO-2040-495	2/8/2006 2:11:43 PM	3.4938	0.3482	93.4747
1x20551(1:25);1y20552(1:25)	CRYO-2040-495	2/9/2006 1:38:52 PM	4.053	0.3477	93.4794
1x20561(1:25);1y20560(1:25)	CRYO-2040-495	2/10/2006 6:08:14 AM	4.0461	0.35488	93.4383
1x20590(1:25);1y20591(1:25)	CRYO-2081-581	3/2/2006 9:44:49 AM	7.6931	0.26549	97.6428
1x20601(1:25);1y20600(1:25)	CRYO-2080-582	3/3/2006 7:04:48 AM	4.6593	1.4777	95.9618
1x20605(1:20,22:26);1y20604(1:25)	CRYO-2080-582	3/6/2006 5:59:07 AM	4.1652	0.3519	95.7148
1x20613(1:25);1y20614(1:25)	CRYO-2080-582	3/7/2006 7:18:34 AM	4.2931	0.31041	95.1915
1x20618(1:25);1y20619(1:25)	CRYO-2085-600	3/9/2006 6:34:52 AM	3.9534	0.18384	95.035
1x20652(1:25);1y20653(1:25)	CRYO-2085-600	3/10/2006 9:55:32 AM	3.8013	0.41233	94.8712
1x20659(1:25);1y20660(1:25)	CRYO-2085-600	3/13/2006 6:35:05 AM	4.5652	0.19327	94.805
1x20725(1:25);1y20726(1:25)	CRYO-2036-546	5/16/2006 6:18:14 AM	3.0259	0.38908	95.3254
1x20727(1:25);1y20728(1:25)	CRYO-2036-546	5/16/2006 1:13:47 PM	2.571	0.34433	95.3385
1x20733(1:16);1y20734(1:21)	CRYO-2036-546	5/17/2006 11:30:22 AM	3.9387	0.34709	95.1467
1x20737(1:25);1y20738(1:25)	CRYO-2036-546	5/17/2006 5:23:09 PM	2.5272	0.34213	95.6633
1x20742(3:11,13:22);1y20741(1,2,4,5,9:11,13:15,18:25)	CRYO-2036-546	5/18/2006 6:39:41 AM	5.1975	0.36165	94.9047

Fig. 3. The Layer Analysis Table. This is automatically updated with each layer analysis

Every time a layer for a target is analyzed, this table is automatically updated. This table contains information such as ice smoothness values, ice thickness values, and numerous other data. In order to make this table effective, query features were created so that a user can filter necessary data. The completed table is available online for easy access (see figure 4).

The impact of this table has been substantial. Now, the whole organization has access to the same data in real time. Decisions based on layer quality are now more objective because they are data based. Reports can be quickly assembled and the layer process development has been made more efficient.

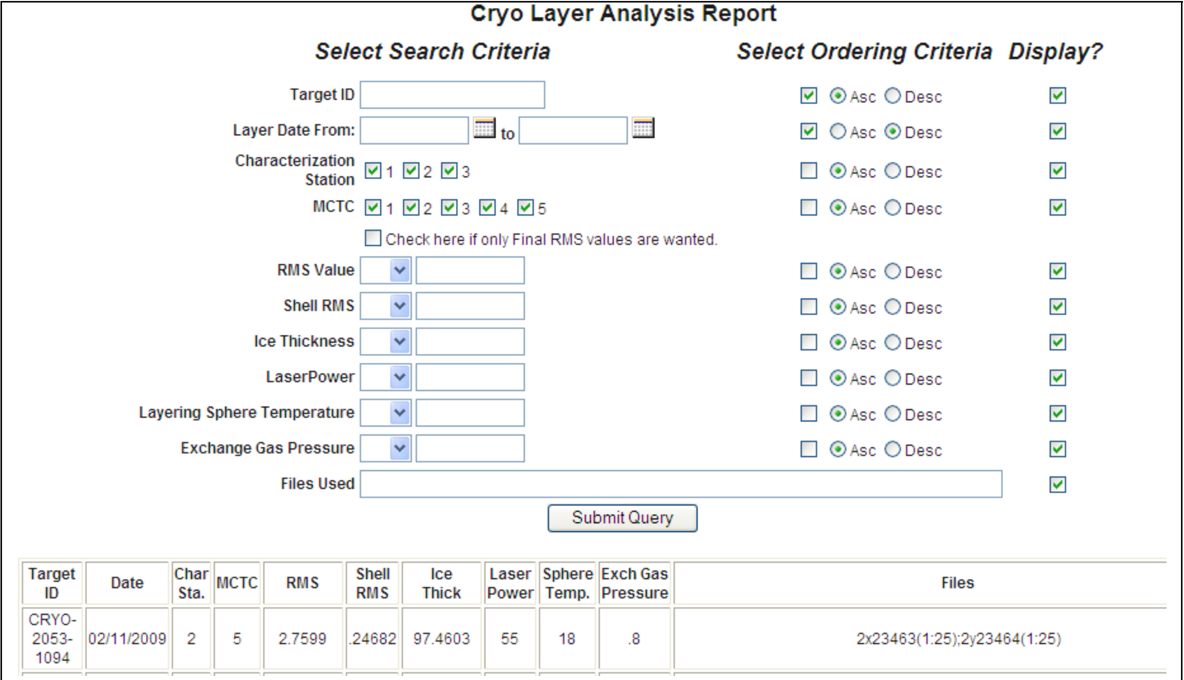

Cryo Layer Analysis Report

	Select Search Criteria	Select Ordering Criteria	Display?
Target ID		☑ ● Asc ○ Desc	☑
Layer Date From:	to	☑ ○ Asc ● Desc	☑
Characterization Station	☑ 1 ☑ 2 ☑ 3	☐ ● Asc ○ Desc	☑
MCTC	☑ 1 ☑ 2 ☑ 3 ☑ 4 ☑ 5	☐ ● Asc ○ Desc	☑
	☐ Check here if only Final RMS values are wanted.		
RMS Value		☐ ● Asc ○ Desc	☑
Shell RMS		☐ ● Asc ○ Desc	☑
Ice Thickness		☐ ● Asc ○ Desc	☑
LaserPower		☐ ● Asc ○ Desc	☑
Layering Sphere Temperature		☐ ● Asc ○ Desc	☑
Exchange Gas Pressure		☐ ● Asc ○ Desc	☑
Files Used			☑

Target ID	Date	Char Sta.	MCTC	RMS	Shell RMS	Ice Thick	Laser Power	Sphere Temp.	Exch Gas Pressure	Files
CRYO-2053-1094	02/11/2009	2	5	2.7599	.24682	97.4603	55	18	.8	2x23463(1:25);2y23464(1:25)

Fig. 4. Graphical user interface for the new Target Layer Analysis Table. A target's layer history is displayed based on user input

3.2 All Targets Query

In order to connect all of the existing databases and to display shot outcomes, the All Targets Query was created. This query also serves as the primary place for starting a search. The All Targets Query allows a user to search for multiple targets based on fields such as the target transfer result, shot number, and target fate. It then gathers information from the existing databases and automatically generates a report showing all of the targets that meet the search criteria (see figure 5). The query was created so that any user can find specific information about any target. An essential component of the query was the ability to allow a user to bring up a list of targets that meet specified input characteristics.

The All Targets Query has reduced the time required to produce target production statistics by a substantial amount. It has led to standardizing terminology for target outcomes and has made data searches more effective.

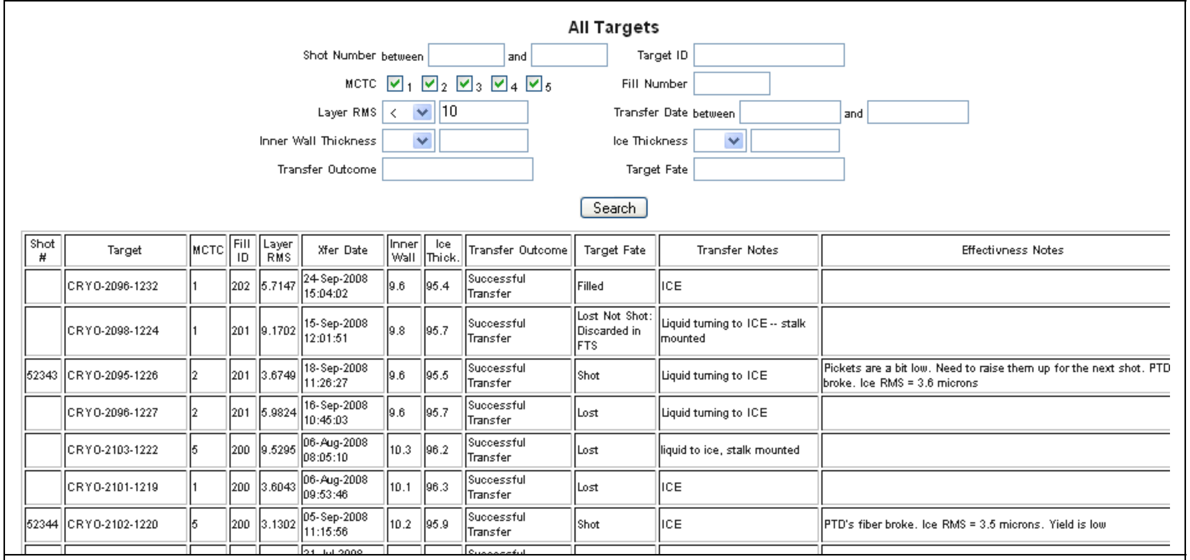

MCTC ☑ 1 ☑ 2 ☑ 3 ☑ 4 ☑ 5

Layer RMS < 10

Shot #	Target	MCTC	Fill ID	Layer RMS	Xfer Date	Inner Wall	Ice Thick.	Transfer Outcome	Target Fate	Transfer Notes	Effectivness Notes
	CRYO-2096-1232	1	202	5.7147	24-Sep-2008 15:04:02	9.6	95.4	Successful Transfer	Filled	ICE	
	CRYO-2098-1224	1	201	9.1702	15-Sep-2008 12:01:51	9.8	95.7	Successful Transfer	Lost Not Shot: Discarded in FTS	Liquid turning to ICE -- stalk mounted	
52343	CRYO-2095-1226	2	201	3.6749	18-Sep-2008 11:26:27	9.6	95.5	Successful Transfer	Shot	Liquid turning to ICE	Pickets are a bit low. Need to raise them up for the next shot. PTD broke. Ice RMS = 3.6 microns
	CRYO-2096-1227	2	201	5.9824	16-Sep-2008 10:45:03	9.6	95.7	Successful Transfer	Lost	Liquid turning to ICE	
	CRYO-2103-1222	5	200	9.5295	06-Aug-2008 08:05:10	10.3	96.2	Successful Transfer	Lost	liquid to ice, stalk mounted	
	CRYO-2101-1219	1	200	3.6043	06-Aug-2008 09:53:46	10.1	96.3	Successful Transfer	Lost	ICE	
52344	CRYO-2102-1220	5	200	3.1302	05-Sep-2008 11:15:56	10.2	95.9	Successful Transfer	Shot	ICE	PTD's fiber broke. Ice RMS = 3.5 microns. Yield is low

Fig. 5. All Targets Query Page. A table of all targets that meet the criteria selected by the user is automatically generated

4. Further Improvements

A dynamic system such as the CTIS will always require changes in order to meet current demands. One such addition that could not be developed to completion was a graphing utility that functioned alongside the Layer Analysis Table. The purpose of this was to enhance the ability of the table to prepare statistics by graphing data onto a plot as well as displaying it in the current online table. Other changes include modifying the data fields that are searchable. One such modification could allow for a target search based on the type of fuel a target was filled with, such as deuterium or DT. The ultimate goal of this system is to consolidate all of the existing data systems further into a universal query.

5. Acknowledgements

I would like to thank my advisor, Mr. Roger Janezic, for investing so much time into me and for guiding me through this project. I would also like to thank Mr. Luke Elasky, Mr. Thomas Klingenberger, Dr. Dana Edgell, Mr. Gary Wainwright, Mr. Tim Duffy, and everyone else who made this project possible. The immense amount of work that was done would not have been possible without their unwavering support and assistance. I would like to thank Dr. Craxton for accepting me into the prestigious Laboratory for Laser Energetics Summer research program and for giving me the unique opportunity to work in a highly professional, research oriented environment.

6. References

1. Duffy, Tim, and R. Janezic, Cryogenic Target Handling System Operations Manual Rev. A, 1-2, 2004

2. Emmett, J., J. Nuckolls, and L. Wood, *Fusion Power by Laser Implosion,* Scientific American, 24-37, June 1974.

3. Gresh, Lois. *Inertial Confinement Fusion: An Introduction,* University of Rochester Laboratory for Laser Energetics, 23, 2009.

Investigating the Causes of and Possible Remedies for Sensor Damage in Digital Cameras Used on the OMEGA Laser Systems

Krysta Boccuzzi

Investigating the Causes of and Possible Remedies for Sensor Damage in Digital Cameras Used on the OMEGA Laser Systems

Krysta Boccuzzi

Our Lady of Mercy High School
Rochester, NY

Advisor: Eugene Kowaluk

Laboratory for Laser Energetics
University of Rochester
Rochester, NY

August 2008

Abstract

When a target is imploded using the OMEGA laser system, various types of radiation, including neutron radiation, are produced. Cameras using charge-coupled devices (CCDs) are used to record these implosions. However, the CCDs are vulnerable to neutron irradiation. The CCD used on the Neutron Temporal Diagnostic (NTD) shows significant increases in dead pixels in conjunction with high neutron yield shots. The high energy neutrons collide with the sensitive structure of the CCD, causing physical damage to the device. These physical defects are reflected in the images produced by the CCD in a Nikon D100 digital camera as noise, stuck pixels, and hot pixels that lead to line defects and in the images from the CCD in the NTD as dead pixels. The CCD soon becomes unable to function. Research into solutions for this problem has shown that little can be done to prevent or reverse the damage. While a polyethylene shield decreases the damage by a factor of two, a significant amount of radiation is still able to reach the CCD. Scientists must learn to work with the damage and develop a system to determine when the CCDs should be replaced.

1. Introduction

At the University of Rochester’s Laboratory for Laser Energetics (LLE), research on inertial confinement fusion is conducted through the implosion of cryogenic targets. Images of these implosions are recorded by a Nikon D100 digital camera located on the outside of the target chamber, approximately 1.8 meters from target chamber center. These images, such as those shown in figure 1.1, allow LLE scientists to record valuable information about what occurs in the target chamber during an implosion. However, the CCD becomes damaged after being exposed to numerous implosions over an extended period of time. The damage is obvious in the images taken by the device and lessens the amount of information scientists are able to gather from the image.

Figure 1.1: Examples of images taken by the damaged CCD in the Nikon D100 digital camera.

A CCD works by converting photons to voltage. When a camera takes a picture, it gathers the information in terms of photons. In each individual pixel on the CCD, this charge is converted to electrons and sent to an output node, where the electrons are converted to voltage and sent to the camera circuit board as an analog signal. At the circuit board, the analog signal is converted to a digital signal. The information is now in a form that a computer can read and convert to an image. Damage to the CCD occurs when this process is interrupted or otherwise malfunctioning.

The damage appears in the image as hot pixels, stuck pixels, and noise, as can be seen in figure 1.2(b). Hot pixels are permanently lit pixels that appear white and can lead to line defects, such as the vertical white line seen in figure 1.2(b). In a CCD, the charge from each pixel travels down a vertical line of pixels in order to reach the output node. If one of the pixels in this line has a defect, it can not correctly transfer the electrons to the output node, leading to a line defect. Stuck pixels occur when one or more sub pixels are permanently either lit or unlit, causing the pixels to always appear red, blue, or green. This can explain the many red and blue spots in the blank shot from figure 1.2(b). Noise is a statistical variation that can appear as monochromatic grain or colored waves. Figure 1.3 gives histograms of the red, green, and blue pixels in the image in figure 1.2(b) and indicates the presence of dark current, which occurs when a pixel is charged even though there is no incident light to produce a charge in that pixel. A histogram of a blank shot should show that the red, green, and blue color values for all the pixels are 0. However, the histogram of figure 1.2(b) shows that these color values vary between 0 and 255, indicating that the pixels are producing a charge when there is none.

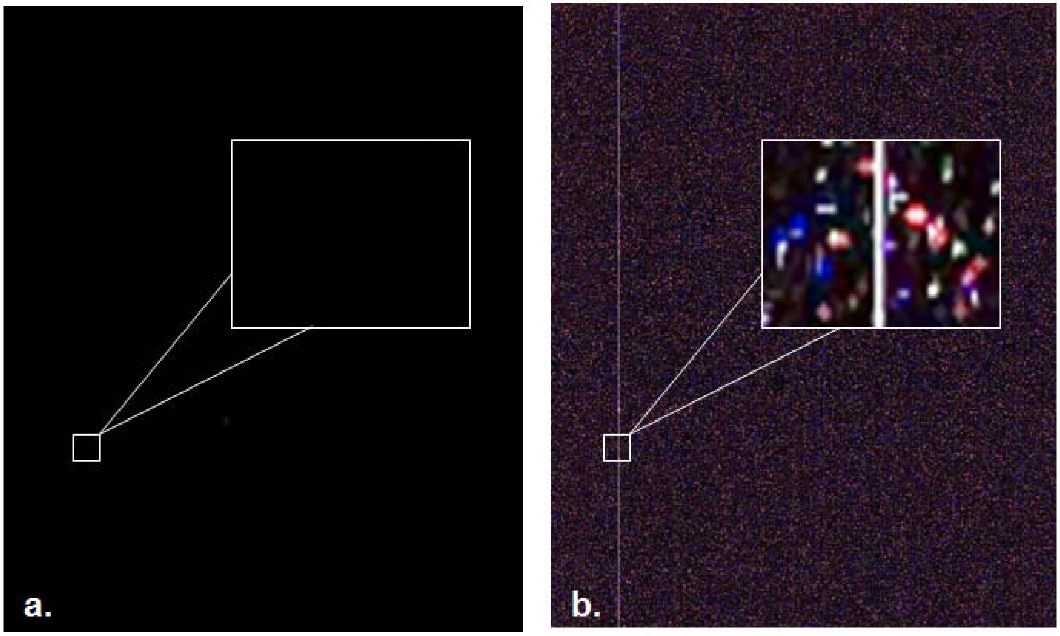

Figure 1.2: (a.) A blank shot taken with the D100 before being placed outside the target chamber
(b.) A blank shot taken with the D100 after 13 months outside the target chamber

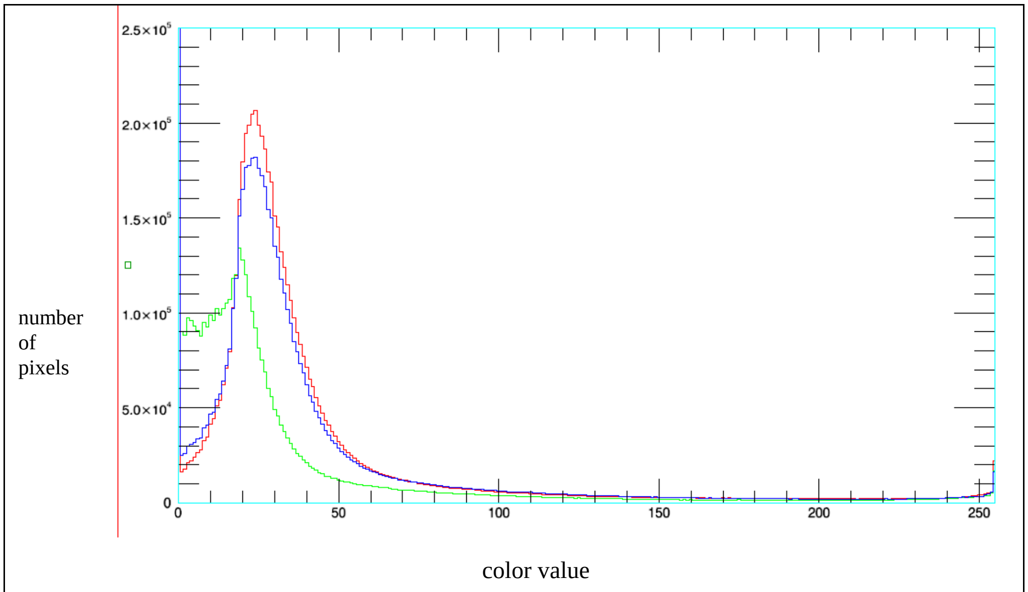

Figure 1.3: Histograms of red, green, and blue pixels corresponding to the image in figure 1.2(b)

2. Causes of the Damage

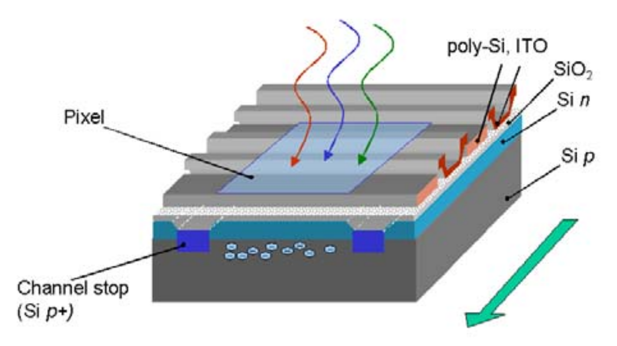

Figure 2.1: A cross-section of a CCD

The damage to the CCD is caused mainly by neutron irradiation of the device. A CCD is composed of several layers of silicon, each layer including a different form of silicon. These layers can be seen in figure 2.1. Previous research has shown that neutrons with energy of 190 eV or greater can displace the silicon atoms from their lattice positions, creating trapping sites in the signal channel. This causes bulk damage, making it difficult for the information from the pixels to correctly reach the output node and resulting in low charge transfer efficiency.[1] Other research has yielded similar results.[2,3]

The damage can be seen not only on the images but also on the CCD sensor. When the imager was examined under a stereo microscope, many small white spots could be seen around the surface of the device, as can be seen in figure 2.2. These spots could be the result of the device being pelted with high energy particles, such as neutrons.

Figure 2.2: A 12.1 mm long and 15.6 mm wide (1536 by 2000 pixels) section of the damaged CCD taken from the Nikon D100

Further evidence for neutrons being the cause of damage to CCD sensors used on the OMEGA laser systems is provided by data from the Neutron Temporal Diagnostic (NTD). The

NTD includes a streak camera that utilizes a CCD and gathers information about the neutron burn history.[4] The CCD sensor used on the NTD showed significant damage, mainly in the form of dead pixels, or pixels that are permanently unlit and appear black. Analysis of images from the streak camera includes the implementation of an algorithm that calculates the number of dead pixels in that image, among other calculations. The graph in figure 2.3 shows the progression of the amount of dead pixels over a time period of 6 months. The graph contains 157 data points, beginning at shot 46068, when the current CCD was first used, and ending at shot 47970. In this time period, the two most noticeable spikes include a rise from 13 dead pixels in the image from shot 46825 to 36 dead pixels from shot 46827 and an increase from 13 dead pixels in the data from shot 47485 to 77 dead pixels from shot 47575. Both spikes correspond to shots with high neutron yields. The graph shows some decrease in dead pixels over time, as it is possible for dead pixels to resurrect.

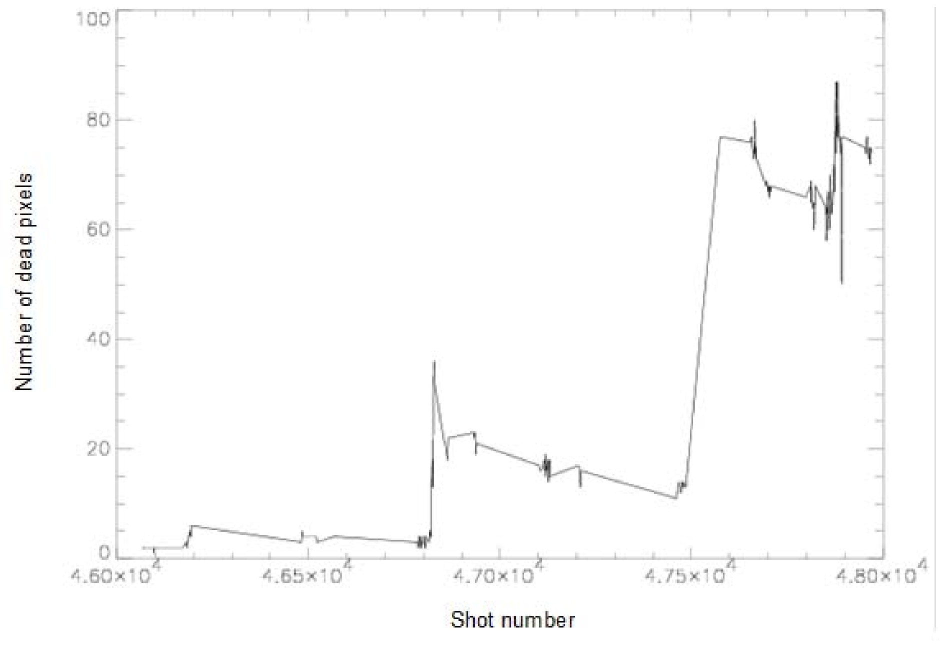

Figure 2.3: A graph representing the progression of damage to the CCD in the Neutron Temporal Diagnostic. Noticeable spikes correspond to high neutron yield shots

Further research is needed to confirm the conclusion that neutron irradiation causes the CCD to become damaged, as there are other possible causes. Proton and gamma ray irradiation can cause damage similar to that of neutron irradiation.[1] Direct hits by lasers can also damage CCD sensors,[5] though neither the Nikon D100 nor the streak camera in the NTD is exposed to direct hits by the laser beams.

3. Possible Remedies

With current technology, it is difficult to find an effective method of protecting CCD sensors from radiation damage. However, shielding can increase the life of the device. For example, when 1 meter of polyethylene shielding was placed in front of the NTD, the damage was decreased by a factor of two.[6] Other types of shielding, such as paraffin wax, concrete, water, and boron have been found to be somewhat effective.[7] Future research may reveal other means to extend the period of time in which the CCD can be utilized.

One possible solution for the problem is to use a different, more radiation-tolerant camera sensor. An example of such a sensor is the charge injection device (CID), which has several inherent features that make it more able to withstand radiation than the CCD. Such features include a single transfer sense, meaning that the charge from the photon is sensed at the pixel site. Therefore the sensing of the charge is not destructive to the device and a good charge transfer efficiency is not as essential as in a CCD. A CID can accommodate a large full well, using up to 90% of the pixel area for charge storage. The sensor is anti-blooming, as the charge never leaves the pixel. Any excess charge is transferred to a reverse biased substrate, which acts as a buried collector and eliminates any path that would allow the signal to cause blooming. CID sensors also have improved design and improved process that minimize dark current, radiation damage, and threshold shift as a result of ionizing radiation.[8] Unfortunately, CID imagers are not readily available in the applications needed on the OMEGA laser systems. A special camera would most likely have to be built by LLE scientists in order to utilize a CID.

4. Conclusions

Further research is needed to confirm that damage to CCD sensors in cameras used on the OMEGA laser systems is caused mainly by neutron interaction with the devices. Currently, there is no known method to prevent or reverse this damage to the CCD sensors. Scientists must learn to work with the damage, by developing a system to determine when the sensors should be replaced or by using a camera with a sensor that is more tolerant to radiation exposure.

5. Acknowledgements

I would like to thank Dr. Stephen Craxton for giving me the opportunity to participate in the program. I would also like to thank my advisor, Eugene Kowaluk, for all his help and support in completing my project, as well as the many other LLE scientists and engineers who helped in my research, including Steve Stagnitto, Paul Jaanimagi, Christian Stoeckl, Amy Rigatti, Fred Marshall, Larry Iwan, and Terry Kessler.

6. References

1. J. Janesick, T. Elliott, and F. Pool. “Radiation damage in scientific charge-coupled devices.” IEEE Trans., Vol. 36, No. 1, p.572 (1999).
2. R. Korde, A. Ojha, R. Braasch, and T. C. English. “The effect of neutron irradiation on silicon photodiodes.” IEEE Trans., Vol. 36, No. 6, p.2169 (1989).
3. P. A. Jaanimagi, R. Boni, and R. L. Keck. “Neutron-induced background in charge-coupled device detectors.” Rev. Sci. Instrum., Vol. 72, No. 1, p.801 (2001).
4. “A TIM-based neutron temporal diagnostic for cryogenic experiments on OMEGA.” LLE Review, Vol. 92, p.156.

5. C. Zhang, L. Vlarre, R. M. Walser, and M. F. Becker. “Mechanisms for laser-induced functional damage to silicon charge-couple imaging sensors.” Applied Optics, Vol. 32, No. 27, p.5201 (1993).
6. Christian Stoeckl, private communication (2008).
7. A. Kalicki. “The measuring station for research of effects of increased radiation on CCD and CMOS sensors.” TESLA Report (2005).
8. J. Zarnowski, J. Carbone, R. Carta, and M. Pace. “Radiation tolerant CID imager.” SPIE, Vol. 2172, p.187 (1994).

Controlling a Data Acquisition System with Java

David Brummond

Controlling a Data Acquisition System with Java

D. Brummond
Advised by Dr. Christian Stoeckl

Laboratory for Laser Energetics
University of Rochester
250 East River Road
Rochester, NY 14623
August 29, 2008

Abstract

PC-based data acquisition systems have the capability to replace oscilloscopes, signal generators, and certain digital input/output communications in laboratory diagnostics setups. Though proprietary software exists for controlling these systems, this software has no flexibility to be adapted for LLE use. Instead an open-source C library for Linux machines (Linux Control and Measurement Device Interface (COMEDI)) has been used. This library supplies functions for communicating with a PC-based data acquisition system. The goal of this project was to adapt ScopeControl, a preexisting program written in Java for controlling oscilloscopes, to monitor and save data from a PC-based data acquisition system using the COMEDI library. Programs were written in both C and Java and the Java Native Interface was used to allow these programs to communicate. Once ScopeControl had been successfully modified, additional hardware and software features present in the data acquisition systems were explored, including analog waveform generation and remote data monitoring through the network.

Outline

1 Introduction

The purpose of the University of Rochester Laboratory for Laser Energetics (LLE) is to conduct experiments in laser-driven inertial confinement fusion. Experiments are conducted in the Omega and Omega EP laser systems and vast amounts of data are produced. In order to collect this data and monitor lab equipment, many oscilloscopes and signal generators are utilized. Recently an alternative technology is available in PC-based data acquisition systems that would simplify data collection and give laboratory operators a more flexible user interface. However, a program to support PC-based data acquisition systems needed to be developed.

1.1 Current Hardware

Figure 1.1: A standard oscilloscope

For most data collection needs at LLE, oscilloscopes are used (see fig. 1.1). Oscilloscopes are a common piece of laboratory hardware that can connect to an analog channel and collect any signals that are generated. Oscilloscopes have been utilized in laboratories for decades, but the possibility of replacing some with PC-based data acquisition systems is being investigated. Oscilloscopes can have a very high sampling rate and are easily capable of sampling signals on the order of nanoseconds (or smaller), such as those produced during laser shots on Omega or Omega EP. However, for slower signals and monitoring lab equipment, a regular oscilloscope may be more accurate than is necessary. Also, most oscilloscopes are limited to monitoring four analog channels at a time. For specialized tasks this is acceptable, but if many signals need to be monitored at any given time this could be a costly limitation.

1.2 PC-Based Data Acquisition Systems

With the advent of the PC in the laboratory setting, many pieces of specialized laboratory equipment have been replaced by peripheral devices connected to a computer. A PC-based data acquisition system (see fig. 1.2) is a peripheral device that works with a computer to perform tasks formerly done by oscilloscopes or signal

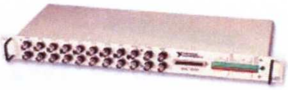

Figure 1.2: A PC-based Data Acquisition System

generators. These data acquisition systems have the capability of monitoring and producing both analog and digital signals. The number of analog channels that can be monitored on a PC-based data acquisition system is generally greater than that of oscilloscopes. By combining a large number of analog channels with the capability to produce both digital and analog signals, PC-based data acquisition systems can greatly simplify tasks normally performed by numerous lab instruments.

1.3 Program Overview

A preexisting program, ScopeControl, was modified so that it could receive analog input from a data acquisition through the Comedi library (see section 2.4). ScopeControl was created to provide a user interface that could control a multitude of various makes and models of oscilloscopes. The Comedi library already supports a large number of various PC-based data acquisition systems. The goal of this project was to give ScopeControl the capability to monitor data from any of the data acquisition systems supported by Comedi, thereby increasing the functionality of ScopeControl. A program was written in the C programming language (gpibni) that provided an interface to the Comedi library for ScopeControl. ScopeControl was then modified to communicate with gpibni through the Java Native Interface.

2 Programming Technologies

Between ScopeControl and the Comedi library, many layers of code exist that must communicate with each other successfully in order for the program to function. To understand how this code works, it is appropriate to have an understanding of the various programming technologies involved.

2.1 The Java Programming Language

The Java Programming Language is a portable, object-oriented programming language. Portability was a necessity of this project, as LLE is host to many computers and a variety of operating systems. ScopeControl was originally designed with this portability in mind, and it assisted in the final incorporation of data acquisition system support. More important for Java though is its object-oriented nature. An object-oriented programming language possesses a hierarchical program structure with abstract and super classes at the highest levels and specific subclasses at the lower levels. Without an object-oriented programming language, this project would have been next to impossible. As ScopeControl holds a Scope super class, only a data acquisition system subclass needed to be created in ScopeControl. This prevented the necessity of a full program overhaul and simplified programming.

2.2 The C Programming Language

The C Programming language is a relatively fast, lower level programming language. It is machine specific, which reduces overhead that exists in Java, but also removes portability. The C programming language was used for this project because it offers the speed necessary for a data acquisition system as well as the ability to communicate with data acquisition systems through the Comedi library.

2.3 The Java Native Interface

The Java Native Interface, or JNI, is a programming framework that allows programs written in Java to call and be called by machine-specific native programs such as those written in the C programming language. For the purposes of this project, the JNI allowed ScopeControl to give commands to C programs for data acquisition, as well as receive the data generated by these programs.

2.4 The Comedi Library

Comedi, or Linux Control and Measurement Device Interface, is a set of device drivers, tools, and libraries that can be used to control certain PC-based data acquisition systems. Comedi supplies the ability for programs written in C to control and obtain data from data acquisition hardware. This removes the tedious task of hardware-level programming for data acquisition and allows focus to remain on higher-level control programs.

3 Program Design

Due to the object-oriented nature of ScopeControl, adding PC-based data acquisition system features required few changes to existing code. A new program had to be written in C that could talk to the Comedi library and certain classes had to be added to ScopeControl. In a few situations, existing ScopeControl code had to be modified, such as the graphical user interface (GUI) and the 16-channel support.

3.1 Class Overview

ScopeControl has an abstract class Scope whose properties are inherited by the individual Scope classes. These classes hold the information on how the program should operate with each individual make and model of scope. A new Scope class was written, ScopePCI6251 (named after the PC-based data acquisition system that it was used on), that would allow ScopeControl to function though the Comedi library. However, it would be impractical for ScopeControl to talk directly to the Comedi library because of the limitations of Java. In order to circumvent this, a C program was written (gpibni) that receives commands from ScopePCI6251 through the Java Native Interface. It then executes any commands given, receives data from Comedi, and processes the data. Once the data is in the form of a byte buffer, it can be sent back through the Java Native Interface to ScopePCI6251. ScopePCI6251 works together with gpibni and the rest of ScopeControl through the abstract class ScopeConnection. A new ScopeConnection class was written that could utilize the Java Native Interface and communicate with both gpibni and ScopePCI6251.

3.2 Program Interface

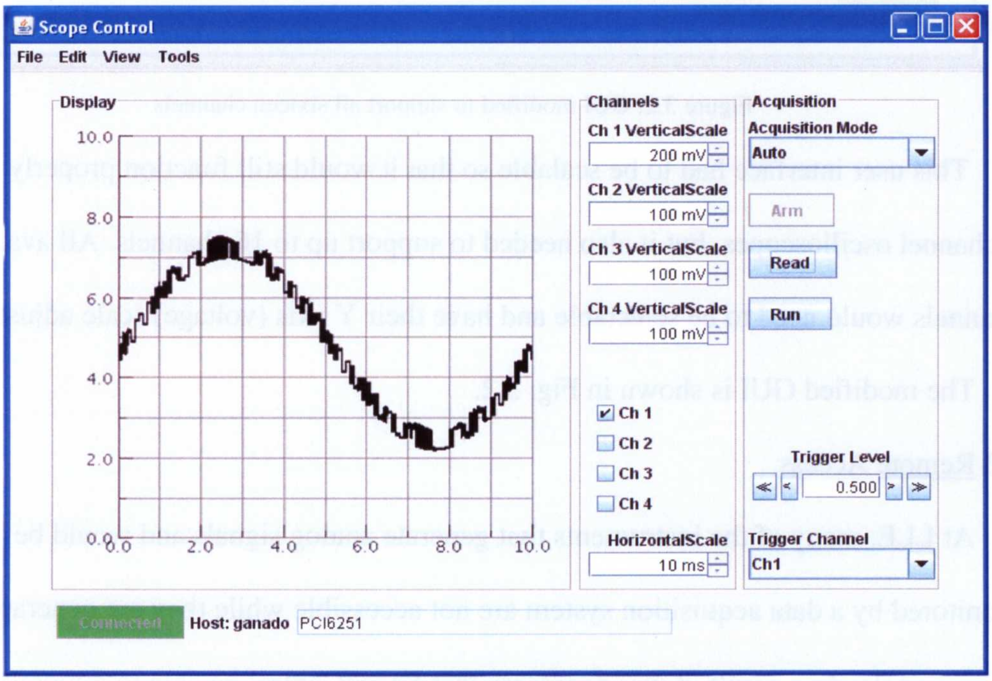

Ch 1 VerticalScale 200 mV
Ch 2 VerticalScale 100 mV
Ch 3 VerticalScale 100 mV
Ch 4 VerticalScale 100 mV
☑ Ch 1
☐ Ch 2
☐ Ch 3
☐ Ch 4
HorizontalScale 10 ms
Acquisition Mode Auto
Trigger Level 0.500
Trigger Channel Ch1
Host: ganado PCI6251

Figure 3.1: GUI with only four-channel support

ScopeControl was originally written to communicate with standard oscilloscopes, not data acquisition systems. As most oscilloscopes are limited to 4 analog input channels, ScopeControl was written to support only 4 channels (see Fig. 3.1). In some cases, modifying ScopeControl was as simple as changing the value of a variable. However, in the case of the GUI, a new user interface had to be created.

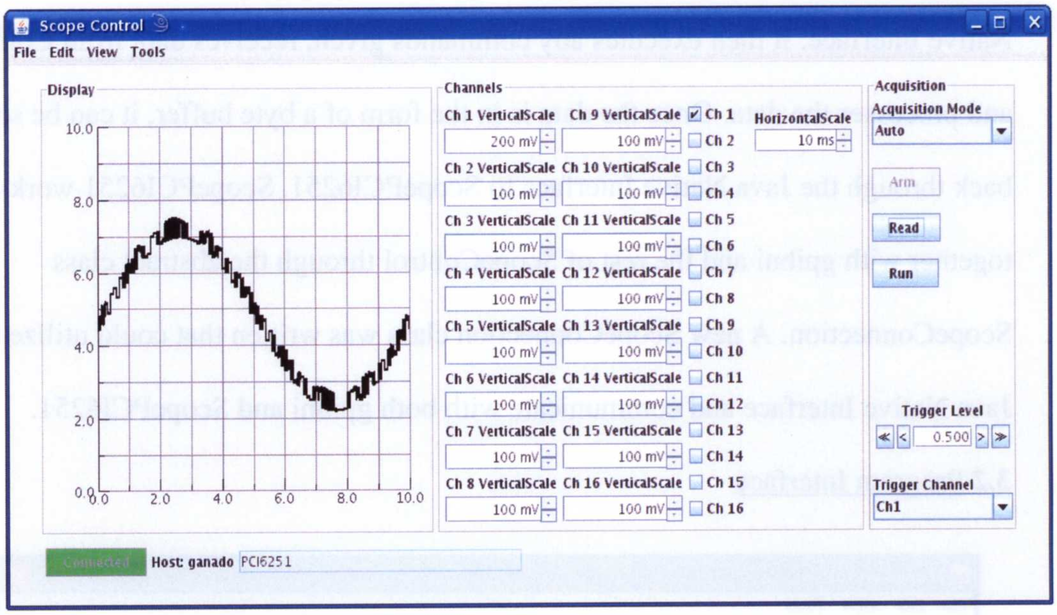

Ch 1 VerticalScale 200 mV
Ch 2 VerticalScale 100 mV
Ch 3 VerticalScale 100 mV
Ch 4 VerticalScale 100 mV
Ch 5 VerticalScale 100 mV
Ch 6 VerticalScale 100 mV
Ch 7 VerticalScale 100 mV
Ch 8 VerticalScale 100 mV
Ch 9 VerticalScale 100 mV
Ch 10 VerticalScale 100 mV
Ch 11 VerticalScale 100 mV
Ch 12 VerticalScale 100 mV
Ch 13 VerticalScale 100 mV
Ch 14 VerticalScale 100 mV
Ch 15 VerticalScale 100 mV
Ch 16 VerticalScale 100 mV

☑ Ch 1
☐ Ch 2
☐ Ch 3
☐ Ch 4
☐ Ch 5
☐ Ch 6
☐ Ch 7
☐ Ch 8
☐ Ch 9
☐ Ch 10
☐ Ch 11
☐ Ch 12
☐ Ch 13
☐ Ch 14
☐ Ch 15
☐ Ch 16

HorizontalScale 10 ms
Acquisition Mode Auto
Trigger Level 0.500
Trigger Channel Ch1
Host: ganado PCI6251

Figure 3.2: GUI modified to support all sixteen channels

This user interface had to be scalable so that it would still function properly with 4-channel oscilloscopes, but it also needed to support up to 16 channels. All available channels would need to be selectable and have their Y axis (voltage) scale adjustable. The modified GUI is shown in Fig. 3.2.

3.3 Remote Access

At LLE, many of the instruments that generate analog signals and would be monitored by a data acquisition system are not accessible while they are generating these signals. As a result, it was necessary that ScopeControl be able to remotely monitor analog signals from a data acquisition system. TEK7000Server is a preexisting program that already has the capability to create a server socket and communicate with a client computer through a network connection. It already had the capability to monitor an oscilloscope, so it was only necessary to add the code to interface to the PC-base data acquisition system . The client computer can then run ScopeControl and connect to the server through a network connection.

3.4 Future Adaptations

The object-oriented nature of ScopeControl made the inclusion of data acquisition system support possible. It also makes possible any number of future upgrades that may be added to ScopeControl. Functionality for more oscilloscopes and data acquisition systems could be added in a similar manner to the Comedi-supported data acquisition systems. Another future adaptation is hardware triggering. Comedi does not currently support hardware triggering for analog input channels. Gpibni was designed so that should this support ever be given to Comedi, Gpibni could be easily modified for hardware triggering. Although analog signal output was not heavily investigated for this project, it is possible for analog output to be added to ScopeControl. However, a separate program may fulfill this role better than a modification of ScopeControl.

4 Program Testing

Throughout the process of program design, it is necessary to test the program often so that any errors will be quickly discovered. ScopeControl now has two main methods of reading an analog signal. These are software-triggered and untriggered data acquisition. Both required extensive testing to ensure proper functionality.

4.1 Untriggered Data Acquisition

Untriggered Data Acquisition refers to simply reading signals from an analog channel and displaying them. When the computer is told to read data under untriggered data acquisition, it immediately begins reading the data. In order to test data acquisition in ScopeControl, a signal generator was connected to the data acquisition system and analog signals were produced. After the signal was displayed by ScopeControl, the analog channel was connected to a regular oscilloscope and the accuracy of ScopeControl was determined. When the signal displayed by ScopeControl was the same as that displayed by the oscilloscope, it was known that ScopeControl was properly reading the signal.

4.2 Software-Triggered Data Acquisition

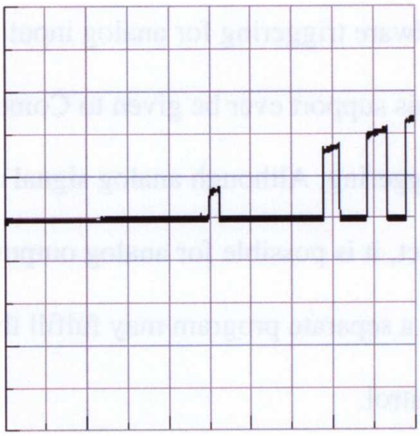

Figure 4.1: The beginning of an analog signal displayed by the data acquisition system

Software-triggered data acquisition is similar to its untriggered counterpart except that the computer now determines when to start recording the analog signal, rather than the user. As Comedi does not currently support hardware-triggered data acquisition, it was necessary that triggering be created in the software. Currently, all triggering is done by gpibni. If ScopeControl tells gpibni that the next data read is to be software triggered, gpibni creates a ring buffer with which to store incoming analog data. A ring buffer stores data points in a virtual ring. As new data comes in, it overwrites old data. When a data point is read that exceeds the trigger value, the ring buffer ceases to overwrite old data points and places any new data in a separate buffer. The two buffers are then combined into a single set of data and sent back to ScopeControl. Software triggering can be done to prevent an incoming signal from "rolling" across the display, or it can be used to catch and view the beginning of a signal (see Fig. 4.1). Because regular oscilloscopes feature triggering, testing the functionality of software-triggered data acquisition was done in the same manner as untriggered data acquisition. The signal displayed by ScopeControl was compared to the signal displayed by the oscilloscopes and any errors were corrected.

5 Conclusion

Through experiments at LLE, vast amounts of data are collected and many laboratory instruments need to be monitored. In order to collect all this data, many oscilloscopes are in use at LLE. However, certain oscilloscopes can now be replaced by newer PC-based data acquisition systems. These data acquisition systems can monitor more channels, provide higher flexibility, and are relatively inexpensive compared to oscilloscopes. In the future, data acquisition systems can continue to replace current lab equipment by acting as signal generators and digital IO in a laboratory environment.

6 Acknowledgements

I would like to thank my advisor, Dr. Christian Stoeckl, for his assistance, help, and guidance on my project. I would also like to thank Benjamin Smith for helping me to understand the Comedi library and ScopeControl. Finally, I would like to thank

Dr. Stephen Craxton for giving me the opportunity to participate in the 2008 University of Rochester Laboratory for Laser Energetics Summer Program.

High-Speed Measurements of Target-Support Vibrations Using Line-scan Cameras

Nicholas Hensel

High-Speed Measurements of Target-Support Vibrations Using Line-scan Cameras

Nicholas Hensel

Advisor: Dr. Douglas Jacobs-Perkins

Laboratory for Laser Energetics
University of Rochester
250 East River Road
Rochester, NY 14625-1299

Summer High School Research Program
2008

Abstract:

The Laboratory for Laser Energetics (LLE) houses the OMEGA 60-beam laser, which is used to carry out inertial confinement fusion (ICF) experiments. The 60 beams delivered by the laser are all focused on a fusion target that is less than a millimeter in diameter. To properly carry out an ICF experiment, the target has to be uniformly irradiated by all 60 of the laser beams. Target vibrations are a critical source of error because they shift the position of the target, disrupting the uniformity of target irradiation. Deviations in target location as little as 20 microns from target chamber center (TCC) can seriously affect the implosion.

Line-scan cameras capture images that represent displacement in one dimension as a function of time, and can therefore be used to capture target movement. Displacement data extracted from the images can then be analyzed using a Fast Fourier Transform (FFT) to identify resonant frequencies of the target. This provides valuable information about the target support structure, its responses to various vibration sources, and the possible effects of engineering improvements.

Optical measurement techniques are superior to other possible options because they do not directly contact the target. However, camera resolution and image quality limit the camera’s ability to capture data for targets that are resonating at high frequencies with small displacements.

1. Introduction:

Inertial confinement fusion (ICF) experiments at the University of Rochester's Laboratory for Laser Energetics (LLE) are conducted with both the OMEGA and OMEGA EP lasers. The fundamental concept of an ICF reaction is to compress and heat a target using lasers so that fusion conditions are met and fusion reactions can occur. At LLE, the target is a plastic shell approximately 3µm thick and 860 µm (1µm = 0.001 mm) in diameter that is filled with frozen deuterium (D_2) or deuterium-tritium (DT). The target is suspended from a stalk by spider silks to minimize surface contact and ensure an even surface for fusion (see Fig. 1). The stalk is positioned so that the target is located at the convergence of the beams at the target chamber center (TCC). In order for effective ICF reactions to occur, the target must be evenly irradiated. Otherwise uneven ablation will result in uneven compression and limit the amount of material that effectively fuses, decreasing the yield from the fusion reactions. In order for an even compression to occur, the target must be located very precisely at TCC.

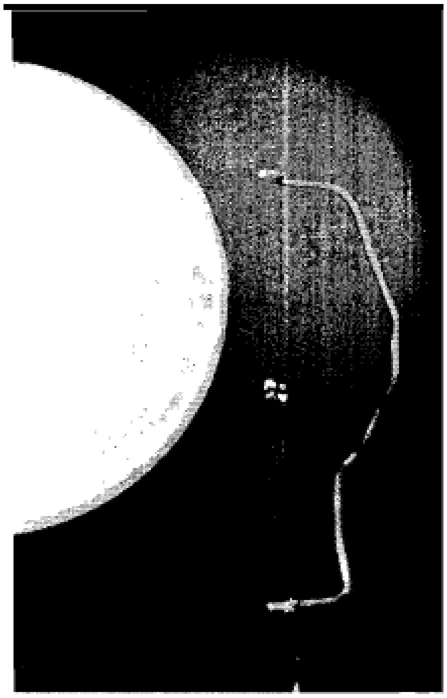

Figure 1: A target mounted on a stalk next to a penny.

The exact positioning of the target is critical. A displacement of as little as 20 µm will seriously impair the compression. Static and dynamic position errors jointly contribute to the maximum allowable error. The target is particularly susceptible to dynamic error because the target mount is susceptible to environment-induced vibrations. Sources including vacuum pumps and machinery attached to the chamber along with machinery in the building and even vehicles driving on the freeway outside the building all contribute to the background vibration that the target experiences. If the resonant frequencies of the target can be isolated, engineering modifications can be made to the stalk to minimize the effect of these frequencies on the target, greatly reducing the dynamic position error of the target.

Scientists at LLE have used traditional two-dimensional (2D) high-speed cameras to observe target vibrations. From vibration data collected by these cameras, resonant frequencies of the stalk can be extracted from Fourier transforms used on position data of the target over time. However, the high expense of the 2D high-speed cameras makes purchasing multiple units for testing purposes costly. In order to minimize the cost, LLE is looking to find an inexpensive camera alternative for use in laboratory development settings. In that regard, the line-scan cameras are highly appealing because of their low costs and variety of capabilities.

2. Line-scan Camera Usage for Vibration Analysis:

Cameras are fundamentally an appealing form of measurement for target vibrations for a number of reasons. The primary reason is that they are a non-contact form of measurement. Unlike accelerometers, which require contact and alter how the stalk reacts, cameras do not require any direct interaction with the stalk, allowing for accurate measurement without disrupting the fusion process in any way. Another important advantage of using a camera rather than an accelerometer or other form of measurement is that a camera naturally measures displacement. An accelerometer however, functions by measuring accelerations. The data gathered from an accelerometer must therefore be double integrated to get displacement. Integration errors are cumulative and do not allow accurate determination of absolute position.

In place of a traditional 2D high-speed camera, it is also possible to use a line-scan camera to capture similar data for analysis. A line-scan camera differs from a normal camera in that an image created by a line-scan camera shows the position of an object along a single dimension as a function of time, rather than showing the position of an object in 2D space at an instant of time. The difference is a result of how a line-scan camera’s method of capturing an image differs from that of a traditional 2D digital camera. Both types of digital camera have an image sensor that converts optical data to an electrical signal. Commonly, the image sensor is a charge-coupled device (CCD) with a photoactive region. The CCD captures photons and outputs an electrical signal that is used to create an image. In a 2D camera, the CCD captures photons in a grid of specific height and width and uses the data to compose an image of a certain number of pixels in both rows and columns. A line-scan camera differs in that the CCD has only a single column of photon collectors (pixels). To form a complete image, a line-scan camera collects many individual lines of data. The rate at which lines of data are acquired determines the rate at which position can be measured. The exposure time of each line image is kept very short to minimize motion-induced blur. Each line represents the position of an object along a single dimension in space and as lines are built upon each other, an image is formed which shows how position changes over a period of time (see Fig. 2).

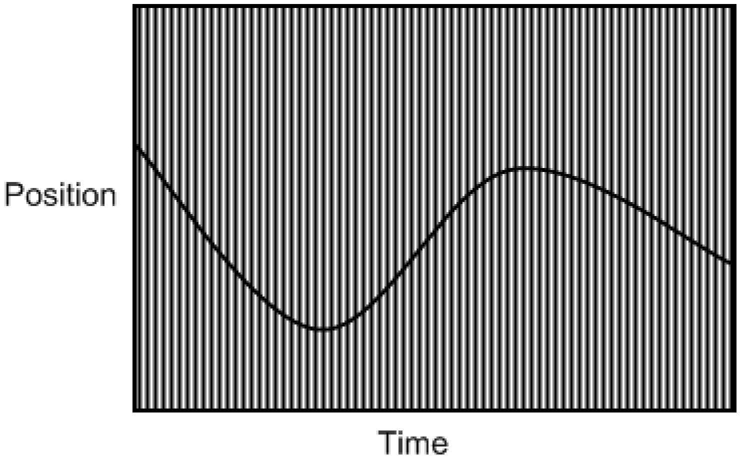

Figure 2: Line-scan camera image. Each vertical line represents a single image capture and the moving line shows position over time.

Line-scan cameras have a major advantage over traditional 2D high-speed cameras in that they cost only a fraction of what a standard camera would. The 2D cameras that are currently being used on the LLE target chamber cost over fifty thousand dollars, whereas a reasonable quality line-scan camera costs less than a thousand dollars. The line-scan camera is also advantageous because it allows the user to easily isolate movement along a single axis, which is highly useful in finding vibration frequencies for that particular axis. The ease of capturing movement, combined with the relatively low cost of each camera, leads to a more advanced usage of the cameras wherein multiple cameras could be used to capture images of the same target from multiple angles, enabling a virtual representation of the object to be built up in three-dimensional space. This approach is feasible in this application because the object of interest is a simple geometric shape, i.e. a cylindrical stalk or a spherical target.

The use of multiple line-scan cameras placed orthogonal to each other would provide a powerful new aspect of target analysis because of the added dimensional information that each new camera would provide. However, there are a number of issues that would have to be resolved individually and collectively before such a setup would be effective. The primary issue is one of lighting, which is a problem when using any high speed camera. If the target is not sufficiently illuminated, the high speed cameras, which have extremely low exposure times, will not be able to collect enough photons to form sufficiently bright images. The problem is exacerbated when multiple cameras are present, because the target then has to be illuminated from all angles to ensure total lighting. Another issue that has to be resolved is line-capturing synchronization for each of the cameras. Because each camera is capturing different information from different angles, the images will not necessarily coincide with each other upon inspection, so it is critical to ensure that the cameras are capturing data at the same time as each other. Furthermore, the cameras need to be capturing images at the same time as the target is illuminated, so a controller is needed to ensure that the light sources are on at the same time as the cameras are capturing information. In order to facilitate these multiple processes, a trigger system was developed to coordinate data gathering across multiple cameras (see Fig. 3).

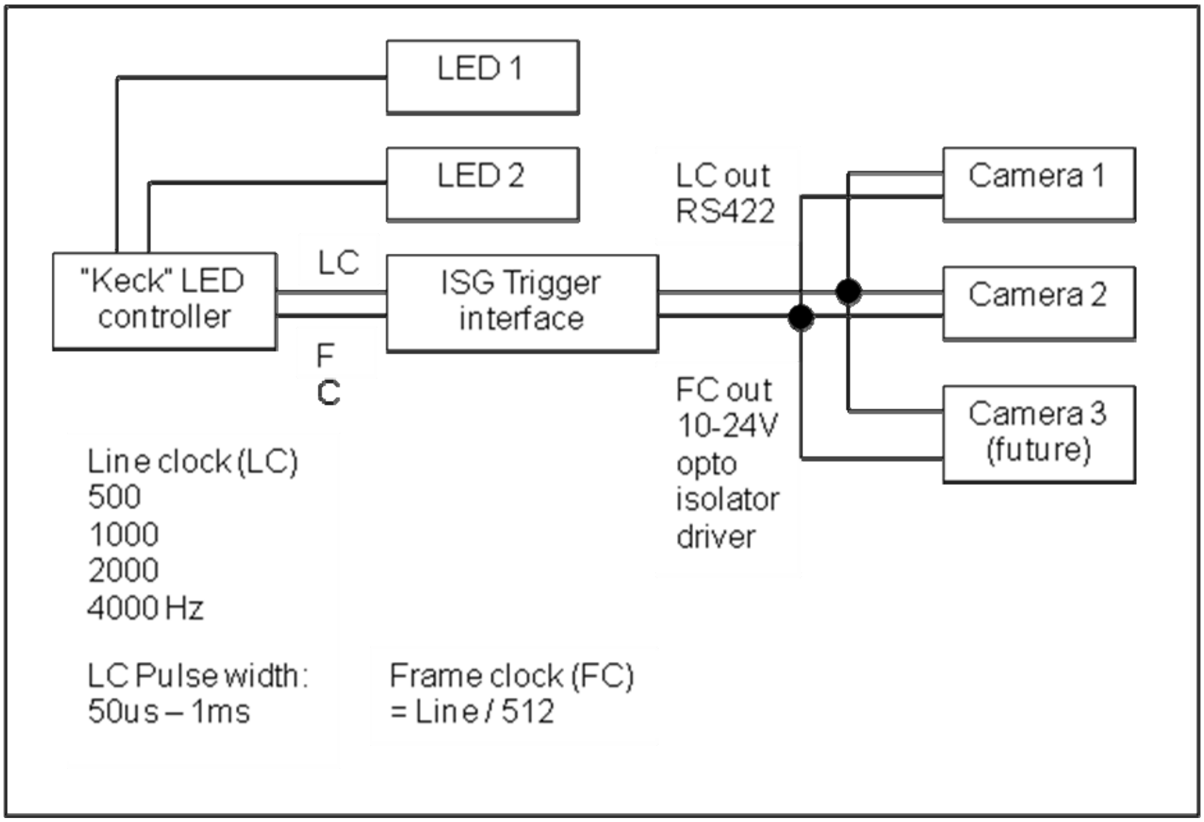

Figure 3: Controller interface for synchronizing camera line acquisition. The "Keck" LED controller illuminates the source at the same time as the cameras are commanded to gather line data. Both can be controlled at a range of frequencies from 500 Hz to 4000 Hz

3. Image Testing with Line-scan Cameras

The use of line-scan cameras for target vibration characterization is an appealing prospect to LLE because of their advantages. However, before the cameras are implemented, they must be tested to ensure that they will provide useful feedback. The first step to testing the line-scan cameras involved simple image collection. First, a sine wave was generated using the Matrix Laboratory (MATLAB) programming environment. The sine wave was then converted to an image with a chosen line thickness, printed on paper, and wrapped around a cylinder of known radius that could be driven at a known number of rotations per minute. The synthesized waveform was then recaptured using a line-scan camera calibrated to the image (see Fig. 4). The image portrayed has time along the y axis, and displacement along the x axis. Initial images captured from the rotating shaft had a number of problems, the primary of which was uneven and insufficient lighting. Additionally, the image was not continuous, as the camera did not capture each line to build an image at a rate directly proportional to the number of rotations of the shaft per minute. Finally, the image captured was not significantly magnified, which made any data extracted from the image noisy and inaccurate. Attempts to recreate the sine wave from this initial test image were unsuccessful.

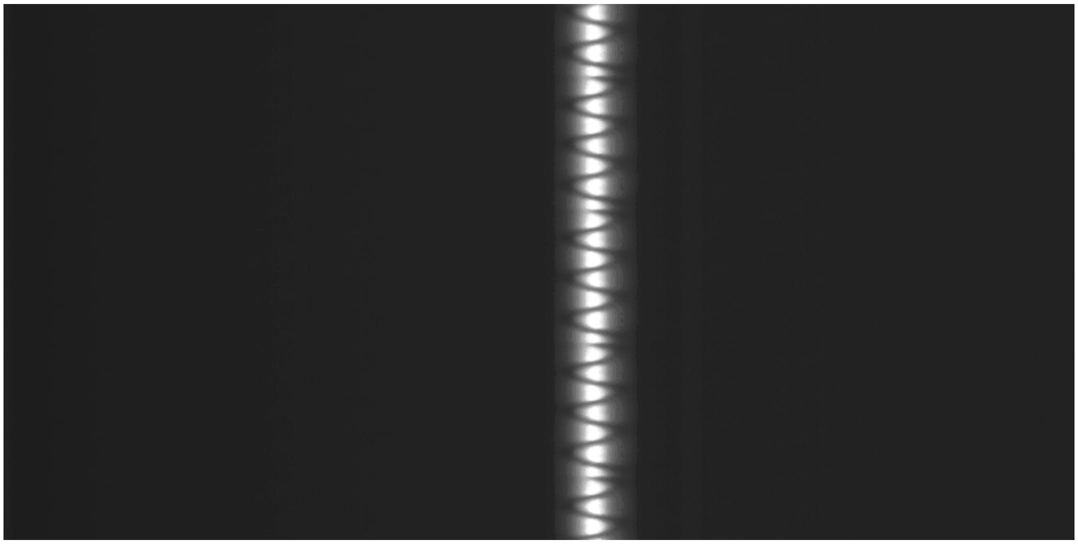

Figure 4: A test image capture from a constructed sine wave rotating on a cylinder driven by a motor. The image is insufficiently magnified, not well illuminated, and discontinuous. The time axis is vertical.

After image capturing with the motor and cylinder proved ineffective, the camera was mounted to a new setup with a lens that increased the zoom. Additionally, by using the “Keck” LED controller, the target could be more uniformly illuminated with a blue LED rather than using a laser pointer focused on the target. Now, rather than focusing on a rotating shaft, the camera was used to take images of an old target stalk, a much more representative situation for how it would be used in actual application. The stalk was mounted to an electrodynamic shaker that could then be driven at a known frequency and amplitude. The stalk itself was attached to a moving table that oscillated in and out based on the movement of a surface which functioned much like a speaker coil. When given a commanded frequency, waveform, and amplitude in volts, the shaker table would vibrate back and forth, and the camera captured that vibration. The results from the shaker table experiments were much more promising, because the images yielded were at a much higher magnification and the object was more evenly illuminated (see Fig. 5).

Figure 5: An example image taken with a line-scan camera of a vibrating target stalk mounted on a shaker table. The stalk itself is magnified to approximately 6 cm in width. The time axis is vertical.

4. MATLAB Analysis Routines

After the collection of data from the electrodynamic shaker table and target stalk, the images were processed in MATLAB to extract useful data on waveforms and resonances. In order, the steps are: cropping, normalization, spline interpolation, binarization, edge pixel finding, and graph analysis.

In the first step, one edge of the target stalk vibration is cropped, to capture only the region of interest and nothing else. The advantage of cropping is that it yields a smaller, more manageable image, and eliminates problems with isolating the desired waveform later in processing. An example of this cropping is show in Figure 6.

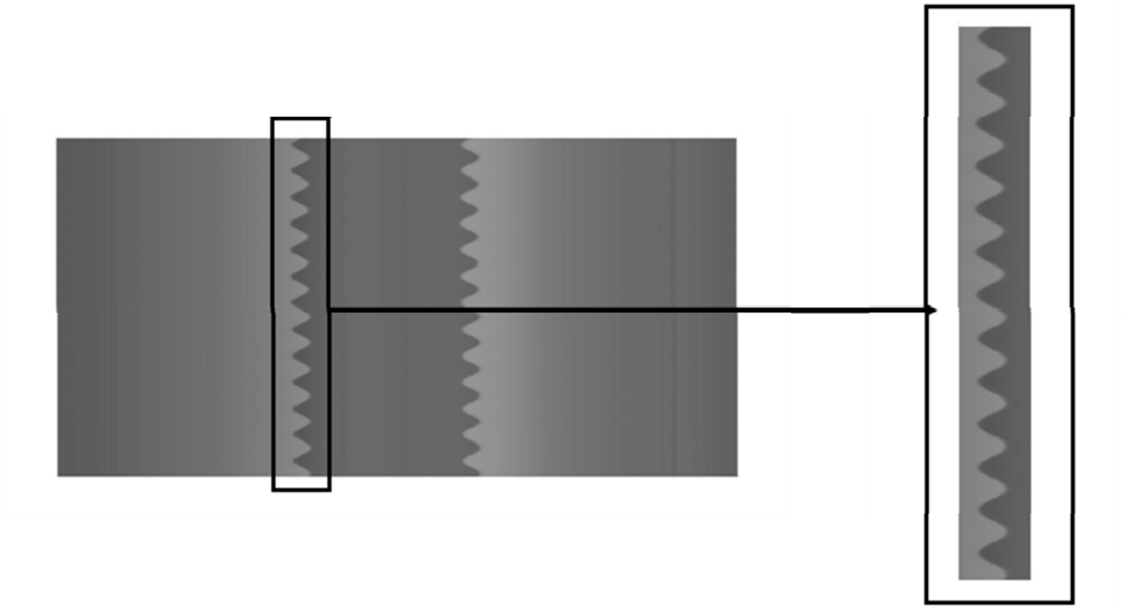

Figure 6: A test image with a cropped region shown. This image takes only the left edge of the vibrations, to ensure that only a single waveform is processed.

The second step, normalization, is only necessary when the image is not continuous and needs to be manipulated to ensure continuity. Because the captured waveform is evenly continuous and has a clear border, this step is not necessary.

Next, the cropped image is spline interpolated to create sub-pixel resolution. The purpose of the spline interpolation is to increase the sensitivity of the camera to vibration, effectively increasing the range of amplitudes that the camera can observe. Figure 7 shows the cropped image before and after a spline interpolation.

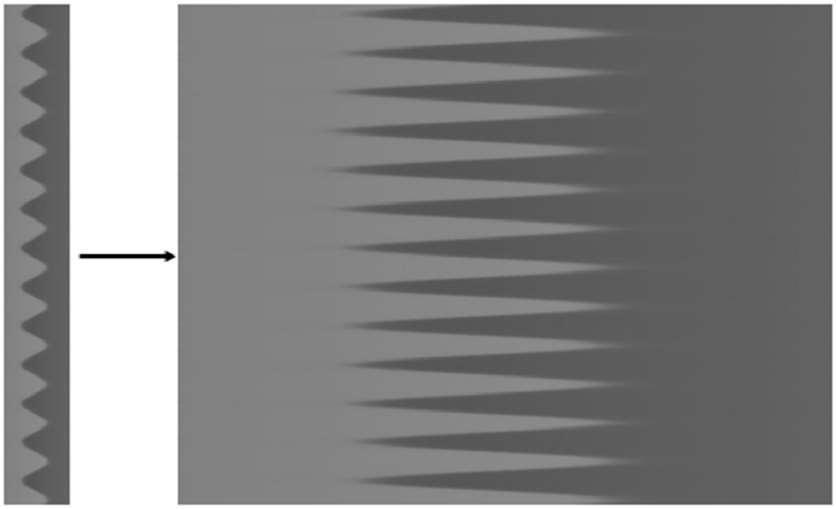

Figure 7: Cropped image before and after spline interpolation. Cubic spline interpolation in the horizontal direction is applied to the graph line by line, so that the resolution can be increased by virtual means. The aspect ratio of the interpolated image is not accurate, because sub-pixel values have to be displayed, so the image appears stretched.

After the image is interpolated, it has to be broken into true and false regions so that the image can eventually be converted into an actual graph. This step involves creating a brightness range, with all values within the range becoming true and all values outside the range false. For the example image, a range of values from 0 to 101 (on a scale of 0 to 255) were set as true. The result of the binarization is shown in Figure 8.

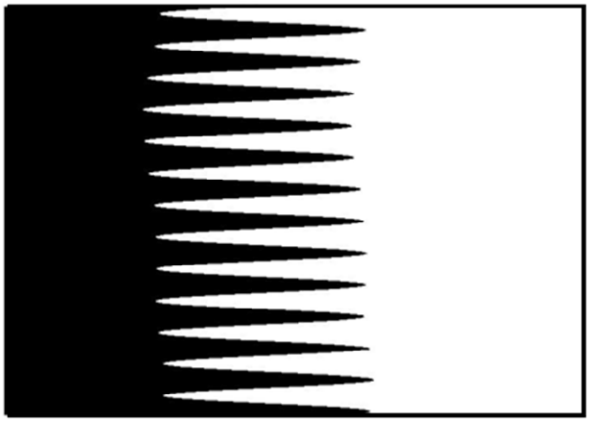

Figure 8: Binarization of the interpolated waveform. The true range is set as values from 0 to 101 (on a scale of 0 to 255).

After the image is converted to a binary map, the edge of each line where the image switches in Boolean value can be considered a data point. Processing each line of the image yields a set of coordinates that create a graph when plotted. The result of edge finding on the binarized image is shown in Figure 9.

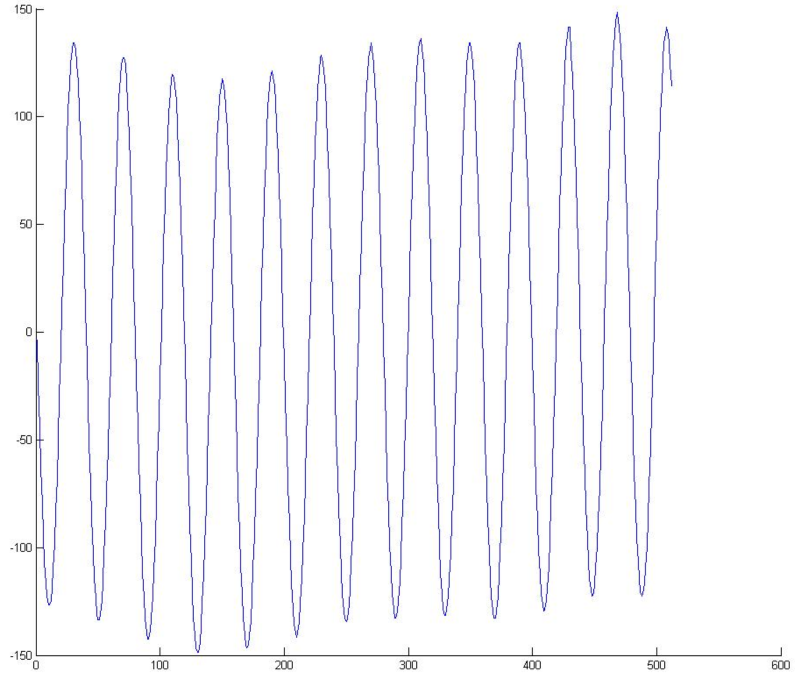

Figure 9: A graph of edge detected points. The X value is the line number from the image (row value, corresponding to time) and the Y value is the displacement from the middle of the image in pixels.

Following the construction of the waveform shown in Figure 8, a critical step is the execution of a Fast Fourier Transform (FFT) to isolate key frequencies present in the waveform, indicating the resonant frequencies of the target stalk. An FFT performed on the test data can be used to calibrate the camera because the electrodynamic shaker's motion can be measured with a calibrated accelerometer. The data taken from the shaker could then be used with results from the image processing to calibrate amplitude and frequency. An FFT performed on an actual target stalk would show the key frequencies at which the target resonates. Following the discovery of such frequencies, the stalk and support structure could be redesigned to eliminate or dampen the effect of those frequencies.

5. Camera Limitations

The major question that needs to be resolved related to the use of the line-scan cameras is exactly how useful they will be at measuring target vibrations in actual chamber conditions. Specifically, what level of resolution can the camera obtain, and at what frequencies? The camera, with magnification, operates at about four microns per pixel resolution. With an added spline interpolation, the magnification can be increased somewhat, though the process of interpolating invites possible error if the interpolation proves inaccurate. As a result, the camera will not effectively record any displacement less than 4 µm.

Past data indicates that the target assemblies resonate at relatively high frequencies, reaching as high as 305 Hz in some cases. Figure 10 shows that if these resonances are observed, the target must be experiencing accelerations in excess of 1g. At resonance, the target motion may be greater than the input excitation by several orders of magnitude, so it is important to be able to measure this response. However, the fact that the target may oscillate at displacements smaller than the camera's optical sensitivity of 4 µm is not of great concern, because only displacements of over 20 µm have a substantial impact on ICF experiments. The camera is clearly able to measure displacements of order 20 µm. During Fourier analysis of the motion waveforms, component frequencies over 100 Hz may not be effectively captured, but the components would fall outside of the frequencies of concern.

An additional capability of the line-scan cameras to strengthen the quality of Fourier data is their ability to store many consecutive frames for processing. By building waveform data from frame to frame, random noise and variation is minimized, yielding a cleaner image with more distinct wave properties.

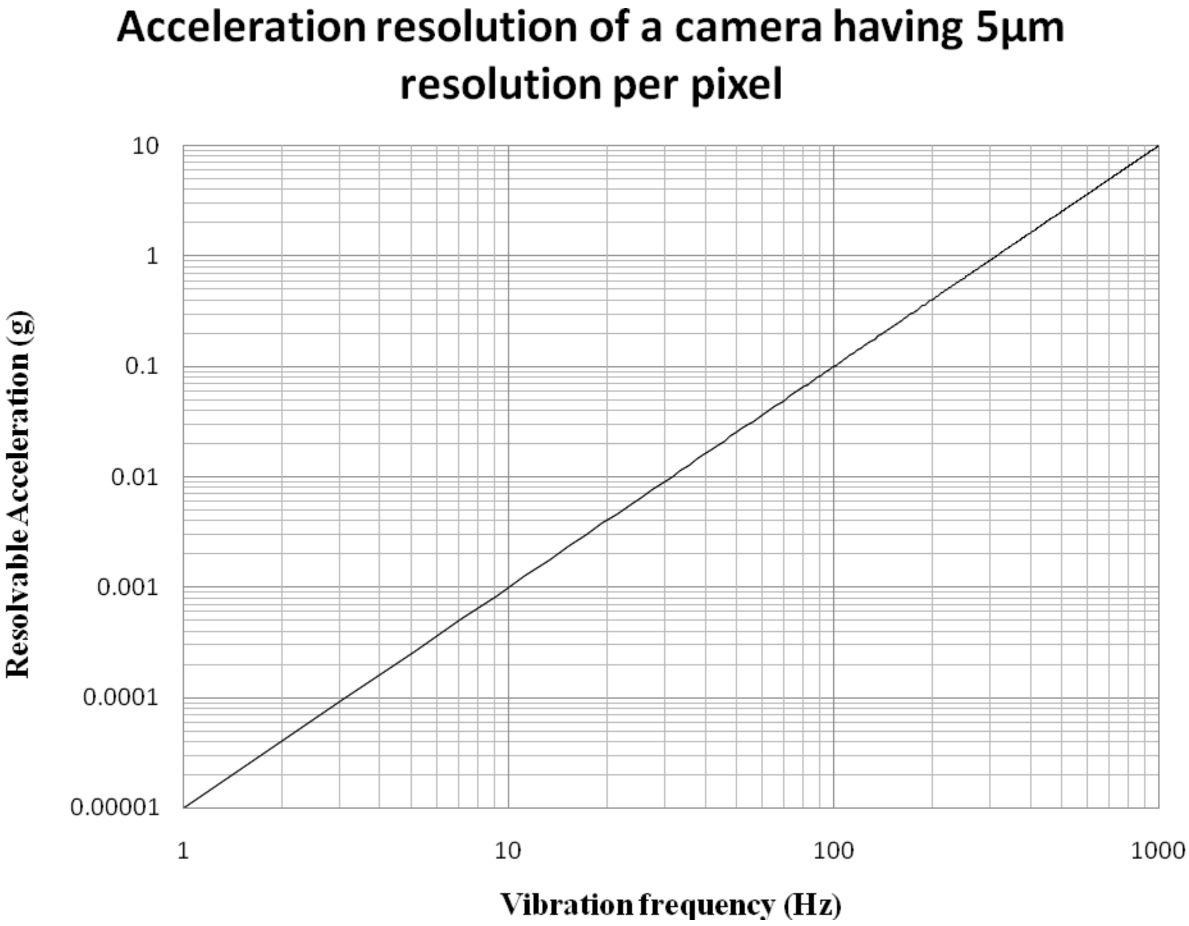

Figure 10: Optical resolution limitations of the line-scan camera. The graphed line shows the acceleration which the camera can resolve for a variety of frequencies ranging from 1 Hz to 1000 Hz. The logarithmic scale shows that the resolvable acceleration increases as the square of the vibration frequency.

6. Conclusion

The fundamental limitation of using optical measurement techniques is that they are only useful in measuring vibrations when the displacements exceed the minimal optical resolution. The issue of optical sensitivity is particularly critical when measuring target vibrations because the displacements may be very small. However, line-scan cameras, with appropriate optical magnification, are able to obtain an optical sensitivity of 4 µm per pixel.

Though the line-scan cameras have definite limitations in measurement capabilities for high-frequency oscillations at low accelerations, they are still useful for characterizing target vibrations relevant to ICF experiments.

Further testing with line-scan cameras inside the target bay and with other optical fixtures may improve the sensitivity of the cameras and provide further data on their functionality for measuring target oscillations. Additionally, the process of networking multiple cameras to build a two or three dimensional representation of the target movement was largely untested and work can still be done in determining the plausibility of such measurements.

7. Acknowledgements

I would like to thank Dr. Douglas Jacobs-Perkins for finding a project for me on short notice, and for taking time to help me when possible, even with the new responsibilities he took on over the course of the summer.

I would also like to thank Gerald Abt for taking time to talk to me about my project and for offering to help teach me about different functionalities in MATLAB.

Finally, I would like to thank Dr. R. S. Craxton for working with all of the high school students year after year to continue making the program as successful as it is, and the Laboratory for Laser Energetics for continuing to hold the program. The summer experience was highly rewarding.

Characterization of a Cryogenic Fuel Capsule in a Transparent Hohlraum

Rachel Kurchin

Characterization of a Cryogenic Fuel Capsule in a Transparent Hohlraum

Rachel Kurchin

The Harley School
Rochester, NY

Advisors: Dr. R. S. Craxton, Mr. M. Wittman

Laboratory for Laser Energetics
University of Rochester
Rochester, NY
November 2008

Abstract

Characterization of a spherical cryogenic fuel capsule in a cylindrical hohlraum is important for indirect-drive inertial-confinement-fusion implosions, as the capsules must be as uniform as possible. Shadowgraphic image analysis techniques developed for spherical capsules have been adapted to evaluate the uniformity of capsules in hohlraums. An existing ray-trace code has been extended to add the hohlraum and predict the apparent outer capsule radius and bright ring radius as functions of angle around the viewing direction. The extended code can also make predictions for capsules that are displaced within the hohlraum. The predictions of the code have been confirmed by data obtained under a microscope using a surrogate capsule (a thick, spherical plastic shell) in a glass hohlraum. By subtracting the predicted distortions from the measurements of the bright ring radius, the uniformity of the inner surface of the capsule can be assessed. The uniformity of capsules in hohlraums can now be evaluated to a degree of accuracy constrained primarily by the uniformity of the hohlraum.

1. Introduction

Fusion is extremely promising as an almost limitless source of energy and is being investigated around the world. It is cleaner and potentially more cost-effective than current nuclear energy sources because it avoids the production of long-lived radioactive waste. Fusion is based upon combining two smaller atoms to make a larger one – the way the Sun creates energy. The fusion reaction generally attempted on Earth proceeds thus:

$$^{2}H + {}^{3}H \rightarrow {}^{4}He + n,$$

where ^{2}H is deuterium, the hydrogen isotope with one neutron, ^{3}H is tritium, the isotope with two neutrons, ^{4}He is helium, and n is a high-energy neutron. However, this seemingly simple reaction poses many problems because fusion must occur at an extremely high temperature, and it is difficult to contain the reactants under such extreme conditions.

There are two main techniques being investigated to contain the deuterium and tritium: magnetic confinement and inertial confinement. In magnetic confinement, the deuterium and tritium are maintained in a vacuum chamber at high temperature for long times (seconds and longer) by large magnetic fields. In inertial confinement, high-power laser beams are used to rapidly heat and compress a capsule typically consisting of a thin plastic outer layer and a thick layer of deuterium-tritium (DT) ice. Once the capsule has been compressed, the deuterium and tritium are confined only by their own inertia. Inertial confinement fusion reactions occur much faster than in magnetic confinement, typically finishing on the order of nanoseconds rather than seconds.

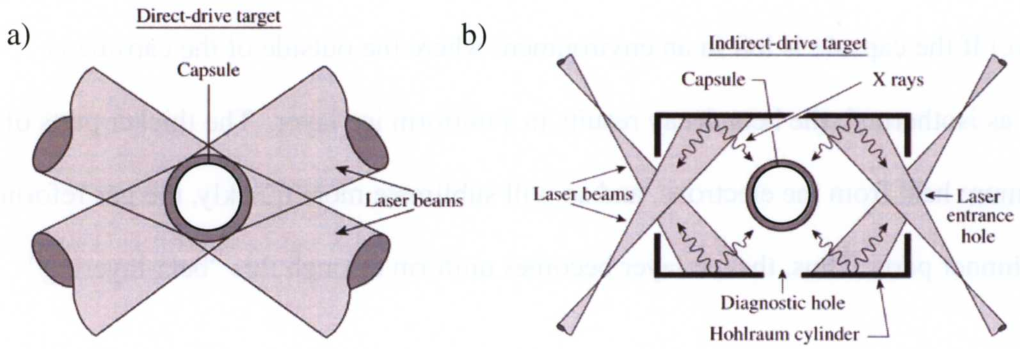

Figure 1: a) Direct- and b) indirect-drive fusion. In direct drive, the lasers directly hit the capsule, and in indirect drive, they hit the inside of a cylinder, producing X-rays which then hit the capsule.

There are two general categories of inertial-confinement fusion: direct drive[1] and indirect drive.[2] In direct drive, the capsule is directly irradiated by the laser beams (see **Figure 1a**), causing the plastic layer to ablate. The reaction force to the ablation compresses the DT fuel forcing it to implode. In indirect drive, the subject of this paper, the lasers irradiate the inside of a cylinder known as a hohlraum. The cylinder produces X-rays, which reflect around the inner surface, eventually hitting the capsule from various directions (see **Figure 1b**). This results in a more uniform irradiation but lower efficiency because most of the energy is lost to the hohlraum and thus not transferred to the capsule.[2] The National Ignition Facility[3] (NIF), a large laser due to be completed in 2010, will use indirect drive. Inertial confinement fusion requires the maximum possible capsule uniformity since thinner parts of the capsule implode more quickly, magnifying nonuniformities.

Typical cryogenic capsules[4] start as only the plastic shell. On the NIF, they will be filled with DT gas using a very small "fill tube" attached to the capsule. The fill tube is also attached to a reservoir of DT and is sealed off once the desired amount is inserted in the capsule. Next, the shells are gradually cooled for the ice layer to form. The naturally formed ice layer is never uniform, but since tritium is radioactive, the electrons produced by its beta decay will heat the ice. (In beta decay, one of tritium's neutrons decays to a proton, an energetic electron, and an antineutrino.) If the capsule is left in an environment where the outside of the capsule is maintained as isothermal, the beta decay results in a uniform ice layer. The thicker parts of the ice absorb more heat from the electrons, and so will sublimate more quickly, the gas reforming as ice on the thinner parts. Thus, the ice layer becomes uniform through this "beta-layering" process.[5]

Before it is shot, the uniformity of the capsule is evaluated. On the NIF, this will be done using a technique called X-ray phase contrast imaging.[6,7] Off-line experiments used to develop the layering process for capsules in hohlraums will use both X-ray phase-contrast imaging and shadowgraphy. Shadowgraphy consists of passing light through the capsule, taking an image of the capsule, and using patterns in the image to determine the layer uniformity. Shadowgraphy has been used extensively in the past to characterize cryogenic capsules; a direct comparison between shadowgraphy and X-ray phase-contrast imaging will allow a valuable cross calibration

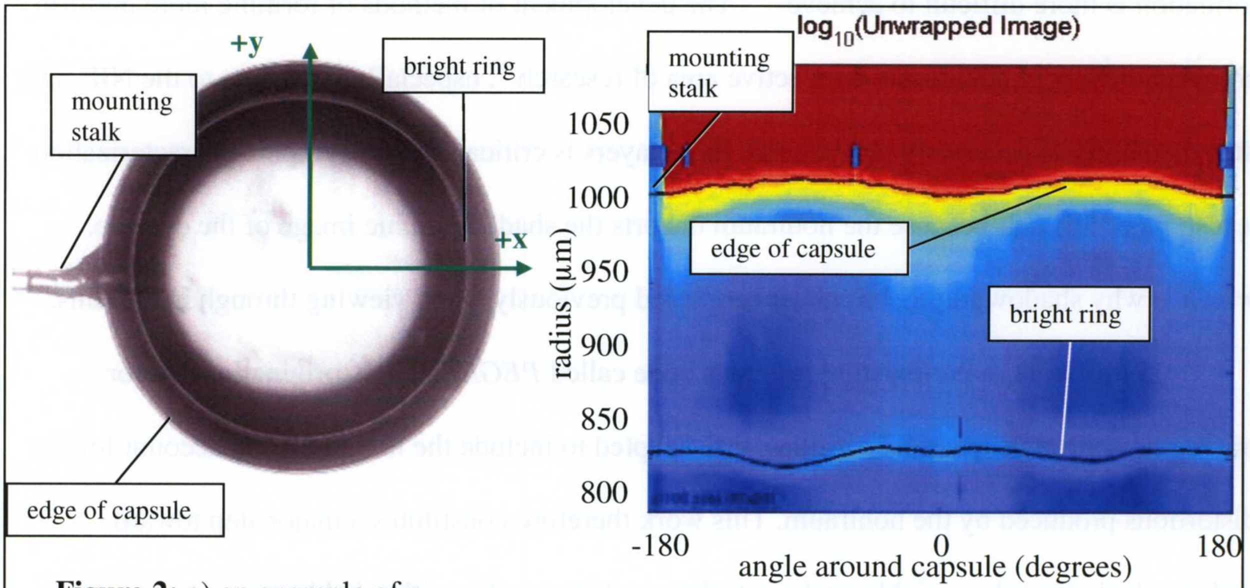

Figure 2: a) an example of a shadowgram of a thick spherical plastic shell in a glass hohlraum

b) Image produced by *VIEWCRYO* from an image such as that in (a).

of the two techniques.

An example of a shadowgram can be seen in **Figure 2a**, in which a plastic shell (rather than a DT layer) is used as a surrogate to test the effect of a hohlraum on shadowgraphy before a cryogenic experiment is attempted. In the image, the light regions outside the capsule edge and in the center correspond to the light source being transmitted without much loss. The darker areas are where the rays are blocked by the capsule. While the rings in the image (the outer edge and bright ring) appear circular, they contain deviations from constant radius that can be directly used to evaluate the capsule nonuniformity. An analysis program called *VIEWCRYO*[8], used in the experimental part of this work, produces an image such as that in **Figure 2b** from a shadowgram, showing the variations in radius of these two rings. The curves seen in **Figure 2b** are typical of the distortions created by the hohlraum, and to evaluate the uniformity of a capsule, they must be accounted for.

When the capsule is layered inside a hohlraum, as must be done for indirect drive, it is more difficult to layer it evenly because the isothermal environment required for uniform layer formation is more difficult to achieve[9,10]. The development of methods of forming more uniform cryogenic layers in hohlraums is an active area of research[10], especially important to the NIF, and thus the ability to accurately characterize these layers is critical. Shadowgraphic characterization is also more difficult because the hohlraum distorts the shadowgraphic image of the capsule, which is why shadowgraphy has never been used previously when viewing through hohlraums.

In this work, a pre-existing ray-trace code called *PEGASUS*,[11,12] originally used for tracing rays through spherical capsules, was adapted to include the hohlraum and account for the distortions produced by the hohlraum. This work therefore constitutes a major step toward making shadowgraphy a viable analysis technique for capsules within hohlraums.

2. Analysis of Shadowgraphy

The origin of the features visible in **Figure 2a** can be explained with **Figure 3**. This figure shows ray trajectories through a spherical glass capsule placed inside a cylindrical hohlraum. A-rays pass directly through all surfaces of the hohlraum and capsule, forming the light region in the center of **Figure 2a**. B-rays (shown in **Figure 3a**) are reflected off the inner ice surface and when projected back appear to come from a very small region known as a bright ring[13]. C-rays do not hit the capsule, thus forming the lightest region outside the image of the capsule. Note that the C-ray path length increases with increased distance y from the horizontal axis, as in a (concave) divergent lens which is thicker further from the center, so the C-rays emerge diverging. U- rays (shown in Figure 3b) are similar to B-rays, but reflect off the inner ice surface from the inside. It should be noted that the ray traces in **Figure 3** do not include the full range of rays that would pass through the target. Some C- and A-rays are omitted for clarity, and the B- and U-rays are omitted if their angles of deflection upon emergence are too great to be collected by the lens. The bright ring formed by B rays has been used consistently as the main

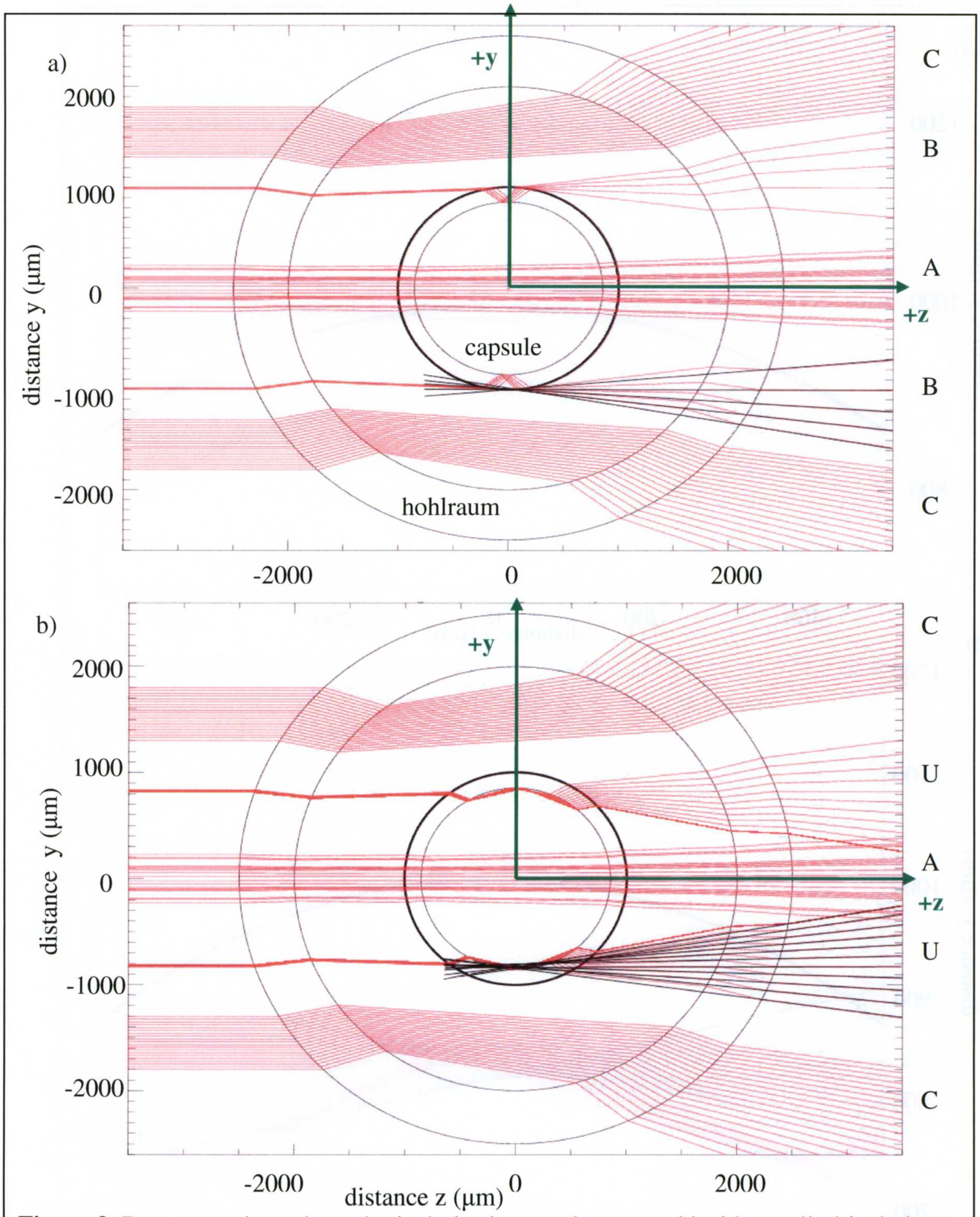

Figure 3: Ray traces through a spherical plastic capsule centered inside a cylindrical glass hohlraum, showing the different types of rays refracting/reflecting through the setup. Bright rings are formed from the B rays (shown in **a**) and the U rays (shown in **b**); the bottom half of each vertically symmetrical trace shows these rays back-projected in black, demonstrating the small regions that the rays appears to come from. Note that the positive x-axis goes into the page.

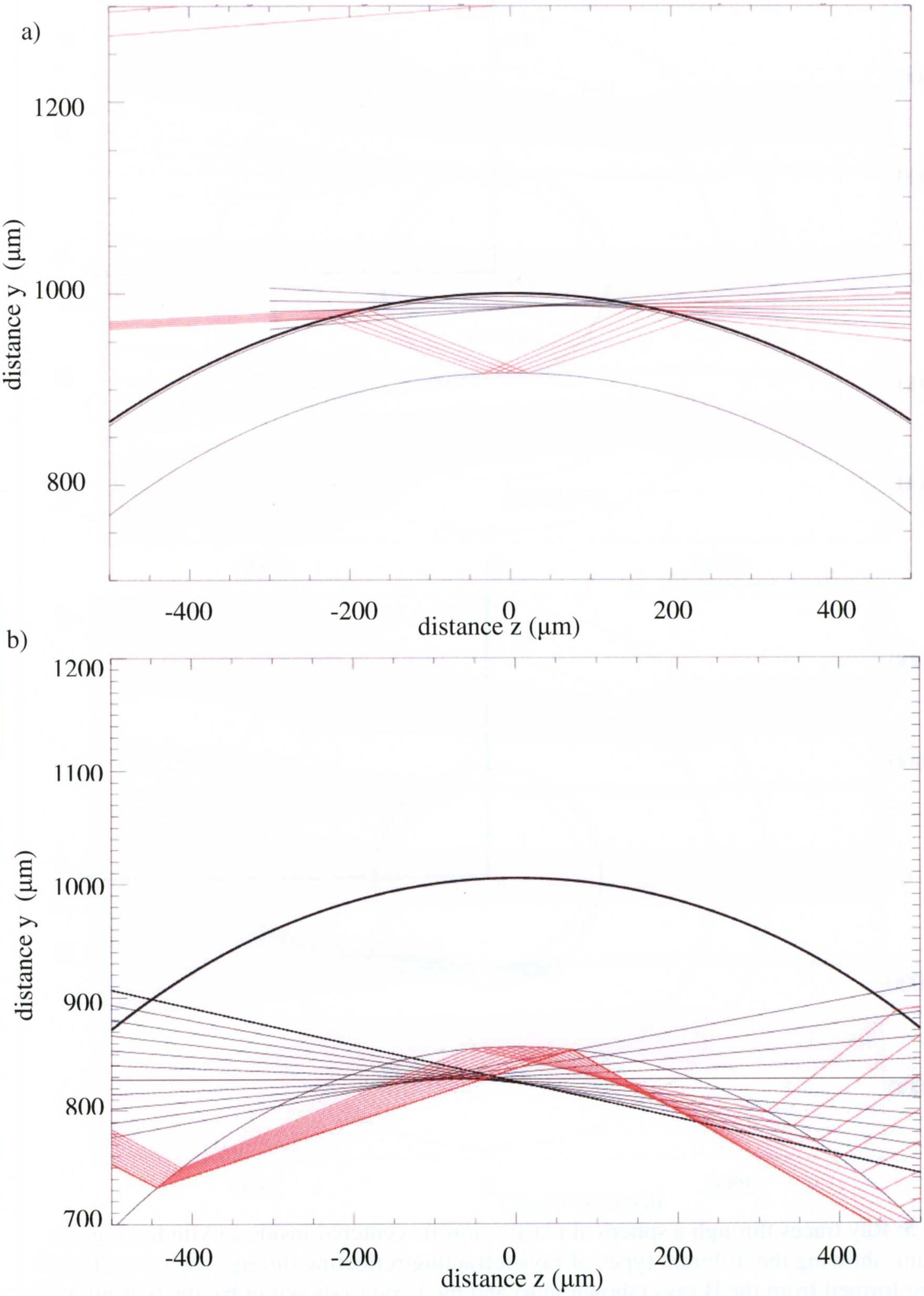

Figure 4: Zoom on the caustic regions corresponding to **Figure 3**. a) B-rays, b) U-rays The black lines indicate back-projected rays.

indicator of cryogenic layer uniformity[8,13,14]. The radius of the ring is not equal to the actual inner ice surface radius, but it is a reliable indicator of nonuniformity nonetheless because changes in the inner surface radius correspond closely to changes in the ring radius

In this experiment, the plastic surrogate capsule had a different refractive index and thickness than a DT capsule, so the rays behave slightly differently. While the ring formed by the B rays is the most visible for cryogenic capsules, the most visible ring for the surrogate capsule is formed by U-rays. This can be seen in Figure 4, which shows blowups of (a) the backprojected B rays and (b) the backprojected U rays. When the microscope used to view the capsule is focused on the point on the caustic where the rays cross (just to the right of z=0 for B rays and just to the left for U-rays), a bright ring is seen. From **Figure 4a**, the place where the B-rays appear to come from in the surrogate capsule is too close to the edge of the capsule to be distinguished from it. Thus the U rays were used. They have never before been used for the analysis, although they have been observed[8], so a model for them was added to the code. As can be seen in **Figure 4b**, the rays, when projected backwards, form a distinct ring far enough inwards from the capsule edge to be accurately imaged and analyzed.

3. Code Development

The code *PEGASUS*, which included routines for the refraction of rays through planes and spherical surfaces using Snell's Law, was modified to model the distortion introduced by the hohlraum by adding a routine for refraction through cylindrical surfaces. The code is written to be as general as possible, and thus includes many different parameters describing the objects through which the rays travel. In addition to the radius and refractive index of each layer of the capsule and hohlraum, the position of the sphere within the cylinder can be modified such that the code can also be used for capsules that aren't perfectly centered. The direction of the cylinder axis can also be modified. In addition, a U-ray model was built and added to the code to model surrogate capsules.

The bright ring and outer radius of the capsule are calculated using a binary search algorithm, as indicated in **Figure 5**, for each angle θ in the image (see **Figure 6**). The bright ring radius at each angle is defined by the B-ray (or U-ray) which enters and exits the hohlraum horizontally. The outer radius at each angle is defined by the C-ray that just misses the capsule as it goes through the inside of the hohlraum. To find the bright ring radius, the binary search starts with two arbitrary radii and gradually refines its calculations based on whether the rays emerge too high or too low. To find the outer radius, it instead tests for whether the rays hit or miss the capsule. The user can specify the accuracy by choosing how many passes the search routine should make. The code typically calculates these radii for 360 angles θ around the capsule image (see **Figure 6**) and graphs them.

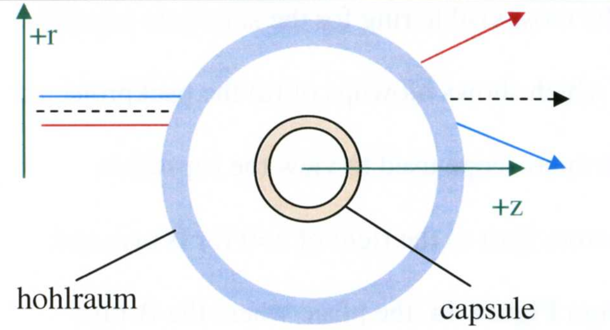

Figure 5: Schematic illustrating how the bright ring radius is found. A ray launched at the hohlraum/capsule combination from too large a radius (blue) will emerge too low, and vice versa (red). The ray that enters and exits horizontally (dashed black) is found using a binary search and defines the bright ring radius.

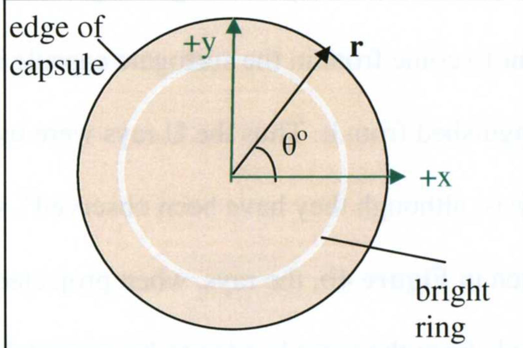

Figure 6: Diagram showing how the angle θ around the capsule image is defined. At each value of θ, the radii of the bright ring and the edge of the capsule are calculated.

4. Experimental Results

A) Experimental Setup

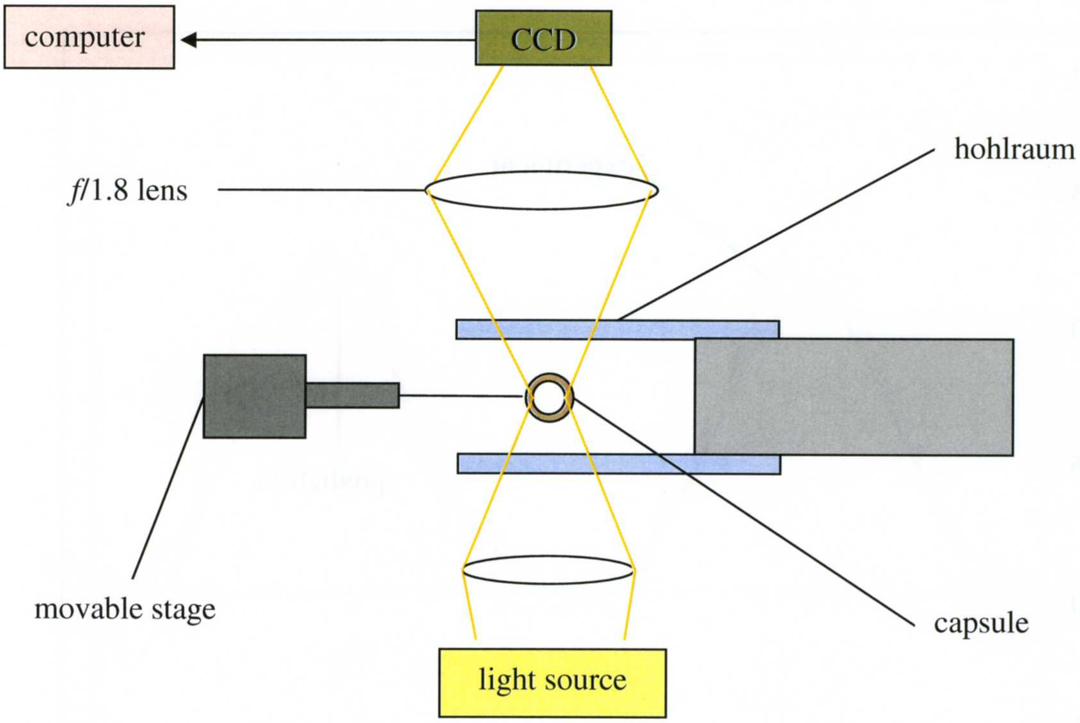

Figure 7: Schematic of the experimental apparatus. The capsule is illuminated by a light source and viewed using a microscope with an f/1.8 lens. An image of the capsule is formed on a CCD camera and stored in the computer. The position of the capsule can be adjusted in three dimensions.

A schematic of the experimental apparatus is shown in **Figure 7.** The plastic capsule was mounted on a stalk and manipulated on a movable stage adjustable in three dimensions. The hohlraum was mounted across from the capsule and the capsule could be moved in and out of the hohlraum. The capsule/hohlraum setup was viewed using a traveling microscope connected to a readout giving coordinates of the locations of the capsule and hohlraum in three dimensions, with uncertainties of ±10 μm in the z-axis (toward and away from the lens) and ±5 μm in the x- and y-axes. Photographs of the capsule were taken with a digital camera (with a resolution of ~2 μm/pixel) attached to the microscope and then stored in a computer. The shadowgram in **Figure 2** was obtained using this setup.

B) Measurements of the Outer Radius

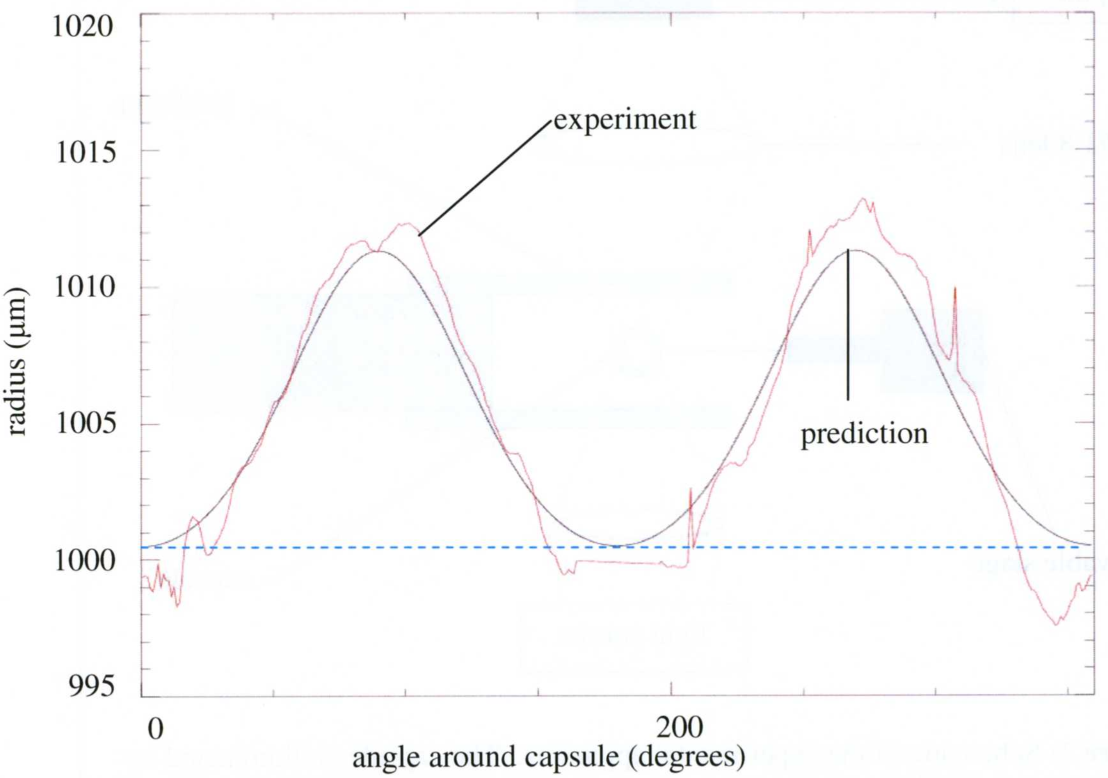

Figure 8: Predicted and measured outer radius of a capsule viewed through a hohlraum as functions of angle. The blue dotted line represents the actual (average) capsule radius.

Code predictions and measured data for the outer radius of the capsule as a function of the angle around the capsule are shown in **Figure 8**. The code predicted a pattern with two maxima and two minima and the measured data supported these predictions very well. This pattern is in accordance with expectations. The maximum distortion is predicted at 90° and 270°, where the hohlraum surface is tipped furthest away from the ray path, and no distortion is predicted at 0° and 180°, where looking through the hohlraum is analogous to looking through a plane parallel plate and should cause no distortion. The flat portion of the experimental graph around 180° appears because *VIEWCRYO* cannot locate the edge of the capsule due to the presence of the mounting stalk (see **Figure 2a**) and ignores this data.

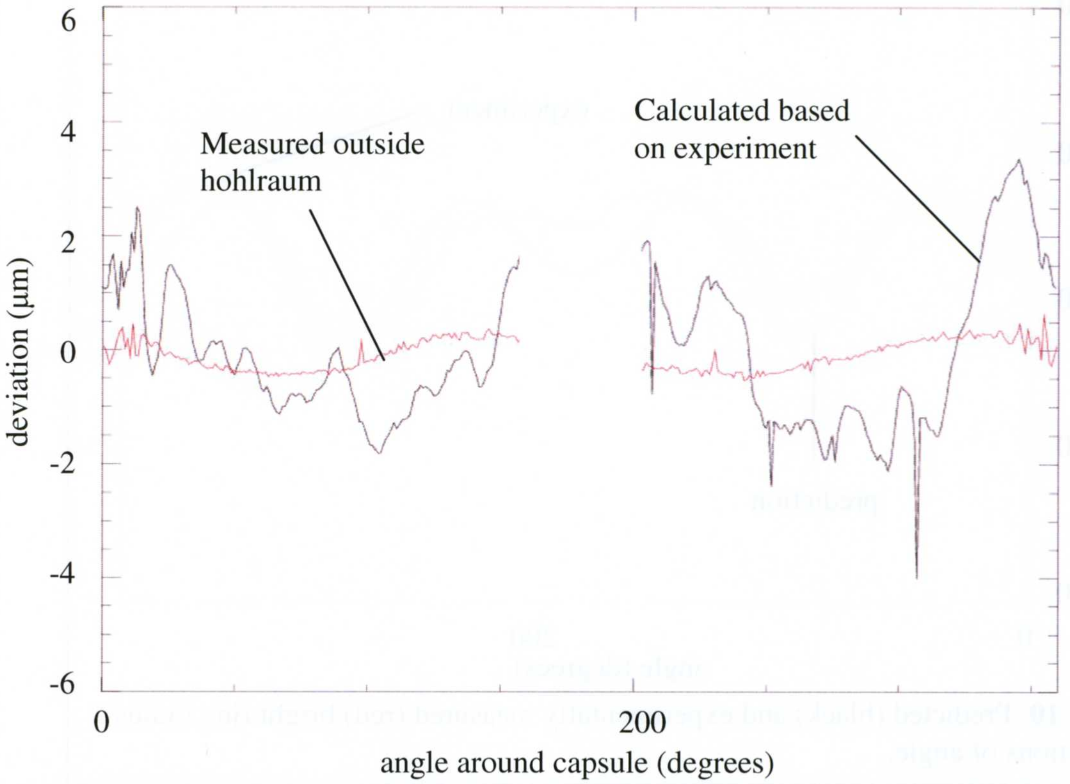

Figure 9: Calculated and measured capsule nonuniformity, with data omitted for the portion interfered with by the stalk. The calculated nonuniformity is found by subtracting the two curves shown in **Figure 8**.

By subtracting the predictions from the measured data, effectively "canceling out" distortions from the hohlraum, one can obtain a graph of the nonuniformity of the capsule's outer surface. This is shown by the black line of **Figure 9**. However, when this was compared with a measurement of the capsule's outer radius outside the hohlraum, shown as the red line in **Figure 9**, it was seen to be slightly inaccurate (±2 μm in a capsule radius of 1000 μm). This is probably due to the nonuniformity of the hohlraum, which is not known and could not be taken into account in the original calculation.

C) Measurements of the Bright Ring Radius

A graph comparing predictions and measured data for the bright ring radius is shown in

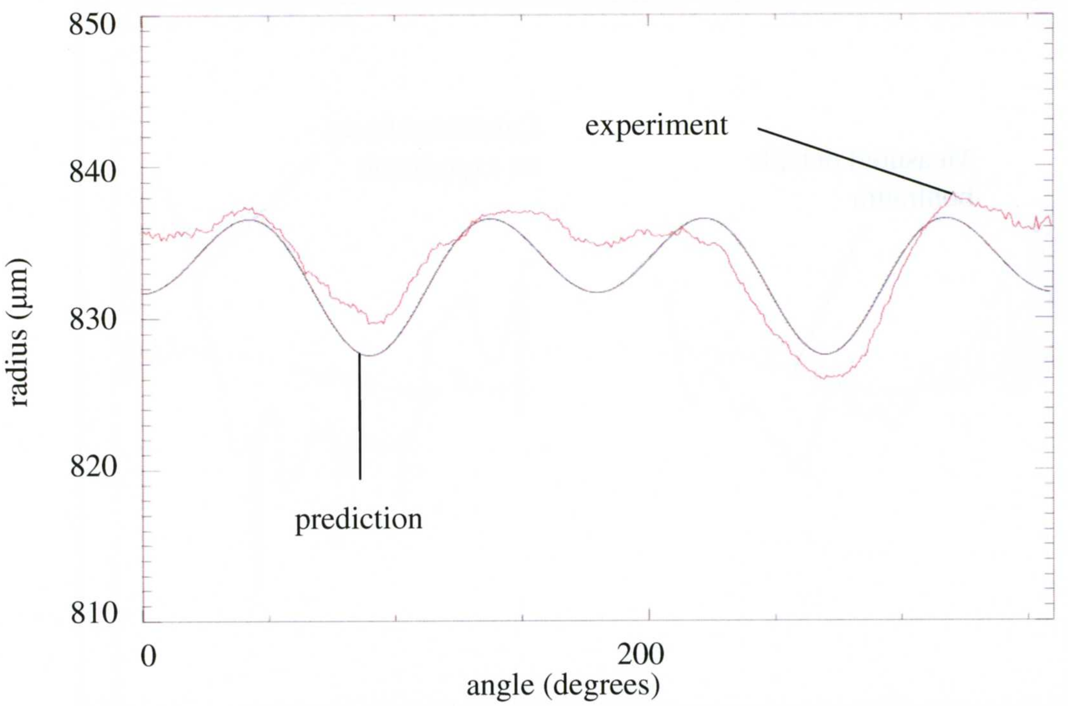

Figure 10: Predicted (black) and experimentally measured (red) bright ring radius as functions of angle.

Figure 10. In contrast to **Figure 8**, the code predicted a four-lobe pattern, which was unexpected. The data support the predicted trend fairly closely.

The difference between the two curves of **Figure 10** was plotted as the black curve in **Figure 11** providing a graph indicating the nonuniformity of the bright ring radius. The red curve represents the measured nonuniformity outside the hohlraum. Again, the lack of correlation is probably due to the nonuniformity of the hohlraum. It should be noted that the measured nonuniformity of the bright ring radius outside the hohlraum is greater than that of the outer radius (red curve of **Figure 9**). This could be because the inner surface is less uniform than the outer surface, but it is more likely because the U-rays travel through the nonuniform outer surface of the capsule and also sample the inner surface in three places, resulting in several nonuniformities adding up to an overall error of ±4 μm.

When similar experiments are performed with cryogenic capsules using the B rays, this

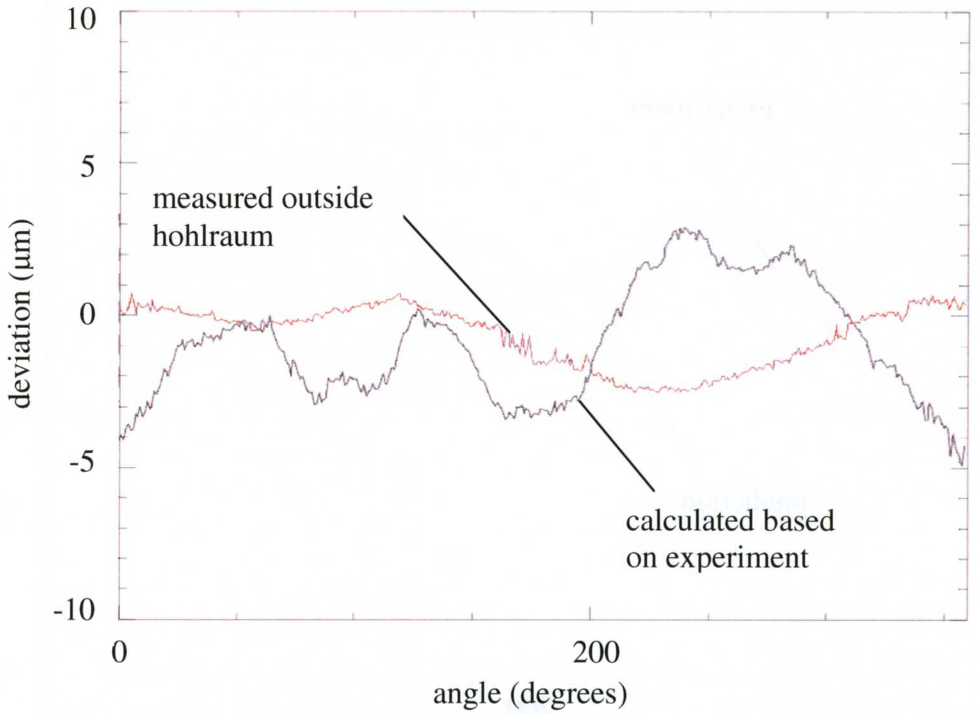

Figure 11: Calculated and measured nonuniformity of the bright ring as functions of angle. The calculated nonuniformity was obtained by subtracting the two curves shown in **Figure 10**.

effect should be reduced because the B-rays do not sample as many surfaces as do the U-rays. In particular, they only sample the inner surface in one place. More importantly, tight specifications must be imposed on the uniformity of the hohlraum if accurate data are to be obtained for both the outer and bright ring radii.

D) Displaced Capsule

The code was also tested for a capsule that was off-center within the hohlraum. The experimental setup was the same as before but the capsule was intentionally displaced by a known amount in the y-direction (the x-axis being along the cylinder and displacement along it therefore irrelevant). For a displacement of 100 µm, much greater than the positioning accuracy of the capsule, the data matched predictions as well as they did for the centered capsule (see **Figure 12**). Similar results were obtained for displacement in the z-direction. Having this

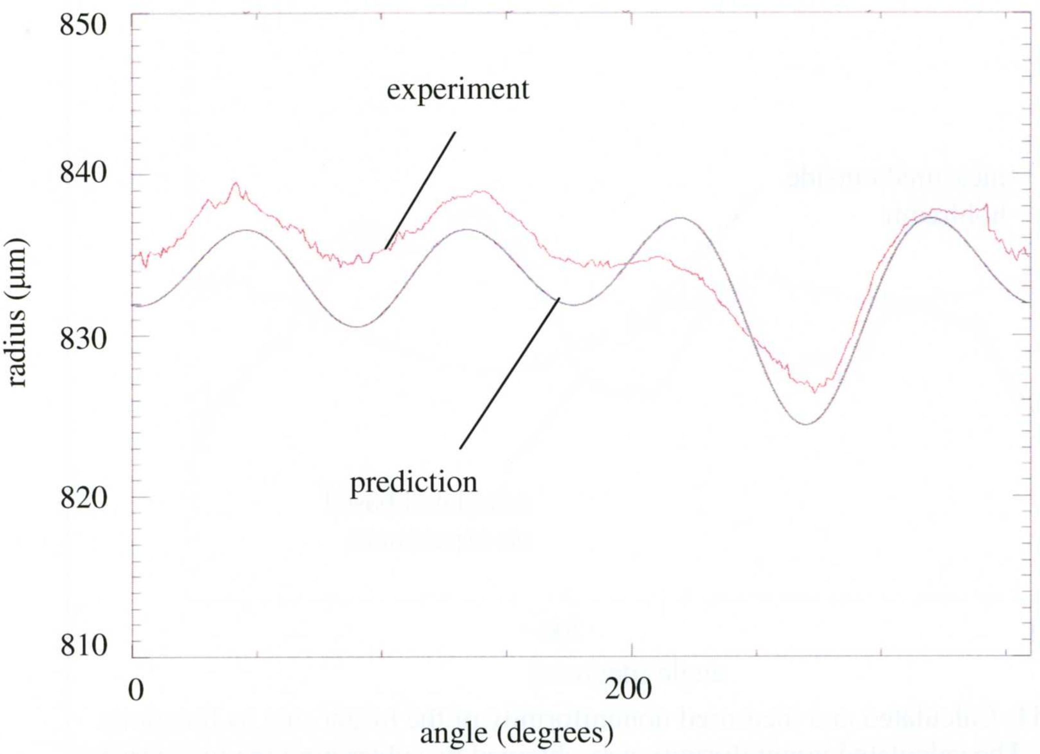

Figure 12: Predicted and experimentally measured bright ring radius for a capsule displaced 100 μm in the y direction.

capability in the code is important because it will allow detection of and compensation for small errors introduced by capsule mispositioning.

In **Figure 12**, a small adjustment of the (R, θ) values produced by the code was necessary to compare with *VIEWCRYO*, which was not designed for use with a hohlraum and therefore finds the center slightly incorrectly as the centroid of the image. In a hohlraum setup with a capsule displaced in the y-direction this does not correspond to the center because one side will necessarily be distorted more due to the hohlraum. The details of this adjustment are given in the Appendix.

5. Conclusion

Uniform DT cryogenic layers are of critical importance for the hohlraum targets proposed for the NIF. Layering techniques for capsules within hohlraums are currently under development.

A code was developed to address the problem that shadowgraphy could not previously be used to measure the uniformity of a capsule in a hohlraum. The code calculates the distortion introduced by the hohlraum to the image of the capsule, enabling this to be compensated for.

The predictions of the code were tested using a plastic surrogate capsule inside a glass hohlraum. Experimental data confirmed the predicted pattern for the outer radius as well as the unexpected four-lobed pattern predicted for the bright ring radius. The code enabled the nonuniformity of the outer surface of the capsule to be calculated very accurately (±2 μm in a radius of 1000 μm) and the bright ring to a lesser degree of accuracy (±4 μm). The accuracy of both was limited primarily by the uniformity of the hohlraum, and therefore demonstrated the necessity of more uniform hohlraums for future experiments. The bright ring measurements were also affected by the rays sampling many imperfect surfaces, producing deviations that were too large. However, when similar work is done with cryogenic capsules, this should not be an issue because the B-rays will be used, and they only sample the inner DT ice layer at one point. The results of this work show that shadowgraphy can indeed be used to evaluate the uniformity of capsules in hohlraums.

6. Appendix

Because *VIEWCRYO* was designed for shadowgrams of unenclosed capsules rather than capsules in hohlraums, its algorithm for finding the center of the capsule image consistently calculated it incorrectly for images of capsules displaced in the y direction. This is because *VIEWCRYO* calculates the center as the centroid of the capsule edge (the average x,y values), which will fail for the y value because the hohlraum-induced distortions at the top and bottom of the image are different. Thus, in order for a viable comparison to be made, *PEGASUS* has to compensate for this by altering its predictions such that they are based on where *VIEWCRYO* would calculate the center to be. It does this by finding the centroid, and then recalculating the radius and angle values for each data point.

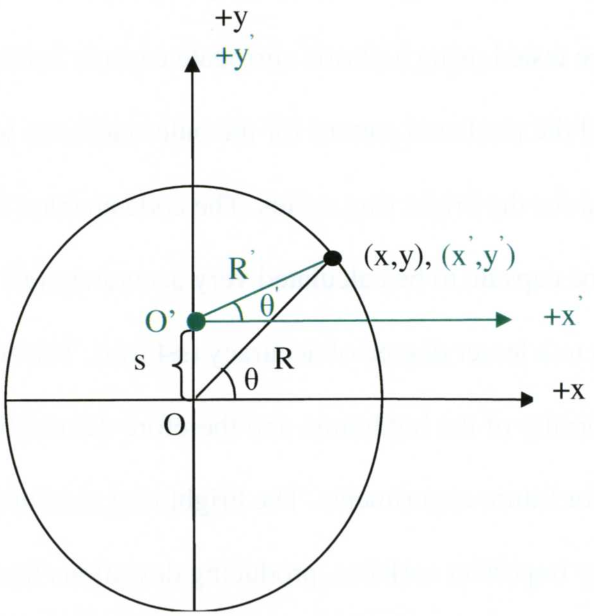

Figure 13: Diagram demonstrating how the R(θ) curves calculated by *PEGASUS* are adjusted to match the R'(θ') curves generated by *VIEWCRYO* based on the primed (green) coordinate system. The distance s is exaggerated for clarity.

Mathematically, this proceeds as follows (see **Figure 13**): The origin O' of the *VIEWCRYO* coordinate system (x', y'), is shifted a distance *s* in the y direction. The x coordinate does not change. Thus:

$$x' = x$$

$$y' = y - s.$$

For any point along the capsule edge for which R has been calculated, its coordinates can be expressed as:

$$(x,y) = (R\cos\theta,\ R\sin\theta)$$

or, in the new coordinate system, as:

$$(x',y') = (R'\cos\theta',\ R'\sin\theta')$$

Using the above definitions of (x', y'), R' and θ' can now be found as

$$R' = \sqrt{(x'^2 + y'^2)}$$

$$\theta' = \tan^{-1}(y'/x').$$

R' and θ' are then used to generate new graphs that can be viably compared to *VIEWCRYO*'s data. The same process occurs for the bright ring data.

7. Acknowledgments

I would like to extend my heartfelt gratitude to Dr. R. Stephen Craxton for being my endlessly patient theoretical advisor, to Mr. Mark Wittman, my experimental advisor, for patiently explaining the experimental process and helping me along the way, and to Dr. Dana Edgell for his help in using the *VIEWCRYO* program for my project.

8. References

---

[1] J. Nuckolls, *et al.*, "Laser Compression of Matter to Super-High Densities: Thermonuclear (CTR) Applications", *Nature*, **239**, 139 (1972)

[2] J.D. Lindl, "Inertial Confinement Fusion", Springer-Verlag, New York (1998)

[3] E. M. Campbell, W. J. Hogan, "The National Ignition Facility – Applications for Inertial Fusion Energy and High-Energy-Density Science," *Plasma Physics Control. Fusion*, **41**, B39 (1999)

[4] D. R. Harding, *et al.*, "Producing Cryogenic Deuterium Targets for Experiments on OMEGA", *Fusion Science and Technology*, **48**, 1299, (2005)

[5] A. J. Martin, R. J. Simms, R. B. Jacobs, "Beta energy driven uniform deuterium-tritium ice layer in reactor-size cryogenic inertial fusion targets", *J. Vac. Sci. Technol.*, **A 6 (3)**, 1885, (1988)

[6] D. S. Montgomery, A. Nobile, P. J. Walsh, "Characterization of National Ignition Facility cryogenic beryllium capsules using x-ray phase contrast imaging", *Review of Scientific Instruments*, **75**, 3986, (2004)

[7] B. J. Kozioziemski, *et al.*, "Quantitative characterization of inertial confinement fusión capsules using phase contrast enhanced x-ray imaging", *Journal of Applied Physics*, **97**, 063103 (2005)

[8] D. H. Edgell, *et al.*, "Three-Dimensional Characterization of Cryogenic Target Ice Layers Using Multiple Shadowgraph Views", *Fusion Science and Technology*, **49**, 616 (2006)

---

[9] B.J. Kozioziemski, *et al.*, “Infrared heating of hydrogen layers in hohlraums”, *Fusion Science and Technology* **41**, 296 (2002).

[10] J.D. Moody, *et al.*, “Status of cryogenic layering for NIF ignition targets”, *J. Physics* **112**, 032064 (2008).

[11] S. Jin, "A Ray-Tracing Model for Cryogenic Target Uniformity Characterization," 2002 Summer High School Research Program at the University of Rochester's Laboratory for Laser Energetics. LLE Report No. 329.

[12] G. Balonek, “How Good is the Bright Ring Characterization for Uniformity of Deuterium Ice Layers within Cryogenic Nuclear Fusion Targets?”, 2004 Summer High School Research Program at the University of Rochester’s Laboratory for Laser Energetics. LLE Report No. 337.

[13] D. N. Bittner, *et al.*, “Forming Uniform HD Layers in Shells Using Infrared Radiation”, *Fusion Technology*, **35**, 244 (1999)

[14] J.A. Koch, *et al.*, “Numerical raytrace verification of optical diagnostics of ice surface roughness for inertial confinement fusion experiments”, *Fusion Science and Technology*, **43**, 55 (2003)

Counting System for the Carbon Activation Diagnostic

Alexis Kurmis

Counting System for the Carbon Activation Diagnostic

Alexis Kurmis

Greece Arcadia High School
Rochester, NY 14612

Advisor: Craig Sangster

Laboratory for Laser Energetics
University of Rochester
Rochester, NY

February 2009

Abstract

Multi-step nuclear reactions in the core of an OMEGA implosion can be used to infer the density of the deuterium-tritium (DT) fuel at peak compression, an important measure of the implosion performance. A three-step process leads to the production of tertiary neutrons with energies up to 30 million electron volts (MeV), more than twice the energy of the primary neutrons (14.1 MeV) from the direct fusion of DT[1]. The tertiary-to-primary neutron yield can be measured using a neutron-induced reaction on ^{12}C that is energetically not possible at the primary neutron energy. The (n, 2n) activation reaction on ^{12}C leads to the production of ^{11}C, which is unstable and has a half-life of 20.3 minutes[1]. The ^{11}C decays to ^{11}B and emits a positron (the antimatter equivalent of an electron) and a neutrino. The positron immediately annihilates with a neighboring electron, in the process emitting two 511-keV (thousand electron volts) gamma rays in opposite directions. LLE is developing a high-counting-efficiency detector system (in collaboration with the SUNY Geneseo physics department) to measure the number of activated ^{12}C atoms in a sample of graphite exposed to the tertiary neutron flux on the OMEGA laser. As part of this development process, measurements were made of the background sensitivity of the detectors to determine the shielding requirements. Counting efficiency in normal and Compton coincidence modes was explored. The first activated Cu-diamond mixture to be used for an absolute calibration of detector sensitivity was also part of this project.

1. Introduction

In an inertial confinement fusion (ICF) implosion, multiple nuclear reactions occur that lead to the creation of high energy neutrons with energy up to 30 MeV. Three reactions occur in an ICF implosion, as shown in Figure 1.1.

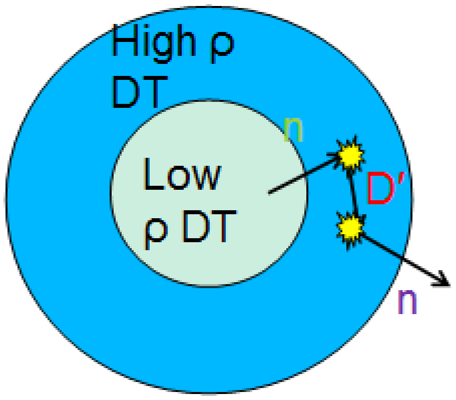

Figure 1.1
Three step process that creates tertiary neutrons. Primary neutrons are produced in the primary fusion reaction with 14.1 MeV energy. These may interact with a deuteron, transferring energy. If this energetic secondary deuteron fuses with a triton, the resulting tertiary neutron can have up to 30 MeV energy. This reaction takes place in the dense DT shell surrounding the low density, high temperature central region where fusion is initiated.

In the initial reaction, a deuterium atom fuses with a tritium atom to produce an alpha particle and a neutron with 14.1 MeV energy.

$$\mathrm{D} + \mathrm{T} \rightarrow {}^{4}\mathrm{He} + \mathrm{n}\ (14.1\ \mathrm{MeV})$$

This primary neutron can then interact with another deuterium atom and transfer some of its energy, up to 12 MeV.

$$\mathrm{N}\ (14.1\ \mathrm{MeV}) + \mathrm{D} \rightarrow \mathrm{n}' + \mathrm{D}'\ (0\text{-}12\ \mathrm{MeV})$$

This energetic deuterium can then fuse with another tritium to produce another alpha particle and a tertiary neutron.

$$\mathrm{D}'\ (0\text{-}12\ \mathrm{MeV}) + \mathrm{T} \rightarrow {}^{4}\mathrm{He} + \mathrm{n}''\ (0\text{-}30\ \mathrm{MeV})$$

Because the probability of these reactions is related to fuel density, and there are two additional reactions necessary to produce a tertiary neutron, the ratio of tertiary neutrons to primary neutrons is proportional to the square of the fuel density.

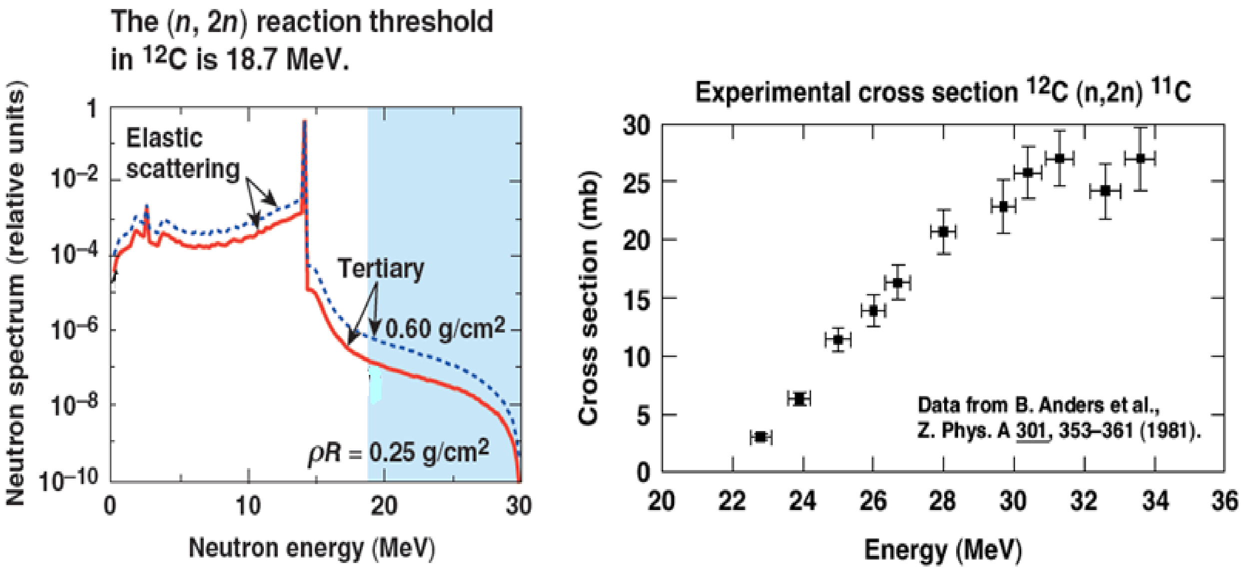

(a) (b)

Figure 1.2
Simulated neutron spectrum from an ICF implosion and carbon cross section. (a) The blue area shows the energy that is only reached by tertiary neutrons, and the peak is the amount of primary neutrons. (b) This shows the energy needed for the (n,2n) activation reaction of ^{12}C, which is well into the tertiary range.

One goal of experiments at LLE is to achieve a fuel areal density (ρR) of 0.20 g/cm^2, but the current diagnostics for DT fuel are unable to measure densities this high. Carbon activation can be used to solve this problem because only tertiary neutrons activate carbon (Figure 1.2b). The tertiary neutrons are only produced by the reactions described, and there are a million times fewer tertiary neutrons than primary neutrons, as Figure 1.2a shows. By counting the gamma rays produced using a system of known sensitivity, the number of ^{11}C can be calculated, which leads to the number of ^{12}C activated and then the number of tertiary neutrons. The number of primary neutrons, which is needed to find the ratio, is measured by other diagnostics. Ultimately, the National Ignition Facility (NIF) will use the neutron activation system to measure ρR up to 2.0 g/cm^2. With a ρR of 0.20 g/cm^2, OMEGA is an appropriate place to test the diagnostic.

The prototype counting system for carbon activation has been set up and consists of detectors, electronics, and a computer program for data acquisition and analysis. Sodium iodide scintillators are arranged in a face centered cubic array to cover as much of the solid angle coming from the source as possible. When a gamma ray from the source hits the detector, the energy deposited is converted to visible light, which is further converted to an electrical pulse by a photomultiplier tube (PMT) attached to the detector. This signal is then amplified and shaped in a preamplifier and amplifier. Next, the signal is sent to an analog-to-digital converter (ADC), which takes the pulse and changes it to numbers that can be understood by the computer[2]. The computer program, called MPANT, records all of the signals as the ^{11}C decays and produces a spectrum for each detector consisting of the number of counts as a function of the initial gamma ray energy. Plots can also be made of counts over time and coincidence counts.

2. Background

Background radiation is the natural radiation that exists everywhere. It mostly comes from space, but it can also come from radioactive materials in the surrounding area, like ^{40}K in concrete walls or floors. Understanding the background is important because the number of ^{11}C produced by tertiary neutrons on OMEGA will be comparable to the signal from the background. This background needs to be understood so that it can be subtracted from the carbon signal for more accurate measurement of the tertiary yield. As Figure 2.1 shows, even when the detectors are completely shielded by lead, the background contributes a significant number of counts per minute, especially relative to the counts that would be expected from a carbon source.

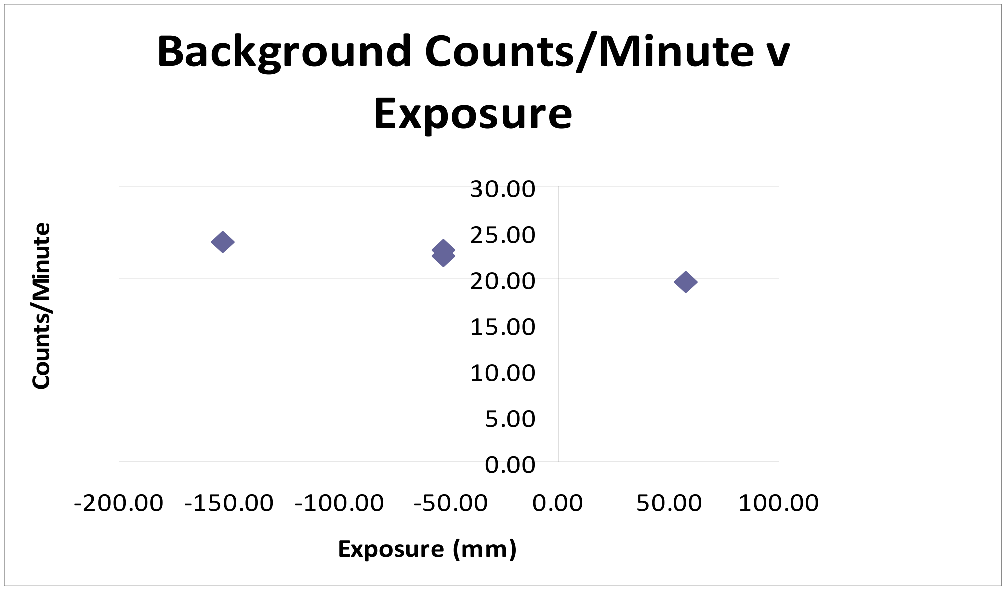

Figure 2.1
511-keV counts for one detector as a function of the exposure. A negative exposure means that part of the detector was not covered while a positive exposure means that the detector was completely covered.

Lead shielding is used to reduce the background signal that gets to the detectors, so tests were conducted to determine the optimal amount of shielding. This proved to be difficult with the detectors on the top and the bottom because it would require lead to be stacked vertically, but a new design is being developed to fix this problem. Tests with three detectors were run to see how the background signal changed with the addition of more lead. Both counts (Figure 2.1) and variation (Figure 2.2) were plotted against exposure, which is how much of the detector was covered by lead, measured from the end of the detector to the edge of the last piece of lead on top. A negative exposure means that the lead did not fully cover the detector and a positive exposure means that the lead extended past the end of the detector. A detector with an exposure of 58 mm had a background rate of 19.6 counts per minute in the 511 keV energy range, but the rate for this same detector when the exposure was -153 mm was 24.0 counts per minute. The standard deviation of the background rate also was lowered by the addition of more lead, from 39.97 when the exposure was -52 mm to 24.84 with a 58 mm exposure. Based on these results, a new design is being developed for the system to get the best possible coverage in terms of shielding detectors equally and using enough shielding.

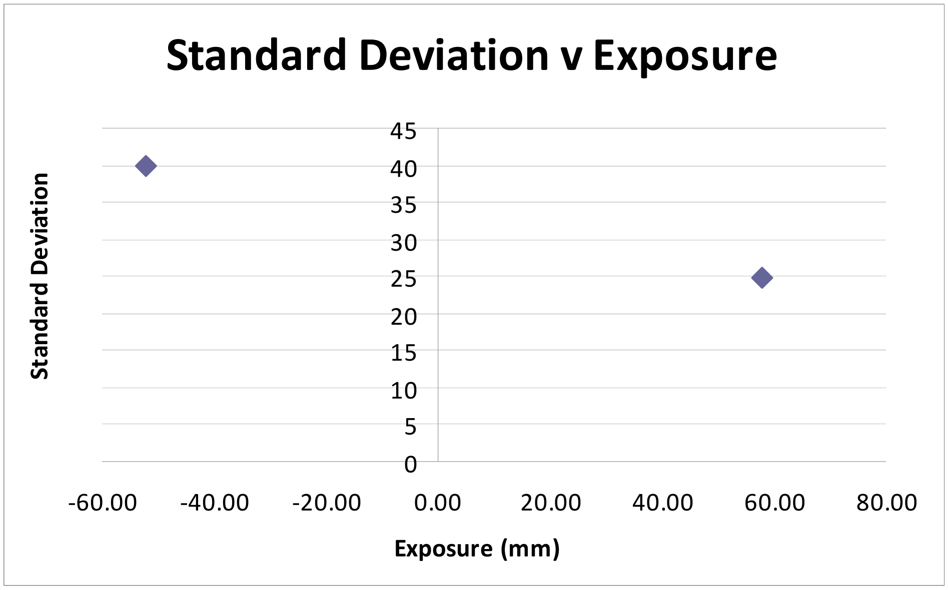

Figure 2.2
Standard deviation of 511-keV counts as a function of exposure.

3. Counting Efficiency

A coincidence count is defined as two detectors recording a signal at the same time. Coincidences are important because the positron emitted when a ^{11}C decays to a ^{11}B produces two back-to-back 511 keV gamma rays. Both of these gamma rays need to be identified because if there was only one, it could have easily come from space. The standard method for counting coincidences has been counting only the 511 keV coincidences, but the efficiency of this method is low. Both 511 keV gamma rays need to be detected for a positive identification, but they may not both arrive at the detectors with their full energy. After a gamma ray has been emitted from the source, it is possible that it will interact with an electron and lose some of its energy in a process called Compton scattering. This gamma ray will no longer have 511 keV, but it is still part of the signal and can be used to improve the signal-to-background ratio.

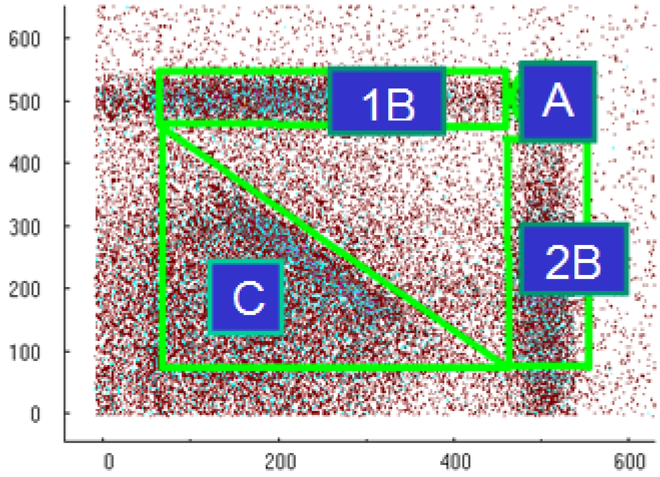

Figure 3.1
Energy recorded in detector 1 (keV) v energy detected in detector 2 (keV). Area A shows 511-511 keV coincidences, areas 1B and 2B show 511-Compton coincidences, and area C shows the Compton-Compton coincidences.

To capture as many counts as possible, coincidences are counted when both detectors register a 511 keV gamma, when one registers a 511 keV gamma and the other registers a Compton ray, and when both detectors record a Compton gamma ray. This is illustrated in Figure 3.1, which shows the area used for counting each of the different types of coincidences. The background levels are measured prior to the experiment and can be subtracted from the recorded counts. This is done by finding the average background counts per minute and multiplying by the time the experiment ran to get the expected counts for a certain amount of time. Once the background is subtracted, the process of calculating the counting efficiency can begin.

The experiment described here was done using ^{64}Cu that was activated by being exposed to the DT neutron flux on the OMEGA laser. The copper was placed at a distance of 40 cm from the center of the target chamber and was allowed to cool off for four and a half hours before counting to prevent saturation of the detectors. Before the sample was placed in the counting system, it was mixed with diamond powder until it was evenly distributed and then placed in a container. Diamond powder was used to simulate graphite because solid graphite has the same density as diamond powder and the signal attenuation would be as close as possible to the same in both. Graphite will be the ultimate activation sample used for the operational diagnostic, so it was important to get similar results from the tests. The first step in measuring the counting efficiency is finding the activation ratio, A_r, which is how many activated atoms are produced per source neutron. This ratio is given by Equation 1[3]:

$$A_r = n_s * t_s * \sigma_s * \Omega \tag{1}$$

where n_s is density of the source in atoms per cubic centimeter, t_s is the thickness of the source, σ_s is the cross section, and Ω is the solid angle. Once this ratio is known, the number of total decays expected can be calculated using Equation 2[3]:

$$CC = A_r * C_{eff} * Y_r * Y_p B_r \tag{2}$$

The total decays expected, CC, is the product of the activation ratio, A_r, the counting efficiency, C_{eff}, the tertiary to primary yield ratio, Y_r, the primary neutron yield, Y_p, and the branching ratio, B_r, which is the fraction that decays by positron emission. This equation can be used to determine the total *counts* expected if the counting efficiency is known, but if not, it can be used to calculate the total *decays* expected by assuming that the counting efficiency is 100%. This number will then be used to find the actual counting efficiency.

The counting efficiency is simply the fraction of the expected decays that were actually measured. Because of equipment problems, the experiment using activated copper was conducted with only three operational detectors instead of six. As shown in Figure 3.2, two detectors were set up across from each other (1B and 2B) and one detector was placed at a right angle to both (2A). Figure 3.2 shows this arrangement. Counts are considered a signal if they are located in the 511-511 range, either 511-Compton range, or the Compton-Compton range. The average of the counts from the right angle spectra, which were 1B with 2A and 2B with 2A, was multiplied by four to give the number of counts that would be expected for a detector with all four detectors at right angles operational. This number was added to the back-to-back counts to get the total counts for one detector. A background measurement was taken prior to this experiment and the background rate in counts per minute was calculated for each of the four regions that were counted (the regions are shown in Figure 3.1). This rate was then multiplied by the number of minutes the copper experiment ran and subtracted from the total counts to give the total measured signal counts for the experiment.

The number of expected decays for the experiment was calculated using the total decays expected and the nuclear decay equation. This equation can be used to determine the counts expected at the beginning of the experiment and the counts remaining at the end of the experiment. The difference is the amount of decays expected for the time the experiment was run. To get the counting efficiency, C_{eff}, Equation 3 can be used:

$$C_{eff} = \text{counts recorded / expected decays} \qquad (3)$$

The counting efficiency for this system came out to be 9.9% based on the experiment done with the copper.

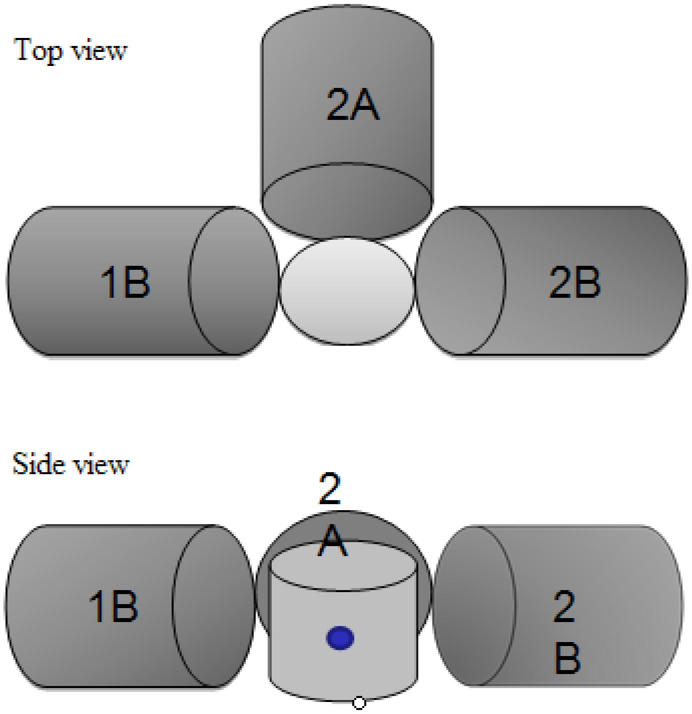

Figure 3.2
Top and side views of detector setup. The light gray cylinder in the middle is the diamond powder, with the blue dot in the middle representing the source. The source was actually distributed throughout the diamond to more closely simulate the eventual graphite source.

4. Conclusions

This project helped to advance the development of a key diagnostic for the OMEGA laser. Background studies confirmed that all detectors should be shielded as evenly as possible to make it easier to separate signal counts from background radiation. Experiments using copper and diamond powder were done to determine the counting efficiency of the system, which will be important when carbon is used as the source.

Ultimately, the carbon activation diagnostic will be used by the NIF to measure the density at the center of their ICF implosions.

5. Acknowledgements

I would like to thank my advisor Dr. Craig Sangster and Tim Duffy for their help and patience throughout the project. Dr. Padalino and his students Cassie Brown and Melissa Cummings, from SUNY Geneseo, were very helpful when I was first learning how the system works. Finally, I would like to thank Dr. Stephen Craxton for running the high school program and for giving me a chance to participate.

6. References

(1) Glebov, V. Yu, C. Stoeckl, T.C. Sangster, D. D. Meyerhofer, P.B. Radha, S. Padalino, L. Baungart, R. Colburn, J. Fuschino. "Carbon activation diagnostic for tertiary neutron measurements." Review of Scientific Instruments 74(2003): 1717-1721.

(2) Knoll, Glenn. Radiation Detection and Measurement. First edition. John Wiley & Sons, 1979.

(3) LLE PDM# D-ES-X-157 Rev B: Omega Tertiary Activation Diagnostic Engineering Optimization Study. 23 Sept. 2007.

Contamination Resistant Sol-Gel Antireflective Coatings by Vapor-Phase Silanization

Mangaladevi Patil

Contamination Resistant Sol-Gel Antireflective Coatings by Vapor-Phase Silanization

Mangaladevi Patil

Pittsford Mendon High School
Rochester NY, 14534

Advisor: Kenneth L. Marshall

Laboratory for Laser Energetics
University of Rochester
Rochester, NY
November 2008

Abstract

Silica-based sol-gel antireflective (AR) optical coatings are critical components of high peak power laser systems. Water vapor and volatile organic compounds can contaminate these coatings, reducing both their antireflective efficiency and laser-damage resistance. Previous work has shown that alkylation of free hydroxyl groups on the silica sol-gel with organosilicon compounds in solution can improve the contamination resistance of silica sol-gels. In this work, alkylation with organosilanes in the vapor state was studied as an alternative to solution-based methods. Sol-gel AR coatings were vapor-phase treated with hexamethyldisilazane (HMDS), tetramethyldisilazane (TMDS) and bis-(trifluoropropyl)-tetramethyldisilazane (FTMDS), at both room temperature and 50˚C. Contact angle measurements were taken to discern the degree of silanization as a function of exposure time to the reactive silane vapor. The contamination resistance of these vapor-phase treated sol-gels was determined by exposing them to a saturated vapor environment of a common organic contaminant (vacuum pump oil) at 60°C and 80 mtorr for 24 hrs. Results suggest that elevated temperatures enable higher degrees of silanization and therefore increase contamination resistance. Contamination testing suggests that HMDS treatment is more effective than TMDS and FTMDS treatments. However, none of the vapor phase techniques have provided as good protection against vacuum pump oil contamination as solution-based methods.

I. Introduction

The Laboratory for Laser Energetics (LLE) at the University of Rochester houses the OMEGA and OMEGA EP laser systems. The facility engages in research involving high-energy-density physics and laser-induced fusion. OMEGA and OMEGA EP are high-peak-power laser systems used to irradiate and compress targets composed of deuterium and tritium (hydrogen isotopes). The resulting fusion reaction yields helium and energetic neutrons. The immense amount of energy released during this process can be captured and converted into other energy forms such as electricity. Ultimately, LLE aims to develop fusion energy as an alternative energy source. However, the current goal is to produce more energy than what is consumed by the laser. These high-power laser systems employ a large number of optical components. To increase the efficiency of laser-induced fusion, it is important that these optics function to transmit as much light energy as possible.

Differences between the indices of refraction of air (1.0) and of the fused silica glass (1.5) used in the optics result in a portion of the light incident on the glass being reflected. Accordingly, each optical element will experience a 4% loss of transmission (Fresnel loss) for each surface exposed to air. To avoid these losses, thin-film anti-reflection (AR) coatings are applied to the optical surfaces to gradually change the refractive index between the air and the substrate. Two common methods for achieving this goal are vacuum deposition of metal oxide layers and solution deposition of silica nanoparticles formed by the sol-gel process[1]. This gradual change results in a much lower transmission loss (as low as 0.1%)[2]. The sol-gel process is generally preferred for AR coatings in high-peak-power systems because of the ease of deposition, higher laser damage thresholds, and ease of removal from the optical element in the event of coating damage. However, because of their porous and particulate nature, sol-gel AR coatings are susceptible to contamination by trace amounts of water vapor and other volatile organic compounds that accumulate with time in the laser and target bays. This absorption not only modifies the refractive index of the sol-gel coating, which in turn reduces its AR efficiency, but also lowers the laser damage resistance of the AR coating. Because of the large number of coated optics in these laser systems (200-300 elements), replacement of contaminated optics becomes a substantial labor and cost burden.

Earlier work done at LLE has shown that chemical treatment of colloidal silica sol-gels with alkoxy silanes in a solution-based process is an effective method for increasing their resistance to water vapor and volatile organic contaminants without compromising their AR capabilities and laser damage threshold[6]. This work investigates an alternative process, vapor phase silanization, which is simpler and more convenient to implement than the currently used solution-based silanization methods and could yield AR coatings with equivalent or superior resistance to airborne contaminants.

a. Sol-Gel Formation

Silica-based sol-gels are formed by alkaline hydrolysis of tetraorthosilicate (TEOS) with NH_4OH in ethanol solution (Fig. 1). The resulting reaction cleaves off the ethoxide groups, and in the presence of a base the free hydroxyl groups on adjacent molecules combine ("condense") to form a larger molecule. This "condensation" reaction continues in three dimensions until all of the reactants are consumed to form colloidal silica particles.(3, 4) After removal of excess base, the colloidal silica particles can be deposited on a substrate by either dip-coating or spin-coating to produce an AR coating.

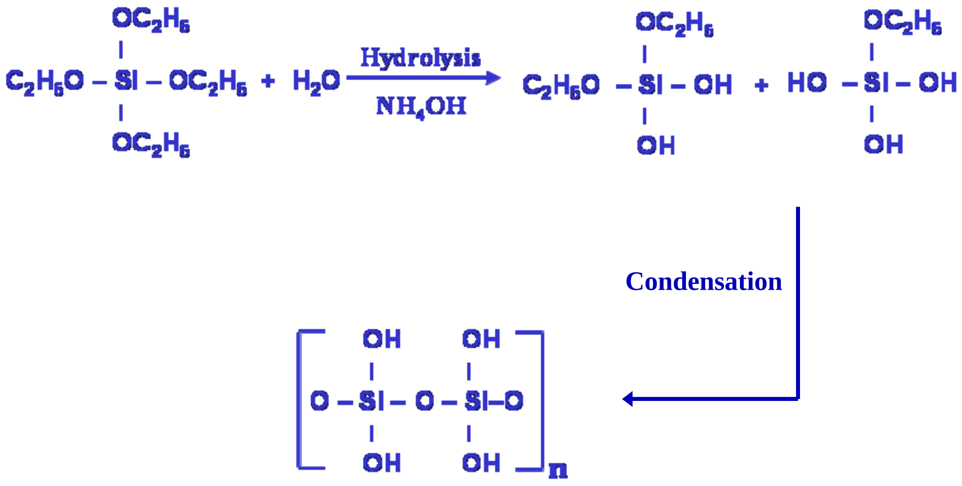

Fig.1: Formation of a silica sol-gel by alkaline hydrolysis of TEOS in ethanol solution.

b. Solution-Based Silanization Methods

By reacting silica sol-gel particles with organosilanes, absorption of contaminants such as water vapor and organic compounds can be inhibited. The organosilanes bond with the available polar hydroxyl groups of the sol-gel, (Fig. 2), resulting in a hydrophobic outer shell that resists water vapor absorption, reduces the number of sites available for hydrogen bonding with polar species, and produces a more tightly woven sol-gel particle, preventing the penetration of larger contaminants.(3, 5)

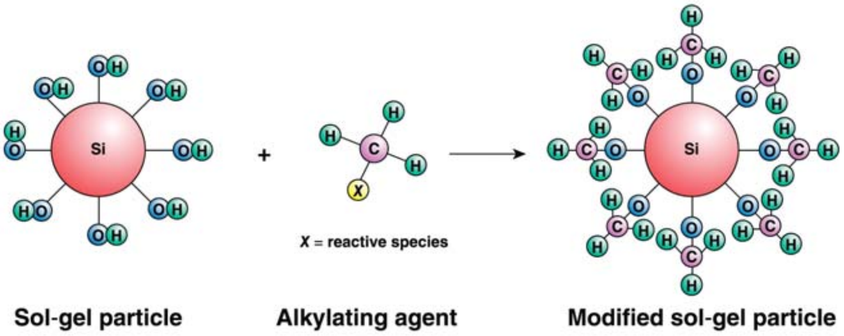

Fig. 2: Reaction of a sol-gel particle with a reactive organosilane aklylating agent. The reactive species X can be any organosilicon compound that is capable of reacting with surface hydroxyl groups.

Previous work done at LLE has shown that treatment of colloidal silica sol-gels with alkoxysilanes such as methyltriethoxysilane (MTES) and dimethyldiethoxysilane (DDS) is an effective method for increasing their resistance to water vapor and volatile organic contaminants. The AR properties at 351 nm of sol-gel coatings prepared by treatment of conventional silica sol-gel particles with these organosilanes remain unchanged after exposure to a fully saturated vapor-state environment of vacuum pump oil for twenty-four hours at 80 mtorr and 60°C, while the transmission of conventional sol-gel coatings drops by up to 4% [6]. These remarkable results, along with the high laser damage resistance of these solution-based silanized coatings[6] have resulted in their recent implementation as the new base-line sol-gel AR coating formulation in OMEGA and OMEGA EP.

c. Vapor-Phase Sol-Gel Silanization

Silanization of silica-based materials using a reactive silane such as hexamethyldisilazane (HMDS) in the vapor state is an alternate process for increasing the contamination resistance of silica-rich surfaces. The molecular structure of HMDS is shown in Fig. 3.

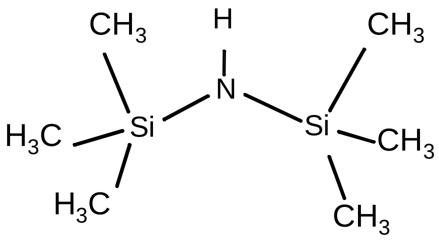

Fig 3: The molecular structure of the reactive silane HMDS.

Vapor-phase silanization has a number of advantages over solution-phase silanization. Only pure vapor comes into contact with the surface to be modified, which eliminates any higher-molecular-weight impurities that could compromise the laser damage threshold of the modified coating (similar to distillation). Any excess of unreacted material that could potentially cause changes in the AR properties of the coating with time is avoided, as only the amount needed to fully functionalize the coating surface is deposited. The vapor-phase process is exceedingly simple to implement as well; the untreated sol-gel AR optic is exposed to organosilane vapor either at ambient or at elevated temperature for an extended period of time. This method of deposition is a distinct advantage over solution deposition techniques, especially for the very large optics that would be employed in OMEGA EP. The chemical composition of the hydrocarbon layer can be easily adjusted by co-depositing several different organosilane materials simultaneously. Achieving the same results with a solution-based process requires preparation and deposition of separate sol-gel optical coatings for each composition to be evaluated, which is a much more complex and lengthy process.

Silica sol-gels treated with HMDS in the vapor phase experienced < 1% loss in transmission after exposure to a vapor-saturated environment of vacuum pump oil at 60°C and 80 mtorr for 24 hrs, while the transmission of untreated sol-gel control samples dropped approximately 3.5 % under the same exposure conditions (Fig 4)[6].

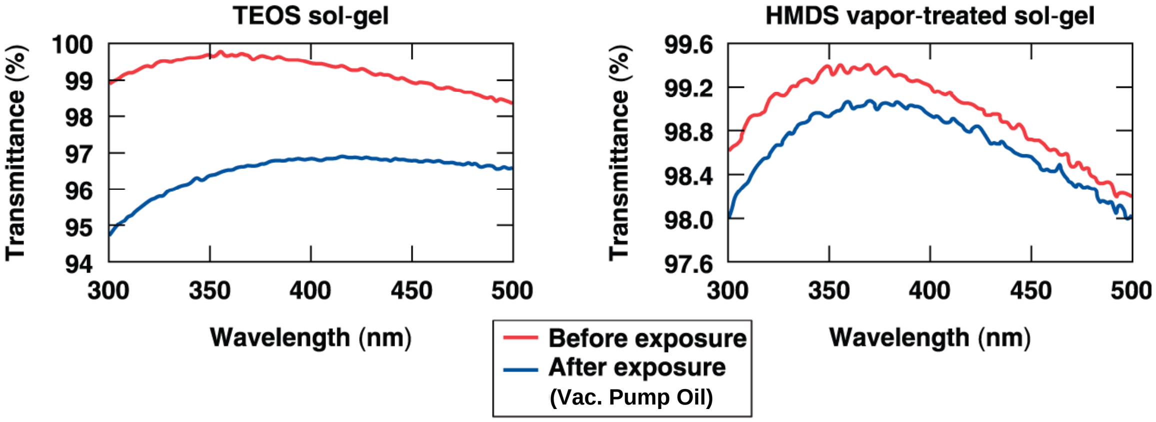

60º C for 28 hr at ~ 80 mtorr

Fig. 4: Transmission spectra contrasting the contamination resistance of standard silica sol-gel AR coatings versus those treated with HMDS in the vapor phase [~~6~~].

.

Figure 4 shows that, unlike for the solution-based silanized sol-gel AR coatings currently in use, the HMDS treated sample does shows a discernable drop in transmission when exposed to a saturated vacuum pump oil environment. The goal of this work was aimed at identifying other volatile organosilanes that may be more effective than HMDS in increasing sol-gel AR contamination resistance. Two such materials, tetramethyldisilazane (TMDS) and bis (trifluoropropyl)-tetramethyldisilazane (FTMDS), were selected for this study.

d. Chemistry of TMDS and FTMDS

TMDS is structurally similar to HMDS, but contains fewer bulky methyl groups than HMDS. In theory, because of the smaller molecular size of TMDS, it should be able to penetrate more deeply into the pores of the sol-gel coating and thus be more effective than HMDS at preventing contamination from larger organic molecules. FTMDS is a fluorocarbon known for being exceptionally hydrophobic, which would allow sol-gels treated with FTMDS to effectively resist contamination from polar substances such as water vapor. The molecular structures of TMDS and FTMDS are shown in Fig 5.

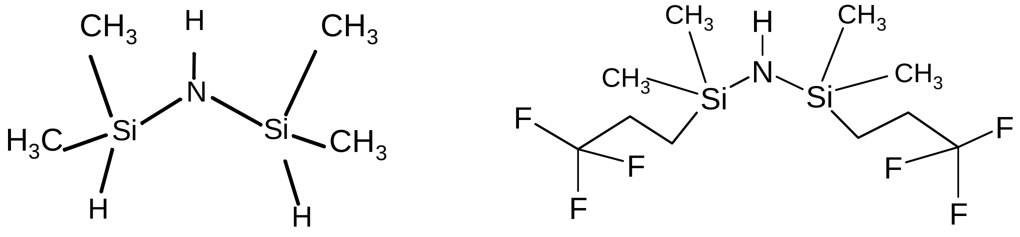

TMDS FTMDS

Fig. 5: Molecular structures of TMDS and FTMDS used for vapor phase silanization. The molecular structure for HMDS can be compared in Fig 3.

The effect on laser damage resistance at 351 nm of modifying the surfaces of high-peak-power laser optics using organic materials is always a concern. For HMDS, TMDS and FTMDS , previous work has shown that surface modification of multi-layer deposited (MLD) gratings does not reduce their laser damage thresholds, and in certain cases actually increased the laser damage threshold of these optics[7].

II. Experimental

Sol-gel coated optics (approx 2” dia) prepared by LLE’s Optical Manufacturing Group were treated with TMDS and FTMDS both at room temperature and at 50˚C to determine the effect of higher temperatures on organosilane saturation in the treatment chamber. Elevated temperatures increase the amount of reactive silane in the vapor phase, and this higher degree of vapor saturation would be expected to provide more opportunities for the organosilane molecules to react with the sol-gel. Vapor-phase treatment was conducted in the large glass chambers shown in Fig 6. The sol-gel coated optics were held in Teflon racks and placed in the chamber with the liquid organosilanes contained in 10 ml glass beakers. For elevated temperature studies, the chambers were placed on a digital hotplate set at 50°C.

Fig. 6: General silanization setup used for all experiments. The substrates are held in Teflon racks and placed into the large glass chambers for silanization. The reactive silane is placed in the chamber and the chamber is covered. For elevated temperature studies, the chambers were place on a digital hotplate (not shown).

a. Contact Angle Measurements

Contact angle measurements of a droplet of water on the treated sol-gel surface were taken using the VCA 2500XE contact angle instrument (AST Products, Inc) to identify the degree of silanization, or how completely the organosilanes had reacted with the surface hydroxyl groups of the sol-gel particles. A schematic diagram of the contact angle instrument is shown in Fig 7.

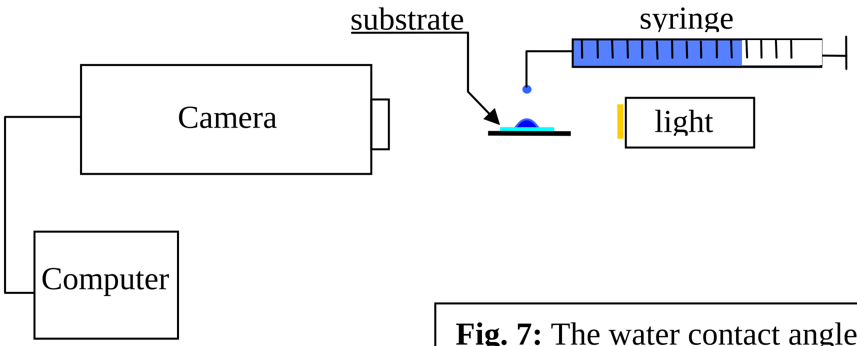

Fig. 7: The water contact angle meter setup

The contact angle measures the degree of hydrophobicity, or resistance to water, of a material. A higher contact angle indicates a greater resistance to water. As the organosilanes react with the sol-gel particles, the outer shell of the sol-gel particles become increasingly hydrophobic, tapering off to a maximum value when all of the surface hydroxyl groups have been consumed in the silanization reaction. Therefore, the contact angle can be used as a measure of the extent of silanization.

Contact angle measurements were taken at 24 hour intervals for sol-gel coated substrates exposed to TMDS and FTMDS vapor for 96 hrs at both ambient temperature and 50°C. The data, shown in Fig 8, implies that, for FTMDS, elevated temperatures during vapor phase silanization resulted in a substantially more complete reaction of the silanes with

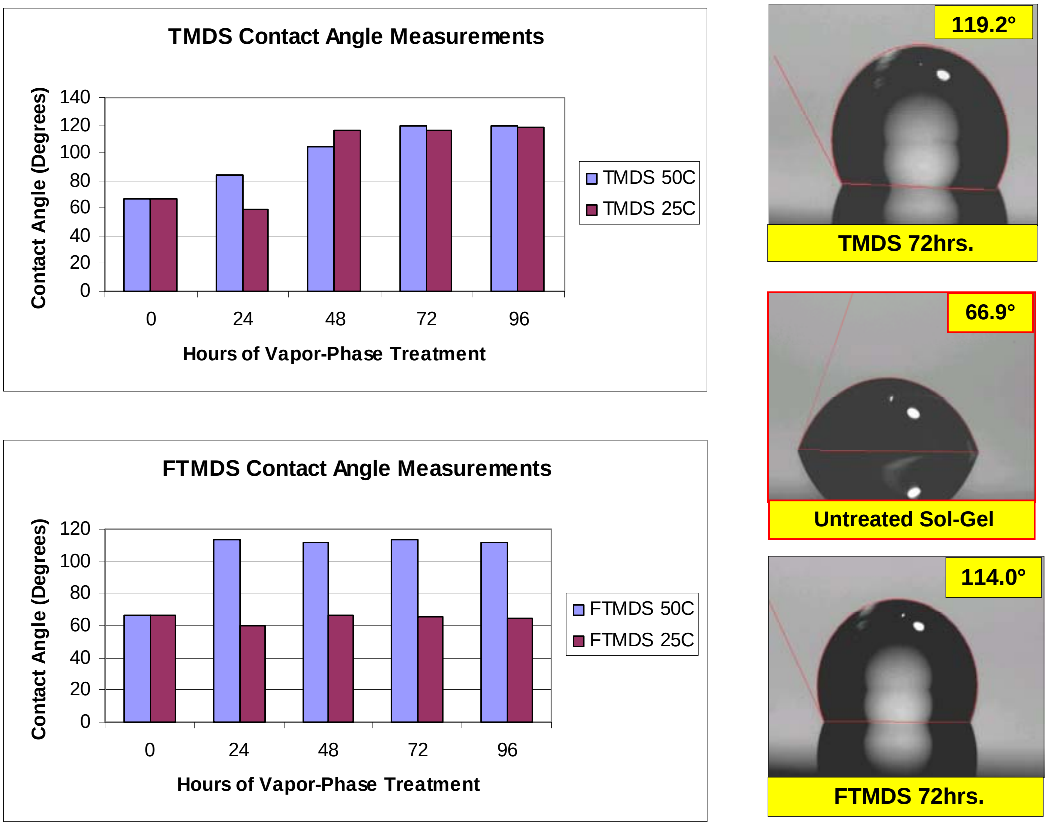

Fig. 8: (Left) - results of TMDS and FTMDS contact angle measurements;
(Right) - photographs of contact angles of a water droplet on treated and untreated sol-gel surfaces.

surface hydroxyl groups, while for TMDS only a small difference was observed at higher temperatures. With respect to length of exposure, the FTMDS-treated optic reaches its optimum contact angle (and thus complete saturation of the sol-gel surface) only at 50 ^{o}C and within 24 hrs. In contrast, TMDS reaches its peak contact angle after about 48 hrs of treatment at room temperature and, due to its higher vapor pressure, elevated temperature has little effect on the rate of silanization. Sol-gel AR-coated optics treated with TMDS and FTMDS displayed higher contact angles (119.2^{o} and 114.0^{o}, respectively) than reported for HDMS in earlier studies (107.7^{o}). These results can be interpreted to mean that TMDS and FTMDS form a denser layer over the surfaces of the sol-gel particles, and should therefore provide increased contamination resistance.

This hypothesis was tested experimentally by exposing both TMDS and FTMDS vapor-phase treated sol-gel AR coatings to an environment saturated with vacuum pump oil at 60^{o}C and 80 mtorr, using the same testing methodology as implemented earlier for both HDMS vapor-phase silanized sol-gels and the baseline solution-silanized sol-gel coatings. The transmission spectra of these samples before and after exposure to the saturated vacuum pump oil environment are shown in Fig 9. Both TMDS and FTMDS do provide a significant level of protection against vacuum pump oil vapor as compared to the untreated sol-gel control sample shown earlier in Fig. 4. The transmittance of the vapor-phase treated sol gels in Fig. 9 drops ~ 1.5% for TDMS and ~2.3% for FTMDS, while the transmission of the untreated control sample drops ~3.5 to 4% (Fig 4). Under the same conditions, the sol-gels treated with HMDS in the vapor state exhibited a change in transmission of < 1%.

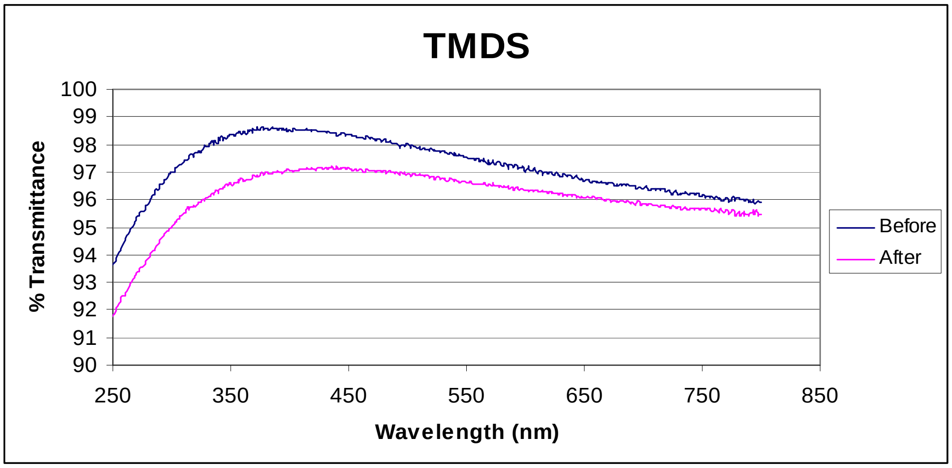

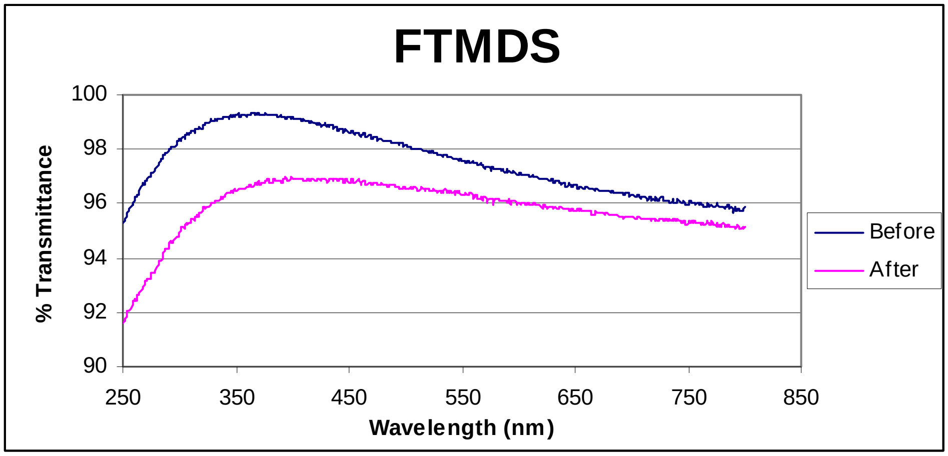

Fig. 9: Transmission spectra for sol-gel coated optics treated with TMDS and FTMDS before and after exposure for 24 hrs to an environment saturated with vacuum pump oil vapor (60°C, 80 mtorr)

III. Discussion

Comparison of the results from Fig 9 with the contact angle measurements in Fig 8 shows some correlation between contact angle and resistance to vacuum pump oil contamination for TMDS and FTMDS vapor-phase treated sol-gel AR coatings. The TDMS-treated samples, which showed a 1.5 % drop in transmission, possessed a contact angle of 119.2°, while the FTMDS-treated sample showed a drop of 2.3% and a contact angle of 114^o. These results support, to some extent, the prediction that higher contact angles are representative of increased reactions between the organosilane and sol-gel, and therefore improved contamination resistance. However, HMDS treated sol-gels have a lower contact angle (107^o) than either TMDS or FTMDS, yet show a smaller transmission loss (<1%). This result is somewhat counter-intuitive, as one would expect that the smaller molecular size of TMDS (which allows it to penetrate deeper into the porous sol-gel structure) and the fluorinated groups on FTMDS (which are extremely hydrophobic) would do a better job of blocking access of contaminants to the pores on the sol-gel particles than would HMDS.

Taken at face value, the relatively higher contact angle measurements of TMDS and FTMDS suggests that they had reacted with the sol-gel particle more effectively than HMDS. However, the contact angle measurements only measure the hydrophobic nature of the *surface* of the modified sol-gel particle. These measurements give no good indication of how far or how well the organosilanes have reacted with the interior of the sol-gel particles. The sol-gel particle surface is not uniform and smooth, and contains numerous channels to the interior which would also be susceptible to contamination. One potential cause of the poorer performance of FTMDS as compared to HMDS may be attributed to the inability of the larger organosilane to penetrate and react with the interior of the sol-gel particle.

IV. Conclusions

Vapor-phase silanization of sol-gel AR coatings using TDMS and FTMDS was studied for the purpose of providing a greater degree of contamination resistance than could previously be attained using HMDS. The observed poorer performance of TMDS and FTMDS vapor-treated sol-gels to vacuum pump oil contamination is related in part to their apparent inability to reach and protect the interior of the sol-gel particle. Although for less volatile organosilanes like FTMDS elevated temperatures do result in higher contact angles, the contact angle data might not be accurately reflecting the degree of silanization of the entire sol-gel particle, particularly the interior. A different means must be used to assess the degree of silanization of the entire sol-gel particle, not only its surface.

It is important to note that the contamination-testing conditions used in this study (a saturated environment of vacuum pump oil vapor at 60˚C and 80 mtorr) are far more severe than what any optical element would ever experience in OMEGA and OMEGA EP over even a 10 yr life cycle. Even though the TMDS- and FTMDS vapor-treated sol-gels examined in this study were not as resistant to oil contamination as HMDS vapor-treated or alkoxysilane solution-treated optics, their resistance may still be good enough for them to be used successfully in many applications areas in OMEGA and OMEGA EP. Additionally, since the complete nature of all contaminants that could be inadvertently introduced into these large laser systems is not well understood, TMDS and FTMDS vapor-treatment may be more effective than HMDS vapor-treatment or alkoxysilane solution-based methods in increasing resistance against these yet-to-be-identified contaminants. Future efforts should be directed toward studying the interaction of suspected potential contaminants with these two organosilanes (and others) to develop treatment processes that will protect against a broad range of contaminants. For organosilanes that have low volatility, both higher reaction temperatures and lower pressures during the vapor-phase silanization process should be investigated in order to increase their concentration in the vapor state and allow maximum saturation of the sol-gel AR coating in the treatment chamber. Mixtures of multiple organosilanes with different molecular structures should also be tested to determine if simultaneous treatment increases the contamination resistance of sol-gels.

VI. Acknowledgements

I thank my advisor, Kenneth L. Marshall, for his supervision and guidance throughout my research. I thank the Laboratory of Laser Energetics for allowing me use of their facility and equipment. I also thank Dr. R. Stephen Craxton for selecting me for the Summer High School Research Program. I thank the Optical Manufacturing Group (OMAN) and all the students and staff in the Materials lab for their support and assistance.

VII. References

(1) J. D. Zuegel et al., *Laser Challenges for Fast Ignition*, Fusion Science and Technology, 49 Apr. 2006.

(2) Marshall, Kenneth, Laboratory for Laser Energetics, personal communication (2008).

(3) Comparative study on hydrophobic anti-reflective films from three kinds of methyl-modified silica sols. Y.Xu, D.Wu, Y.Sun et.al. Journal of Non-crystalline Solids. 351(2005):258-266

(4) Antireflective silica with thin films with super water repellence via a sol-gel process. Y.Xu, W.Hao, Z.Li et.al. Applied Optics, 42(2003) n1:108-112

(5) Durable solgel antireflective films with high laser-induced damage thresholds for inertial confinement fusion. Y.Xu, L.Zhang, D.Wu. et.al. Optical Society of America. 22(2004):905-912

(6) K. L. Marshall, V. Rapson, Y. Zhang, G. Mitchell, and A. L. Rigatti, “Contamination Resistant Sol-Gel Coatings for High Peak Power Laser Applications,” published in the Proceedings of the OSA Topical Meeting on Optical Interference Coatings, Tucson, AZ, 3–8 June 2007.

(7) K. L. Marshall, Z. Culakova, B. Ashe, C. Giacofei, A. L. Rigatti, T. J. Kessler, A. W. Schmid, J. B. Oliver, and A. Kozlov, “Vapor-Phase–Deposited Organosilane Coatings as ‘Hardening’ Agents for High-Peak-Power Laser Optics,” in *Thin-Film Coatings for Optical Applications IV*, edited by M. J. Ellison (SPIE, Bellingham, WA, 2007), Vol. 6674, p. 667407.

Optimization of Cone-in-Shell Implosions

Angela Ryck

Optimization of Cone-in-Shell Implosions

Angela Ryck

Fairport High School
Fairport, New York

Advisor: Dr. R. S. Craxton

Laboratory for Laser Energetics
University of Rochester
Rochester, New York

November 2008

Abstract

This report investigates the effectiveness of laser-driven fusion when cone-in-shell targets are used. Fast ignition, one method of laser-driven fusion, employs an energetic short pulse laser beam that irradiates an imploded target. Cone-in-shell targets, in which a gold cone is embedded in a shell of deuterium-tritium fuel, are one design proposed for fast ignition. Laser beams arrayed uniformly around the target implode the fuel to high densities. Energy from the short pulse laser is then funneled through the cone to ignite the dense fuel. Fast ignition is most effective when high fuel densities are achieved. The implosions of cone-in-shell targets that have been shot on OMEGA were simulated using the hydrodynamics code SAGE including laser ray tracing. It was found that portions of the shell near the cone were imploded with slower velocities, negatively impacting the uniformity of the implosion and the density of the fuel. By altering beam pointings and energies, improved implosions were found with somewhat higher peak fuel densities. Since there are many more combinations of pointing and energy adjustments than were explored, this technique opens the possibility of obtaining a near-uniform implosion even in the presence of the cone.

Introduction

Nuclear fusion is a promising way to provide fresh and plentiful energy in the future.[1] When two hydrogen nuclei are merged, it is called fusion, and this process can release large amounts of energy. Inertial confinement fusion is one approach to obtaining this energy. A target, a thin plastic shell containing fusion fuel, is irradiated from all directions by laser beams or x rays. The shell is ablated, causing the fuel inside to reach extremely high temperatures and densities. Because the fuel becomes so dense and hot, the atomic nuclei are able to fuse despite the electrostatic force that is driving them apart. Deuterium and tritium, both isotopes of hydrogen, combine to form a helium nucleus and an energetic neutron. Most of the fusion energy is carried away by the neutrons. If the target is large enough and compresses to a high density, the energy of the helium nucleus is deposited into the fuel, causing what is known as ignition. Ignition is required to achieve the condition (known as breakeven) where the energy released from the reaction is greater than the energy used to create the reaction. Fusion energy becomes a viable source of energy when the energy released is 100 times the input laser energy.

Direct drive[1] and indirect drive[2] are the two main methods of accomplishing laser fusion. The OMEGA laser at the University of Rochester's Laboratory for Laser Energetics is constructed to perform direct drive fusion, in which laser beams irradiate the target uniformly from all directions. However, with indirect drive fusion, a cylindrical gold hohlraum surrounds the target so that laser beams only enter through the top and the bottom of the cylinder. The energy that is needed for target compression with indirect drive fusion can be found in the x rays that are emitted from the hohlraum when the laser beams strike it. In this process, only about 20% of the initial energy from the laser is absorbed by the target. The rest of the energy is mainly absorbed by the gold hohlraum or lost through the openings of the hohlraum. While this may be seen as a disadvantage, the benefit is that the x rays irradiate the target more uniformly than the lasers alone. The National Ignition Facility (NIF) at the Lawrence Livermore National Laboratory has been configured to perform indirect drive fusion.

Fast Ignition

Fast ignition[3] is an important concept in inertial confinement fusion that is attracting a lot of attention worldwide[4]. After the target is imploded, a high-energy, high-intensity laser beam produces energetic electrons that heat the compressed fuel to even hotter temperatures. Using cone-in-shell targets is one method of bringing the short-pulse laser to the core of the target. For optimal fast-ignition energy gain, the short-pulse energy must be efficiently coupled to the compressed core by being focused through the cone at the optimum time. The hydrodynamics code SAGE[5] was used to simulate the use of cone-in-shell targets for fast ignition with OMEGA. Figure 1 shows a gold cone embedded in a target that is being imploded by laser beams. It displays the gold cone, one of the laser beams, and the plastic target with the different colors indicating different densities.

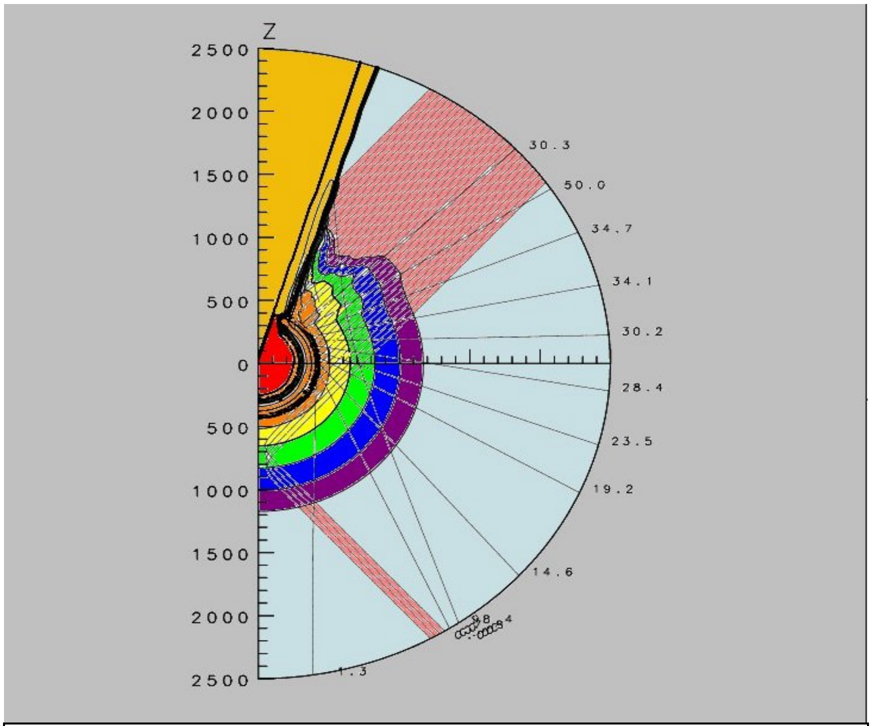

Figure 1. Simulation of a cone-in-shell target using the hydrodynamics code SAGE, showing the gold cone (yellow), laser rays (orange), and density contours (colored bands). In this and similar figures, the target is rotationally symmetric about the vertical (z) axis and distances are labeled in microns (µm).

The OMEGA Laser

The OMEGA laser at the University of Rochester's LLE is based on the structure of a soccer ball. The laser has eight rings containing a total of 60 beams. Each beam would be the equivalent of a corner of a black pentagon on the ball. There are five beams in the first ring, and they are configured at an angle of 21 degrees to the vertical. The first ring is situated at what would be the top of the soccer ball. The second ring contains five beams at a 42-degree angle. Table 1 illustrates the configurations of the eight rings on OMEGA. The first ring of beams is not used in the cone-in-shell simulations due to the position of the cone. Rays from the second ring (shown in Figure 1) strike the gold cone as well as the plastic shell.

Ring	Angle	Number of Beams
1	21˚	5
2	42˚	5
3	59˚	10
4	81˚	10
5	99˚	10
6	121˚	10
7	138˚	5
8	159˚	5

Table 1. Arrangement of the 60 beams on LLE's OMEGA laser system. They are organized in 8 rings with varying angles.

Parameters for Optimization

The parameters available for use include shifting the beam pointings and adjusting the energies of the beams. Rings of beams can be shifted up or down, can have their energies changed, and can even be turned off completely. Simulations were run with various combinations of parameters to determine which configuration would yield the most uniform implosion of the target.

The Cone-in-Shell Target

Cone-in-shell targets are spherical plastic (CH) shells with a gold cone embedded in the wall. Targets may vary in size, but the shell wall is typically ~24 µm thick, while the cone opens at either a 35° or 70° full angle. The shell is filled with deuterium-tritium fuel that is heated and ignited by the short-pulse laser. When cone-in-shell targets are used for fast ignition, they present the problem of an implosion that is not uniform. With decreased uniformity also comes lower temperatures and decreased density of the fuel.

Implosions of Cone-in-Shell Targets

The decreased uniformity of cone-in-shell targets is caused by the presence of the gold cone in the shell's wall. Laser beams cannot irradiate the target from all directions at equal angles since the cone prevents the use of the first ring of beams. Because of this, the parts of the shell closest to the cone often implode at a slower rate than the rest of the shell. Figure 2 shows the peak density of the initial design as a function of time, which at its peak reaches 34 g/cm^3. In this design, the sections of the shell that were touching the cone fell behind the rest of the shell in the implosion, reducing the compression of the fuel in the center.

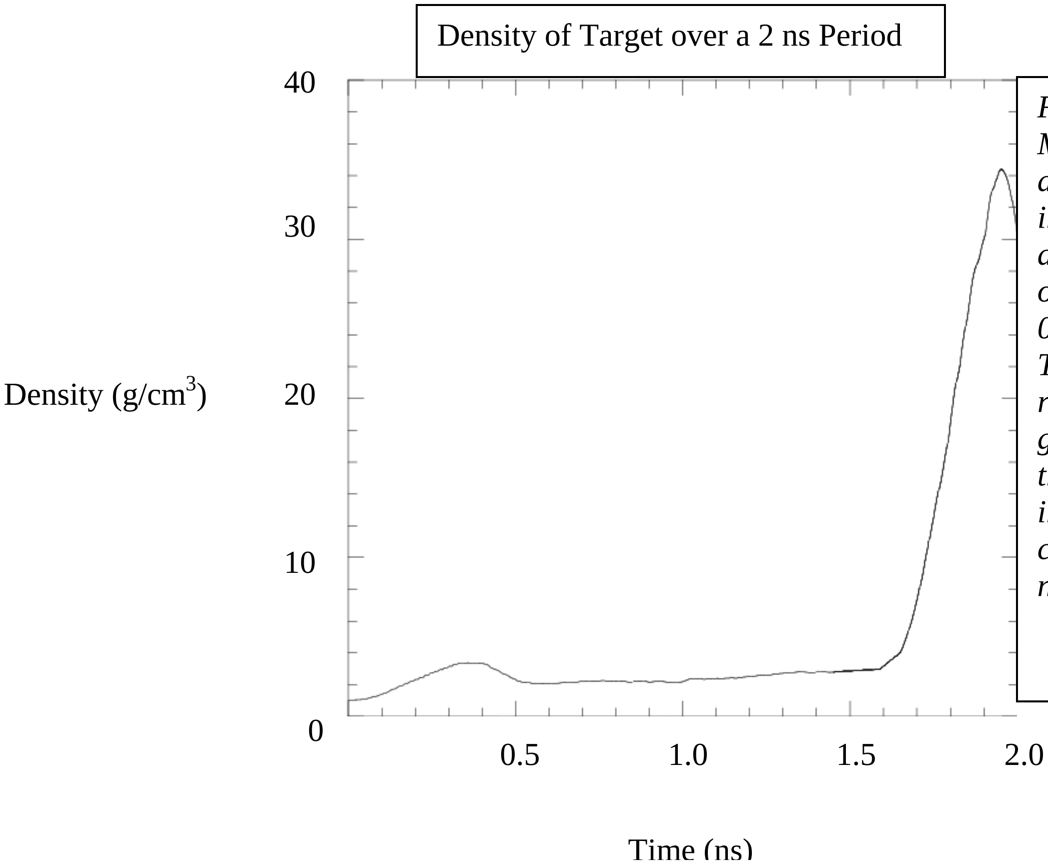

Figure 2. Maximum density of the initial design as a function of time from 0 to 2.0 ns. The density reaches 34 g/cm^3 near the end of the implosion, close to 2.0 ns.

Improved uniformity was achieved by shifting the second ring of beams up 12 µm toward the cone, and decreasing the energy of the third ring to 70%. Making these changes focused more energy on the section of the shell that was imploding too slowly, and took some energy from other areas. The series of plots, shown below in Figure 3, shows the uniformity of the implosion and the approximately circular shape the shell takes on as it implodes. The shell, colored red, becomes thicker as time passes from 1 nanosecond to 1.6 nanoseconds. The outside of the shell ablates because of the extensive amount of heat that the beams irradiate it with.

Figure 3. Density contours of a cone-in-shell target of initial radius 400 µm at four successive times. The plastic shell is shown in red and the gold cone in yellow. (a) The implosion of the target has already commenced by 1.0 ns.

(a)

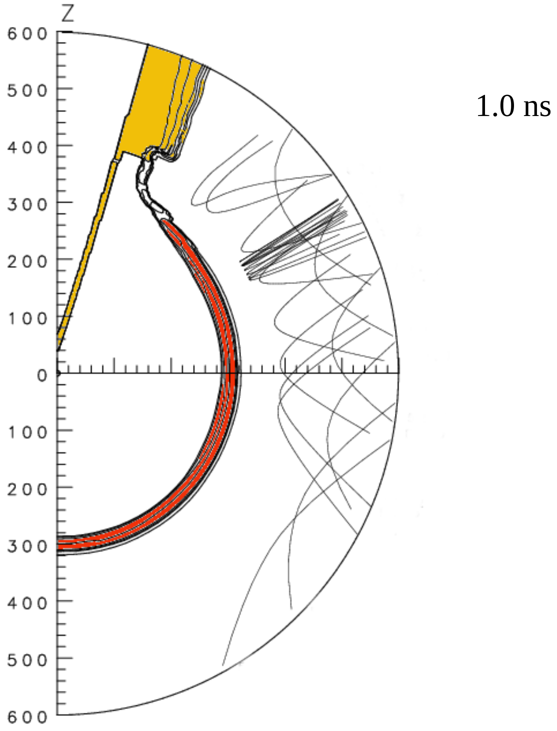

Figure 3. (b) At 1.2 ns, the shell has grown thicker as it becomes hotter.

(b)

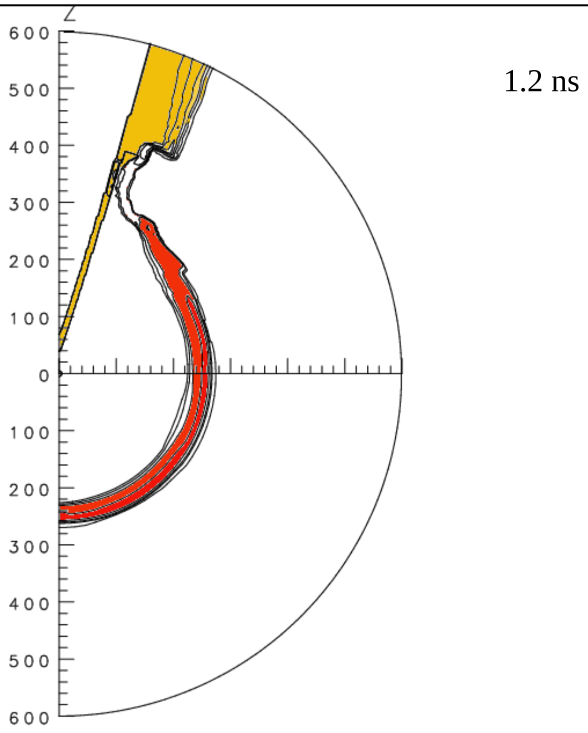

Figure 3. (c) By 1.4 ns, the shell has ablated a great amount, and has a significantly smaller diameter than before.

(c)

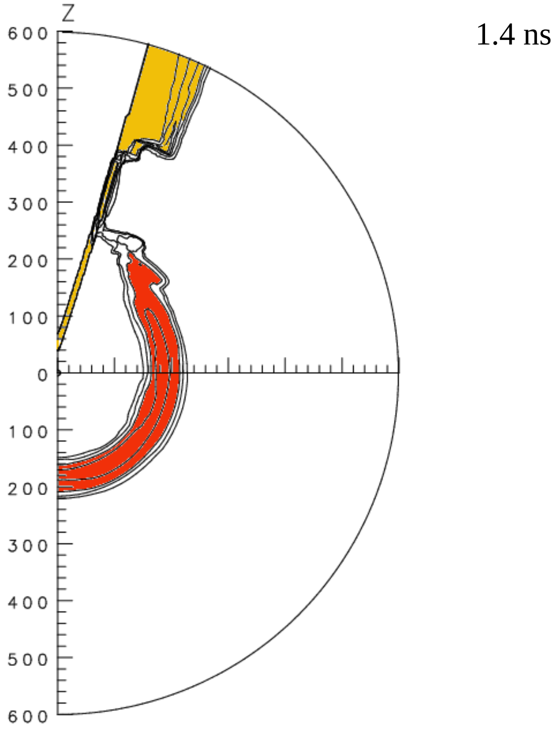

Figure 3. (d) The target reaches its densest and hottest point so far at 1.6 ns. The uniformity of the shell is generally good.

(d)

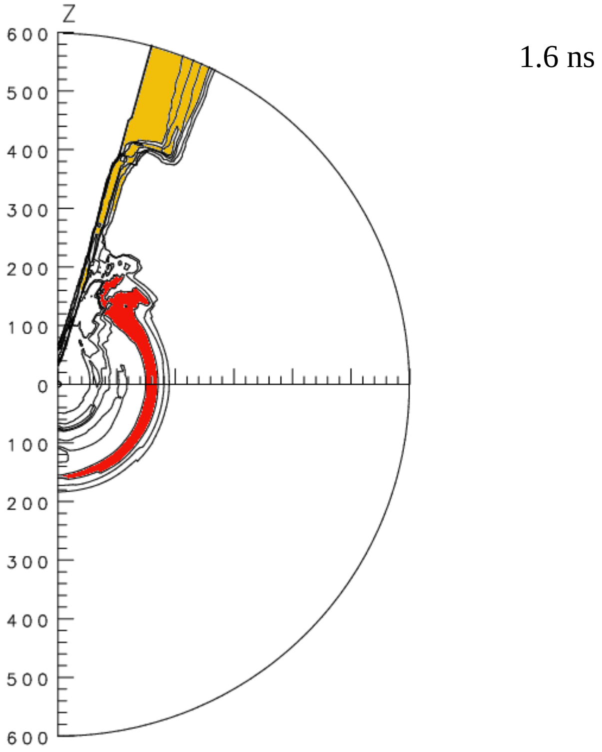

These results, obtained with the modified beam arrangements, suggest that adding more energy near the cone is beneficial to the uniformity of the implosion. However, adding too much heat to the volume surrounding the cone can cause a large amount of erosion of the gold cone. This in turn can cause the nearby shell to decrease in velocity as it implodes. It is important to add an amount of energy that improves the uniformity of the implosion, but does not interfere with the cone. The improved design proves that this is a possibility with cone-in-shell targets. The density as a function of time for the new design, shown in Figure 4, has a peak value of 51 g/cm^3, which is a 50 percent increase from the original. However, it should be cautioned that the maximum density is often found in a small portion of the compressed fuel and thus may not always be representative of the overall compressed fuel density.

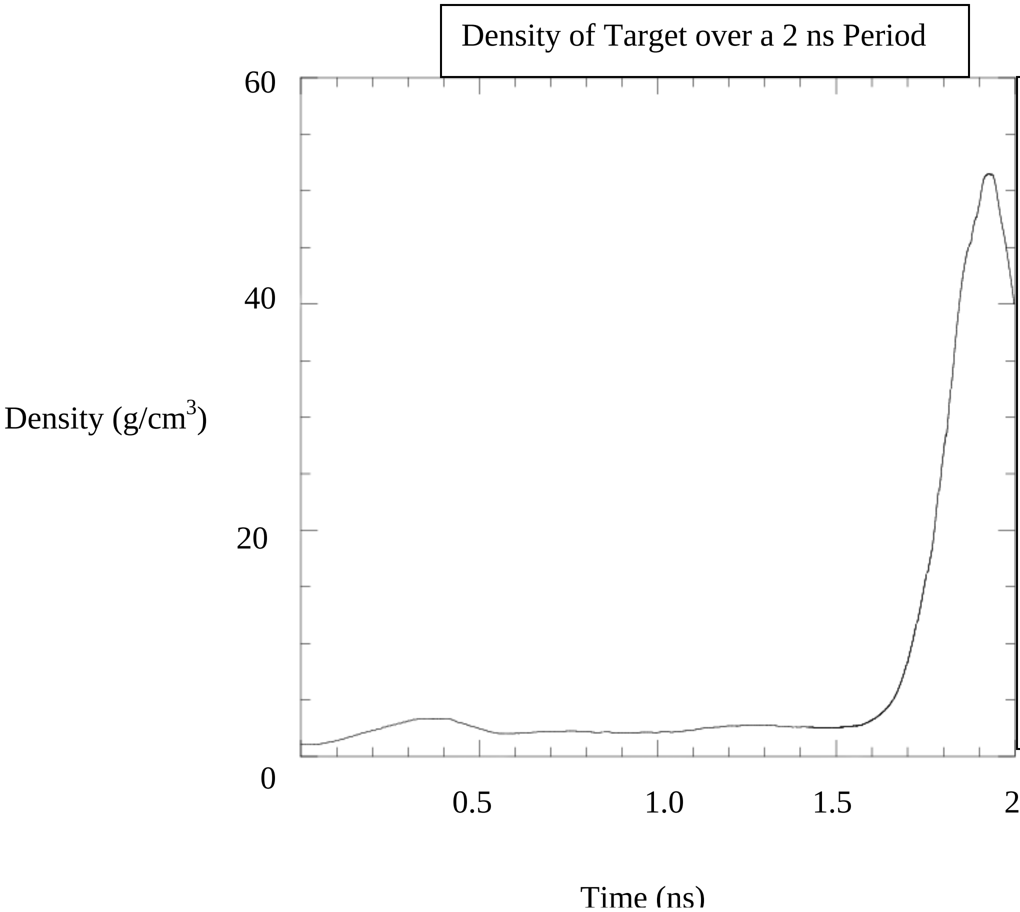

Figure 4. Maximum density of the imploding target as a function of time after adjustments in beam pointings and intensities. The density reaches its peak value of 51 g/cm^3 at a time close to 2 ns

Conclusion

Through the use of the hydrodynamics code SAGE, it can be seen that the implosion of the target is fairly uniform in spite of the presence of the cone in the target. Since both the beam pointings and beam energies can be changed on seven of the eight rings of beams, there are many more possible combinations for changing these parameters than have been investigated in the present work. There is thus room for future improvement.

The amended design suggests that adding more laser energy to the areas of the shell closest to the cone will increase the implosion velocity in this area, leading to a higher fuel density in the center of the target, but more simulations are needed to confirm this. The combination of a high fuel density with the extremely hot temperature expected from the short-pulse laser will hopefully cause a large improvement in the fusion energy output from the center of the target. Experiments will soon be done on OMEGA to test this. The simulations done with SAGE suggest that cone-in-shell targets have the potential to produce implosions that are nearly as uniform as for targets without cones. Because of this, cone-in-shell targets are a promising method to achieve fast ignition.

Acknowledgements

I would like to thank my advisor Dr. R. Stephen Craxton for his invaluable guidance and knowledge, and for the donation of his time for the success of my project. I also greatly appreciate the assistance and support I received from Katherine Manfred. Finally, I would like to thank Dr. Craxton and the Laboratory for Laser Energetics for the opportunity to participate in the high school internship program.

References

1. J. Nuckolls *et al.*, "Laser Compression of Matter to Super-High Densities: Thermonuclear (CTR) Applications," Nature **239**, 139 (1972).
2. J.D. Lindl, "Development of the Indirect-Drive Approach to Inertial Confinement Fusion and the Target Basis for Ignition and Gain," Phys. Plasmas **2**, 3933 (1995).
3. M. Tabak *et al*., "Ignition and High Gain with Ultrapowerful Lasers," Phys. Plasmas **1**, 1626 (1994).
4. Kodama *et al*., "Fast Heating of Ultrahigh-Density Plasma as a Step Towards Laser Fusion Ignition," Nature **412**, 798 (2001).
5. R.S. Craxton and R.L. McCrory, "Hydrodynamics of Thermal Self-Focusing in Laser Plasmas," J. Appl. Physics. **56**, 108 (1984).

Minimization of Tritium Contamination on Surfaces

Collin Sowinski

Minimization of Tritium Contamination on Surfaces

Collin Sowinski

Minimization of Tritium Contamination on Surfaces

Collin Sowinski

Penfield High School

LLE Advisor: Walter Shmayda

Abstract

Tritium is a radioactive hydrogen isotope used in fusion reactions. Plasma decontamination is one of the methods used to remove tritium from the surface of objects. Although plasma decontamination is very efficient at removing surface activity, it cannot easily remove tritium beneath the surface of a material. To improve the process, the properties of the plasmas used in this process are being studied by varying the operating pressure of the plasma. The results of these experiments will be used to find the optimal settings for plasma decontamination so that the temperature of the item being decontaminated is at its highest. Hydrogen mobility increases with increasing temperature, enabling hydrogen present in the bulk to migrate more freely to the surface where it is removed by the plasma.

Introduction

Tritium is a radioactive isotope of hydrogen that is used in fusion reactions. It has a half-life of approximately 12 years and emits a low-energy beta particle. When tritium decays, it becomes helium-3. Tritium has the ability to spread through air. Cross contamination can occur if a contaminated object is present in the environment and is not in a sealed container. Tritium can also migrate into the bulk of a material. This can cause decontamination to be inefficient. If the surface of a contaminated material is cleaned, surface contamination can re-appear due to tritium migration from the bulk metal.

Tritium has the ability to replace normal hydrogen atoms in molecules. This is known as tritiation. Polymers are at highest risk of tritiation, due to the high hydrogen content within the molecular structure. When tritium is incorporated in a molecule and decays, it changes the molecular structure. The site in the molecule that normally contains a hydrogen atom becomes unoccupied when the hydrogen transmutes to helium and diffuses away. This can weaken a material over time. Tritiation also presents a health hazard. When tritium is incorporated in water, the tritiated water can be absorbed into the blood stream, bringing tritium directly in contact with the inner body.

Plasma decontamination is a process by which particles are removed from the surface of an object through an event known as sputtering. Sputtering is the action of ions or atoms slamming against the surface of an object and removing particles from the surface. Plasma decontamination takes place in a vacuum, usually in the 10-90 mTorr range.

Experiment

The apparatus used in the research (see Fig. 1) is equipped with a voltmeter used to measure floating voltage, an ammeter, and a thermocouple. The gas used to generate the plasma was argon. The plasma was generated using an RF generator set to 100 watts. Experimental runs were conducted at 10 mTorr intervals starting at 90 mTorr and ending at 10 mTorr. During each run, voltage, temperature, and current data were recorded at five-second intervals. Most experimental runs ran for 1200 seconds (20 minutes); however, some were longer in order to obtain data on the end result of extended decontamination. Typical results of an experimental run are shown in figures 2 through 4.

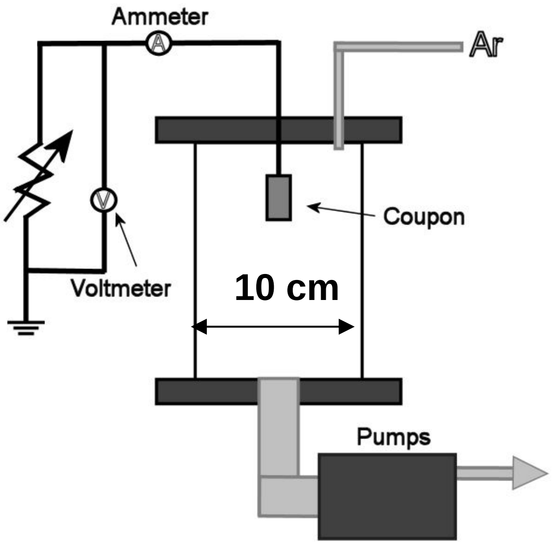

Figure 1. Diagram of experimental set up.

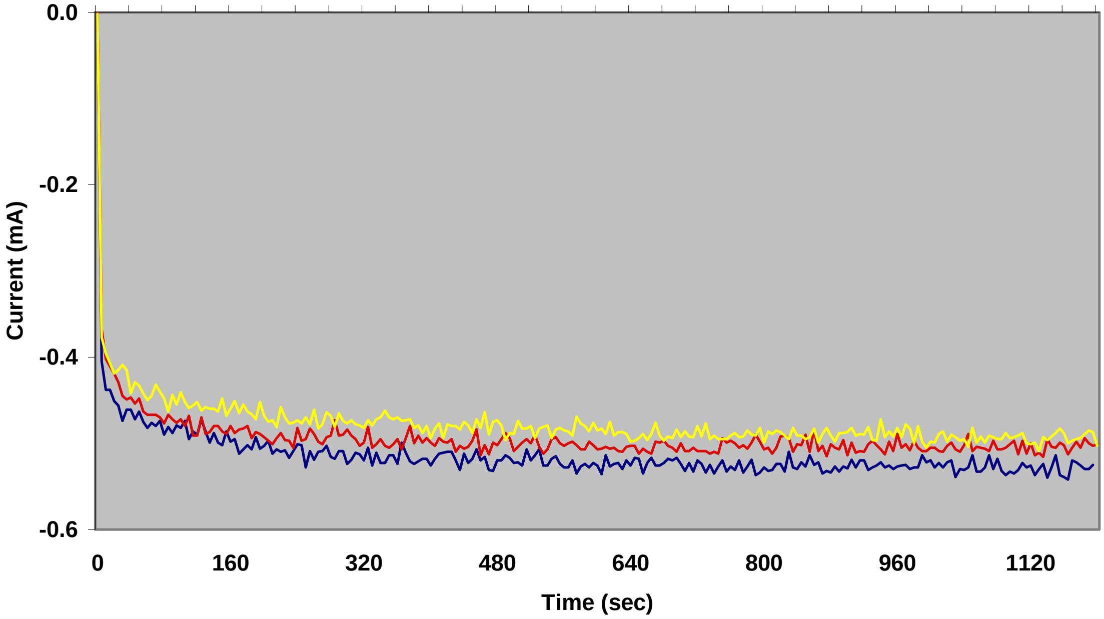

Figure 2. Current in milliamps over time of three experimental runs at 70 mTorr

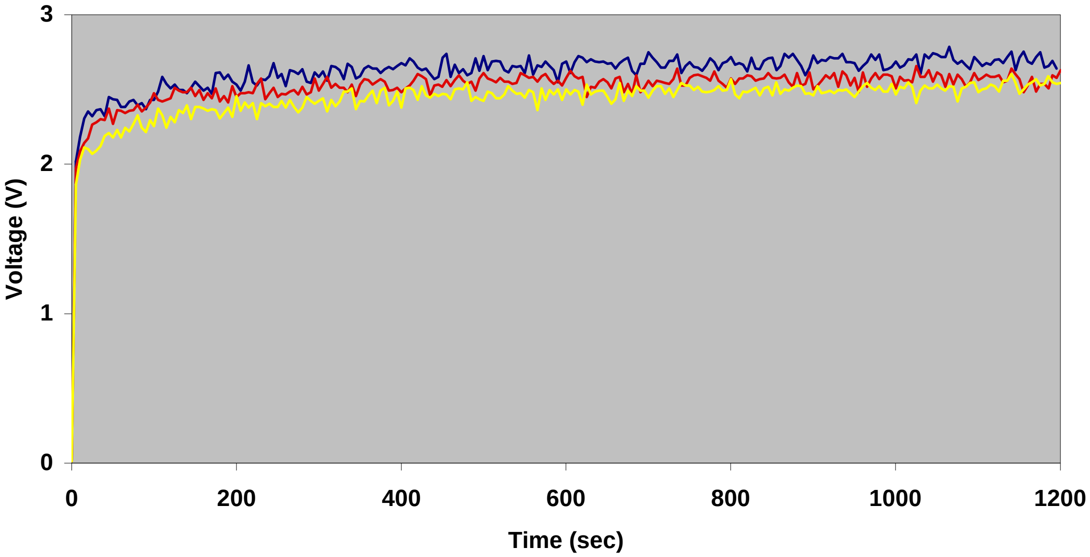

Figure 3. Voltage data of three experimental runs at 70 mTorr.

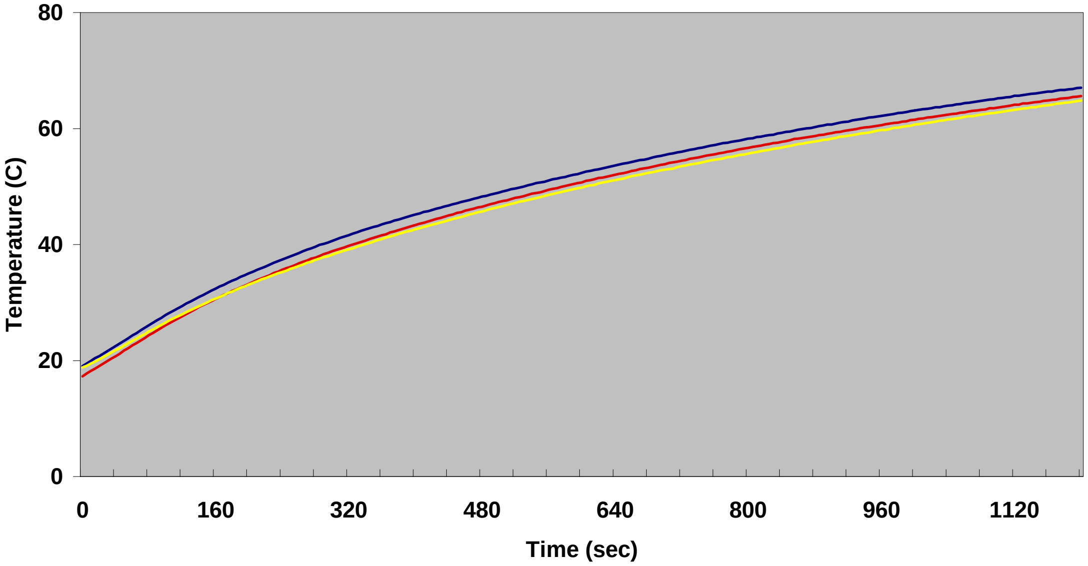

Figure 4. Temperature data of three experimental runs at 70 mTorr.

When sputtering occurs, it takes approximately 25 seconds to remove one monolayer of material. It was calculated that any particles in the chamber will only be in the chamber for approximately 0.3 seconds. Based on this, it can be assumed that the majority of the particles removed cannot reattach to the metal coupon.

.

Previous studies show that when a sample is subject to plasma decontamination, surface activity, radiation on the surface of an object, decreases rapidly within the first few minutes and decreases at a slow rate past the first few minutes. This occurs due to the rapid removal of surface activity and the slow removal of tritium from within the bulk of the sample. Sputtering is effective at removing surface activity; however the rate of removal from the bulk is reliant on the rate of tritium migration to the surface. The easiest way to influence the rate of migration is by changing the temperature of the sample.

Varying the neutral gas pressure changes characteristics in the plasma such as the rate of energy deposition by the ions on the metal coupon. By changing the energy deposition, one can control the temperature gain or loss of a sample immersed in the plasma. By increasing the temperature, the rate of tritium diffusion from the bulk increases, thereby increasing the overall efficiency of the decontamination process.

Figure 5 shows temperature over time as a function of pressure. The graph indicates that at 50 mTorr pressure, the average coupon temperature is highest. This means that at 50 mTorr, tritium removal from the bulk is highest. Figure 6 shows a graph of power delivered to the coupon as a function of pressure. As pressure increases, the rate of power injection into the coupon decreases until the mean free path of the neutral particles in the plasma is equal to the radius of the chamber. Beyond this point power injection becomes independent of pressure.

New measurements indicated that the discontinuity previously observed between 50 and 60 mTorr is not evident (figure 7) and may be related to an offset in the measurements. The new measurements suggest that the heating effect discussed above increases continuously with increasing pressure over the pressure range 10 to 57 mTorr.

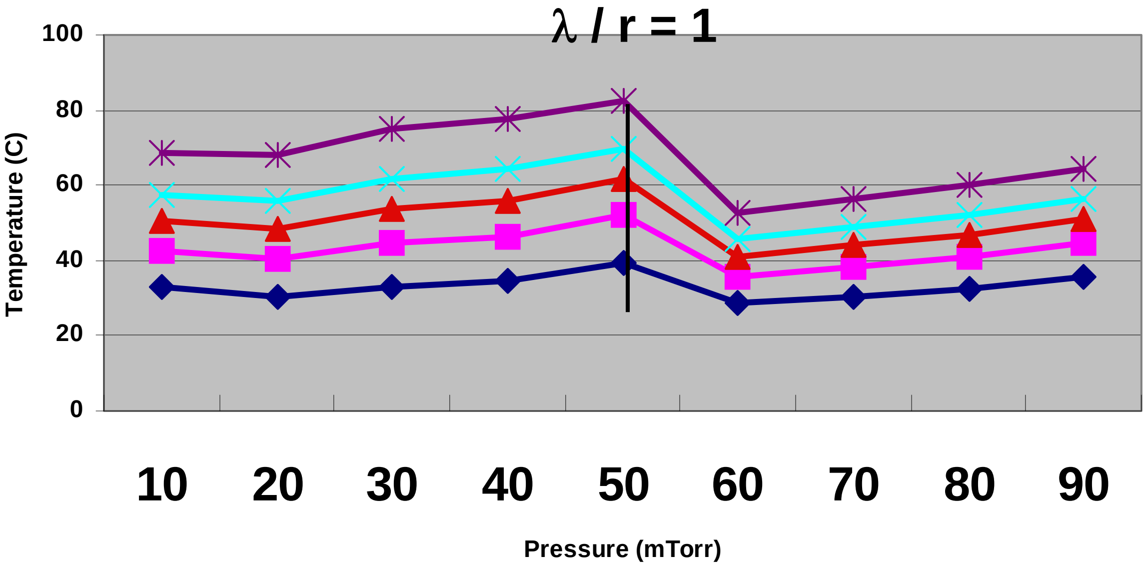

Figure 5. Graph of temperature over time as a function of pressure. The blue line represents the average temperature at 300 seconds into the experiment at various pressures. The pink line represents 600 seconds, the red is 900 seconds, the teal is 1200 seconds, and finally the purple line is 1500 seconds.

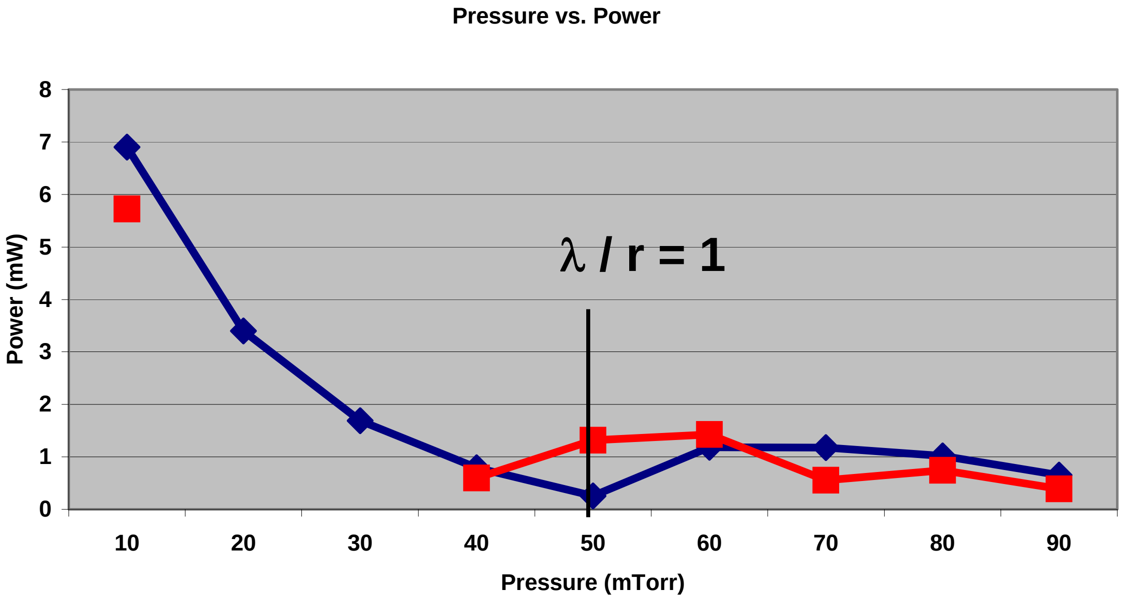

Figure 6. Graph of average power as a function of pressure. The blue line represents the first set of data collected, whereas the red line represents the second set.

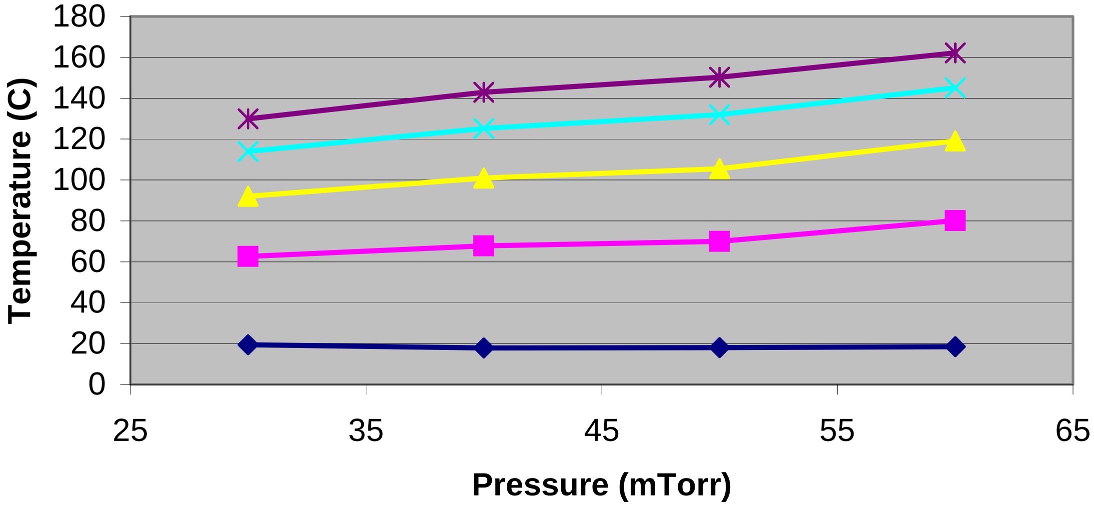

Figure 7. Graph of temperature over time as a function of pressure. The blue line represents the average temperature at 0 seconds into the experiment at various pressures. The pink line represents 300 seconds, the yellow is 600 seconds, the teal is 900 seconds, and finally the purple line is 1200 seconds.

Conclusions

The temperature of a metal coupon immersed in a low pressure, RF driven plasma increases as the neutral gas pressure increases. As coupon temperature increases, the rate of tritium diffusion from the coupon increases. The highest temperature change of the coupon occurred at 50 mTorr, where the mean free path of gas ions is equal to the radius of the chamber. Recent data, however, have shown that the discontinuity in the previous measurements observed at pressures above 50 mTorr may be related to a zero shift in the diagnostic. This conclusion needs to be verified by additional measurements.

Acknowledgements

I would like to thank Dr. Walter Shmayda for his mentoring and support throughout this project as well as his lessons on various topics related to the project. I would also like to thank Professor Udo Schroeder for his support and guidance, Matthew Sharpe for his support and instructions on how to work with the experimental equipment, and Michael Quinlan for his continued support throughout my research.

Investigation of Brushless DC Motor Commutation Techniques

Jack Stokes

Investigation of Brushless DC Motor Commutation Techniques

Jack Stokes

Fairport High School
Fairport, NY

Advisors: Scott Ingraham and David Lonobile

Summer High School Research Program

Laboratory for Laser Energetics
University of Rochester
Rochester, NY

January 2009

Abstract:

Brushless DC (BLDC) motors are cleaner and more reliable than their brushed counterparts. For this reason, a number of BLDC motors are used in the OMEGA laser system. Because of the extreme conditions these motors are exposed to during a laser shot, including a powerful electromagnetic pulse (EMP), the Hall effect sensors that govern the motors' commutation cycles sometimes sustain serious damage. This damage may render the motors inoperable using the installed motor drivers. This necessitates a difficult extraction process to recover the motors for repair. This project investigated sensorless motor commutation as a potential solution to this problem. With a sensorless commutation scheme, the motors could be extracted without the use of the damaged Hall sensors. Therefore, a test fixture has been developed that is capable of driving a BLDC motor sensorlessly. This will aid in extracting the target positioner and the off-axis parabola inserter/manipulators after Hall sensor damage has occurred.

Introduction:

In order to conduct inertial confinement fusion research at the Laboratory for Laser Energetics, a small target is exposed to high-intensity laser beams within the target chamber. This target is precisely positioned before an experiment by the target positioner, a mobile device which transports the target down a wide metal tube to the chamber. The target positioner is driven by a brushless DC (BLDC) motor.

Because BLDC motors lack contact brushes, commutation must be regulated electronically. The current hardware driving the target positioner's motor utilizes three Hall effect sensors. During a laser shot event, the target positioner is exposed to extreme conditions, namely a high-intensity electromagnetic field. This sometimes results in damage to the Hall effect sensors, effectively rendering the BLDC motor on the target positioner inoperable. This necessitates a difficult and time-consuming process to manually extract the device for repair.

It is possible, however, to effect commutation of the BLDC motor entirely without the use of its sensors. Rather than directly sensing the rotor's magnetic field, the back electromotive force (BEMF) generated in the stator windings can instead be sensed. Because this can be done without additional onboard hardware, such sensorless commutation would allow the target positioner to be extracted under its own power when its sensors fail.

This project investigated the possibility of sensorless commutation for the purpose of removing the target positioner and/or off-axis parabola inserter/manipulators (OAPI) in the event of sensor failure. Although no further onboard hardware (such as sensors) is required for this approach, a new controller is necessary to interpret the BEMF and, using this feedback, commutate the motor. This controller would be a separate unit that could be connected to the target positioner externally when needed.

Project Goals:

The main goal of this project was to investigate the feasibility of sensorless commutation as a secondary mode of operation for the target positioner and OAPI. To accomplish this, a proof-of-concept test fixture was created to evaluate this commutation technique. First and foremost, this fixture needed to be capable of driving a BLDC motor using sensorless feedback. It had to be capable of doing this at relatively high power outputs (24V at 5A or more), in order to drive the target motors. The test fixture also needed to be self-contained and portable, to allow for practical usage and avoid unnecessary complexity. Last, the fixture needed to incorporate commercial “off the shelf” hardware if possible, in order to minimize development time and simplify the end product.

Current Commutation Techniques:

The target positioner and OAPI are currently driven using Hall effect sensor feedback. This technique uses three digital Hall sensors evenly distributed around the stator (see Fig. 1). As the rotor spins, the magnetic field produced by its permanent magnet(s) shifts accordingly. This change in relative field strength as observed by the Hall sensors allows the motor controller to determine the approximate orientation of the rotor. With this information and a known cycle of corresponding “Hall states” and phase voltages, the motor can be commutated effectively.

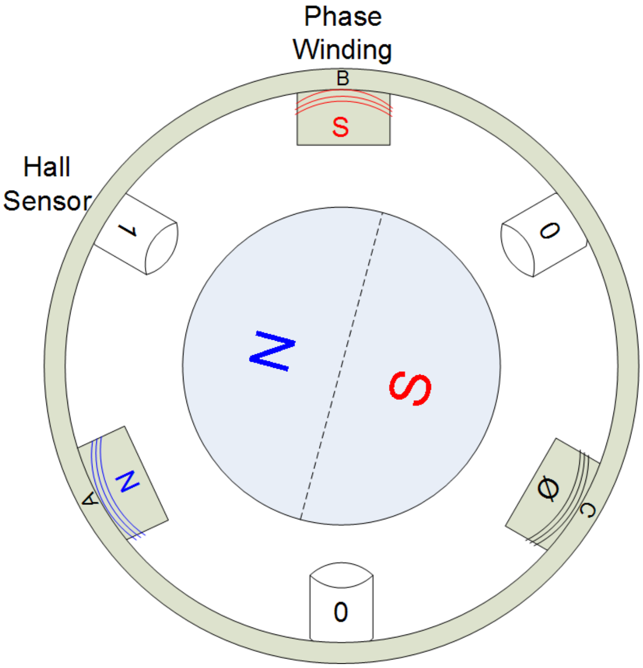

Figure 1: An example of a three-phase BLDC motor, in which Hall effect commutation directly senses the rotor's changing magnetic field.

In addition to the Hall effect sensors, the BLDC motors used in the target positioner and OAPI are equipped with encoders. Although these encoders are not used in typical operation, they provide an auxiliary method of commutation in the case that the Hall sensors are damaged, but the encoder is still operational. However, the encoders experience failure rates greater than that of the Hall sensors, so this is sometimes not an option.

Sensorless Commutation:

Much like Hall sensor commutation, sensorless commutation relies on the sensing of magnetic fields. However, rather than directly detecting the rotor's field, the BEMF is sensed. BEMF is induced in the motor's phase windings as the rotor's spinning magnetic field interacts with them. Because only two of the phases have voltage applied across them at any given moment, the third, inactive phase can be used to sense the induced current (BEMF) across it (see Fig. 2). This provides an analog indication of the rotor's orientation, which takes the shape of a sinusoidal wave. The frequency of this wave, calculated by determining zero-crossing points, can then be used to estimate when to commutate the motor.

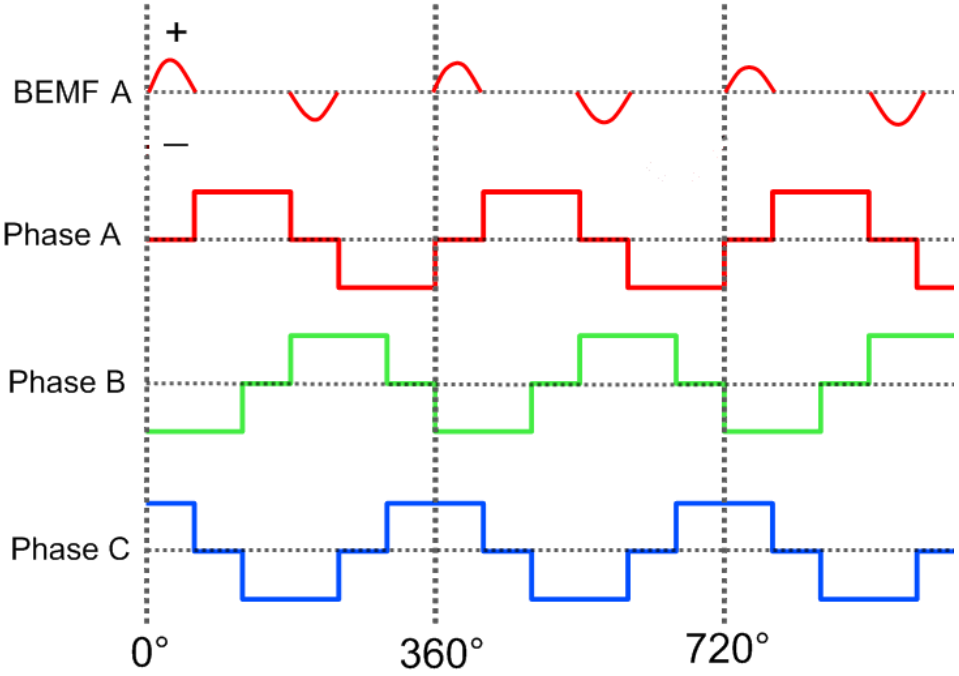

Figure 2: An example of the voltage waveforms as a three-phase BLDC motor operates. Note that the BEMF shown is only as read from phase A; it can only be sensed when the phase is inactive.

Because sensorless commutation relies on BEMF, the rotor must be spinning fast enough to induce a usable voltage for it to commutate reliably. This means that for low-speed applications, or for those where precise position control is necessary, sensorless commutation is not a viable option. Additionally, a smooth startup sequence is not possible, because the rotor's initial orientation cannot be determined. For this reason, many controllers begin in an arbitrary state and blindly cycle through the commutation sequence until the rotor is spinning fast enough to begin proper electronic commutation.

Although this works, it often results in an amount of “shuddering” during the startup sequence, and the rotor may momentarily spin in reverse.

However, although these properties limit sensorless commutation's application range, there are also advantages over Hall effect commutation. Most importantly, sensorless commutation does not require any onboard sensors. This means that it can be used in situations where extreme conditions may make Hall effect sensors or encoders unreliable, such as the OMEGA target chamber. While sensorless commutation is not an attractive option for normal operation of the target positioner and OAPI, it is excellent for short-term extraction in the event of sensor failure. Therefore, a test fixture was created to evaluate its effectiveness for this task.

Test Fixture Creation:

Because an “off-the-shelf” implementation was preferable for this project, it was necessary to select and purchase a commercial controller. Many packages were considered, and Luminary Micro's BLDC development kit was ultimately chosen, for several reasons. First, it shipped pre-loaded with Luminary's BLDC demonstration program, which could interface with a PC running a GUI client. Luminary's solution also offered several development environments to choose from, including Code Red's red_suite, CodeSourcery, IAR Embedded Workbench, and the ARM/Keil Microcontroller Development Toolkit for ARM. The development kit also featured the Stellaris LM3S8971 microcontroller (based on 32-bit ARM Cortex-M3 architecture), which was a very capable processor for the task. All of these points, combined with a very affordable price, made the Luminary Micro development kit the best option for this project.

The RDK-BLDC kit's included BLDC motor control software allowed the user to control drive parameters in real time from a connected PC over an ethernet interface. This functionality was very useful in zeroing in on the optimal parameters for driving the specific motors used in the target positioner and OAPI. These parameters were later inserted into the final source code as constants.

To program the microcontroller, a separate Luminary product, the LM3S8962 Evaluation Kit, was used. This kit was capable of programming the motor control board over USB/JTAG, an interface commonly used to test and program microcontrollers. It also included a daughter board, which could be connected via CAN (controller area network), a protocol used for communication between electronic control units. This board included several pushbuttons, which made it a useful addition to the motor control board.

To begin, Luminary's stripped-down version of the motor control source code was loaded in IAR Embedded Workbench. This version had the ethernet, serial, and CAN interfaces removed, and simply started and stopped the attached motor. Using preprocessor commands and jumper settings on the board, it could be toggled between Hall effect and sensorless commutation. After much experimentation and editing of the source code (in the C language), the code was modified to accept input over the CAN interface. This allowed for easy push-button control when testing; however, it also resulted in communication that was sometimes unreliable.

Because motor control requires completely dependable controls, the CAN interface was removed. In its place, several external pushbutton switches were connected to the board's inputs that were normally reserved for the motor's Hall sensors – in this application, they are not necessary, freeing up three input screw terminals.

The code was then further modified to handle limit switches. The target positioner and OAPI both utilize these switches in order to ensure a safe operating range, and so the test fixture had to incorporate these inputs in its design. Care was taken to thoroughly test the logic governing motor operation, to prevent the motor from running in unsafe ways when the user presses an unforeseen combination of buttons.

Next, the source code was further modified to accept an analog input, provided by an external potentiometer. Because the original code was designed to run at a fixed speed, major changes were necessary to allow the speed to change. In the final implementation (Fig. 3), the user can adjust the speed in real-time using scaled input from the potentiometer.

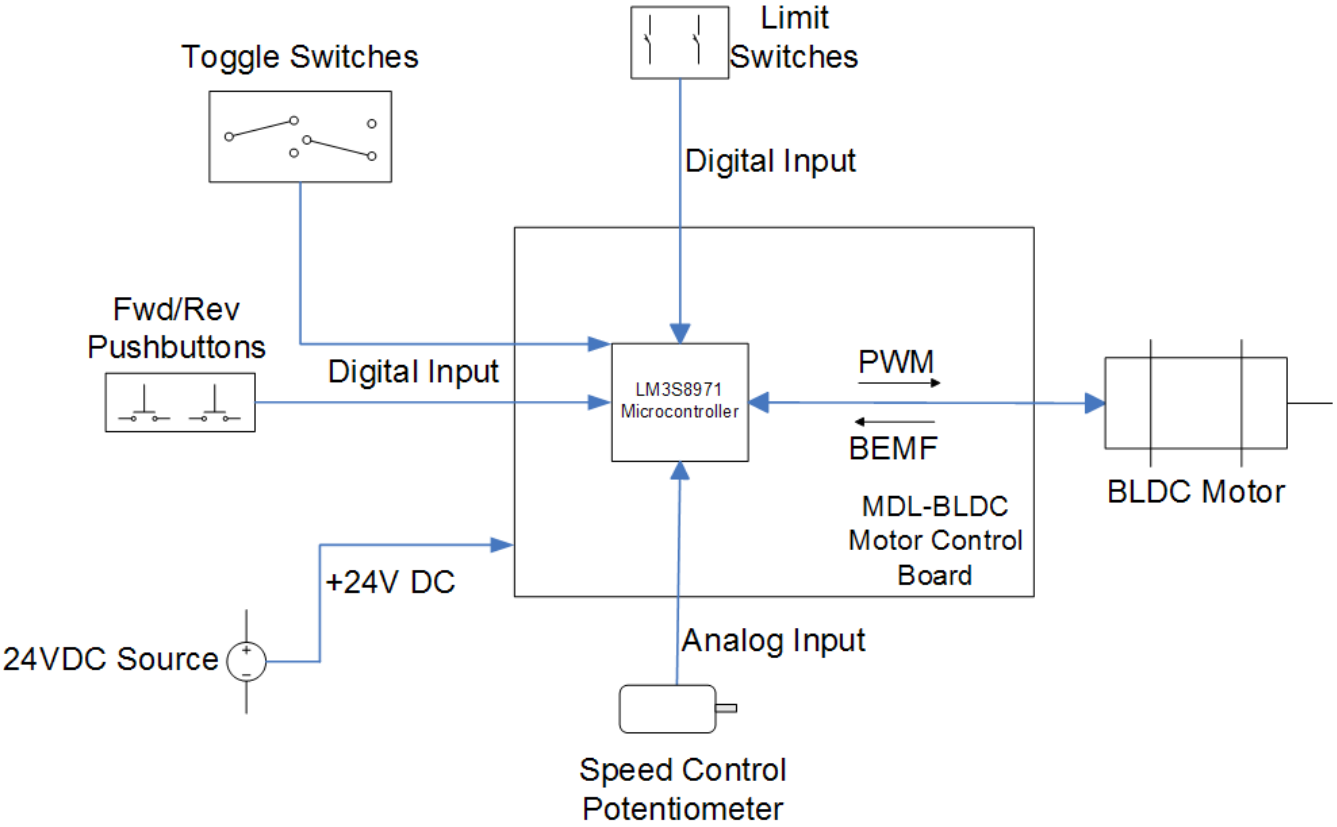

Figure 3: A block diagram of the final implementation of the test fixture. The microcontroller receives input from the user and from the motor's BEMF, and drives the motor using pulse-width modulated (PWM) signals.

Finally, toggle switches were added to allow the user to select between the target positioner and OAPI motor parameters at startup, as they required different voltage ranges (see Fig. 4). Additionally, a “hold” switch was added to allow the motor to be operated for longer time periods without forcing the user to hold down a pushbutton. This switch effectively preserves the state of the forward/reverse buttons while it is on, acting as a sort of “cruise control”. Of course, the limit switches can still stop the motor in this state, to maintain safety while adding convenience.

To accomplish the design goal of creating a self-contained, portable device, an appropriate enclosure was purchased to contain the electronics. Holes for the various user interface elements were drilled, as well as those for the electrical connections to external elements. For simplicity and ease of use, two circular plastic connectors were used – one for the power connection, and the other for the motor's phases and the limit switches. Different sizes were chosen to make it impossible to confuse the power and motor/limit switch connectors, which might result in damage to the device.

Figure 4: Photograph of the finalized test fixture. The CPC connectors on the right side provide connections to a power source and the motor, as well as the limit switches.

Conclusions:

The final implementation of the test fixture demonstrates that sensorless commutation is a viable technique for extracting stranded devices such as the target positioner and OAPI. While it is an experimental unit, it has been used successfully in the OMEGA EP laser bay. This project has met all of its original goals and has produced a device useful to LLE in the process.

However, there is still room for improvement. Due to time constraints, several minor issues remain. Because the motor control board was mounted in the center of the enclosure, it is currently difficult to reprogram, as the JTAG cable will not fit. This means the board must be removed before it can be programmed, which is inconvenient when testing. If the mounting holes could be relocated, more space could be allocated to allow for this.

Additionally, the “hold” switch is currently nonfunctional. This is because during development, one of the board's digital inputs (Quadrature Encoder B) was accidentally damaged and is no longer usable. Therefore, although the code for this feature is fully functional, the switch is currently useless. If this switch could be wired to an alternative input somewhere on the board, this problem could be eliminated as well.

Acknowledgements:

I would like to thank Scott Ingraham and David Lonobile for their continual guidance and support during my project. Their mentorship was invaluable to my project and taught me a great deal about the design process.

I would also like thank Dr. R. S. Craxton for accepting me into this incredible program, and the entire Laboratory for Laser Energetics for continuing to provide such an outstanding opportunity to high school students.

K-Shell Emission-Line Backlighter Source Optimization

James Tsay

K-Shell Emission-Line Backlighter Source Optimization

James Tsay

Phillips Academy
Andover, MA

LLE Advisor: Reuben Epstein

Laboratory for Laser Energetics
University of Rochester
Rochester, NY
November 2008

Abstract:

X-ray backlighting is an important diagnostic technique used in laboratory experiments conducted on the OMEGA laser system. To obtain images of imploding cryogenic targets, short-pulse, high-energy laser beams are directed at a thin slab of solid material, creating plasma backlighters that project images of the target onto a photographic film. For ample image contrast, x-ray intensities of backlighters must exceed the continuum intensity of targets. Therefore, high-intensity spectral lines are desirable. The K-shell lines of He-like species hold particular interest due to the strength of their emission, as well as the sharpness of the line. Moreover, using Al as a backlighter source positions these He-α lines within a photon energy range where about 1/e of the light is absorbed by the target. PrismSPECT, a spectral analysis code simulating the atomic and radiative properties of plasmas, can reveal the effect of certain parameters on He-α line emission. With the program, the optimal temperatures were obtained for x-ray emissions of steady-state Al plasmas at given mass densities and thicknesses.

1. Introduction

Laser-powered fusion is becoming an increasingly significant point of interest in the scientific community. Ongoing research shows that, if fully realized, fusion can provide a sustainable, alternate form of energy devoid of harmful waste products like carbon dioxide. The most immediately promising nuclear reaction to be used for fusion power is the D-T fuel cycle, in which two hydrogen isotopes, deuterium and tritium, fuse together to produce an alpha particle, a neutron, and 17.6 MeV of kinetic energy shared between the two products,[1]

$$D + T \rightarrow {}^{4}He + n \qquad . \tag{1.1}$$

This energy, converted to electricity, would be both clean and abundant. Large quantities of deuterium exist naturally in seawater, and tritium can be synthesized from lithium. Although the lithium supply is more limited than that of deuterium, it is still large enough to supply the world's energy demand for thousands of years.

At the University of Rochester's Laboratory for Laser Energetics (LLE), researchers are investigating fusion with the OMEGA laser system. The OMEGA laser beams are focused onto a target, a thin plastic shell coated on the inside with a layer of cryogenic DT, causing the target to implode. Measuring and evaluating these implosions employs diagnostic techniques like x-ray backlighting, which produces radiographs of the imploded cryogenic pellet. These imploded fusion targets emit spectral radiation across a broad range of photon energy. The backlighter must therefore "outshine" the miniature star-like implosion over a certain range of photon energies. Sharp, high intensity spectral lines can provide good picture contrast, and K-shell lines of He-like or H-like species are preferred. A thin slab of aluminum is chosen as a backlighter source because it positions these lines within a photon energy range where about 1/e of the light is absorbed by the target. This assures that variations in the attenuation due to the spatial structure of the imploded target will produce measurable image contrast. The Al forms a plasma, which radiates these He-α lines, among many others, isotropically. The radiation that travels towards and through the imploding target casts a shadow, projecting a replica image onto an image plate. For best results, the He-α lines should be "optimized" for maximum specific intensity by adjusting parameters such as temperature, mass density, thickness, and time.

2. Radiative Transfer

In order to optimize the emission of He-α and H-α lines in our Al backlighter, we must understand what happens when a laser beam strikes any given medium. In radiative transfer, the atomic processes of absorption, emission, and scattering affect the propagation of radiation through some medium. First, we introduce a fundamental quantity of a field of radiation: the specific intensity, I_v.[2] The amount of radiant energy dE_v in the frequency interval ($v, v + dv$) transported across an area $d\sigma$, within solid angle $d\omega$, and during time dt is related to specific intensity by

$$dE_v = I_v \ \cos\theta \ dv \ d\sigma \ d\omega \ dt \quad , \tag{2-1}$$

with θ representing the angle between the outward normal of the area element $d\sigma$ and the direction of propagation of the radiation within the solid angle $d\omega$.[3] By optimizing the Al backlighter, we mean to maximize the spectral intensity of the He-α line, within a nominal photon energy range 1595 to 1600 eV, centered at the line energy. To describe the variation of intensity in a medium, we have the basic differential equation of transfer

$$\frac{dI_v}{ds} = \frac{\varepsilon_v}{4\pi} - \kappa_v I_v \quad , \tag{2-2}$$

where κ_v is the absorption coefficient, ε_v is the emissivity, and ρ is the density of the absorbing plasma in g cm^{-2}. Simply put, the equation of transfer states that as a beam of electromagnetic radiation propagates through a medium, it loses energy through absorption and gains energy through emission. The solution to this equation for the special case of a homogeneous medium is

$$I_v(s) = \frac{\varepsilon_v}{4\pi\kappa_v} + (I_v(0) - \frac{\varepsilon_v}{4\pi\kappa_v})e^{-\kappa_v s} \tag{2-3}$$

for the specific intensity $I_v(s)$ at a distance s starting from an initial condition $I_v(0)$ at s=0.[4]

3. Einstein Coefficients and Spectral Line Formation

Two kinds of atomic spectral lines exist: emission lines and absorption lines. When an electron makes a transition from a particular, excited energy level to a lower energy state, it ejects a photon of a particular energy and wavelength, forming an emission line. When an electron makes the reverse transition, from a lower to a higher energy state, a photon becomes absorbed in the process, forming an absorption line. Depending on whether a photon is ejected or absorbed, a spectrum of such photons will show an emission spike or absorption drop at the associated wavelength. When the upper level is a continuum state, the absorption can occur over a broad range of energy. It is continuum absorption by the imploded target that forms the shadow in the radiographic image and continuum emission that competes with the emission-line backlighter by obscuring the shadow.

Three processes occur in the formation of a spectral line: spontaneous emission, stimulated emission, and absorption.[5] For each of these three processes, there is an associated Einstein coefficient, the probability of the associated process occurring. For example, we take the Einstein A_{ji} coefficient, which describes the rate at which the number density of atoms in level j, n_j, decays to a state i. The rate, then, at which spontaneous emission occurs is

$$\frac{\partial n_i}{\partial t} = A_{ji} n_j \quad , \tag{3-1}$$

where the subscript pair j and i denotes the transition of the electron from state j to lower state i. The Einstein coefficients B_{ji} and B_{ij} apply to stimulated emission and spectral absorption, respectively. Stimulated or induced emission refers to the process by which a photon at or very near the frequency of a certain transition induces an electron to make that transition, resulting in the emission of an additional photon with the same phase, frequency, polarization, and direction as the original. The rate at which stimulated emission occurs is

$$\frac{\partial n_i}{\partial t} = B_{ji} I_{\nu} n_j \quad , \tag{3-2}$$

for the emitting transition from state *j* to state *i*.[3] The rate of both spontaneous and stimulated emission is proportional to the number of atoms in the excited state, n_j. Lastly, absorption occurs at the rate

$$\frac{\partial n_i}{\partial t} = -B_{ij} I_{\nu} n_i \quad . \tag{3-3}$$

Like the rate of stimulated emission, the absorption rate is proportional to the radiation intensity at the frequency ν, as well as the number of atoms n_i in the initial state, but, in this case, the initial state is the state of lower energy, which is depleted by the absorption of a photon. Given the way the three Einstein coefficients, A_{ji}, B_{ji}, B_{ij}, are defined,[3] Eqs (3-2) and (3-3) have been written in terms of I_{ν}, the value of the specific intensity at the average frequency of the transition. This is a good approximation if the specific intensity does not vary significantly over the spectral width of the transition. Otherwise, an appropriate spectral average of the specific intensity is used.

The three Einstein coefficients, A_{ji}, B_{ji}, B_{ij}, are fixed probabilities, depending only on the properties of the associated atom. From this fact, we know that the relations we find between these coefficients at thermal equilibrium apply even if the state of the gas is not in equilibrium. At equilibrium, the net change in the number of excited atoms is zero, meaning opposing processes cancel each other out. Therefore, we have the relationship governing equilibrium between the two states *i* and *j*,

$$0 = A_{ji}n_j + B_{ji}I_\nu n_j - B_{ij}I_\nu n_i \quad . \tag{3-4}$$

If we assume Local Thermodynamic Equilibrium—that intensive parameters like temperature and mass density vary so slowly in space and time that one can assume thermodynamic equilibrium in some neighborhood about any given point—we know that, for a certain temperature, the population distribution of atomic states located near a given point will obey statistical distributions, such as the Maxwell-Boltzmann distribution, which describes the probability of finding a particle in certain energy states under conditions of equilibrium,

$$f(E)=Ae^{-\frac{E}{kT}} \tag{3-5}$$

where A is a constant, E is the energy of the energy state, T is the absolute temperature, and k is the Boltzmann constant, with k=1.381 x 10^{-23} J/K = 8.62 x 10^{-5} eV/K. We also consider some non-equilibrium conditions where the simplicity of LTE does not apply.

4. Non-LTE Atomic Rate Equations

Unlike in LTE plasmas, where the derivation of population numbers is based on a purely local equilibrium, the atomic level populations of non-LTE plasmas depend on the surrounding radiation field, and on the time history of these populations. This requires a detailed consideration of the atomic processes that populate and de-populate the energy levels. We begin by introducing the basic time-dependent rate equation:

$$\frac{d}{dt}n_i = \sum_j n_j P_{ji} - n_i \sum_j P_{ij} \tag{4.1}$$

The leftmost expression indicates the change in the population of level *i* with time, the inner expression indicates the sum of the population processes into level *i* from all other levels *j*, and the rightmost expression indicates the sum of the population processes out of level *i*. In the equilibrium case, the populating processes are balanced by the depopulating processes, and the populations do not evolve. This gives our second equation,

$$\sum_j n_j P_{ji} - n_i \sum_j P_{ij} = 0 \tag{4.2}$$

The rate coefficients P_{ij} represent sums of all relevant collisional and radiative processes, including ionization, recombination, excitation, and decay. The time-dependent rate equations of the form of Eq. (4.1) for all the significant atomic states are solved by the spectral analysis code PrismSPECT.

5. PrismSPECT

PrismSPECT is a spectral analysis code that simulates the atomic and radiative properties of plasmas.[6] By utilizing a database of the required atomic constants, such as oscillator strengths, atomic level energies, and transition energies, for the elements hydrogen through krypton, PrismSPECT can compute atomic level populations, ionization properties, and emission and absorption spectra for LTE and non-LTE plasmas.[7] As a result, we can easily investigate how properties of our plasma backlighter change with temperature, density, and plasma size.

6. Varying Parameters

We seek to understand the effect of independent parameters on the spectral intensity of our aluminum backlighter. To do so, we simply vary a parameter in question while holding the others constant within a PrismSPECT equilibrium simulation, looking to the atomic spectra between the photon energies of interest. We inspect the effects of temperature, mass density, and plasma thickness on spectral intensities. Remember that we are interested in the maximum intensities for the Al K-α line, that is, the line centered around approximately 1600 eV.

Figure 6-1: Spectra from a 4 μm Al foil at 5.4 g/cm^3 density plotted for various temperatures.

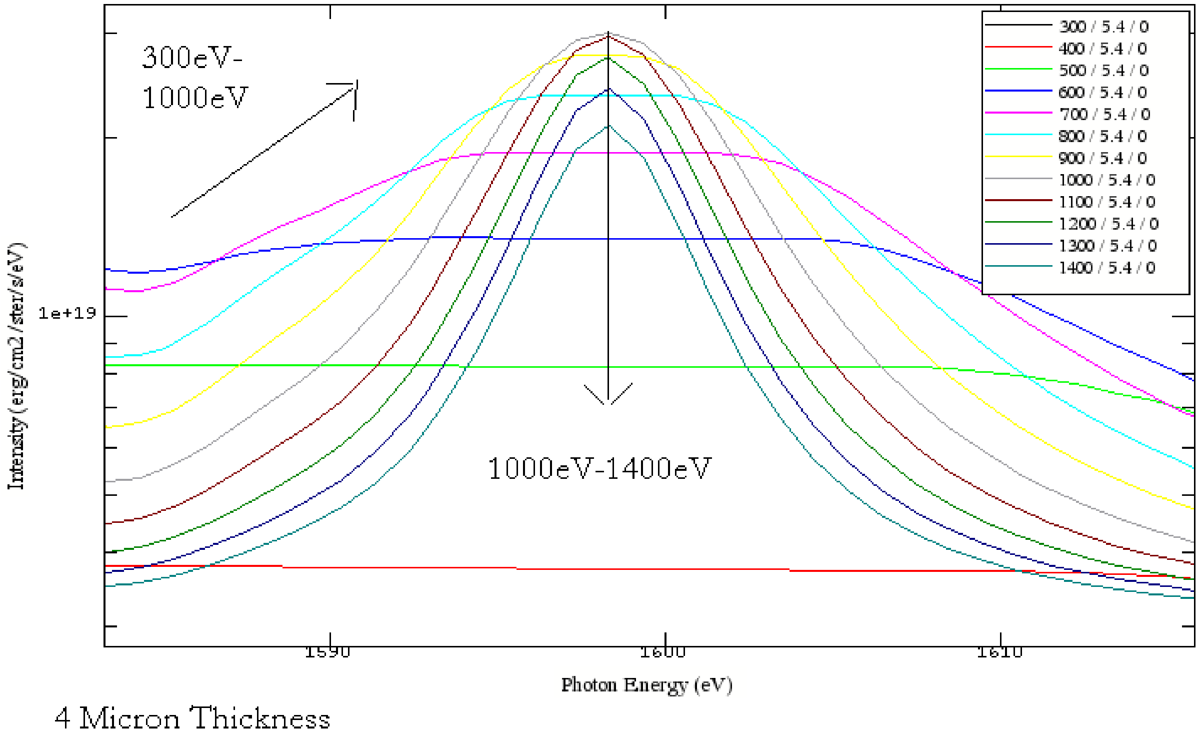

In Figure 6-1 we observe the effect of temperature on the K-α line for a sheet of Al at 4 μm thickness and a mass density of 5.4 g/cm^3, twice the density of cold Al. The temperatures are labeled in eV.

For temperatures between 300 eV to 1000 eV, we see an increase in the K-α line to a peak near 1 keV. However, as the temperatures continue to increase, the spectral intensities actually decrease. This suggests that an optimal temperature exists for every given density and thickness.

Figure 6-2: Spectra from a 10 µm Al foil at kT=800 eV temperature plotted for various densities.

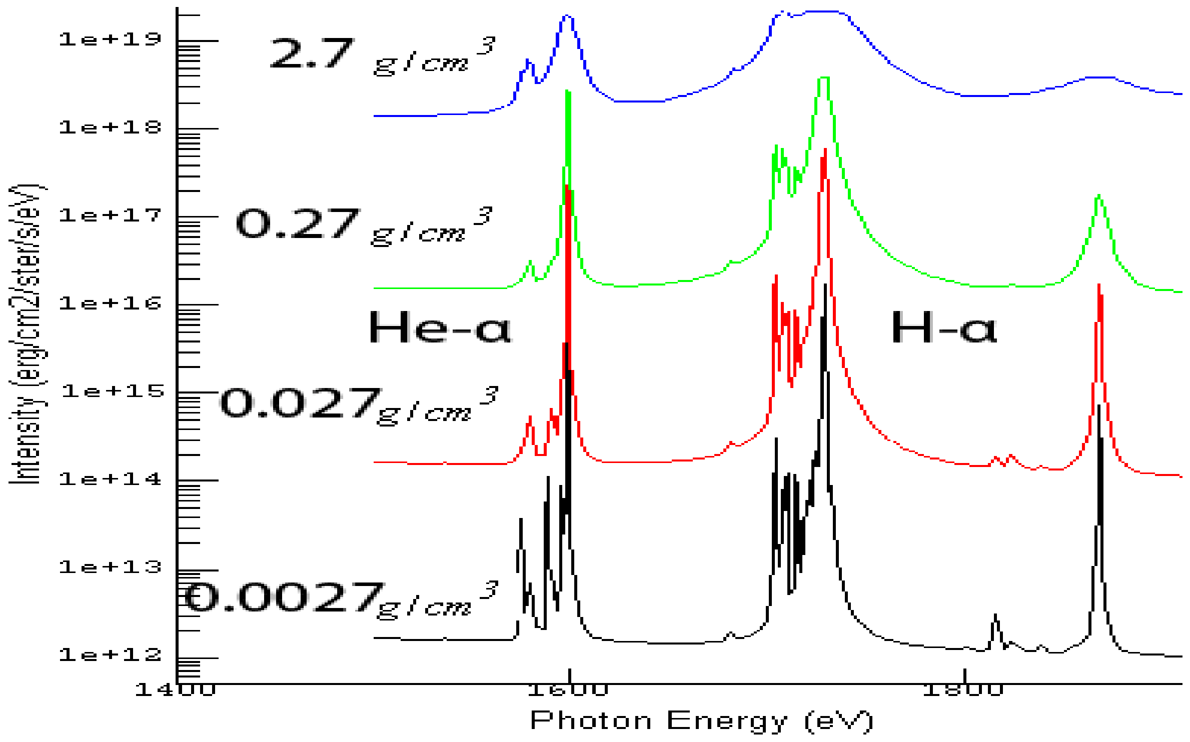

If we plot four more spectra at varying mass density, again, leaving all other parameters constant, we get spectra akin to those in Figure 6-2. The sheet is 10 µm thick, and the temperature is 800 eV. We display the starting mass density 2.7 g/cm^3, the density of aluminum at room temperature.

Notice that for every factor of ten with which the density decreases, the intensity decreases by a factor of one hundred. This observation makes sense, since ten times fewer particles are in the aluminum plasma, and, at the same time, the density is reduced while keeping the foil thickness constant. The second factor of 10 reduction is the result of the reduced collisional excitation rate at this lower density. Conversely, denser aluminum emits higher intensity K-shell lines.

Figure 6-3: Spectra from Aluminum foils at 0.027 g/cm^3 density and at kT=400 eV temperature plotted for various foil thicknesses differing by factors of 10.

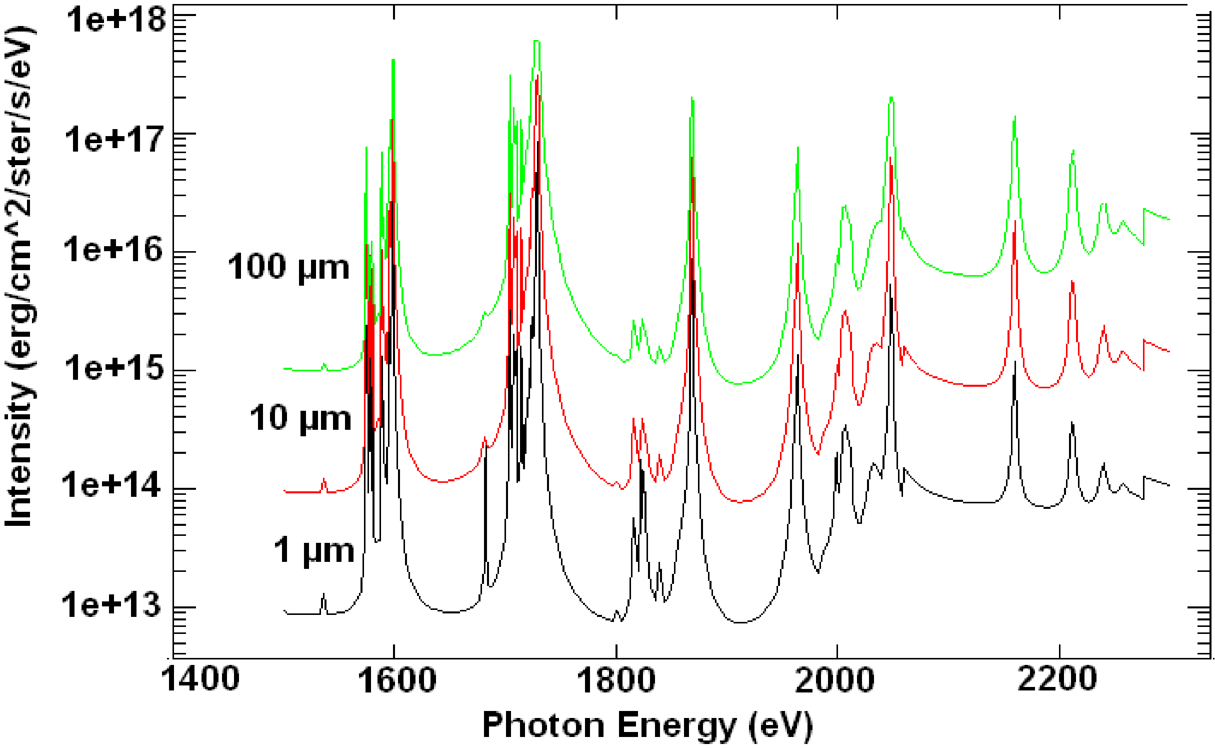

In Figure 6-3, we see three spectra at mass density 0.027 g/cm^3 and temperature kT=400 eV. Only thickness is varied. As the thickness of the aluminum increases by a factor of ten, so do the emitted spectral intensities. If density is constant and thickness is varied, then an increase in volume corresponds to an increase in mass with a proportional change in the number of emitting atoms.

One might expect the spectra to vary with thickness as the previous density spectra varied with density, and since both series show the variation of spectra with the number of particles. Here, the spectral intensities do rise by a factor of ten with ten times the number of emitting particles and nothing more, because the number of emitters increases at constant density without increasing the excitation rate.

7. Optimized Temperatures for an Al K-α Backlighter

Under the range of conditions considered here, the spectral intensities appear to increase without bound for high densities and large thicknesses. So, in order to maximize the emitting intensities, we need only to find the optimal temperatures for given densities and thicknesses. We know that we can only elevate a given quantity of aluminum to emitting temperatures, so we concentrate on the foils usually used, those with thicknesses between 4 μm and 20 μm. Below, Figures 7-1, 7-2, and 7-3 each concern a foil of different thickness.

With PrismSPECT we can plot the integrated intensities of a spectrum between any two chosen photon energies. If we choose energies between 1597 and 1599 eV, we isolate the K-α line intensities, in which we are interested. We can plot these integrated intensities against the plasma temperature of our Al foil to find the optimal temperatures for K-α emission.

Figure 7-1: Spectral intensities integrated over the range of energy 1597-1599 eV centered at the Al He-α line plotted as functions of the temperature of a 4 µm thick Al foil.

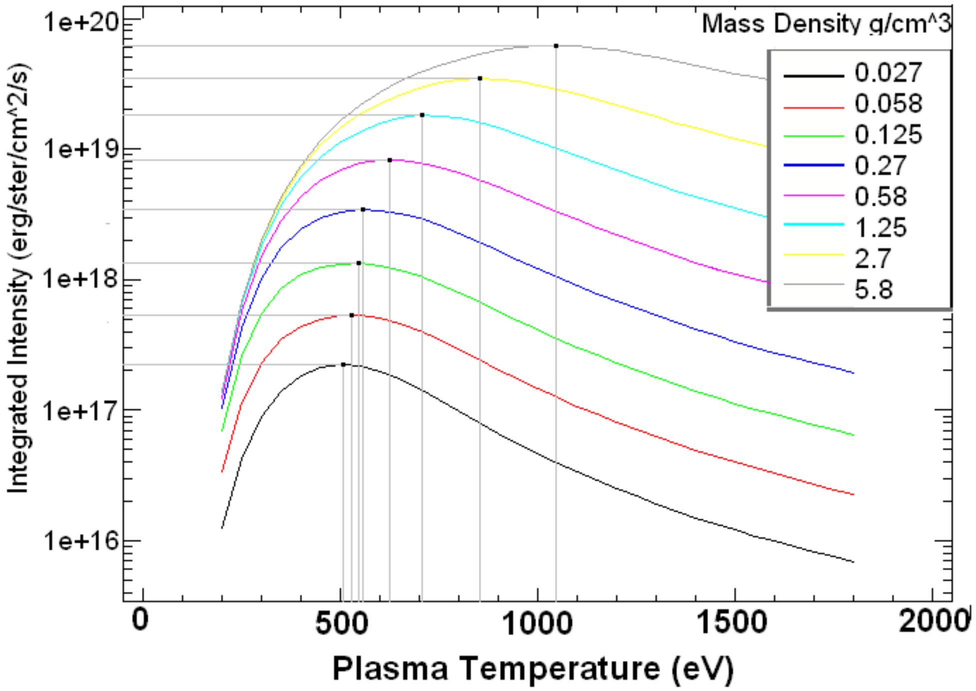

Figure 7-2: Spectral intensities integrated over the range of energy 1597-1599 eV centered at the Al He-α line plotted as functions of the temperature of a 10 µm thick Al foil.

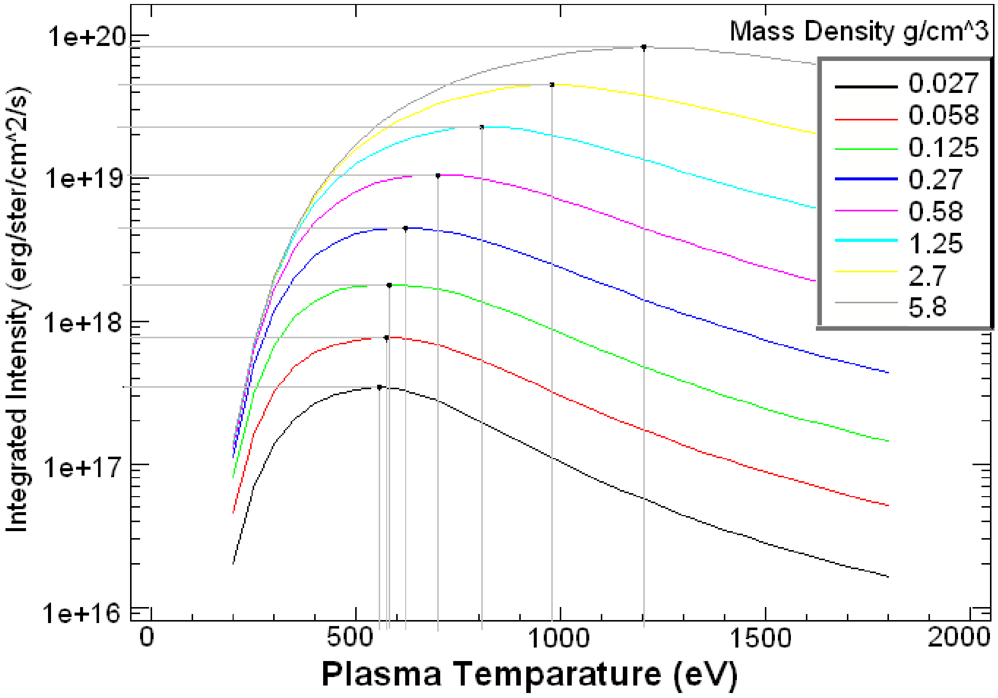

Figure 7-3: Spectral intensities integrated over the range of energy 1597-1599 eV centered at the Al He-α line plotted as functions of the temperature of a 20 μm thick Al foil.

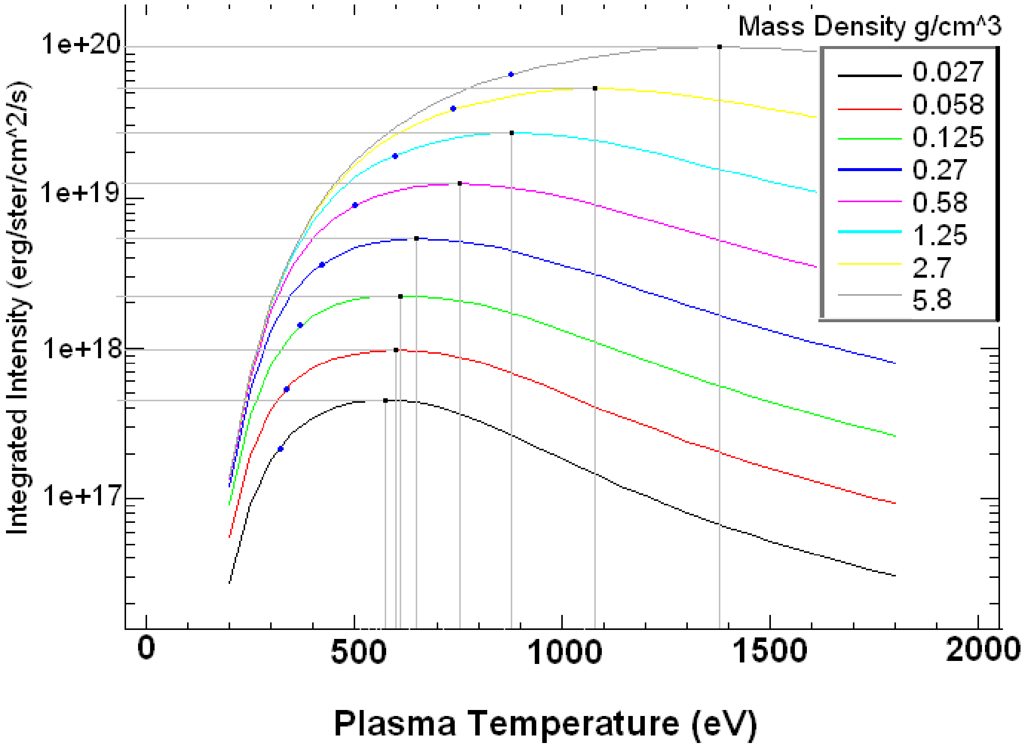

8. Conclusions

The study of Al H- α line intensities using PrismSPECT has thus far produced preliminary but useful results for optimizing emission-line backlighter sources. Within a plausible range of temperatures, densities, and foil thicknesses, the line intensity increases with the thickness of the foil at a given density and with the density of the foil at a given thickness. The limit on the amount of emitting material that can be brought to optimum emitting conditions will come from considerations such as the available backlight driver energy and the blackbody limit, which, thus far, has not been a significant limit in the cases considered here. While the line intensity increases with the source density, the optimum emitting temperature also increases with density, making increased demands on the backlight driver. Guided by the results obtained thus far, future work would include using hydrodynamic simulations of backlight foils to determine the feasibility of obtaining optimum emitting conditions, including time-dependent atomic population calculations to verify that emitting conditions can be attained within the lifetimes of the hot plasmas.

Acknowledgements

I would like to thank my adviser Dr. Reuben Epstein for guiding me through my project, Dr. Stephen Craxton for accepting me into the program, and all of the other students at LLE's Summer Internship for High School Juniors for being great friends.

References

1. Craxton, R. S., R. L. McCrory, and J. M. Soures, *Progress in Laser Fusion*, Scientific American, Vol. 255, 68-79. August 1986.

2. An Introduction to Radiative Transfer, Annamaneni Peraiah, 1987 Cambridge University Press.

3. Foundations of Radiation Hydrodynamics, Dimitri Mihalas and Barbara Weibel-Mihalas, 1984 Oxford University Press

4. Stellar Atmospheres, Dimitri Mihalas, 1978 W H Freeman & Co.

5. Radiation Hydrodynamics, John I. Castor, 2004 Cambridge University Press.

6. PrismSPECT, Prism Computational Sciences, Inc., http://www.prism-cs.com/

7. Macfarlane, Joseph, et al. *PrismSPECT and SPECT3D Tools for Simulating X-ray, UV, and Visible Spectra for Laboratory and Astrophysical Plasmas*, American Physical Society, May 2003.

The Effects of Space Charge on Electron Pulse Broadening in Streak Cameras

Brian Wang

The Effects of Space Charge on Electron Pulse Broadening in Streak Cameras

Brian Wang

Webster Thomas High School

LLE Advisors: Paul Jaanimagi and Jason Myatt

Abstract

Streak cameras are used to record the time history of laser pulses and experimental signals at LLE. However, space charge effects can distort images recorded on the phosphor screen of streak cameras, making it difficult to impossible to accurately interpret the image. Space charge effects are caused by the interactions between the photoelectrons while in transit in the streak tube. These interactions cause the electrons to repel, making the entire pulse broaden. For this project, a computer program was written to simulate the movement of electrons through the streak camera. This program enables one to accurately predict the amount of space charge broadening that would occur with given initial conditions for a particular design. This predictive capability will lead to improvements in streak cameras in the future, allowing streak cameras to record pulses with sub-picosecond temporal resolution.

Introduction

Streak cameras are essential for the work done at the Laboratory for Laser Energetics (LLE) at the University of Rochester. Streak cameras measure the time history of pulses by converting the temporal dimension into a spatial dimension. In a standard streak camera at LLE, a laser pulse is first converted into electrons at the photocathode via the photoelectric effect.

These electrons then go through a short accelerating region, in which they spend < 100 picoseconds. For the next 2 to 3 nanoseconds, the electrons pass through an electron lens, which focuses them. The electrons then enter a drift region that includes a pair of deflection plates, which have a time-varying electric field applied between them. This time-varying electric field deflects the electrons sideways; electrons later in the pulse are deflected more than electrons earlier in the pulse. As a result, the electrons develop a streak pattern. Finally, after a two to three nanoseconds flight time in the drift region, the electrons hit a phosphor screen, which converts the electron energy back into photons. The phosphor screen is connected to a charge-coupled device (CCD), which is used to electronically record the streak pattern. Since the photoelectric effect linearly converts photons into electrons, the number of electrons incident on any spot on the image recorded on the phosphor screen is proportional to the intensity of the laser pulse at that time (see Figure 1).

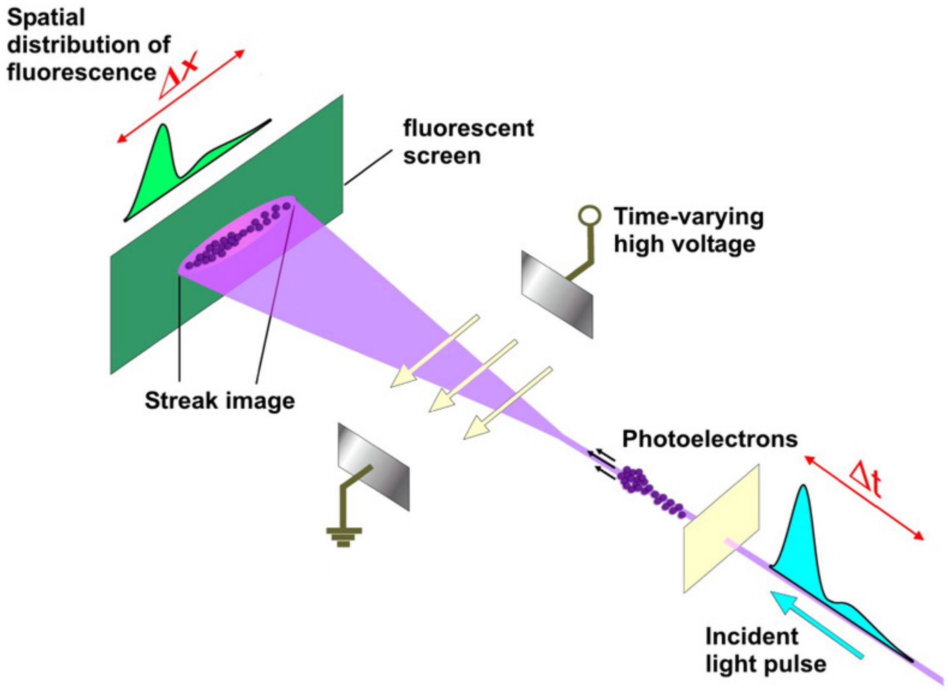

Figure 1- Diagram of a simple streak camera. More electrons on the phosphor screen corresponds to a greater intensity in the laser pulse.

Electrostatic repulsion between the electrons (termed the space charge effect) affects all electron beams. Although a 100 fs space charge broadening of a nanosecond duration pulse may not be measureable, it would be a significant distortion on a picosecond duration pulse. When the electrons inside a streak camera repel each other, the electron pulse broadens in all three spatial dimensions, and the information carried by these electrons can be distorted, since the electrons will not end up at their projected positions on the phosphor screen. Since space charge is a nonlinear effect, information about the original pulse cannot generally be recovered. Other considerations such as initial electron energy spread can also cause distortions of the image recorded on the phosphor screen, but the main problem addressed here is the electron pulse broadening due to space charge.

Past Work

In the past, models were created to simulate the movement of electrons through the drift region of a streak camera. One of these models is a one-dimensional fluid model.[1] This model ignores the movement of electrons in the radial direction, assuming that magnetic coils in the streak camera will constrain the motion to the axial direction. However, no such magnetic coils are used in LLE streak cameras, and so the one-dimensional fluid model is not a good model for LLE streak cameras. This model predicts that the temporal broadening Δt due to space charge in the drift region scales as

$$\Delta t \propto \frac{L^2 N}{V^{3/2} r^2} \qquad (1)$$

where L is the length of the region, N is the number of electrons in the pulse, V is the initial potential, and r is the radius of the pulse. However, this seems to fit only for short periods of time, since only then could one safely assume a constant radius. Other models that allow the electrons to move radially are more reliable.

Another model used in the past was the mean-field model, which included movement in the radial direction.[2] This model is expected to give better agreement for an actual streak camera, but it assumes non-relativistic electrons, rather than the relativistic electrons common to streak cameras at LLE. So, although a better model than the one-dimensional fluid model, the mean-field model does not perfectly represent what happens in an actual streak camera. Also, this mean-field model was only useful for the drift region of a streak camera; external fields were not taken into account.

Methods

In order to improve a streak camera's resilience to the damaging effects of space charge, a program was written to simulate the movement of electrons through the drift region of a streak camera. It is in this region that electrons have the most time to interact with each other, hence broadening the electron pulse significantly. The electromagnetic interaction between electrons is given by the Lorentz force equation

$$F = q(E + v \times B) \qquad (2)$$

where F is the force felt by an electron, q is the charge of the electron, E is the electric field, v is the instantaneous velocity of the electron, and B is the magnetic field. The electrons are assumed to propagate primarily in the z direction; therefore, the magnetic field can be modeled by concentric circles around the z-axis. This magnetic field will have a negligible effect on the motion of the electrons given the small beam currents in a streak tube and was neglected.

The electric field surrounding a charge can be modeled with the equation

$$E = kq\left[\frac{e_{r'}}{r'^2} + \frac{r'}{c}\frac{d}{dt}\left(\frac{e_{r'}}{r'^2}\right) + \frac{1}{c^2}\frac{d^2}{dt^2}e_{r'}\right] \tag{3}$$

where k is Coulomb's constant, q is the charge of the electron, $\boldsymbol{e}_{r'}$ is the unit vector in the direction of r', r' is the displacement between two electrons at the retarded time t_R and c is the speed of light.[3] The retarded time is defined by $t_R = t - r'/c$. The third term, which is the radiation term, has been deemed negligible; the direction of the electrons will not change significantly, making the second time derivative of the unit vector nearly zero. The first term is a slightly modified version of Coulomb's law, and the second term is a correction due to the velocity of the electrons.

Since information can only be carried between electrons at the speed of light, there is a non-zero time taken for one electron to know of another's presence. As a result, the electric field is not calculated at the current distance, but at the distance at the retarded time, as indicated by r'. This causes a sharper leading edge in an electron pulse, and a sparser trailing edge. This effect is most pronounced when the electrons are moving near the speed of light; electrons in a streak tube are accelerated to between 0.2c and 0.3c.

In order to advance the electrons in the computer program, the leap-frog method of integration was used, with a second order degree of accuracy in the time step.

Results

The computer program was run many times, with varying numbers of electrons, beam dimensions, initial electron energy spreads, and distances traveled. First, it was run with no external fields applied, simulating the drift region. When the beam spread of the simulated electron pulse was plotted against time (see Figure 2), it was easy to see that space charge effects significantly broaden electron pulses in the drift region. The particular simulation whose results are shown in Figure 2 was run with 100 electrons, an initial beam energy of 2500 eV, and initial beam dimensions of 100 x 50 x 5 microns. The beam spread shown resulted in a temporal spread of about 3-4 picoseconds.

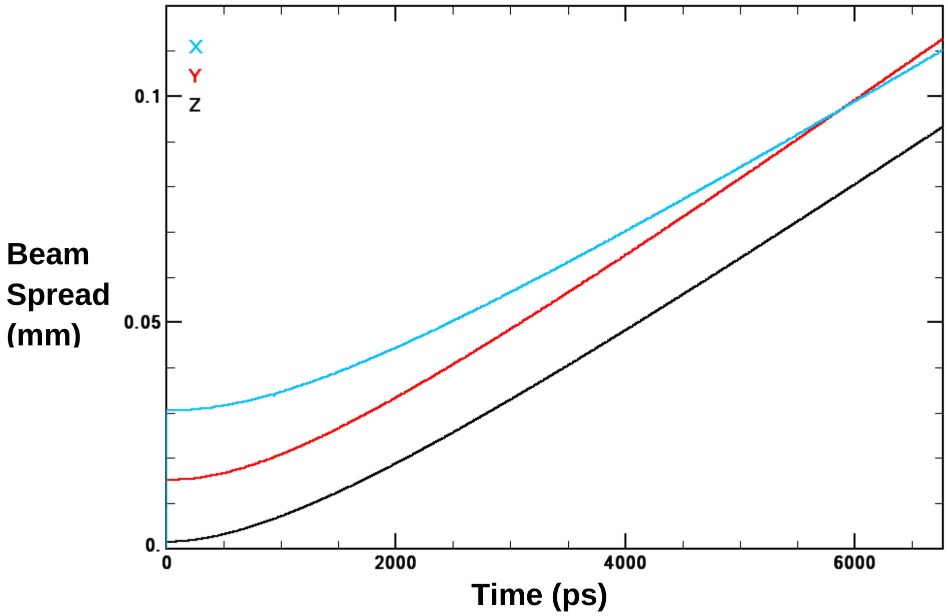

Figure 2-Beam spread plotted against time. As time goes on, the beam spread increases significantly in both the radial and axial directions due to space charge effects.

When the axial velocity was plotted against the axial position, it was evident that the leading electrons gained velocity, while the trailing electrons lost velocity, as shown in Figure 3. This occurs because the electrons in the front will be propelled even farther towards the front by space charge effects, while the electrons in the back will be repelled backwards.

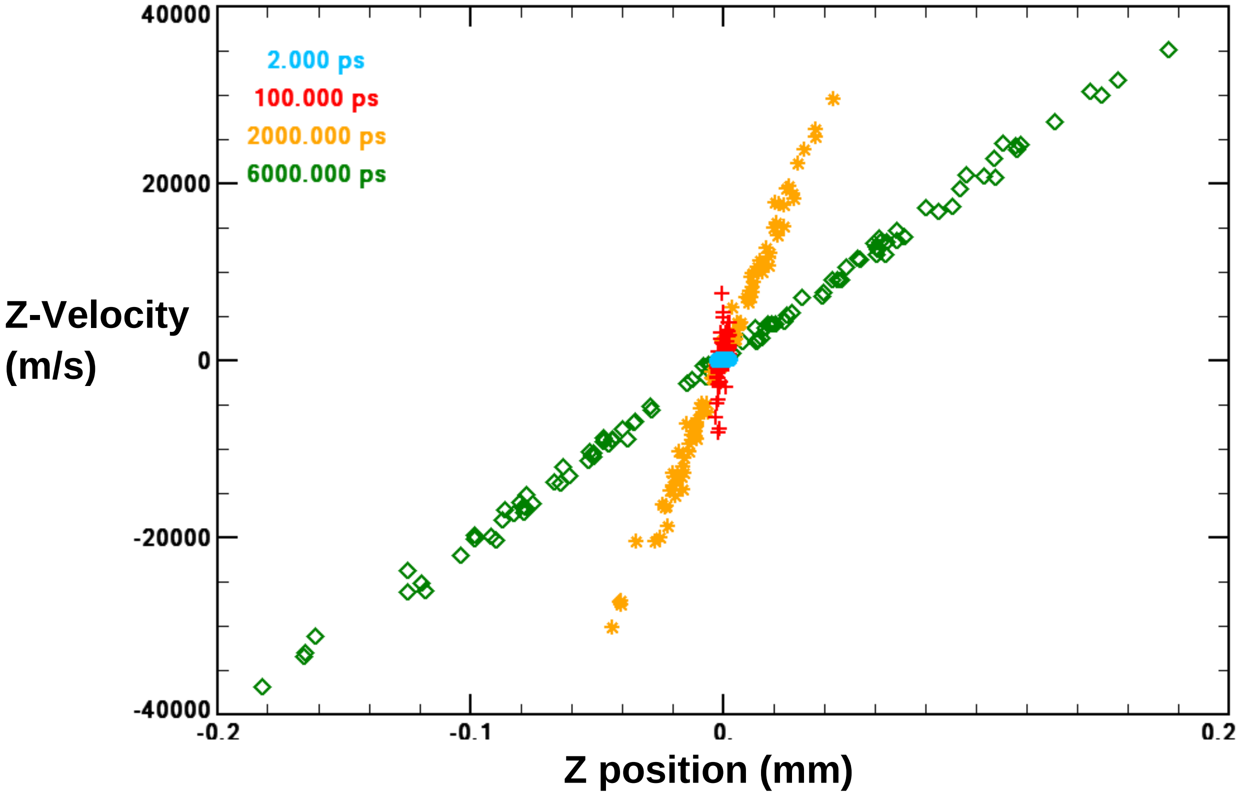

Figure 3-Relative axial velocity plotted against the average axial position for various times. Space charge very quickly generates a linear velocity chirp.

The one-dimensional fluid model predicted that the temporal broadening due to space charge in the drift region scaled as shown in Equation 1. However, analysis of the graphs given by different runs of the computer program shows that temporal broadening scales as

$$\Delta t \propto \frac{L\sqrt{N}}{\sqrt{V}} \qquad (4)$$

where *L* is the length of the region, *N* is the number of electrons in the pulse, and *V* is the initial potential. These scaling laws and other predictive capabilities of the computer program can be used to improve the limiting resolution in streak cameras.

Future Work

Although Figure 2 shows that space charge significantly broadens electron pulses in the drift region, no tests have yet simulated the electron pulse moving through the acceleration region of a streak camera. Simulated electrons could be run through a simple diode in order to confirm or reject the hypothesis that most of the electron pulse broadening due to space charge occurs in the drift region. Also the contribution of relativistic effects to the broadening of electron pulses in streak cameras has not been quantified in detail. The computer program could be run with the non-relativistic Coulomb interaction in place of Eqn. (3) in order to determine the importance of relativity. Similarly, it has only been theorized that the magnetic field and radiation will have negligible effects on electron pulse broadening. Magnetic fields and radiation could be added in to determine their effects on electron movement. More work could also be done to determine how much the beam dimensions of an electron pulse affect temporal broadening.

Instead of using the leap-frog method of integration, the Runge-Kutta method of integration could be used, since it has fourth order accuracy. However, the Runge-Kutta method requires significantly more computational overhead at each time step. The code for the computer program could be optimized further, so that more simulated electrons could be sent through a streak camera at a time, while keeping within a reasonable run-time. Finally, the predictions given by the computer program could be put to practical use through the physical improvement of streak cameras.

Conclusion

The effects of space charge can detrimentally distort the image recorded on the phosphor screen of a streak camera, making it impossible to recover information about the original laser pulse. In order to minimize the damaging effects of space charge, a computer program was written to simulate the movements of electrons through a streak camera. This computer program differs from previous attempts to model the movement of electrons through a streak camera through its inclusion of relativistic effects and its ability to include external fields. The program confirmed that significant broadening occurred in the drift region, and that the effects of space charge generate a linear velocity chirp. Scaling laws were produced that show how temporal broadening changes with the length of the drift region, the number of electrons, and the initial potential. Future work can be done in making the computer program more accurate, and yet more optimal. The predictions of this computer program will eventually be used to develop streak cameras with sub-picosecond resolution.

Acknowledgments

I would like to thank Dr. Paul Jaanimagi and Dr. Jason Myatt for their support throughout this program. Their mentoring and advice were invaluable to me. I would also like to thank Dr. Stephen Craxton for making this internship program available for me and many other high school students; we have undoubtedly gained much experience from this unique program.

References

1. B.-L. Qian and H.E. Elsayed-Ali, *Electron pulse broadening due to space charge effects in a photoelectron gun for electron diffraction and streak camera systems*, Journal of Applied Science, Vol. 91, No. 1, 462-468 (Jan 2002).

2. B.A. Siwick, J.R. Dwyer, R.E. Jordan, and R.J. Dwayne Miller, *Ultrafast electron optics: Propagation dynamics of femtosecond electron packets*, Journal of Applied Science, Vol. 92, No. 3, 1643-1648 (August 2002).
3. R. P. Feynman, R. B. Leighton and M. Sands, "*The Feynman Lectures on Physics*", Vol. 1, pp. 28-2, Addison-Wesley Publishing Company, Reading, Massachusetts (1977).

Automated Determination of Crystal Reflectivity in the X-ray Laboratory

Bradley Wideman

Automated Determination of Crystal Reflectivity in the X-ray Laboratory

Bradley Wideman
University of Rochester Laboratory for Laser Energetics
2008 High School Summer Research Program

INTRODUCTION

The University of Rochester's OMEGA laser [1] is used to research the conditions necessary for inertial confinement fusion. The OMEGA laser produces hot x-ray emitting plasmas when in operation and measurements of the x-ray emission are used to infer conditions in the plasma. One method of observing x rays produced using the OMEGA laser is diffraction by a crystal. The reflectivity of a crystal must be known to infer the absolute x-ray flux from the source. Examples of inferred absolute x-ray spectra obtained from target experiments on OMEGA are given in reference [2].

Crystals are used to diffract x rays. X-ray photons incident on a crystal are preferentially scattered in directions θ that obey the Bragg equation [3]

$$n\lambda = 2d\sin\theta \tag{1}$$

where n is the order of diffraction, λ is the x-ray wavelength, and d is the crystal spacing. The photon energy and wavelength are related by the Planck equation

$$E = \frac{hc}{\lambda} \tag{2}$$

where E is energy, h is Planck's constant, c is the speed of light and λ is the wavelength.

At specific angles, constructive interference (diffraction) occurs. The numbers of incoming and diffracted x-ray photons are measured at specific angles centered on the diffraction peak. Figure 1 shows the reflectivity of a crystal as a function of angle surrounding the Bragg angle. Typical Bragg diffraction peaks have widths of much less than 0.1°.

X rays are produced in the LLE X-ray Laboratory in the following manner: A filament is heated to a high temperature by an electric current thereby emitting electrons in a process known as thermionic emission [4]. A high voltage supply accelerates electrons from the filament towards a metal target. The electrons strike the metal and decelerate, causing x-ray photons to be emitted. The electrons decelerate by different amounts causing a broadband continuum spectrum of x rays to be emitted. Electrons sometimes collide with electrons that are bound within atoms, knocking the electron into a higher-energy bound state or an unbound state. The electrons return to their previous state, producing sharp x-ray peaks at specific energies[5], since electrons contained within atoms have specific energy states.

These x-ray peaks are useful for diffraction measurements because the x-ray photon energy, a parameter of the Bragg angle, is constant. X rays are collimated to minimize angular dispersion. The collimated beam must have a width less than the width of the crystal. A Lithium-drifted Silicon (Si(Li)) detector[6] is used to count diffracted photons. Stepper-motor-driven stages are used for position control. The reflectivity of a KAP (Potassium Acid Phthalate) crystal is determined in this work from measurements taken in the X-ray Laboratory. Other examples of absolute calibrations determined in the LLE X-ray Laboratory are given in references [7,8].

EXPERIMENTS

In order to measure crystal reflectivity, the following apparatus is used (Fig 2). An x-ray source as previously described is contained within a vacuum system. The x rays exit through a thin beryllium window (8.5 μm thick). The source is collimated by a pair of metal slits. The collimated x rays are incident upon a crystal which is mounted on top of 3 stepper-motor-driven stages. A detector is also attached to the stages. The entire path of the x rays after exiting the vacuum system is contained within a helium-filled bag. A viewing scope is placed behind the crystal for alignment purposes.

(a) X-ray Source

The x-ray source is contained within the vacuum system and consists of a filament and a target. Electrons are ejected from the filament through thermionic emission [4] and are accelerated by a 10 kV voltage. A magnet is used to direct the electrons to the target. The bent path minimizes ion contamination from the tungsten filament. In this case, the electrons are incident on a water-cooled aluminum target, producing both broadband x-ray radiation and an Al Kα peak at 1.486 keV.

(b) Collimation

Two slits are used to collimate the x rays. The angular dispersion of a 2-slit collimator can be calculated using the following equation:

$$\theta = 2\tan^{-1}(\frac{d}{x}) \tag{3}$$

where d is the width of the slits and x is the distance between them. A 0.003 inch (76.2 μm) by 10 mm slit is placed near the x-ray source. This slit is assembled by gluing 2 thin metal pieces, separated by 0.003 inch shim material, to a circular aperture. A 0.003 inch (76.2 μm) by 4 mm slit is placed 1.67 m from the first slit, just outside the vacuum system. This slit consists of a micrometer set to the correct width. The angular dispersion in the horizontal direction is calculated to be 0.0052.º The exit slit height is restricted to 4 mm by placing lead tape over the micrometer.

(c) Helium Bag

Once x rays exit the vacuum system they must pass through a gas without excessive attenuation. The transmission T of x rays can be calculated by the following equation:

$$T = \exp[-\mu_{\rho}(E)\rho x] \tag{4}$$

where μ_ρ is the energy-dependent mass absorption coefficient, ρ is the density, and x is the distance. Nitrogen, a major component of air, transmits only 25% of x-ray radiation per centimeter at about 1.5 keV (the energy used in this experiment). Helium transmits 99.7% of x-ray radiation per centimeter at 1.5 keV. Both transmisssions are calculated using tabulated values of μ_ρ given in Henke et al. [9] The x rays must travel about 40 cm outside the vacuum system. Over that distance, nitrogen transmission is essentially zero, while helium transmission is 88.7%. As a consequence, to minimize attenuation, the path of the x rays outside of the vacuum system is contained within a helium-filled bag.

(d) Diffraction

The x rays are diffracted by a potassium acid phthalate (KAP) crystal. This crystal has a 2d spacing of 26.632 Å. [9] The Bragg diffraction angle for the Al Kα peak (at 1.486 keV corresponding to 8.34 Å) is calculated to be 18.25.°

(e) Si(Li) Detector

The Si(Li) detector is used to measure the intensity and energy of the diffracted x rays. The Si(Li) detector must be cooled to 77 K with liquid nitrogen to operate properly. The detector produces a pulse for each x-ray photon that it detects. The height of the pulse is proportional to the energy of the photon. The detector is connected to a multichannel analyzer which records the number of counts per energy interval. See the description of Si(Li) detectors and associated electronics given by Knoll [6]. The detector is effectively 100% efficient for photons transmitted through its entrance window (25.4 μm thick Be). For reflectivity measurements, where the ratio of the number of counts incident to reflected is measured with the same detector, no error is introduced.

(f) Positioning Apparatus

Three stepper-motor-driven stages are used to enable accurate positioning of the crystal and the detector (Fig. 2). The linear stage (motor A) controls the horizontal position of both the Si(Li) detector and the crystal. The rotary stages control the angular position of the Si(Li) detector and the crystal. The stages are arranged on top of each other so that the bottom stage (motor B) rotates both the detector and the crystal while the top stage rotates only the crystal. Rotary stages have a position accuracy of 0.01° per step and the linear stage has an accuracy of 0.0001 inch (2.54 μm) per step. This must be taken into account when performing experiments.

(g) Alignment

Two methods are used to align the three stages. The first method is optical alignment. A viewing scope is positioned along a line containing the x-ray source. The scope is positioned such that light passing through the rear collimation slit can be seen by the viewing scope. The positions of stepper-motor-driven stages are initially aligned by the viewing scope to visually determine when the crystal rotary axis is on a line with the collimator. Alignment is accomplished as follows: First the crystal (motor C) is rotated until it is deemed parallel by viewing through the scope. The linear stage (motor A) is then moved until the crystal edge is centered within the viewing scope. Finally, the detector (motor B) is rotated until it appears centered within the scope. The second method of alignment uses the x-ray detector. Each motor is moved in small increments, and the x-ray count rate is recorded at each location. The correct location for the linear stage (motor A) is the location at which the count rate is one-half the maximum (half of the photons should be blocked by the crystal). The correct locations for the rotary stages are the locations at which the count rate is at a maximum. This method is used for rough initial alignment and later refined during the Bragg angle scan.

(h) Stepper Motor Software

The stepper motors are controlled by programmable controllers with built-in inputs and outputs [10]. These inputs and outputs are connected through use of a patch panel, allowing the motors to communicate with each other. The motor controllers are programmed to make all moves automatically, but the software used to record photon spectra with the Si(Li) detector is separate. Thus the entire process is semi-automatic requiring input from the experimenter. Whenever a spectrum measurement is taken, the motor controllers wait for the user to manually take the measurement and flip a momentary switch to signify completion. The program takes measurements of the spectrum at specific angles centered on the predicted location of the Bragg peak. Spectral measurements are also taken of the non-diffracted x-ray beam at the beginning, middle, and end of the diffraction measurements. The actual program instructions are listed in the Appendix.

(i) Measurements

X-ray spectra are measured over a range of angular positions surrounding the nominal Bragg angle. A spectrum consists of the number of photons that are detected at various photon energies during a period of 30 seconds. The undiffracted beam spectrum is captured with the crystal moved out of the x-ray path (Fig. 3). Spectra are taken with the crystal at 0.02° steps ±0.2° from the Bragg angle (Fig. 4). Each spectrum is saved to a file using the ORTEC Maestro [11] multichannel analyzer software, for later processing.

Measurements are taken in a specific order. First, the undiffracted beam is measured, followed by the first half of the Bragg angle scan. Then, the undiffracted beam is measured again, followed by the second half of the Bragg angle scan. A third and final undiffracted beam measurement is made to complete the measurements.

RESULTS

The integrated reflectivity of a crystal is calculated using the recorded spectra. The results are shown in table 1. The integrated reflectivity is initially calculated in the following manner. The integral number of counts of every spectrum is determined in the region containing the Al Kα line. This is shown in the second column of Table 1. The energy range is chosen such that as much as possible of the Al Kα is included, but as little noise and non-Al Kα is included as possible. The integrals of the undiffracted spectra varied significantly over time. Because of this the reference integrals are fitted to a parabola to model the change over time. (Fig. 5) The reflectivity can be calculated at each angular position by dividing the counts at that position by the computed undiffracted counts at that time. The reflectivity as a function of angle determined by this method is given in Table 1 column 4. The integrated reflectivity is calculated by summing the measured reflectivities and multiplying by the step size (0.349 milliradians). The integrated reflectivity is found to be 0.0798 milliradians.

In order to refine the calculation of the integrated reflectivity, the spectra are fitted to a Gaussian

$$f(x) = \frac{1}{\sqrt{2\pi\sigma^2}} \exp\left(\frac{-(x-\mu)^2}{2\sigma^2}\right) \tag{5}$$

where x is the angular position, μ is the mean, and σ is the standard deviation. The NLINLSQ routine [12] is used to fit the data to the sum of a Gaussian distribution and a quadratic. Figure 6 shows an example fit to the Al Kα line and a quadratic representing non-Al Kα counts of the undiffracted beam while Figure 7 shows an example fit to a diffracted spectrum. The integral is taken only of the Gaussian, eliminating contributions due to electronic noise and broad-band (continuum) radiation. The Gaussian integral of each spectrum is given in Table 1 column 3. The integrated reflectivity is determined from the ratio of these revised values. The resulting reflectivities are given in Table 1 column 5 and are plotted as a function of angle from the Bragg peak in Figure 8. The revised integrated reflectivity is calculated to be 0.0878 milliradians. The error in this value is determined from the variation of the reflectivity at the peak of the diffraction scan determined from two repeated measurements. A 17% variation is noted resulting in an uncertainty in the integrated reflectivity of ±0.015 milliradians.

The revised method for calculating the integrated reflectivity has a larger value due to the removal of continuum background from the undiffracted spectrum. The diffracted peaks contain little background noise and only decrease slightly when background is removed from the integrals. This results in a higher value for the integrated reflectivity.

In Figure 9, the integrated reflectivity of the KAP crystal at 1.48 keV is compared to two KAP integrated reflectivity graphs given in Henke et al [9]. Figure 9 shows two theoretical models of the KAP crystal, the mosaic and the perfect. All real crystals should have an integrated reflectivity between the theoretical models. The integrated reflectivity of the KAP crystal determined in this work compares favorably with previously determined values shown as black symbols in Figure 9.

CONCLUSIONS

The integrated reflectivity of a KAP crystal has been measured and compared to published values. This data can be used as a basis for further work with the crystal. Stepper motor controllers have been programmed to automate the stepper motor motion and reduce the amount of human input required to measure x-ray diffraction. This program can be used to simplify future experiments and can also be used as a basis for additional automation.

ACKNOWLEDGEMENTS

I would like to thank all of the LLE staff for their generous support. I would specifically like to thank Dr. Frederic J. Marshall for helping me to complete my research, and Dr. Stephen Craxton for giving me the opportunity to participate in this research.

REFERENCES

1. T. R. Boehly, D. L. Brown, R. S. Craxton et al., Opt. Commun. 133, 495 (1997).

2. B. Yaakobi et al., Phys. Plasmas. 4, 3021 (1997).

3. B. D. Cullity, S. R. Stock. Elements of X-ray Diffraction, Third Edition. (Prentice Hall, Inc., Upper Saddle River, NJ, 2001), pp.89-96.

4. B. D. Cullity, S. R. Stock. ibid pp.19-26.

5. B. D. Cullity, S. R. Stock. ibid pp.7-11.

6. Knoll, Glenn F. Radiation Detection and Measurement. (John Wiley & Sons, Inc., New York, 2000) pp. 457-476.

7. F. J. Marshall et al., Rev. Sci. Instrum. 77, 10F308 (2006).

8. F. J. Marshall, J. A. Oertel. Rev. Sci. Instrum. 68, 735 (1997).

9. B. L. Henke, E. M. Gullikson, J. C. Davis. Atomic Data and Nuclear Data Tables. 54, 181-342 (1993).

10. IM483I built by Intelligent Motion Systems, Inc. Taftville, CT 06380.

11. Applied Measurement Technology, ORTEC. Oak Ridge, TN 37831.

12. Visual Numerics, Inc. Houston, Texas 77042.

APPENDIX

This appendix describes the stepper motor program that is used for the diffraction measurements.

Inputs / Output Patch Panel:

A OUT 3 → B IN 2
B OUT 3 → C IN 2
B OUT 1 → A IN 1

Program Operation:

Action to perform	Switch to flip after action has been completed
	GO c, b, a
Take Beam Measurement	Return a
Take Diffraction Measurement	Return b
Take Diffraction Measurement	Return b
…	
Take Diffraction Measurement	Return b
Take Beam Measurement	Return c, b, a
Take Diffraction Measurement	Return b
Take Diffraction Measurement	Return b
…	
Take Diffraction Measurement	Return b
Take Beam Measurement	Return a

Motor Controller A Code:

	Instruction	Comment
`0`	`-400.`	Moves crystal out of path so a beam measurement can be taken
`5`	`W0`	Wait for move to complete
`8`	`L2048 5`	Waits for return switch; a beam measurement is taken at this time.
`12`	`+400.`	Returns crystal to original location
`17`	`W0`	Wait for move to complete
`20`	`A32`	Tells controller b to begin sweep by sending a 100ms high pulse from controller a out 3 to controller b in 2.
`22`	`W10`	
`25`	`A0`	
`27`	`L2048 0`	Waits for a high on input 1; this signifies that controller b is done with the sweep.
`31`	`J0 2`	Runs the entire program 2 more times: 1 for the 2nd sweep and 1 only for the final beam measurement.
`35`	`P`	End of Program

Motor Controller B Code:
NOTE: Figure A-1 is a flowchart describing the operation of lines 0-16.

```
      Instruction   Comment
0     L19 3         If input 2 is high jump to line 19.
                    This occurs when controller a signals that the beam measurement is
                    complete and a sweep should begin.
4     L0 5          If return switch is flipped continue, else go back to the beginning.
                    If the return switch is flipped at this point it signals the program
                    that this is the 2nd time it is being run and it should move an
                    additional distance so that the 2nd sweep starts where the 1st sweep
                    left off.
8     +40.          This is the extra move that occurs only before the 2nd sweep.
13    W20           Waits 200 ms to prevent accidental repetition.
16    G0            Returns to beginning.
19    +3600.        Begins sweep by moving into position for the 1st measurement.
24    A32         }
26    W10         } Sends a 100 ms high pulse to controller c.
29    A0          } This tells c to do whatever b just did.
31    W100          Waits 1 sec to prevent accidental repetition.
34    L2048 5       Waits for return switch.
                    This signifies that the spectrum has been recorded.
38    +4.           Moves the motor a small amount so that the next measurement can
                    be taken.
43    j24 9         Repeats lines 24-38 9 more times (for a total of 10)
                    This allows 11 measurements to be taken.
47    W100          Waits 1 sec to prevent accidental repetition.
50    A32         }
52    W10         } Sends a 100 ms high pulse to controller c.
55    A0          } This tells c to do whatever b just did.
57    L2048 5       Waits for return switch.
                    This signifies that the final measurement is complete.
61    A32
63    W10           Sends a 100ms high pulse to controllers a and c.
66    A8            This tells controller a that the sweep is complete.
68    W10           This tells controller c to return to angle 0.
71    A0
73    -3640.        Returns motor to original location.
78    W0            Waits for motor to finish moving.
81    J0 1          Runs entire program again for 2nd sweep
85    -40.          Moves back extra for 2nd sweep only.
90    P             End of Program
```

Motor Controller C Code:

NOTE: Figure A-1 is a flowchart describing the operation of lines 0-16.

	Instruction	Comment
0	`L19 3`	If input 2 is high jump to line 19. This occurs when controller a signals that the beam measurement is complete and a sweep should begin.
4	`L0 5`	If return switch is flipped continue, else go back to the beginning. If the return switch is flipped at this point it signals the program that this is the 2nd time it is being run and it should move an additional distance so that the 2nd sweep starts where the 1st sweep left off.
8	`+40.`	This is the extra move that occurs only before the 2nd sweep.
13	`W20`	Waits 200 ms to prevent accidental repetition.
16	`G0`	Returns to beginning.
19	`+1800.`	Begins sweep by moving into position for the 1st measurement.
24	`W100`	Waits 1 sec to prevent accidental repetition.
27	`L2048 2`	Waits for signal from controller b. This signifies that the spectrum has been recorded.
31	`+2.`	Moves the motor a small amount so that the next measurement can be taken.
36	`W100`	Waits 1 sec to prevent accidental repetition.
39	`j27 9`	Repeats lines 27-36 9 more times (for a total of 10) This allows 11 measurements to be taken.
43	`L2048 2`	Waits for signal from controller b. This signifies that the final spectrum has been recorded.
47	`-1820.`	Returns motor to original location.
52	`W0`	Waits for motor to finish moving.
55	`J0 1`	Runs entire program again for 2nd sweep
59	`-20.`	Moves back extra for 2nd sweep only.
64	`P`	End of Program

Diffracted Spectra

Position (degrees)	Counts		Reflectivity	
	Sum	Fit	Original	Revised
-0.20	23	20	0.0010	0.0010
-0.18	67	90	0.0024	0.0035
-0.16	242	265	0.0072	0.0087
-0.14	446	436	0.0123	0.0132
-0.12	109	133	0.0026	0.0035
-0.10	114	127	0.0025	0.0030
-0.08	156	191	0.0030	0.0040
-0.06	231	261	0.0045	0.0055
-0.04	535	541	0.0091	0.0100
-0.02	2732	2675	0.0432	0.0458
0.00a	6454	6435	0.0986	0.1064
0.00b	9125	9009	0.1268	0.1355
0.02	1207	1189	0.0163	0.0174
0.04	356	376	0.0047	0.0053
0.06	177	226	0.0023	0.0031
0.08	123	139	0.0015	0.0019
0.10	76	84	0.0009	0.0011
0.12	44	75	0.0005	0.0010
0.14	51	75	0.0006	0.0009
0.16	39	60	0.0004	0.0007
0.18	32	11	0.0004	0.0001
0.20	41	60	0.0004	0.0007
Reflectivity Sum			0.2287	0.2514

} repeated measurements

Un-diffracted Spectra

	Counts	
Time	Sum	Fit
11:33	16455	14846
11:53	67682	62507
12:08	96083	89039

Table 1 – Summary of experimental measurements.

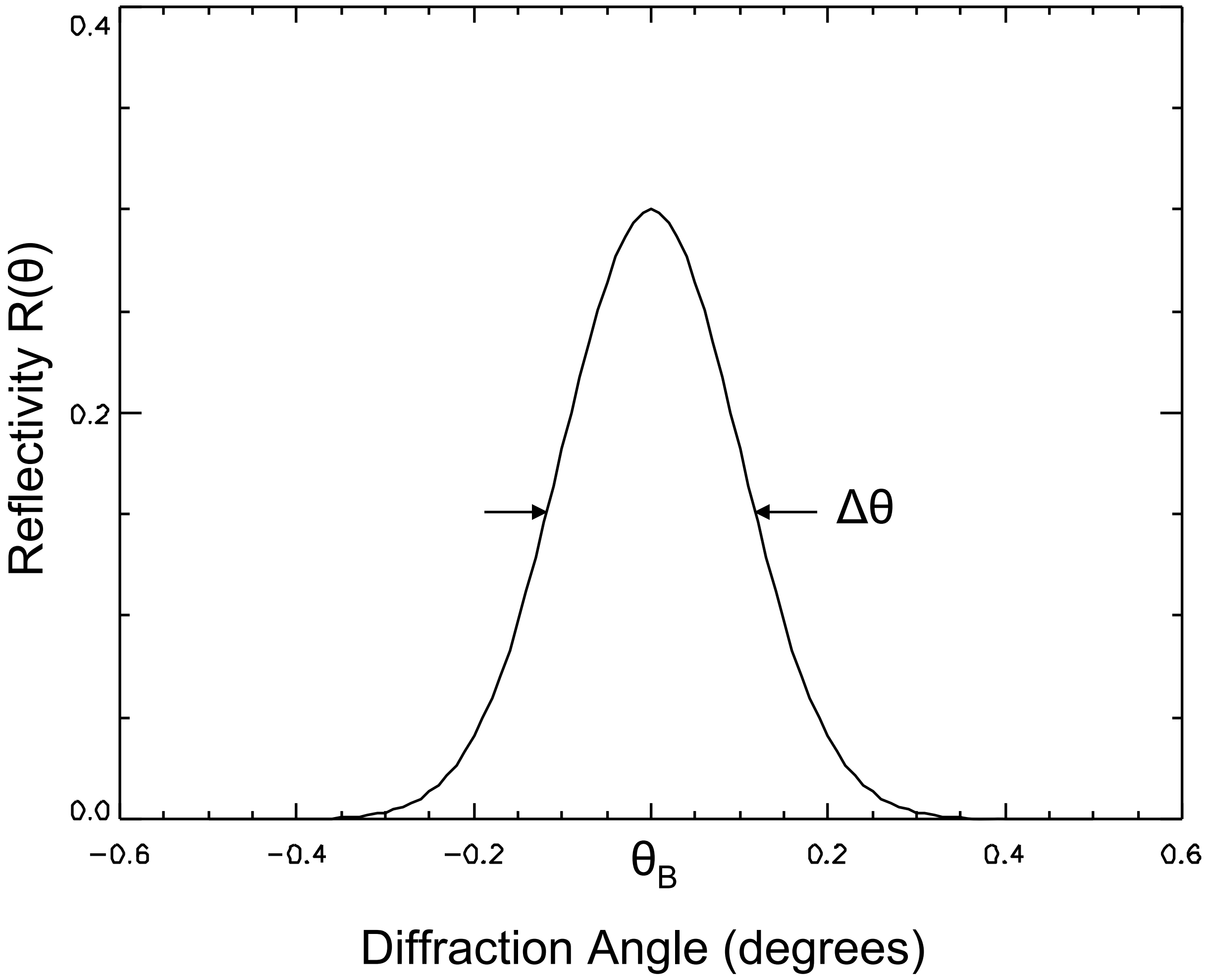

Figure 1 – An idealized example of a Bragg diffraction peak.

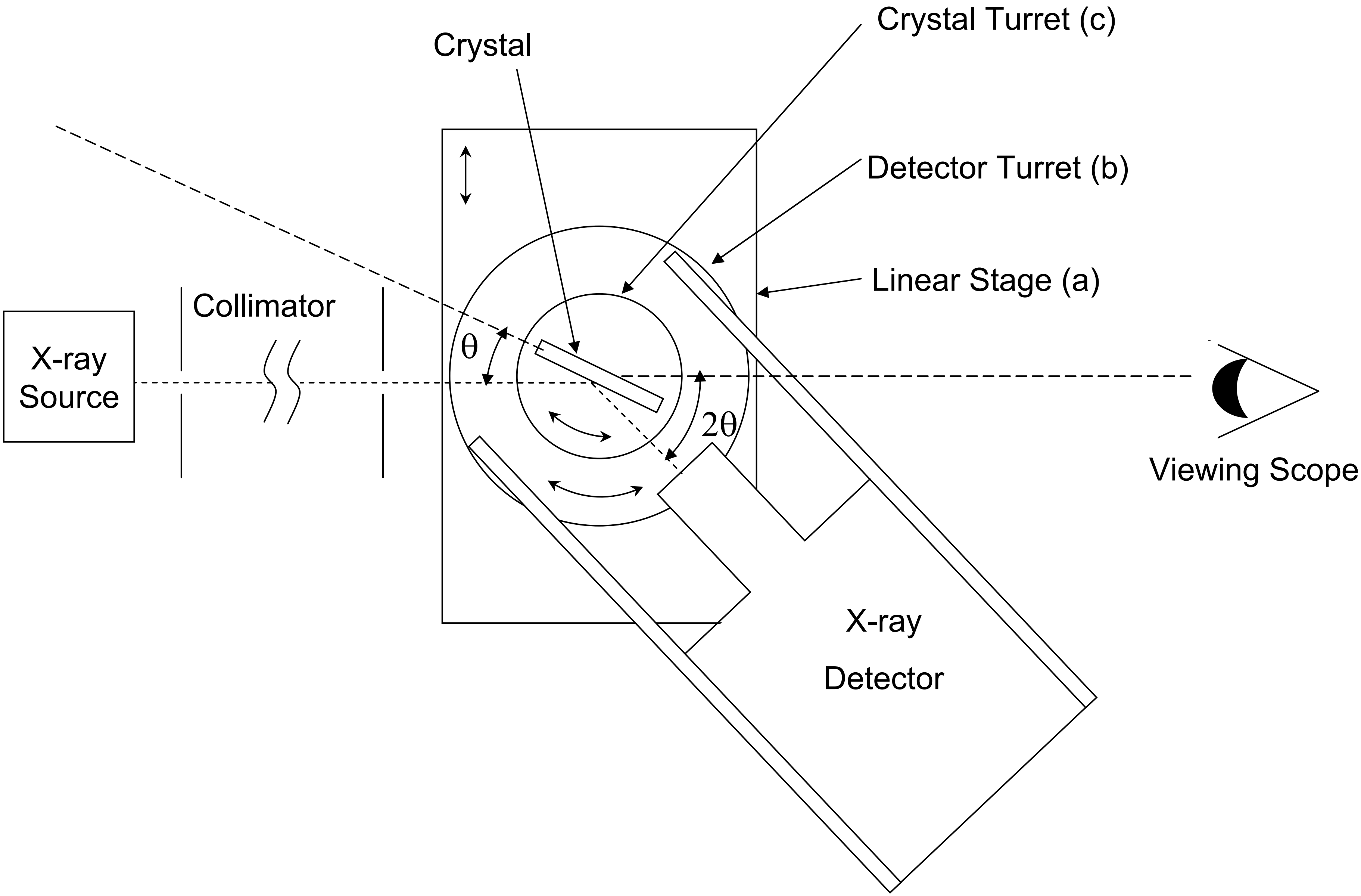

Figure 2 – Diagram of the equipment used for the x-ray diffraction experiment.

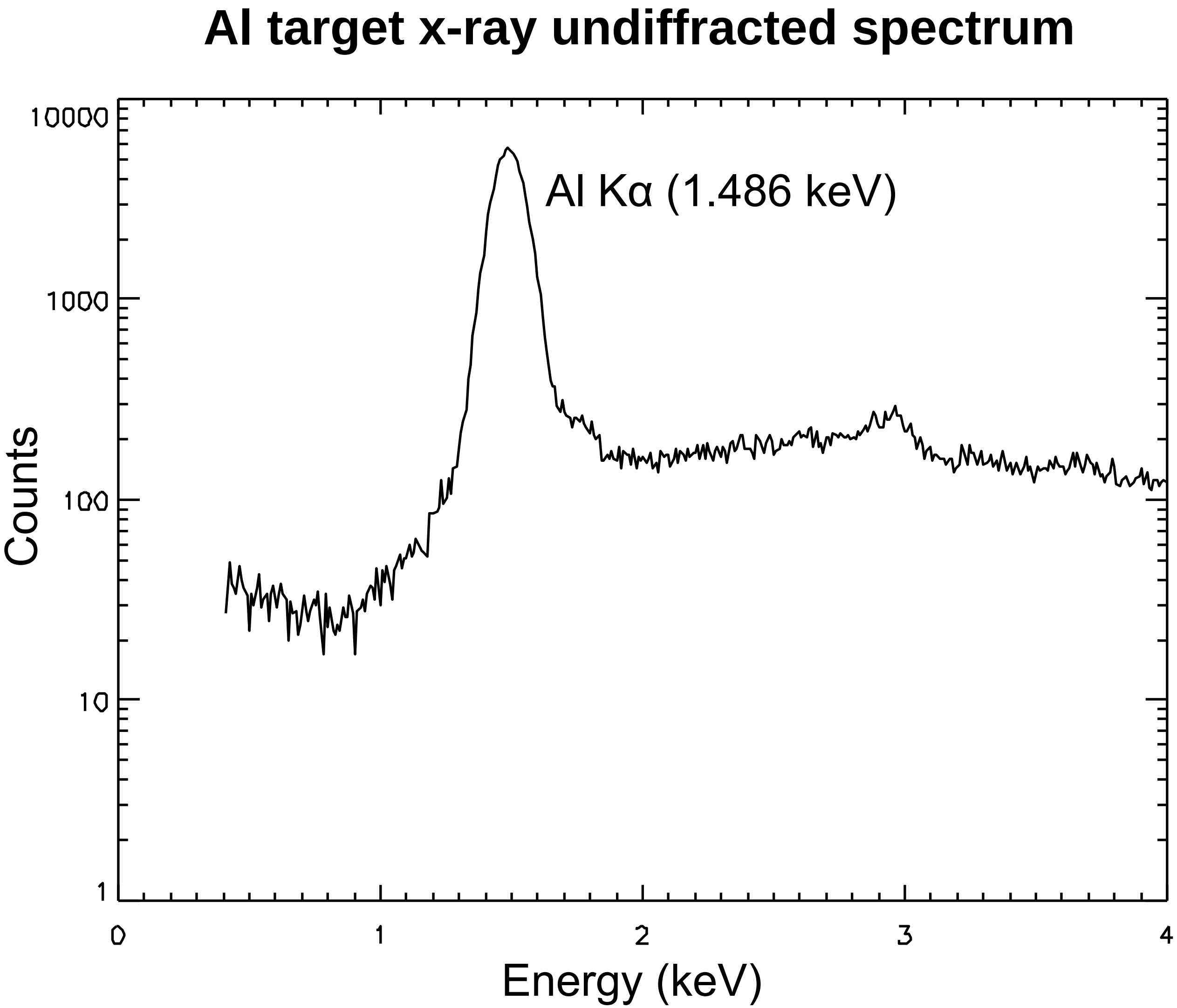

Al target x-ray undiffracted spectrum

Figure 3 – Spectrum of the undiffracted beam.

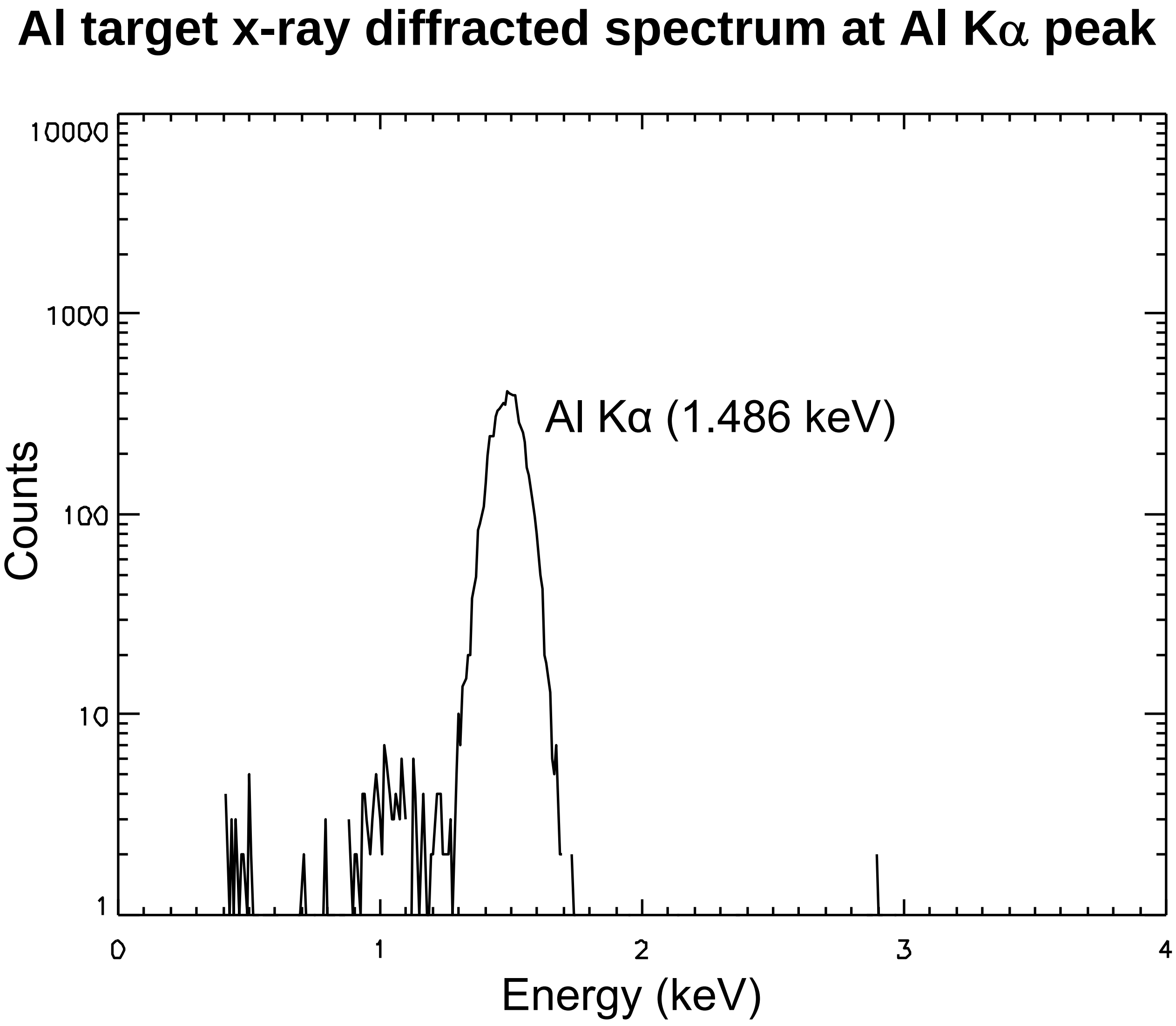

Figure 4 – X-ray spectrum of the KAP diffracted beam.

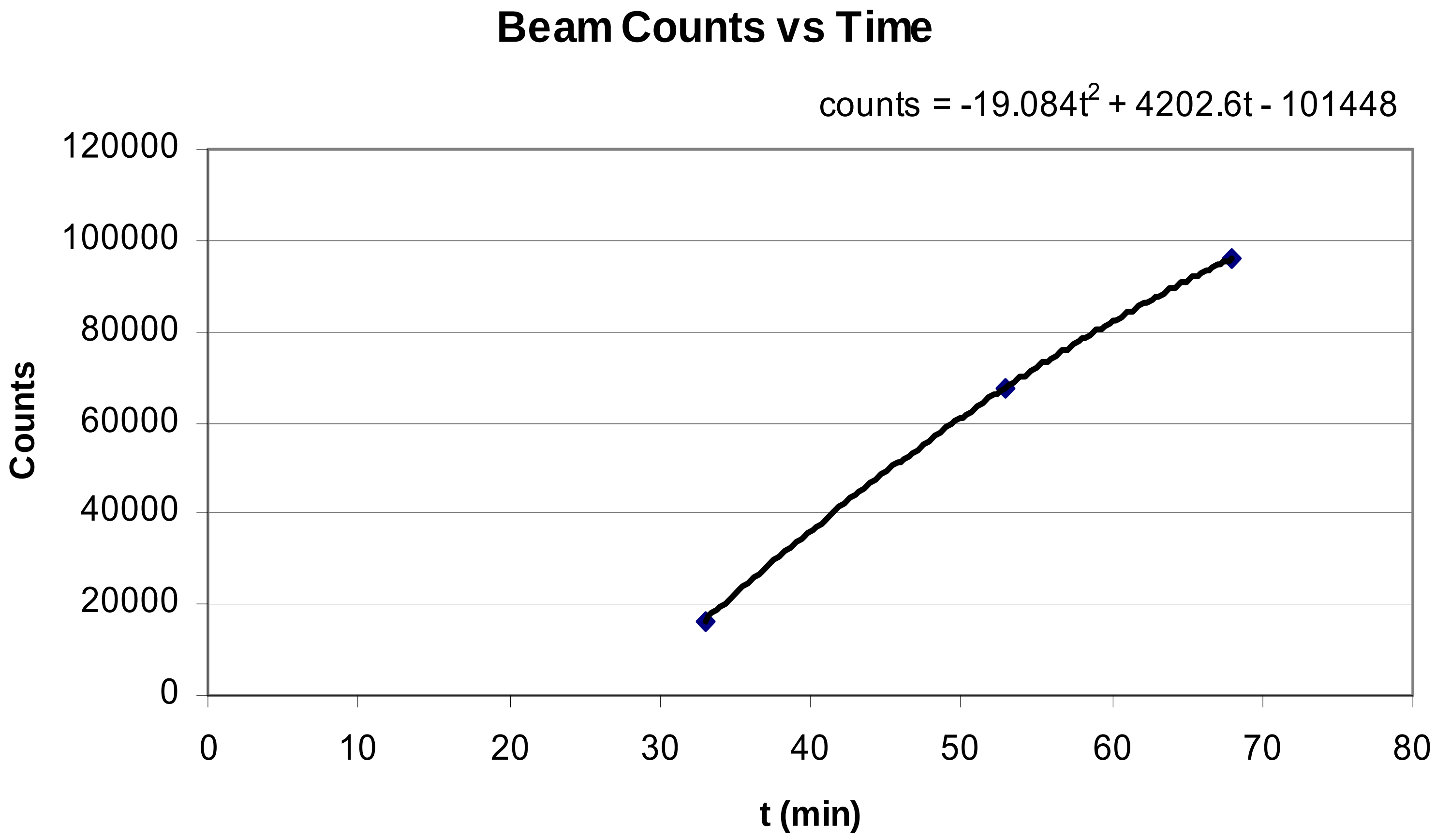

Figure 5 – Undiffracted counts as a function of time.

Al target x-ray undiffracted spectrum

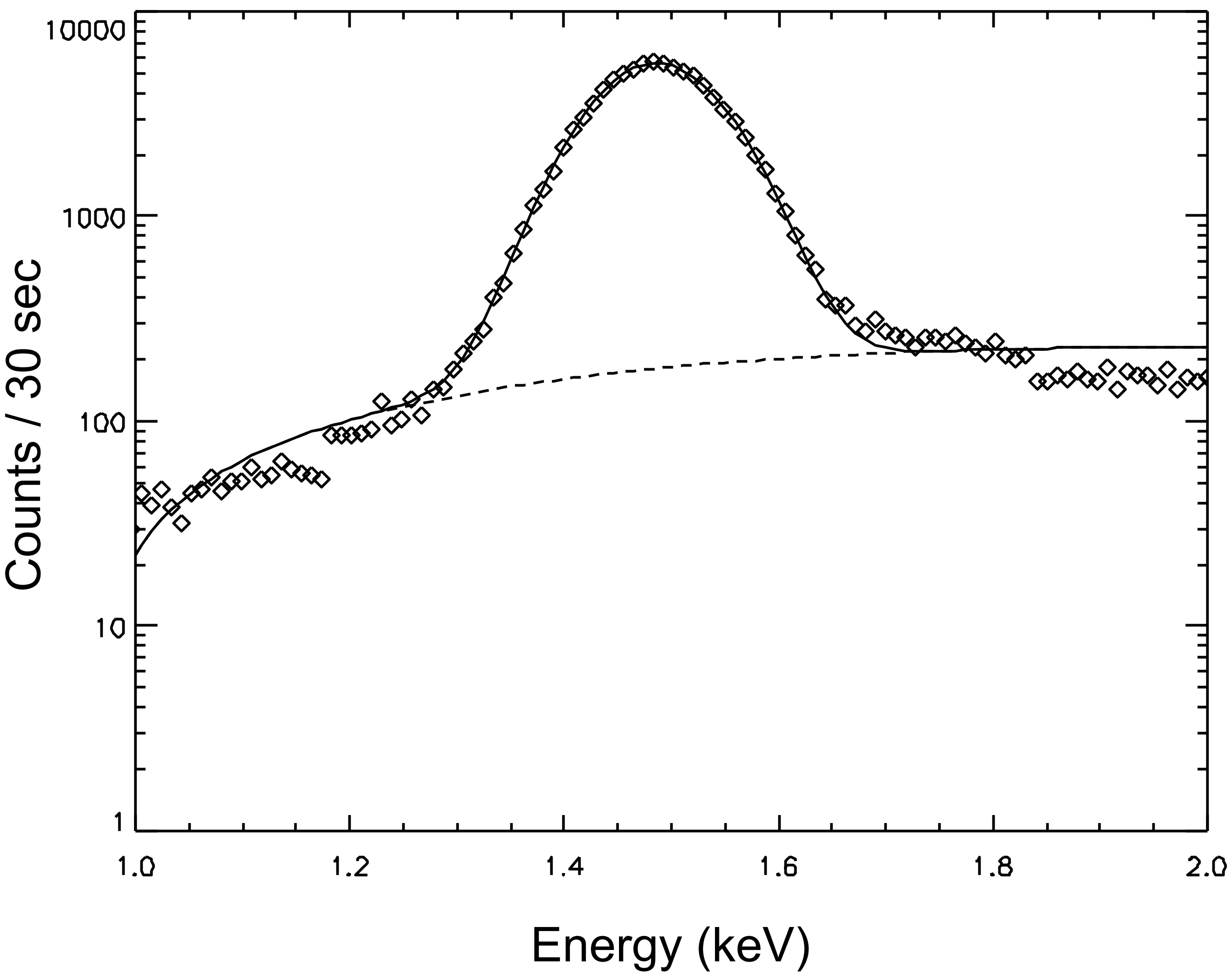

Figure 6 –Gaussian + quadratic fit to the un-diffracted spectrum. The diamonds represent the actual counts observed, the solid line represents the fitted Gaussian, and the dashed line represents quadratic fit to the background.

Al target x-ray diffracted spectrum at Al Kα peak

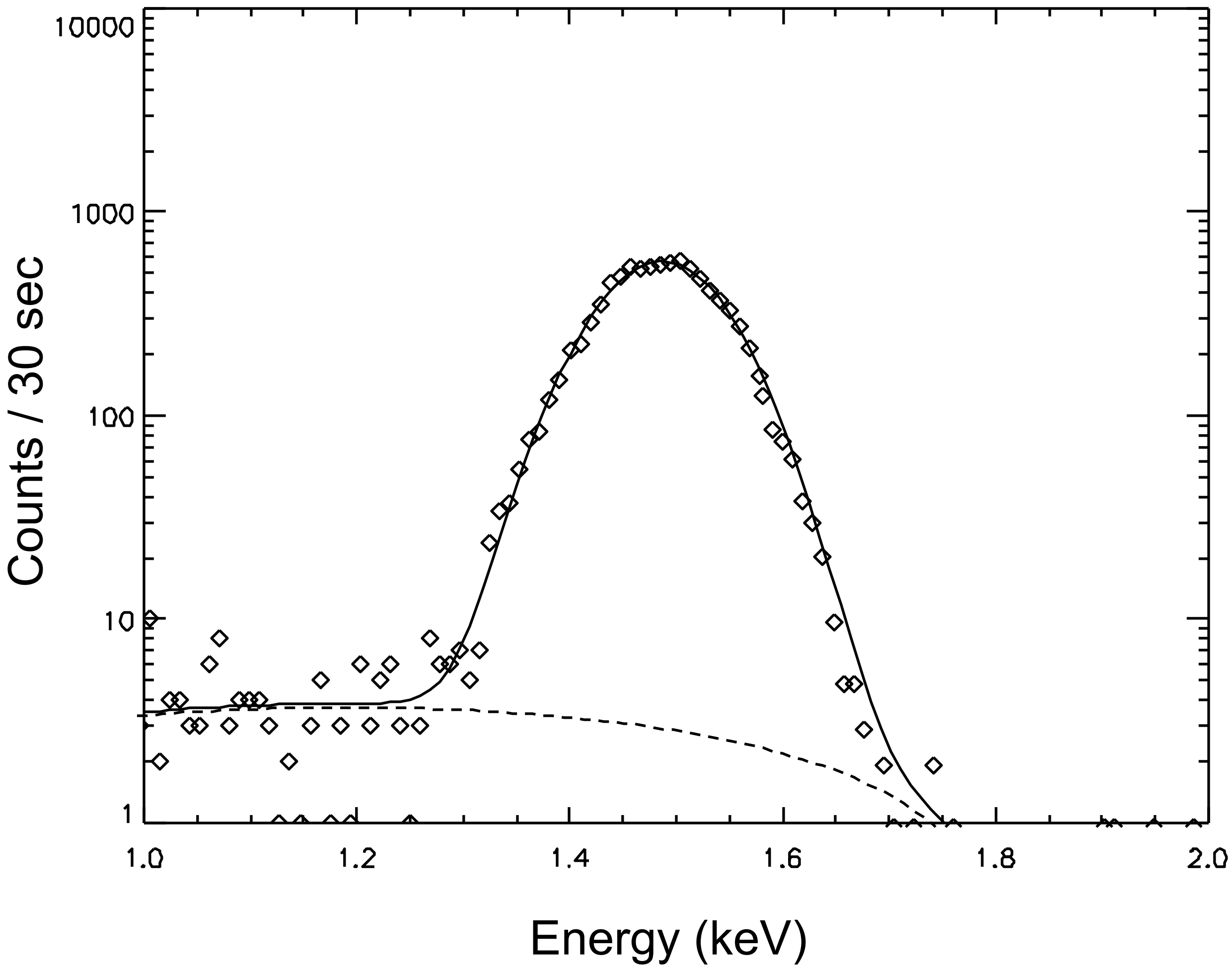

Figure 7 –Gaussian fit + quadratic fit to the diffracted spectrum. See the Figure 6 caption for details.

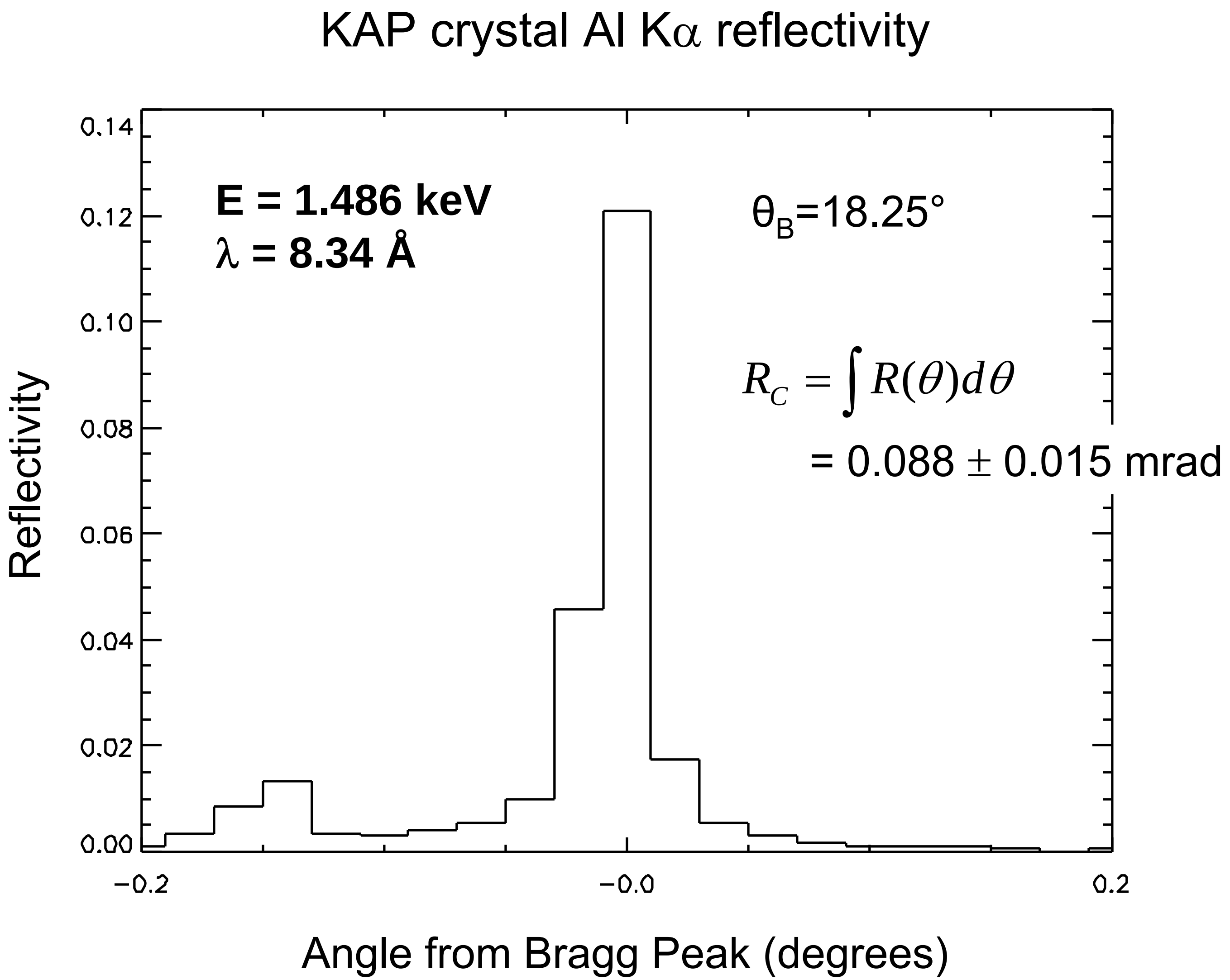

Figure 8 – KAP Crystal Reflectivity as a function of angle from the Bragg peak at 1.486 keV.

KAP crystal integrated reflectivity

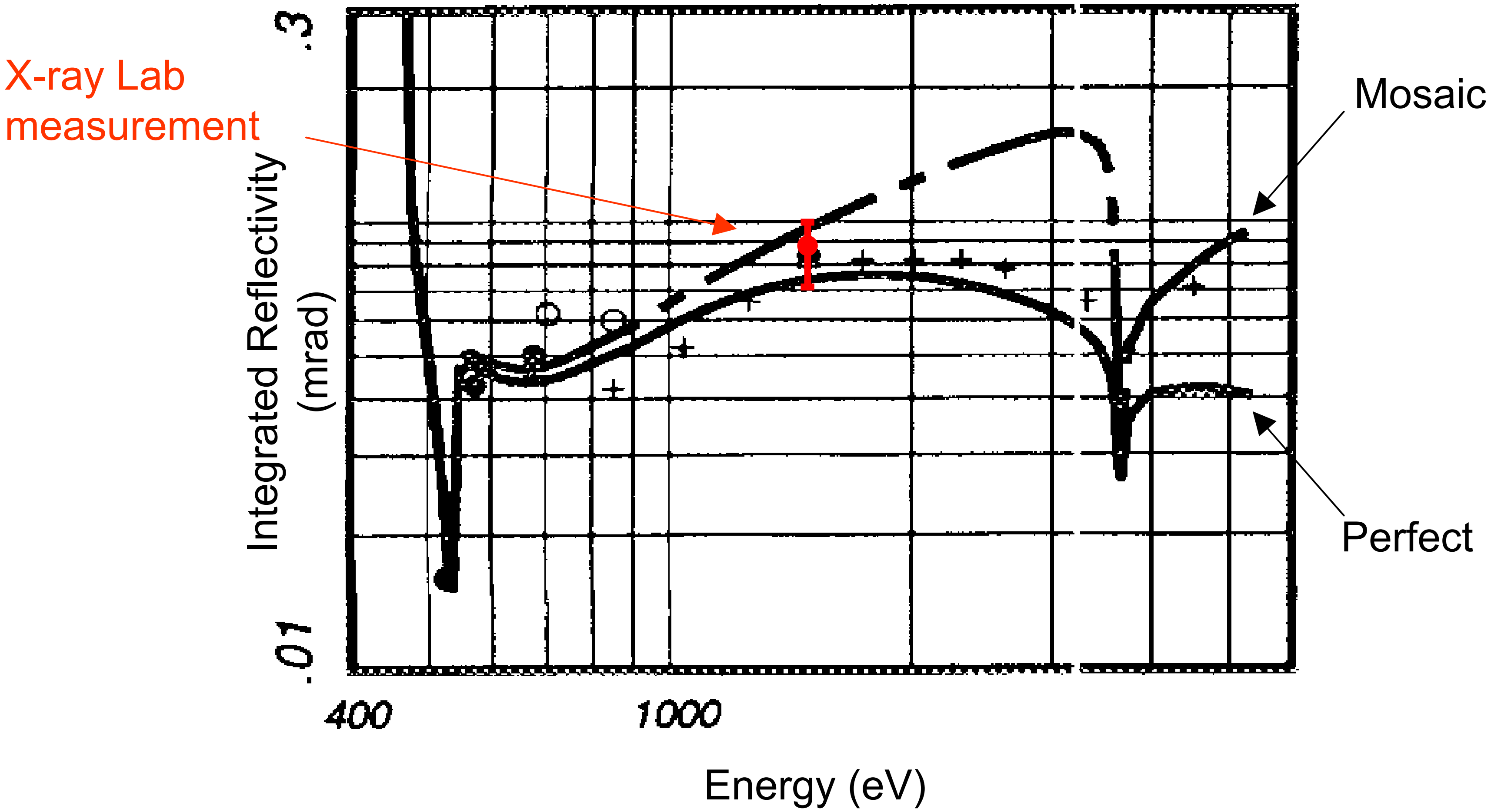

Figure 9 – Graph of KAP crystal integrated reflectivity as a function of energy. Marked in red is the value found in the x-ray laboratory at LLE.

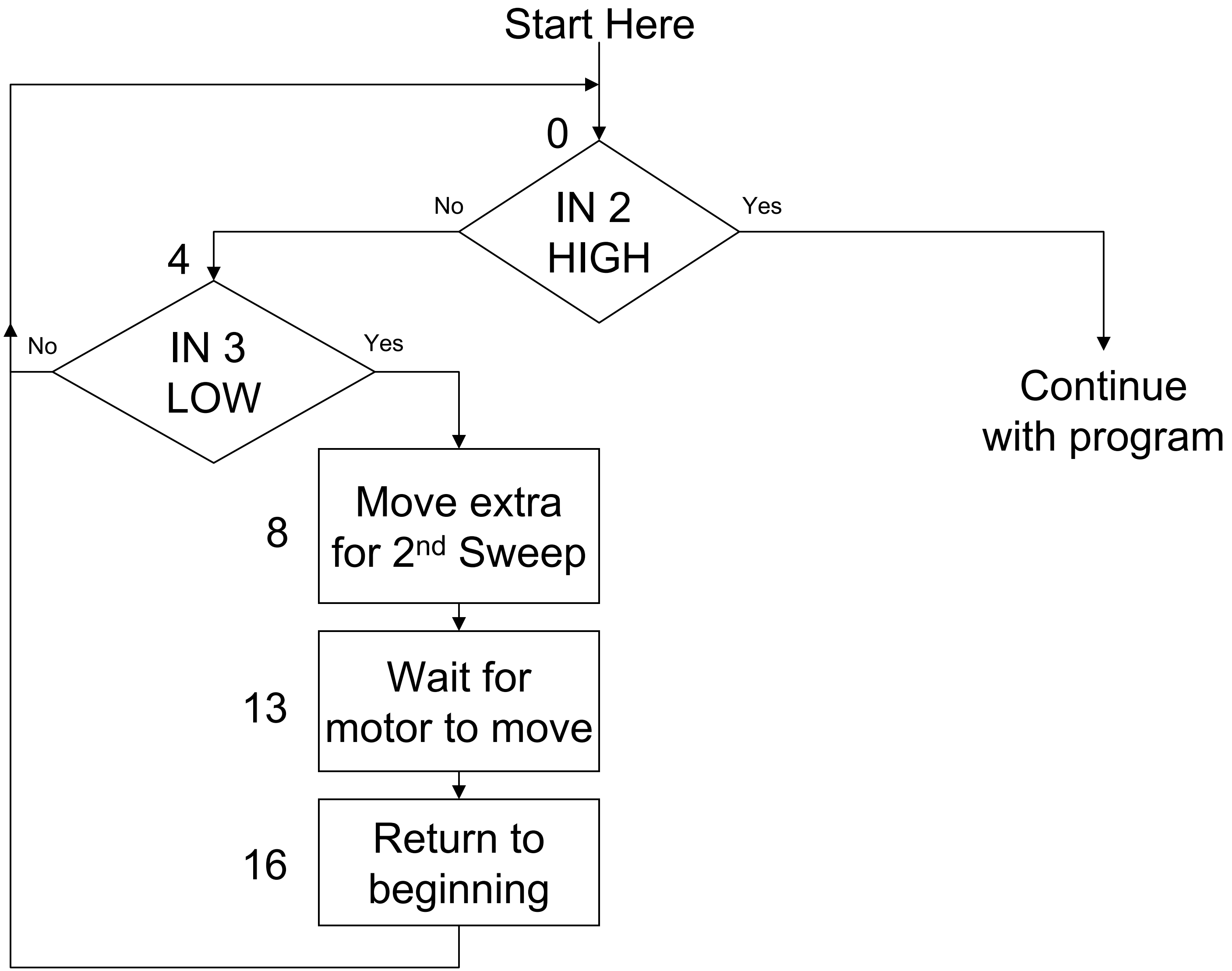

Figure A-1 – A flowchart describing program lines 0-16 on motor controllers b and c.